Inhomogeneous Phases and the Moat Regime in Nambu-Jona-Lasinio-Type Models

Dissertation
zur Erlangung des Doktorgrades
der Naturwissenschaften

vorgelegt beim Fachbereich Physik
der Johann Wolfgang Goethe-Universität
in Frankfurt am Main

von
Laurin Pannullo
aus Karlsruhe, Deutschland

Frankfurt am Main, 2023
(D30)

vom Fachbereich Physik der
Johann Wolfgang Goethe-Universität als Dissertation angenommen.

Dekan: Prof. Dr. Roger Erb

Gutachter: Prof. Dr. Marc Wagner
Prof. Dr. Christian Fischer

Datum der Disputation:

Deutsche Zusammenfassung

Im Rahmen des Standardmodells der Teilchenphysik sind Quarks die elementaren Bausteine der Materie, welche durch die starke Kernkraft zu Hadronen gebunden werden wie z.B. Baryonen, zu denen Protonen und Neutronen gehören. Diese Wechselwirkung wird durch den Austausch von Eichbosonen – den Gluonen – innerhalb der Quantenchromodynamik (QCD) beschrieben. Ein wichtiges Phänomen in der QCD ist die sogenannte spontane Symmetriebrechung, welche bedeutet, dass der physikalisch realisierte Grundzustand bei niedrigen Energien bestimmte Symmetrien nicht besitzt, die jedoch in der mikroskopischen Theorie bei hohen Energien realisiert sind. Die Brechung der sogenannten chiralen Symmetrie ist hierbei von besonderer Bedeutung und bestimmt maßgeblich das beobachtbare Massenspektrum von Teilchen.

Es ist bekannt, dass bei hohen Temperaturen, wie sie zum Beispiel in Kollisionen in Teilchenbeschleunigern auftreten, das sogenannte Quark-Gluon Plasma erzeugt und die chirale Symmetrie (näherungsweise) restauriert wird. Man spricht in der QCD somit von distinktiven thermodynamischen Phasen, welche durch die jeweils realisierte Symmetrie klassifiziert werden. Neben der Temperatur ist die Abhängigkeit dieser Phasen vom sogenannten baryon-chemischen Potential, welches die Baryonendichte kontrolliert, von großer Bedeutung. Die Erforschung des chiralen Phasendiagramms in der Ebene von Temperatur und baryon-chemischen Potential ist Gegenstand aktueller Forschung in Theorie und Experiment, jedoch auf theoretischer Seite aufgrund verschiedenster technischer Hindernisse größtenteils auf den Bereich kleiner chemischer Potentiale beschränkt.

Um zukünftige theoretische Untersuchungen und aktuelle experimentelle Bestrebungen Orientierung geben zu können, ist es jedoch wichtig zumindest qualitative Prognosen über das Phasendiagramm bei endlichen chemischen Potentialen zu formulieren. Ein zentrales Werkzeug hierfür sind Modelltheorien, die gewisse grundlegende Eigenschaften mit der QCD teilen und als effektive Beschreibung bestimmter Aspekte dieser betrachtet werden können.

Die vorliegende Arbeit verfolgt ebendiese Herangehensweise durch sogenannte Vier-Fermi-Modelle – vorangestellt das Nambu-Jona-Lasinio-Modell, um die mögliche Existenz einer sogenannten chiralen inhomogenen Phase und des sogenannten Moat Regimes bei endlichem chemischen Potential zu untersuchen. Eine inhomogene Phase ist eine Phase, die im Phasediagramm der QCD existieren könnte, bei der sowohl die chirale Symmetrie als auch die Translationsinvarianz der Theorie spontan gebrochen. Hierbei ordnet sich die Materie in einer periodischen Struktur mit einer festen Wellenlänge an, weshalb diese Phase auch kristalline Phase genannt wird. Das Moat Regime ist ein Bereich im Phasendiagramm, der sich durch eine nicht-triviale Dispersionsrelation der auftretenden Freiheitsgrade auszeichnet. Diese favorisiert zwar endliche Impulse, aber es findet keine fixe Neuordnung der Materie wie in der inhomogenen Phase statt. Beide Phänomene hängen eng zusammen und würden in Kollisionsexperimenten durch eine verstärkte Produktion von Teilchen mit endlichen Impulsen sichtbar werden. Die vorliegende Arbeit untersucht zwei spezielle Aspekte der inhomogenen Phase und des Moat Regime in Vier-Fermi-

Modellen, um die physikalische Relevanz dieser Modellvorhersagen abzuschätzen. Dies sind die Regularisierungschemaabhägigkeit in Modellen in drei Raumdimensionen und die Abhängigkeit von der Anzahl der Raumdimensionen, was in den folgenden beiden Abschnitten näher erläutert wird.

Einige QCD-ähnliche Modelle in drei Raumdimensionen, zu denen auch das Nambu-Jona-Lasinio-Modell gehört, weisen eine inhomogene Phase auf. Dieses Modell ist jedoch nicht renormierbar, d.h., dass in dem Modell Divergenzen bei hohen Energien auftreten, welche nicht mit geeignet gewählten Parametern absorbiert werden können. Daher muss ein sogenanntes Regularisierungsschemas gewählt werden, um diese Divergenzen zu kontrollieren. Davon hängen die berechneten Ergebnisse möglicherweise ab. In dieser Arbeit wird systematisch untersucht, inwiefern Existenz und Ausmaß der inhomogenen Phase und des Moat Regimes von der Wahl des Regularisierungsschemas abhängt. Der Einfluss der verwendeten Regularisierung auf die inhomogene Phase ist hierbei erheblich, bis hin zur vollständigen Abwesenheit dieser Phase für gewisse Schemen. Des Weiteren bestätigt diese Arbeit die Vermutung, dass die Abhängigkeit des Moat Regimes von der Regularisierung deutlich geringer ist und es somit als ein robusteres Phänomen erscheint.

Während die Existenz der inhomogenen Phase in einer Raumdimension in diversen Modellen innerhalb der sogenannten Molekularfeldnäherung gesichert ist, ist sie in Modellen in zwei Raumdimensionen scheinbar abwesend und in drei Raumdimensionen, wie zuvor erwähnt, stark von der Regularisierung abhängig. Daher wird in dieser Arbeit zudem die Abhängigkeit der Existenz der inhomogenen Phase und des Moat Regimes von der Dimensionalität der Raumzeit untersucht. Um dieser Fragestellung nachzugehen, wird die inhomogene Phase in einem einfachen Vier-Fermi-Modell – dem Gross-Neveu Modell – in nicht ganzzahligen Raumdimensionen analysiert. Dies ermöglicht es, den Effekt der Anzahl der Raumdimensionen als isolierten Parameter zu untersuchen und es kann gezeigt werden, dass ausschließlich diese für das Verschwinden der inhomogenen Phase in zwei Raumdimensionen verantwortlich ist. Darüber hinaus gestattet diese Untersuchung auch die Schlussfolgerung, dass die Existenz der inhomogenen Phase in Nambu-Jona-Lasinio-artigen Modellen in drei Raumdimensionen ausschließlich durch die Verwendung eines Regularisierungschemas erzeugt wird. Dies bedeutet nicht zwingend, dass die inhomogene Phase in diesen Modellen ein reines Artefakt ist, da die Regularisierung ein wichtiger Bestandteil in der Interpretation solcher Modelle als Niederenergiebeschreibung der QCD ist. Jedoch betont dieses Ergebnis noch stärker die Signifikanz der Wahl des Regularisierungsschemas in solchen Modelluntersuchungen von inhomogenen Phasen, welche nicht nur aufgrund von technischen, sondern auch phänomenologischen Aspekten getroffen werden muss.

Contents

Chapter 1

Introduction

As of our current understanding, quarks are the fundamental building blocks of matter and do not possess a substructure. In the vacuum, they are bound to hadrons by the strong force, which is described as being mediated by massless gluons by the SU(3)-symmetric gauge theory named Quantum Chromodynamics (QCD).

Despite its simple action and being formulated over 50 years ago [1, 2], our knowledge about QCD is far from complete. One of the long-standing frontiers in this field of research is the so-called chiral phase diagram of QCD in the plane of temperature T and baryon chemical potential μ. Quarks exhibit the property of chirality or 'handedness', which corresponds to quarks transforming under different representations – left- and right-handed – of the Poincaré group. For massless quarks, one finds that chirality corresponds to the helicity of the particle (alignment of spin with respect to its momentum) and that the action of QCD exhibits chiral symmetry, i.e., invariance under independent chiral transformations of left- and right-handed quarks. Although chiral symmetry in QCD is explicitly broken by the bare quark masses, the light quark masses are small enough such that one retains an approximate symmetry for them. The features in black in Fig. 1.1 sketch what we know about the chiral phase diagram with high certainty.[1] At low temperatures and chemical potentials, the chiral symmetry is spontaneously broken.[2] Signaling the breaking of this symmetry, one finds a chiral condensate $\langle\bar{\psi}\psi\rangle$ that is non-zero and constant in space, i.e., *homogeneous*. Furthermore, the pions are the would-be Nambu-Goldstone bosons with a small mass.[3] We refer to such a phase as homogeneously broken phase (HBP).

When increasing the temperature at vanishing chemical potential, one finds a crossover to the quark-gluon-plasma [6]. In this phase, chiral symmetry is approximately restored, which is signaled by the chiral condensate being approximately zero up to a contribution from the explicit breaking. Due to the chiral symmetry being (approximately) restored, we refer to such a phase as symmetric phase (SP). The crossover line bends down to lower temperatures for increasing chemical potential [7–11]. While these results represent monumental achievements, the chiral phase diagram of QCD in the (μ, T)-plane remains largely unknown as is evident from the absence of any additional black colored features in Fig. 1.1.

The main obstacle responsible for our ignorance of the phase structure at intermediate chemical

1 Note that this only mentions the chiral phases. It is known that there is a Liquid-gas transition of nuclear matter at intermediate chemical potentials and small temperatures. From perturbative calculations of QCD, it is also clear that there is a color superconducting phase for very large chemical potentials [3]. Recently, it was found that there is an approximate chiral spin symmetry realized above the chiral pseudocritical temperature, which is broken again at very large temperatures [4, 5]. While being important, these features of the phase diagram are not key for this work and thus we omitted them for clarity.

2 Here, quarks are also confined to hadrons. However, it is not clear yet, if and how these two phenomena are linked [4, 5].

3 They would be massless, if the chiral symmetry would not be broken explicitly.

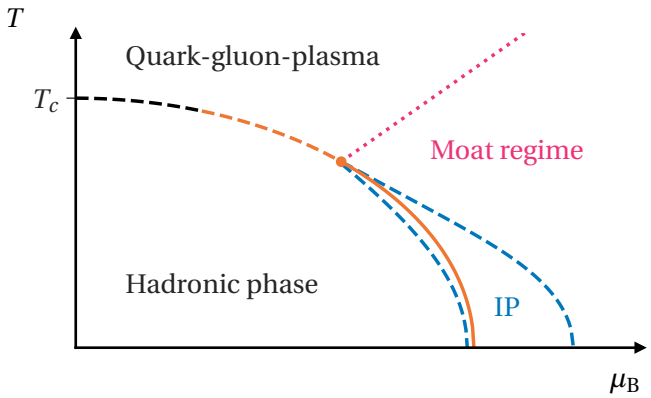

Figure 1.1: A sketch of a conjectured chiral phase diagram of QCD. The black features represent boundaries that are confirmed from theory [7–11]. The colored features represent various conjectures about the phase structure that are explained in the main text. Solid lines are first order phase boundaries, dashed lines are second order boundaries and crossovers, and the dotted line marks the border of the moat regime that is not a real phase boundary. The acronym stands for inhomogeneous phase (IP).

potentials is the infamous sign problem, which hinders first-principle lattice QCD calculations. Other challenges currently prohibit functional methods, such as the functional renormalization group (FRG) [9] or Dyson-Schwinger equation (DSE) calculations [10, 11], from reliably exploring the phase diagram in this region. Thus, with little first-principle evidence, there is a plethora of conjectures about the possible phase structure, which are mainly fueled by calculations in various models. Especially relevant for the chiral phase diagram are the Nambu-Jona-Lasinio (NJL) model [12–14] or quark-meson (QM) model [14–16].[4] As these models form the basis of our expectations regarding the low-energy behavior of QCD, it is important to understand the nature of their results, their range of validity and their relevance for the phase diagram of QCD.

The colored features in Fig. 1.1 show the various parts of the conjectured scenario that we are concerned with in this thesis. The orange part depicts the expectation that the crossover ends in a critical endpoint (CP) at a finite temperature beyond which a first-order phase transition extends down to zero temperature [20]. While this scenario is expected by a large part of the community, it has neither been rigorously confirmed by experiment nor by first-principle theory calculations.[5] Confirming the existence of the CP is the main focus of many current experimental and theoretical efforts [9, 21–26].

Chiral Inhomogeneous Phases

The main focus of the present work is a possibility that is less frequently discussed: the existence of an inhomogeneous phase (IP), sketched in blue in Fig. 1.1. In this phase, one expects a chiral condensate, which is non-zero and exhibits a spatial dependence, i.e., it is *inhomogeneous*. This condensate does

4 Note that both of these are chiral models that do not incorporate the effect of gauge fields and as such they do not exhibit confinement. There are also more involved models that incorporate effects from Polyakov loops, see e.g. Refs. [17–19]

5 The closest results here are obtained with functional methods like the FRG or DSE calculations. Even though these methods start from QCD, they have to impose truncations to their fundamental equations, which can introduce artifacts into the results. Studies with these methods predict the existence of a CP. It is, however, located in a region of the phase diagram, where the results only posses limited validity [9–11].

not only break chiral symmetry, but also translational invariance spontaneously. Such a phase has been observed in various models that bear similarities with QCD (see the detailed discussions in Chapter 3 and for a review Ref. [27]). Arguably, the most prominent examples are the $(1+1)$-dimensional Gross-Neveu (GN) model [28, 29] and the $(3+1)$-dimensional NJL model [14, 30, 31], which is regarded as a low-energy effective model of QCD with respect to its chiral properties. There are even indications for the realization of such a phase in QCD from DSE calculations [32].

Most results find an IP at intermediate chemical potentials and low temperatures between the HBP and SP. To understand this particular location, we consider some general fermionic theory at zero temperature, where a homogeneous chiral condensate forms in vacuum. By increasing the chemical potential, we increase the imbalance of fermions over anti-fermions. This puts tension on the symmetry breaking homogeneous chiral condensate $\bar{\psi}\psi$, which is a condensate formed of a fermion and an anti-fermion with equal momenta of opposite sign totaling zero total momentum [27, 33]. In a purely homogeneous picture, we expect this condensate to melt at a critical chemical potential, when the imbalance is too large for the condensate to remain favored. An inhomogeneous condensate on the other hand pairs a fermion and a fermion-hole of opposite momenta at the Fermi-surface $p \approx p_F = \mu$ [27, 33]. Thus, by creating such an inhomogeneous condensate of total momentum $q = 2\mu$, the system can evade the complete melting of the condensate for some range of the chemical potential. This mechanism is essentially the high-energy description of the Peierls instability (see Section 3.1.3 and Ref. [34]). This argumentation is of course a rather simplified picture, which assumes a sharp Fermi surface (and is thereby only valid for zero temperature) and might not be valid in higher dimensions where the extra dimensions might spoil the pairing mechanism.

The existence of an IP could have profound implications on the phase diagram. The majority of model results, e.g., Refs. [14, 28, 29, 35], suggest that a possible first order phase boundary of the HBP might be completely engulfed by the IP. In most scenarios the CP coincides with the so-called Lifshitz point (LP) from which the IP opens up. Furthermore, the IP is expected to form in a region, where color superconducting phases are predicted by other models. This might lead to a coexistence of an inhomogeneous chiral condensate and a diquark condensate [36]. Moreover, the equation of state in such a phase is different from that of the ordinary SP, which could have implications on objects like neutron stars that are located in the cold-dense regime of the QCD phase diagram. It was, however, found that the impact on the equation of state most likely is small and the existence of an IP has a negligible impact on the mass-radius relation of neutron stars [37]. Thus, this is not a suitable experimental probe to study the existence of an IP. As discussed in the next section, heavy-ion collision might be a better setup to observe an IP and the related moat regime.

The Moat Regime

Fig. 1.1 depicts the so-called moat regime[6] [38] in pink as the remaining part of the conjectured chiral phase diagram. It is closely tied to the IP and can be regarded as a precursor phenomenon thereof [39]. The moat regime is characterized by a non-trivial meson dispersion relation that exhibits a minimum at a non-zero spatial momentum. While this does not necessarily favor an inhomogeneous condensate, it favors particles at this non-vanishing momentum. This would be observable in a heavy-ion collision, if the μ-T-trajectory of the collision matter crosses the moat regime. Then, a particle production that

6 It is called “regime” instead of “phase” as it is not a phase of its own in a thermodynamical sense.

is peaked at a non-zero momentum should be detectable [38, 40–42].[7] A recent investigation of the $(1+1)$-dimensional GN model [39] and FRG calculations of QCD [9] suggest that this regime could already exist at moderate chemical potentials and relatively high temperatures, thus covering a large portion of the phase diagram.

Research Rationale

The general research direction of this work is the investigation of the IP and the moat regime in models that share similarities with QCD. The vast majority of such studies are conducted in the so-called mean-field approximation (MFA), which is a semi-classical approximation that neglects quantum fluctuations for the bosonic degrees of freedom in these models (see Section 2.2). The impact of going beyond this approximation depends on the model and number of space-time dimensions. It can be severe as, e.g., the absence of any condensation at finite temperature as found in Ref. [43], or be limited to altered extents of the phases in the phase diagram as, e.g., found in Refs. [16, 44, 45]. Hence, to come closer to QCD and solidify the predictions made by such models, it is important to study them beyond the MFA. While there are studies with functional methods that investigated the IP in higher-dimensional models that are relevant for QCD (e.g., [16]), an independent lattice analysis is missing up to this date. Lattice Monte-Carlo simulations proved to be an excellent tool for such studies with a focus on the IP in the simple $(1+1)$-dimensional GN model [46, 47]. Building on the expertise from these studies, the original plan of this thesis was to conduct similar studies in higher-dimensional models and to primarily answer the research question:

Q1 *Do inhomogeneous phases exist in higher-dimensional QCD-inspired models beyond the mean-field approximation?*

It became clear that common NJL-type models that exhibit an IP in the MFA in $1+1$ dimensions, lack this phase in $2+1$ dimensions [48–51]. Since bosonic fluctuations typically weaken ordered phases (see, e.g., [43, 44, 46, 52]), it is highly likely that the IP is absent in these models also beyond the MFA. Thus, to answer research question Q1 a study of $(2+1)$-dimensional models was discarded and the $(3+1)$-dimensional NJL model that features an IP in the MFA (see Section 3.2 and, e.g., Refs. [14, 27, 30, 31]) was chosen to be studied via lattice Monte-Carlo simulations.

A caveat of this model is its non-renormalizability. We cannot remove the regulator, but have to keep it at a finite value rendering it a parameter of the theory. This gives rise to the possibility that results of the IP depend on the regularization scheme and are not universal. Even though the homogeneous phase structure of the NJL model has been investigated previously with lattice Monte-Carlo simulations [45], it was not clear whether the emergence of the IP is spoiled by a lattice discretization (as one cannot take the continuum limit due to the non-renormalizability). Past investigations studied the regulator dependence of this model [53–55], but they were neither systematic with respect to the IP nor did they consider lattice regularizations. Moreover, the concept of the moat regime has only been recently introduced, and this regime has not been yet mapped out in this model. This motivated a preceding investigation of the $(3+1)$-dimensional NJL model within the MFA that sought to answer the questions:

Q2 *Are lattice discretizations a suitable regularization scheme to investigate the inhomogeneous phase in the* $(3+1)$*-dimensional Nambu-Jona-Lasinio model?*

7 For a moat regime, this is expected to be a rather broad peak, but if an IP is in fact present, one would expect a δ-peak at a non-zero momentum.

Q3 *Is there a significant impact of the regularization scheme on the inhomogeneous phase in the* $(3+1)$*-dimensional Nambu-Jona-Lasinio model?*

Q4 *What is the extent of the moat regime in the* $(3+1)$*-dimensional Nambu-Jona-Lasinio model and does it depend on the regularization scheme?*

The finding that finite regulators generate an IP in $(2+1)$-dimensional NJL-type models [49], the absence of IPs from a large class of $(2+1)$-dimensional models [48, 49, 51], and the results of the investigations that were meant to answer research questions Q2 and Q3 motivated further research questions:

Q5 *What is the reason for the disappearance of the inhomogeneous phase when going from* $(1+1)$*-dimensional to* $(2+1)$*-dimensional Nambu-Jona-Lasinio-type models?*

Q6 *Is the existence of the inhomogeneous phase in* $(3+1)$*-dimensional Nambu-Jona-Lasinio-type models caused by a finite regulator?*

Even though it is paramount to confirm the existence of IPs beyond the MFA, it has become clear that such a phase and the conditions for its emergence have not yet been fully understood even in the MFA. Although going beyond the MFA was the original goal, research questions Q2 to Q6 can be answered within the MFA and thus all studies in this thesis are conducted in the MFA. Moreover, the results of the investigations that sought to answer research questions Q2 and Q3 (see Chapter 6) make it evident that research question Q1 cannot be answered via lattice Monte-Carlo simulations of the $(3+1)$-dimensional NJL model. We discuss other possible steps towards answering this question in Chapter 8.

Outline of this Thesis

Chapter 2 discusses basic concepts that are vital to calculations within NJL-type models in the MFA. In Chapter 3, we present relevant literature results of specific NJL-type models, primarily focusing on the GN and NJL model, to provide the appropriate context for the main investigations. Different techniques to study the IP and the derivation of the stability analysis technique used in this work are presented in Chapter 4. Chapter 5 benchmarks the stability analysis against the fully solved $(1+1)$-dimensional GN model to study the reliability of this technique. The investigation of the $(3+1)$-dimensional NJL model within the MFA in Chapter 6 provides answers to research questions Q2 to Q4. Chapter 7 focuses on answering research questions Q5 and Q6 by considering the GN in non-integer spatial dimensions in the MFA. We end this thesis by a summary of the key results of the different investigations, the main conclusions to answer research questions Q2 to Q6, and a discussion of further possible steps in Chapter 8. The Appendices contain comments on notation and conventions in Appendix A, some remarks about the Clifford algebra and symmetries of fermions in Appendix B, a collection of relevant formulas for the results of Chapter 6 in Appendix C, and the calculations that correspond to the results as presented in Chapter 7 in Appendix D.

Chapter 2

Nambu-Jona-Lasinio-Type Models in the Mean-Field Approximation

Disclosure *This chapter discusses Nambu-Jona-Lasinio (NJL)-type models, relevant techniques and notation. As such, most aspects are not particularly original to this work and serve rather as a general introduction of how these models are commonly treated.*

In this chapter, we aim to introduce the type of four-fermion (FF) models that the investigations in Chapters 5 to 7 are based on. We call this type of models Nambu-Jona-Lasinio (NJL)-type models, which encompasses all FF models with scalar and pseudoscalar interaction channels. In particular, this includes the Gross-Neveu (GN) model and the eponymous NJL model.

We start by introducing a rather general template model denoted as general Nambu-Jona-Lasinio (gNJL) model from which one can extract the GN or NJL model that our investigations focus on. The most important aspects and techniques in investigations of FF models are discussed using this model in Section 2.1. We continue by discussing the mean-field approximation (MFA) in Section 2.2, within which the later investigations are performed. In Section 2.3, we cover the most important aspects of regularization and renormalization for these models.

2.1 General Nambu-Jona-Lasinio Model

We define the general Nambu-Jona-Lasinio (gNJL) model under the influence of a chemical potential via the Euclidean Lagrange density[1]

$$\mathcal{L}_{\text{gNJL}} = \bar{\psi}(x)(\not{\partial} + \gamma_0\mu)\psi(x) - \left[G_{\text{S}}\left(\bar{\psi}(x)\psi(x)\right)^2 + G_{\text{PSI}}\left(\bar{\psi}(x)\mathrm{i}\gamma_{\text{ch}}\vec{\tau}\psi(x)\right)^2\right], \tag{2.1}$$

where $\bar{\psi}$,ψ are fermion spinors with $\overline{N} = N_\gamma \times N_f \times N$ degrees of freedom. N_γ is the dimension of the representation of the Clifford algebra, i.e., the dimensions of the γ-matrices (see Appendix B.1 for the relevant notation and a basic discussion of the Clifford algebra). N_f is the number of fermion flavors on which the matrices $\vec{\tau}$ act, which are the $N_f^2 - 1$ generalized $N_f \times N_f$ Gell-Mann matrices

1 Technically, the chemical potential is introduced on the level of the partition function and is not a part of the Lagrange density. However, for simplicity we include it already in the Lagrange density.

[56].[2] N denotes all other degrees of freedom in which the interaction vertices of the FF interactions are diagonal, e.g., N_c colors.[3] Generically, we call this degree of freedom "species", whenever we refer to it without a special physical connotation. To ease notation, we implicitly assume unit matrices in the respective diagonal spaces in fermion bilinear terms. The chemical potential μ is a Lagrange multiplier that fixes the expectation value of the fermion density $\langle\bar{\psi}\gamma_0\psi\rangle$ in the path integral. The Dirac matrix γ_{ch} anti-commutes with the space-time Dirac matrix and is also known as γ_5 in $D = 4$ space-time dimensions. The FF interaction $(\bar{\psi}\psi)^2$ is referred to as scalar interaction and $(\bar{\psi}i\gamma_{\text{ch}}\vec{\tau}\psi)^2$ as pseudoscalar (isovector) interaction. These names stem from the transformation behavior of the bilinears under Lorentz transformations. The respective couplings G_{S} and G_{PSI} are introduced as separate variables in order to switch off some of the channels easily to conveniently obtain different models from the same basic Lagrangian. In practice, these couplings are either set to zero or to the same value in order to obtain the Lagrangian of either the GN or NJL model (see Chapter 3). Therefore, the gNJL model serves rather as a common template to unify the derivation and discussion of key quantities than as an actual model of interest.

The partition sum for the gNJL model is represented by the functional integration of the Boltzmann weight over the Grassmann-valued fields $\bar{\psi}$ and ψ

$$\mathcal{Z} = \mathcal{N}\int \mathcal{D}\bar{\psi}\,\mathcal{D}\psi\; \mathrm{e}^{-\mathcal{S}[\bar{\psi},\psi]}, \tag{2.2}$$

where $\mathcal{N}$ is an overall normalization constant such that $\mathcal{Z} = 1$. The Euclidean action is

$$\mathcal{S}\left[\bar{\psi},\psi\right] = \int_0^\beta \mathrm{d}x_0 \int_V \mathrm{d}^d x\, \mathcal{L}_{\text{gNJL}} = \int \mathrm{d}^D x\, \mathcal{L}_{\text{gNJL}} \tag{2.3}$$

with the integration of the temporal coordinate over the compactified extent β, which is the inverse temperature, the d-dimensional spatial integration over the volume V and the number of space-time dimensions D.

2.1.1 Bosonization of the Partition Function

A commonly used transformation of the partition function of FF models is the Hubbard-Stratonovich (HS) transformation, which enables us to eliminate FF interactions by introducing auxiliary bosonic fields. Essentially, the HS is a reversed Gaussian integration on the level of the path integral. We consider the 1-dimensional shifted Gaussian integral

$$\int_{-\infty}^{\infty} \mathrm{d}x \exp\left(-\frac{ax^2}{2} + yx\right) = \sqrt{\frac{2\pi}{a}}\,\exp\left(\frac{y^2}{2a}\right) \tag{2.4}$$

2 These are the three Pauli matrices for $N_f = 2$.

3 It should be noted at this point that all models considered in this work do not contain any gauge fields. Therefore, all interactions are diagonal in the color degree of freedom, causing N_c to appear, at most, as a multiplicative factor. This degree of freedom is introduced nevertheless to facilitate the interpretation of the NJL model as a low-energy effective model for Quantum Chromodynamics (QCD).

and extend it to the functional integral identity

$$\int \mathcal{D}\phi \ \exp\left[-\int \mathrm{d}^D x \left(\frac{a\phi^2(x)}{2} \pm J(x)\phi(x)\right)\right] = \mathcal{N} \exp\left[\int \mathrm{d}^D x \frac{J^2(x)}{2a}\right], \tag{2.5}$$

where ϕ is a generic bosonic field and $\mathcal{N}$ is some normalization constant. Using this to transform the FF interactions in Eq. (2.1) by setting $J = (\bar{\psi}\psi), \phi = \sigma$ and $J = (\bar{\psi}\mathrm{i}\gamma_{\mathrm{ch}}\vec{\tau}\psi), \phi = \vec{\pi}$ results in the partially bosonized partition function

$$\mathcal{Z}_\phi = \mathcal{N} \int \mathcal{D}\bar{\psi}\,\mathcal{D}\psi\,\mathcal{D}\sigma\,\mathcal{D}\vec{\pi}\ \mathrm{e}^{-\mathcal{S}_\phi[\bar{\psi},\psi,\sigma,\vec{\pi}]} \tag{2.6}$$

with the partially bosonized action

$$\mathcal{S}_\phi\left[\bar{\psi},\psi,\sigma,\vec{\pi}\right] = \int \mathrm{d}^D x \left[\frac{1}{4}\left(\frac{\sigma^2}{G_{\mathrm{S}}} + \frac{\vec{\pi}^2}{G_{\mathrm{PSI}}}\right) + \bar{\psi}\mathrm{Q}\psi\right] \tag{2.7}$$

and the Dirac operator

$$\mathrm{Q} = \not{\partial} + \gamma_0\mu + \sigma + \mathrm{i}\gamma_{\mathrm{ch}}\vec{\tau}\cdot\vec{\pi}. \tag{2.8}$$

There is a quadratic mass term for each of the newly introduced auxiliary fields, but no kinetic term reflecting that they are only auxiliary degrees of freedom. In addition, there are corresponding Yukawa interaction terms of the form $\bar{\psi}\phi\psi$, which act as dynamically generated mass terms for the fermion fields.

The bosonized partition function is equivalent to the original partition function of the gNJL model, since we only used identities in the transformation. A major advantage of the bosonized form is that the fermionic fields only appear in bilinear form, which facilitates a simpler treatment of such models on the analytical and numerical level. Moreover, it grants direct access to the (effective) degrees of freedom that are present in the system. In regions of the phase diagram, where a chiral condensate forms, the relevant degrees of freedom are the bosonic ones. In the purely fermionic form of the theory, incorporating these degrees of freedom is challenging and is realized by considering momentum dependent interactions. If one does not do this, one lacks the appropriate degrees of freedom, which is signaled by a divergence of the FF coupling, see e.g. Ref. [57] for a discussion of this.

The newly introduced bosonic fields are connected to the corresponding fermionic bilinears via the Ward identities

$$\left\langle\bar{\psi}(x)\psi(x)\right\rangle = \frac{-\langle\sigma(x)\rangle}{2G_{\mathrm{S}}}, \quad \left\langle\bar{\psi}(x)\mathrm{i}\gamma_{\mathrm{ch}}\vec{\tau}\psi(x)\right\rangle = \frac{-\langle\vec{\pi}(x)\rangle}{2G_{\mathrm{PSI}}}, \tag{2.9}$$

where the $\langle\cdot\rangle$ denotes the path-integral expectation value. A derivation of such identities can be found in, e.g., Ref. [58]. Using these identities allows us to study fermionic quantities such as the chiral condensate solely by inspecting the bosonic fields. This is especially advantageous in certain setups such as lattice investigations, where the direct calculation of fermionic observables is computationally expensive.

2.1.2 Yukawa-Type Models

Closely related to FF models are Yukawa-type models, which can be considered as an extension of the bosonized action of FF models. These models feature additional kinetic terms for the bosonic fields and a more complicated bosonic potential. While we do not conduct calculations within these Yukawa-type

models, we briefly outline some central aspects and their relation to the FF models to give some context to their discussion in Chapters 3 and 8.

We define the action of the Yukawa extension for the gNJL action as

$$\begin{aligned}\mathcal{S}_Y\left[\bar{\psi},\psi,\sigma_Y,\vec{\pi}_Y\right] = \int \mathrm{d}^D x \Big[\bar{\psi}\left(\partial\!\!\!/ + \gamma_0\mu + h\sigma_Y + h\mathrm{i}\gamma_{\mathrm{ch}}\vec{\tau}\cdot\vec{\pi}_Y\right)\psi + \\ + \tfrac{1}{2}\left(\partial_\nu\vec{\pi}_Y(x)\right)^2 + \tfrac{1}{2}\left(\partial_\nu\sigma_Y(x)\right)^2 + U\left(\sigma_Y,\vec{\pi}_Y\right)\Big],\end{aligned} \tag{2.10}$$

where h is the Yukawa coupling, we introduced the rescaled fields $\sigma_Y = \sigma/h, \vec{\pi}_Y = \vec{\pi}/h$ and U is a general bosonic potential. We note that for $D \neq 4$, the Yukawa coupling h is a dimensionful coupling with energy dimension $[h] = E^{\frac{4-D}{2}}$. Hence, also the energy dimensions of the auxiliary bosonic fields and their Yukawa equivalents might be different. The main difference to FF models is that the bosonic fields are now proper independent fields that can propagate. This is reflected by the possible self interactions enabled by U and the appearance of a kinetic term. This kinetic term also changes the canonical dimensions of the fields, which can have an impact on the renormalizability of the theory as evident from power counting arguments. This is particularly relevant in $3+1$ dimensions, where NJL-type models are not renormalizable [59] but their Yukawa extensions are [35]. However, the central features – a theory of bosonic and fermionic fields interacting via a Yukawa interaction – remain unchanged. One regains the action of the FF variant by taking the limit $h \to \infty$ and setting $U = \frac{\sigma^2}{4G_{\mathrm{S}}} + \frac{\vec{\pi}^2}{4G_{\mathrm{PSI}}}$.

For the Yukawa-type model it is possible to derive the Ward identities

$$\left\langle\bar{\psi}(x)\psi(x)\right\rangle = \left\langle\partial_\nu\partial_\nu\sigma_Y(x)\right\rangle - \left\langle\frac{\mathrm{d}U\left(\sigma_Y(x),\vec{\pi}_Y(x)\right)}{\mathrm{d}\sigma_Y(x)}\right\rangle, \tag{2.11a}$$

$$\left\langle\bar{\psi}(x)\mathrm{i}\gamma_{\mathrm{ch}}\tau_i\psi(x)\right\rangle = \left\langle\partial_\nu\partial_\nu\pi_{Y,i}(x)\right\rangle - \left\langle\frac{\mathrm{d}U\left(\sigma_Y(x),\vec{\pi}_Y Y(x)\right)}{\mathrm{d}\pi_{Y,i}(x)}\right\rangle. \tag{2.11b}$$

Even though the bosonic fields are now independent fields, one can still use them as a proxy to study fermionic condensates via these identities.

2.1.3 The Effective Action

The fermionic fields only appear in a bilinear form both in the bosonized action of the gNJL model (2.7) and the action of its Yukawa variant (2.10). Thus, we can directly integrate over them in the path integral. We restrict the following discussion to the gNJL model, but the steps are equivalent for its Yukawa extension. Carrying out the integration over $\bar{\psi}$ and ψ in the bosonized partition function (2.6) yields

$$\mathcal{Z} = \mathcal{N}\int \mathcal{D}\sigma\,\mathcal{D}\vec{\pi}\ \mathrm{e}^{-\mathcal{S}_{\mathrm{eff}}[\sigma,\vec{\pi}]} \tag{2.12}$$

with the so-called effective action[4]

$$\mathcal{S}_{\mathrm{eff}}[\sigma,\vec{\pi}] = \int \mathrm{d}^D x\,\frac{1}{4}\left(\frac{\sigma^2}{G_{\mathrm{S}}} + \frac{\vec{\pi}^2}{G_{\mathrm{PSI}}}\right) - \ln\mathrm{Det}\left[\beta\mathrm{Q}\right], \tag{2.13}$$

4 This should not be mistaken for the so-called *quantum* effective action that also incorporates the quantum effects for the bosonic fields, see, e.g., Ref. [60, pp. 364]. The effective action as shown here only contains the quantum effects for the fermionic degrees of freedom.

where Det denotes a functional determinant of the operator. Additionally, we introduce a factor β in the ln Det in order to maintain a dimensionless argument. This, however, only corresponds to an overall β-dependent factor in the path integral.

At a first glance, the effective action suggests that the bosonic fields are influenced solely by the quadratic potential terms. However, they also appear within the Dirac operator in the ln Det contribution, which encompasses all quantum effects of the fermionic fields. This then *effectively* generates additional terms involving the powers of the bosonic fields and their space-time derivatives. These terms can be seen explicitly by expanding the ln Det contribution in a power series of the bosonic fields and their derivatives (see also Section 4.1.2).

2.2 Mean-field Approximation and the $N \to \infty$ Limit

While the models under consideration may seem simpler than theories like QCD, investigating them can still pose a significant challenge. In some cases, they may be computationally expensive or impossible to explore rigorously. Hence, the usual starting point is to use a semi-classical approximation, which significantly simplifies the calculations in these models. This is the so-called mean-field approximation (MFA) or the equivalent $N \to \infty$ limit in FF models, which we introduce in the following. For the remainder of this work, we exclusively assume this approximation except for discussions of literature results that go beyond it, as in Sections 3.1.4 and 3.2.4.

2.2.1 The Mean-Field Approximation

The mean-field approximation (MFA), as its name implies, involves approximating specific degrees of freedom using an average or *mean-field*. This method is essentially a semi-classical approximation and can be derived in several ways. A prevalent approach in the context of FF models[5] is by starting from the purely fermionic Lagrangian (2.1) and defining the expectation values

$$\left\langle \bar{\psi}(x)\psi(x)\right\rangle = \phi_{\mathrm{S}}(x)\,, \quad \left\langle \bar{\psi}(x)\mathrm{i}\gamma_{\mathrm{ch}}\vec{\tau}\psi(x)\right\rangle = \vec{\phi}_{\mathrm{PSI}}(x). \tag{2.14}$$

Next, we expand the relevant fermionic scalar and pseudoscalar bilinears in the Lagrangian in small fluctuations $\delta\phi$ around the expectation value, i.e., $\bar{\psi}\psi = \phi_{\mathrm{S}} + \delta\phi_{\mathrm{S}}$ and $\bar{\psi}\mathrm{i}\gamma_{\mathrm{ch}}\vec{\tau}\psi = \vec{\phi}_{\mathrm{PSI}} + \delta\vec{\phi}_{\mathrm{PSI}}$. By neglecting the contributions that are quadratic in the fluctuations we obtain the Lagrangian

$$\mathcal{L}_{\mathrm{MF}} = G_{\mathrm{S}}\phi_{\mathrm{S}}^2 + G_{\mathrm{PSI}}\vec{\phi}_{\mathrm{PSI}}^2 + \bar{\psi}\left(\partial\!\!\!/ + \gamma_0\mu - 2G_{\mathrm{S}}\phi_{\mathrm{S}} - 2G_{\mathrm{PSI}}\mathrm{i}\gamma_{\mathrm{ch}}\vec{\tau}\cdot\vec{\phi}_{\mathrm{PSI}}\right)\psi, \tag{2.15}$$

which transforms into the Lagrangian of the bosonized action (2.7) when rescaling the expectation values $-2G_{\mathrm{S}}\phi_{\mathrm{S}} \to \sigma, -2G_{\mathrm{PSI}}\vec{\phi}_{\mathrm{PSI}} \to \vec{\pi}$. It is, however, important to note that neither ϕ_{S} nor $\vec{\phi}_{\mathrm{PSI}}$ are dynamic fields subjected to integration in the path integral. Hence, the partition function does not contain any further functional integration after performing the integration over the fermionic fields. Consequently, the grand canonical potential $\Omega = \frac{1}{\beta V}\ln\mathcal{Z}$ is the simple quantity

$$\Omega_{\mathrm{MF}}[\sigma,\vec{\pi}] = \tfrac{1}{\beta V}\int \mathrm{d}^D x\left(\frac{\sigma^2}{4G_{\mathrm{S}}} + \frac{\vec{\pi}^2}{4G_{\mathrm{PSI}}}\right) - \tfrac{1}{\beta V}\ln\mathrm{Det}\left[\beta\mathrm{Q}\right] \equiv \tfrac{1}{\beta V}\mathcal{S}_{\mathrm{eff}}, \tag{2.16}$$

5 The following discussion is based on similar discussions in Refs. [13, 27, 61].

which we immediately recognize as being proportional to the effective action (2.13).[6] Note that an equivalent procedure would be to conduct the steps in Section 2.1.3 and neglect the bosonic integration in Eq. (2.12). This approach carries through completely analogous for the Yukawa models. In this way, we recognize that the MFA translates to a complete disregard of the quantum fluctuations of the bosonic degrees of freedom.

The principle of minimum energy dictates that the configuration of σ and $\vec{\pi}$ which minimizes Ω is the physically realized one. Therefore, by applying the MFA, we reduce the highly nontrivial functional integration in the partition function to the minimization of Ω in the fields $\sigma, \vec{\pi}$. Even this might be an impossible task depending on the assumptions we make about the space-time dependence of $\sigma, \vec{\pi}$.

Although the minimizing field configuration can have any functional form, one might impose restrictions on the set of configurations over which the effective action is minimized. A drastic one – albeit often used – is the restriction to homogeneous field configurations $\sigma(x) = \bar{\sigma} = \text{const.}, \vec{\pi}(x) = \vec{\bar{\pi}} = \text{const.}$. For such configurations, the effective action is not a functional anymore, but merely a function of the variables $\bar{\sigma}, \vec{\bar{\pi}}$, which we call homogeneous effective potential. We define the homogeneous effective potential as

$$\overline{U}_{\text{eff}}\left(\bar{\sigma}, \vec{\bar{\pi}}\right) := \tfrac{1}{\beta V} \mathcal{S}_{\text{eff}}\left[\bar{\sigma}, \vec{\bar{\pi}}\right], \tag{2.17}$$

i.e., it is the effective action per space-time volume for homogeneous bosonic fields.

2.2.2 The Limit of $N \to \infty$ in Four-Fermion Models

In FF models, it is also common to consider the limit $N \to \infty$ while scaling the couplings as $GN = \lambda = \text{const.}$. When N approaches infinity, individual fluctuations of the fermion species are suppressed and the field value at each point is largely governed by the average behavior over all species. The contributions of any single species become infinitesimally small in this limit making the behavior of each individual species less relevant than the averaged behavior. As a result in this limit, FF models behave as if each fermion species is interacting with an average field, mirroring the assumption made in the MFA. This limit is equivalent to the $N_c \to \infty$ 't Hooft limit in QCD [29, 62].

One can intuitively understand the effect of this limit by considering Eqs. (2.12) and (2.13). With the rescaled coupling λ and the Dirac operator Q being diagonal in N, one finds that the effective action is proportional to N. Hence, in the limit $N \to \infty$, the weight of all configurations is infinitely suppressed. However, since the partition function is normalized to $\mathcal{Z} = 1$, there have to be non-zero contributions. These come from the configurations that minimize $\mathcal{S}_{\text{eff}}$ globally and thus have the largest weight in the path integral. In this way, we recognize that taking the $N \to \infty$ limit has the same effect as the MFA. Therefore, in the context of FF models both approximations are often used as synonyms.[7]

While this is correct, considering N to be large but finite allows a systematic expansion in contributions proportional to powers of $1/N$. This allows a controlled inclusion of effects beyond this limit, which is not available in the context of a MFA.[8]

6 In the MFA, the effective action is equivalent to the quantum effective action as all quantum effects are already incorporated.
7 We mostly use the term MFA to also encompass the Yukawa-type models.
8 Not discarding the terms quadratic in the corrections $\delta\phi$ again results in the original FF action.

2.2.3 Ambiguities of the Minimizing Field Configuration

In Section 2.2.1, we described how the MFA (and for FF models the equivalent $N \to \infty$ limit in Section 2.2.2) neglects the bosonic quantum fluctuations and the path integral is reduced to the sum of configurations that minimize $\mathcal{S}_{\text{eff}}$. This leaves us in a peculiar position in the case of a broken symmetry. There is then not only a single minimizing field configuration, but all further configurations, which are connected by transformations of the broken symmetry of the action. If we were to calculate the expectation value as the sum of the configurations of the bosonic fields, we would not observe the spontaneous breaking of a symmetry. The contributions from the broken configurations would always annihilate each other and average to a symmetric result.

A rigorous approach would actually mirror what is done in lattice simulations. One would apply an explicit breaking of the symmetry, calculate the expectation values for different breaking parameters and extrapolate to vanishing breaking parameter. However, introducing even an infinitesimal breaking in the MFA, reduces the set of minimizing configurations to a single one as it is immediately the only minimizing field configuration. Extrapolating to zero breaking parameter would yield the same configuration as if we would have just picked the corresponding configuration from the set of minimizing configurations without an explicit breaking. Thus, picking a single minimizing configuration is what we do in practice.

An exception to this occurs at a first order phase transition (or in similar situations, e.g., in the $(2+1)$-dimensional GN model, see Section 3.1.3). At these, one finds multiple sets of minimizing configurations, which are internally connected by symmetry transformations, but not with each other. Here, we refrain from evaluating observables, which differ for the two sets of configurations.

2.3 Regularization and Renormalization

In quantum field theory (QFT), two core concepts that play crucial roles in the formulation and interpretation of physical models are regularization and renormalization. Regularization is a mathematical technique employed in QFT to tame the ultra-violet (UV)-divergent expressions that often arise when computing physical observables.[9] There are various schemes to implement the regularization. Most schemes introduce a quantity called the regulator that suppresses contributions from large energy scales, hence rendering the otherwise divergent quantities finite and manageable.

Renormalization, closely following regularization, is the process by which we absorb the regulator dependence into redefined parameters of our theory (such as masses and coupling constants), in such a way that physical observables – quantities we would be able to measure in experiments – are independent of this arbitrary regulator. This is based on the premise that it is the measured quantities that hold physical significance, not the bare parameters of the Lagrangian. This section illustrates these two principles in the context of NJL-type models.

2.3.1 Regularization Schemes

In the following, we discuss different relevant regularization schemes to regulate divergent expressions that involve integration over fermionic momenta. To have a common example, we consider the generic

9 Whenever, we speak about regularization, we refer to the regularization of UV-divergences. There are, however, also theories and situations where one has to deal with infrared (IR)-divergences, which need to be regularized. As these arise in our investigations only in a single instance in the finite temperature calculations done in Chapter 5, we do not need to discuss them, but refer for further details to Refs. [39, 57].

momentum integral

$$I = \sum\!\!\!\!\!\!\int_{p_0} \int \frac{\mathrm{d}^d p}{(2\pi)^d} f\left(p_0, \mathbf{p}, m\right), \tag{2.18}$$

where $\sum\!\!\!\!\!\!\int_{p_0}$ is the summation or integration over the fermionic temporal momenta (depending on whether T is finite), $\mathbf{p}$ are the d-dimensional spatial momenta, m is the (dynamical) fermion mass and $f(p_0, \mathbf{p}, m)$ is some function of these three quantities. As an example, Fig. 2.1 depicts an unregularized function f that is part of the integrand in Eq. (C.28), i.e., an integrand that actually occurs in the investigations in Chapter 6.

Spatial Momentum Cutoff

The spatial momentum cutoff (SC) restricts the region of integration of the spatial momenta $\mathbf{p}$ to a d-dimensional sphere of radius Λ_{SC}, which serves as the regulator in this scheme. This modifies Eq. (2.18) to

$$I_{\mathrm{SC}} = \sum\!\!\!\!\!\!\int_{p_0} \int \frac{\mathrm{d}\Omega}{(2\pi)^d} \int_0^{\Lambda_{\mathrm{SC}}} \mathrm{d}p\, p^{d-1} f\left(p_0, \mathbf{p}, m\right), \tag{2.19}$$

where $\int \mathrm{d}\Omega$ denotes the d-dimensional angle integration. Fig. 2.1 depicts how this scheme leaves the integrand unchanged in the interval $[0, \Lambda_{\mathrm{SC}}]$ and then completely suppresses any contribution for momenta $|\mathbf{p}| > \Lambda_{\mathrm{SC}}$.

A major disadvantage of this scheme is the lack of translational invariance in the radial variable p and the appearance of surface terms when using partial integration. This can make calculations at a finite regulator considerably more challenging. Moreover, this scheme explicitly breaks the Euclidean rotational symmetry $O(D)$, which would be realized at $T = \mu = 0$. It has been used extensively in studies of FF and Yukawa models, e.g., in Refs. [13, 30, 39, 55, 63, 64].

Pauli-Villars

While the SC completely suppresses contributions above the cutoff, the Pauli-Villars (PV) regularization realizes a soft suppression of these high modes. This is achieved by adding further terms to the integrand such that the new integrand vanishes in the UV. The regulated integral has the form

$$I_{\mathrm{PV}} = \sum\!\!\!\!\!\!\int_{p_0} \int \frac{\mathrm{d}^d p}{(2\pi)^d} \sum_{k=0}^{N_{\mathrm{PV}}} c_k f\left(p_0, \mathbf{p}, M_k\right), \tag{2.20}$$

where $M_k = \sqrt{m^2 + \alpha_k \Lambda_{\mathrm{PV}}^2}$ and Λ_{PV} is the so-called PV mass, which serves as the regulator. The $k = 0$ contribution is the original integrand with $c_0 = 1$ and $\alpha_0 = 0$. The remaining real coefficients c_k and α_k are chosen such that the integrand vanishes for $|\mathbf{p}| \to \infty$ (including the additional factors p from the d-dimensional momentum integration). Thus, the suppression of high modes is smooth and in principle all modes contribute with some strength. For the number of required regulator terms N_{PV}, only a lower bound exists. This is determined by the $|\mathbf{p}|$ dependence of the integrand and the number of spacetime

dimensions, and including more regulator terms is not excluded. Note that the coefficients C_k and α_k might change for every N_{PV} and are not unique. For example, for $(3+1)$-dimensional NJL-types model $N_{\text{PV}} \geq 2$ is required and one finds the conditions [12, 65]

$$\sum_{k=0}^{N_{\text{PV}}} c_k = 0 \tag{2.21}$$

$$\sum_{k=0}^{N_{\text{PV}}} \alpha_k c_k = 0, \tag{2.22}$$

which can be solved by $\vec{c} = (1,1,-2)$ and $\vec{\alpha} = (0,2,1)$ for $N_{\text{PV}} = 2$.

Fig. 2.1 depicts how this scheme changes the integrand starting from $p = 0$, which severely dampens the peak in the important regions of the integrand. The part of the integrand, where it is constant zero, is even altered in such a way that it assumes negative values. It has been used extensively in studies of FF and Yukawa models, e.g., in Refs. [14, 35, 49, 66–68].

Lattice Field Theory

The subject of lattice field theory (LFT) and how it is applied in NJL-type models is a vast subject. At this point, we only want to give a crude sketch of the effects on the momentum integration. The central concept of LFT is that we discretize spacetime with a finite, Euclidean lattice with lattice spacing a. Furthermore, we restrict the fermionic and bosonic matter fields to exists only on the lattice points. The finite volume then discretizes the available momenta which reduces the integrals in (2.18) down to a sum resulting in

$$I_{\text{LFT}} = \sum_{p_0 \in \tilde{\Gamma}_0} \prod_{i=1}^{d} \sum_{p_i \in \tilde{\Gamma}_i} f\left(p_0, \mathbf{p}, m\right), \tag{2.23}$$

where $\tilde{\Gamma}$ is the reciprocal lattice and $\tilde{\Gamma}_i$ contains the available momenta in the i-th direction. The maximum momentum per direction is $\pi/a := \Lambda_{\text{LFT}}$. In this way, LFT is similar to the SC scheme as both are cutoff schemes. However, LFT explicitly breaks the rotational symmetry down to a discrete subgroup $\mathrm{O}(D) \to \mathrm{D}_D$ (or to an even smaller group for lattices of unequal extents). Moreover, in the process of discretizing spacetime, one has to discretize the operators in the Lagrangian, e.g., the derivative operator in the Dirac operator. This also has an impact on the fermionic dispersion relation and therefore quantities like the fermion propagator. As this is quite an extensive topic, we do not go into further details at this point. We refer to the discussion in Section 6.1, where we discuss this topic in more detail in the context of the $(3+1)$-dimensional NJL model. LFT has been used in studies of FF and Yukawa models, e.g., in Refs. [45–47, 49, 50, 69–73].

Other Schemes

There are plenty of other regularization schemes that one can apply in investigations of the phase diagram of NJL-type models. Among these are the following:

Space-time momentum cutoff The space-time momentum cutoff (STC) is similar to the SC scheme, but one confines the momenta in all directions to a D-dimensional sphere of radius Λ. This preserves the Euclidean rotation symmetry in vacuum, but makes calculations at finite chemical potential and

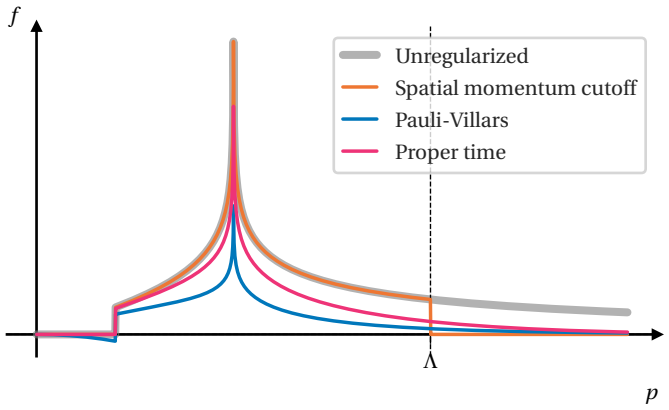

Figure 2.1: Exemplary comparison of the way several regularization schemes suppress the integrand in UV-divergent integrals. The example function is part of the integrand in Eq. (C.28), i.e., an integrand that actually occurs in the investigations in Chapter 6.

temperature considerably more challenging. It has been used in studies of FF and Yukawa models, e.g., in Refs. [54, 55].

Schwinger proper time Similar to the PV regularization, this regularization scheme smoothly suppresses large momentum contribution. This is done by introducing an exponential dampening factor $\propto \exp\left(-p^2/\Lambda^2\right)$. Fig. 2.1 depicts how this scheme changes the integrand, which dampens the peak in the important regions of the integrand. It is, however, less severe as the dampening from the PV regularization and does not affect the constant zero region in the example. It has been used in studies of FF and Yukawa models, e.g., in Refs. [12, 31, 54, 55].

Dimensional regularization This scheme [74] is easily one of the most popular regularization schemes for analytical calculations, especially in perturbative QCD. The central idea is that the divergences only arise in a particular number of space-time dimensions D. These can be rendered UV-finite by altering the number of space-time dimensions to $D-\varepsilon$. In contrast to all other schemes that we discussed, the regulator ε is a dimensionless quantity, which is why one is required to introduce a dimensionful renormalization scale μ. During renormalization, one sends $\varepsilon \to 0$ to remove the regulator, but keeps μ finite. It has been used in studies of FF and Yukawa models, e.g., in Refs. [55, 75]. The ζ-function regularization is equivalent to the dimensional regularization, but more versatile and has also been successfully applied to NJL-type models such as the $(2+1)$-dimensional GN model in Ref. [76].

Functional renormalization group The functional renormalization group (FRG) [77] is a method that mimics the Wilsonian idea of renormalization by integrating out momentum shells from the UV to the IR. These calculations also require the regularization of UV-divergences for which many different FRG-specific schemes exist. Some of these are comparable to the schemes that we have discussed in this section, e.g., the commonly used Litim regulator is comparable to the SC or STC scheme. Even though the results of FRG calculations should in principle not depend on the regularization scheme, the often necessary truncations of the FRG equations introduce a regulator dependence. In mean-field calculations of renormalizable NJL-type models within the FRG, one does not need a truncation and avoids this

regularization scheme dependence. This technique has been used in studies of FF and Yukawa models, e.g., in Refs. [16, 43, 44, 57, 78].

2.3.2 Renormalization

In the renormalization procedure, we seek to absorb the regularized contributions into an appropriate redefinition of the parameters in our theory. This is done on the basis of so-called renormalization conditions. These require that certain observables such as masses assume fixed values after the renormalization procedure. This ensures that the divergences are absorbed into the parameters in the appropriate way.

Renormalization, however, is not always successful. Not all theories are renormalizable, i.e., all divergences can be absorbed into a finite number of physical parameters. Non-renormalizable theories involve divergences that cannot be entirely eliminated, thus yielding predictions that depend on a finite regulator. The criteria for renormalizability crucially depend on the number of spacetime dimensions and the dimensionality of the operators in the Lagrangian.

2.3.3 No Regularization of Medium Contributions

In this work, we encounter loop integrals over combinations of fermionic propagators. The resulting integrals can – for most regularization schemes – be separated into a medium part, which depends on the chemical potential μ and the temperature T, and a vacuum contribution independent of external thermodynamic quantities. In the scenarios that we encounter, only the vacuum contribution is UV-divergent due to exponential dampening by the thermal distribution-functions. This fact is irrelevant in theories that are renormalizable, since the regulator is removed in the renormalization anyway.

On the other hand, regulating the medium contributions in non-renormalizable theories, regulates parts of the theory that are not actually divergent. Thus, the effect of the chemical potential μ and the temperature T is influenced by the applied regularization scheme, which introduces additional regularization artifacts. These are most prominent where the external quantities are in the order of the regulator.

Therefore, to eliminate these artifacts one might remove the regularization of the medium part for schemes that allow a clear separation of vacuum and medium contribution. We denote this deregulation of the medium as no medium regularization (NMR). In the $(3+1)$-dimensional NJL-model, this is observed to have a significant impact on the structure of the phase diagram [55] and physical quantities such as the speed of sound, which violates causality without NMR [63].

The concept of renormalization group (RG) consistency that is discussed in Ref. [79] is closely linked to this idea and provides a procedure that is motivated from RG considerations.[10] The final result is the same: the removal of regularization artifacts affecting the contribution of temperature and chemical potential.

No Sea Approximation

A somewhat extreme version of NMR is the so-called 'no sea'-approximation. Here the medium contribution is not regulated and the vacuum contribution is discarded, which can be regarded as the SC scheme with $\Lambda_{\mathrm{SC}} = 0$. It was believed that this vacuum contribution has only little impact on the phase structure, which can be compensated by choosing appropriate parameters. However, as shown in, e.g., Refs. [35, 80–83], discarding the vacuum contributions can have a severe impact on the phase structure of models

10 Note that this is not related to the FRG, but can be applied in almost any regularization scheme.

such as the quark-meson (QM) model. This might be a decent approximation in regions of the phase diagram, where the thermal contributions completely dominate (this is true for a very large chemical potential and temperature). As we are interested in the region of small to intermediate chemical potential and temperature, we will not consider this approximation.

Chapter 3

Specific Nambu-Jona-Lasinio-Type Models

Disclosure *This chapter discusses several specific NJL-type models and the results of investigations of the models from the literature. This serves as a contextualization of the investigations in the following chapters. Thus, most aspects presented in this chapter are not original to this work. References to the corresponding literature are provided during the discussion. The closed form expression for the renormalized effective potential of the GN model in d spatial dimensions, the corresponding plot and its discussion are the main exceptions.*

In this chapter, we study specific NJL-type models based on our discussion of the gNJL model in Chapter 2. In particular, we cover aspects and the known phase diagrams from the literature of the GN and NJL model in Section 3.1 and Section 3.2 respectively. We discuss the known results in detail, to give an appropriate context and the proper motivation to the investigations in the Chapters 5 to 7. We end the chapter by giving a broad overview of other related models that are relevant for the present work.

3.1 The Gross-Neveu Model

By setting $G_\mathrm{S} = G$, $G_\mathrm{PSI} = 0$, $N_f = 1$, and $N = 1$[1] in the Lagrangian of the gNJL model (2.1), we obtain the Lagrangian of the massless GN model [84]

$$\mathcal{L}_\mathrm{GN} = \bar{\psi}(x)(\partial\!\!\!/ + \gamma_0\mu)\psi(x) - G\left(\bar{\psi}(x)\psi(x)\right)^2 . \tag{3.1}$$

This model has been devised as a simple toy model to study phenomena such as the dynamical breaking of its (discrete) chiral symmetry and asymptotic freedom. It shares these central properties with QCD, but misses others, like gauge fields or renormalizability in $D = 4$ space-time dimensions. Therefore, it is unjustified to conclude anything about QCD phenomenology from this model. Nevertheless, it is certainly a powerful model to study generic features of fermionic theories and mechanisms that are also present in QCD. Being relevant to this work, this includes the behavior of the theory under the influence of external thermodynamic quantities such as the temperature and a chemical potential μ. Beyond this, the model

1 If we would consider the $N \to \infty$ limit, we would keep N arbitrary. Instead, we consider the GN model also in the MFA to unify the discussion with that of the NJL model. Therefore, we set $N = 1$.

was studied under the influence of magnetic fields [85–88], electric fields [89] or other chemical potentials, see, e.g., Refs. [50, 90].

Even though we consider the GN model mainly in the context of high-energy physics, similar models are common in condensed matter physics, see, e.g., Ref. [91] or the discussions in Ref. [92].

3.1.1 Symmetries

Due to the simple form of the Lagrangian, the GN model shares most symmetries with free fermions that are briefly discussed in Appendix B.2 and we will only mention the differences regarding the chiral symmetry here as it is the most relevant to this work. As we are also interested in the spontaneous breaking of translation symmetry, we note explicitly that the action of the GN model in the continuum and infinite volume (or finite volume with appropriate boundary conditions) is invariant under translations.

The scalar FF interaction channel reduces the so-called axial chiral symmetry transformation

$$\mathrm{U}(1)_A: \quad \psi \to \mathrm{e}^{\mathrm{i}\beta\gamma_{\mathrm{ch}}}\psi, \quad \bar{\psi} \to \bar{\psi}\,\mathrm{e}^{\mathrm{i}\beta\gamma_{\mathrm{ch}}} \tag{3.2}$$

that is realized for free fermions, to a discrete symmetry[2] (see e.g. Ref. [58] for a derivation)

$$\mathbb{Z}_2: \quad \psi \to \gamma_{\mathrm{ch}}\psi, \quad \bar{\psi} \to -\bar{\psi}\gamma_{\mathrm{ch}}. \tag{3.3}$$

This symmetry might be spontaneously broken by a non-zero chiral condensate $\langle\bar{\psi}\psi\rangle$, which is not invariant under this transformation. This symmetry is only realized, if there exists a γ_{ch}, whose existence depends on the number of space-time dimensions and the fermion representation. In a non-integer number of space-time dimensions, γ_{ch} can only be ambiguously defined, thus spoiling chiral symmetry (see Section 7.6.1 and Refs. [60, 74]). But even in odd integer number of space-time dimensions, one encounters a problem regarding representations of the Clifford algebra. One needs to consider a reducible representation, where one does not only find a γ_{ch}, but a second matrix that anti-commutes with the space-time Dirac matrices (see Appendix B.1 and, e.g., the discussion in Ref. [93]).

This symmetry carries over to the bosonized version of the model. Here, one finds that the scalar field σ has to transform under the chiral symmetry transformation as

$$\mathbb{Z}_2: \quad \sigma \to -\sigma. \tag{3.4}$$

Thus, the scalar field also serves as an order parameter for the spontaneous breaking of chiral symmetry, which is also evident from the Ward identity for the scalar field in Eq. (2.9).

3.1.2 Renormalization of the Gross-Neveu Model

In this section, we discuss the renormalization procedure of the GN model in the MFA in $1 \leq d < 3$ spatial dimensions. This is done in a very general manner to be used in later calculations. For discussions in fixed, integer number of spatial dimensions, we refer to Refs. [39, 49, 94–96]. The homogeneous phase diagram of the GN model in arbitrary spatial dimensions was already investigated in Ref. [64], where also the renormalization for $1 \leq d < 3$ was discussed. Hence, the following discussion contains similar results, but presented differently. We outline only the central steps. A more detailed derivation can be found in Appendix D.2 and Refs. [97, 98].

2 Up to a phase, which can be transformed by the intact $\mathrm{U}(1)_V$ transformation.

We start by considering the so-called homogeneous effective potential (see Section 2.2 and Eq. (2.17))

$$\bar{U}_{\text{eff}}(\bar{\sigma},T,\mu,d) \coloneqq \tfrac{1}{V\beta}\mathcal{S}_{\text{eff}}[\bar{\sigma}], \tag{3.5}$$

which is the effective action per spacetime volume restricted to homogeneous field configurations $\bar{\sigma}$. The restriction to homogeneous field configurations allows us to calculate the eigenvalues of the Dirac operator and thus to give a meaningful expression for the $\ln\mathrm{Det}\,\beta Q$ term in the effective action. We then find for $\bar{U}_{\text{eff}}$ (see Appendix D.2 for more detailed steps)

$$\begin{aligned}\bar{U}_{\text{eff}}(\bar{\sigma},T,\mu,d) &= \tfrac{\bar{\sigma}^2}{4G} - \tfrac{N_\gamma}{2}\int \tfrac{\mathrm{d}^d p}{(2\pi)^d}\left[E + \tfrac{1}{\beta}\ln\left(1+\mathrm{e}^{-\beta(E+\mu)}\right) + \tfrac{1}{\beta}\ln\left(1+\mathrm{e}^{-\beta(E-\mu)}\right)\right] \equiv \\ &\equiv \tfrac{\bar{\sigma}^2}{4G} - \tfrac{N_\gamma}{2} l_0(\bar{\sigma},T,\mu,d),\end{aligned} \tag{3.6}$$

where $E = \sqrt{p^2+\bar{\sigma}^2}$ and $p = |\mathbf{p}|$. The vacuum part of l_0 is clearly UV-divergent for any number of spatial dimensions $d > 0$. This necessitates a regularization of the integral and a subsequent renormalization of the coupling constant. Since the model is renormalizable for $d < 3$, any suitable regularization scheme is appropriate. In the calculation as presented in Appendix D.2, we use the SC scheme (see Section 2.3.1).

The renormalization of the model happens rather naturally in the GN model as it exhibits spontaneous breaking of the chiral symmetry in vacuum. Thus, we require the expectation value of the auxiliary field (the order parameter of chiral symmetry breaking) to assume a homogeneous, non-zero value $\bar{\Sigma}_0$ in vacuum, i.e., $\langle\sigma\rangle_{T=\mu=0} = \bar{\Sigma}_0$. In the MFA, this translates to the rather easy requirement that $\mathcal{S}_{\text{eff}}$ (and thus also $\bar{U}_{\text{eff}}$ since $\bar{\Sigma}_0$ is homogeneous) is minimal for $\bar{\Sigma}_0$. The necessary condition for this is expressed via the gap equation in vacuum

$$\left.\frac{\mathrm{d}\bar{U}_{\text{eff}}}{\mathrm{d}\bar{\sigma}}\right|_{T=\mu=0,\bar{\sigma}=\bar{\Sigma}_0} = \left.\left[\frac{\bar{\sigma}}{2G} - \bar{\sigma}N_\gamma l_1(\bar{\sigma},\mu,T,d)\right]\right|_{T=\mu=0,\bar{\sigma}=\bar{\Sigma}_0} \overset{!}{=} 0, \tag{3.7}$$

where

$$l_1(\bar{\sigma},\mu,T,d) = \int \tfrac{\mathrm{d}^d p}{(2\pi)^d}\,\tfrac{1}{\beta}\sum_{n=-\infty}^{\infty}\frac{1}{(\nu_n - \mathrm{i}\mu)^2 + E^2} = \int \tfrac{\mathrm{d}^d p}{(2\pi)^d}\,\frac{1-n(E)-\bar{n}(E)}{2E}, \tag{3.8}$$

with $\nu_n = (2n+1)\pi/\beta$ and the Fermi-Dirac distribution

$$n(E) = \frac{1}{\exp\left(\beta(x+\mu)\right)+1}, \quad \bar{n}(E) = \frac{1}{\exp\left(\beta(x-\mu)\right)+1}. \tag{3.9}$$

The vacuum part of l_1 is divergent for $d \geq 1$ and thus we need to regulate it in order to give it a finite value. We denote the regulated integral as $l_{1,\Lambda_{\text{SC}}}$

The gap equation exhibits two kinds of solutions, either $\bar{\Sigma}_0 = 0$, which we neglect as this is a chirally symmetric solution, and $\bar{\Sigma}_0$ that solves $1/(2G) - N_\gamma l_{1,\Lambda_{\text{SC}}}\left(\bar{\Sigma}_0,0,0,d\right) = 0$. We use the latter to set the value of the coupling to $1/(2G) = N_\gamma l_{1,\Lambda_{\text{SC}}}\left(\bar{\Sigma}_0,0,0,d\right)$. Inserting this back into the $\bar{U}_{\text{eff}}$ and sending $\Lambda_{\text{SC}} \to \infty$ yields

the renormalized effective potential

$$\begin{aligned}\overline{U}_{\text{eff, ren}}(\bar{\sigma},T,\mu,d) = \frac{N_\gamma}{2^{d-1}\pi^{\frac{d}{2}}}\frac{(d+1)\Gamma\left(-\frac{d+1}{2}\right)}{8\sqrt{\pi}}\left(-\frac{\bar{\Sigma}_0^{d-1}\bar{\sigma}^2}{2}+\frac{|\bar{\sigma}|^{d+1}}{d+1}\right)+\\ -\frac{N_\gamma}{2}\int\frac{\mathrm{d}^d p}{(2\pi)^d}\left[\frac{1}{\beta}\ln\left(1+\mathrm{e}^{-\beta(E+\mu)}\right)+\frac{1}{\beta}\ln\left(1+\mathrm{e}^{-\beta(E-\mu)}\right)\right],\end{aligned} \tag{3.10}$$

where we neglected a divergent, thermodynamically irrelevant $\bar{\sigma}$-independent term. In the zero temperature limit $T\to 0$, we find the closed form expression

$$\begin{aligned}\overline{U}_{\text{eff, ren}}(\bar{\sigma},0,\mu,d) = \frac{N_\gamma}{2^{d-1}\pi^{\frac{d}{2}}}\left[\frac{(d+1)\Gamma\left(-\frac{d+1}{2}\right)}{8\sqrt{\pi}}\left(-\frac{\bar{\Sigma}_0^{d-1}\bar{\sigma}^2}{2}+\frac{|\bar{\sigma}|^{d+1}}{d+1}\right)+\right.\\ \left.+\frac{\Theta\left(\bar{\mu}^2\right)}{d\Gamma\left(\frac{d}{2}\right)}|\bar{\sigma}|^{d+1}\left|\frac{\bar{\mu}}{\bar{\sigma}}\right|^d\left({}_2F_1\left(-\frac{1}{2},\frac{d}{2};\frac{d+2}{2};-\frac{\bar{\mu}^2}{\bar{\sigma}^2}\right)-\left|\frac{\mu}{\bar{\sigma}}\right|\right)\right],\end{aligned} \tag{3.11}$$

where ${}_2F_1$ is the Gaussian hypergeometric function defined by Eq. (D.1) and $\bar{\mu}^2=\mu^2-\bar{\sigma}^2$. The explicit expressions for $d=1$ and $d=2$ are well known and can be found, e.g., in Refs. [49, 57].

3.1.3 Phase Diagram for $N\to\infty$

The phase diagram of the GN model in spatial dimensions $d<3$ has been thoroughly investigated in the literature. We summarize the key results in this section.

$1+1$ Dimensions

We consider the GN model in $1+1$ dimensions, where the model is arguably most thoroughly investigated. When one restricts the bosonic field σ to be homogeneous in both space-time directions, one finds two chiral phases in the plane of chemical potential μ and temperature T [94], which are depicted in Fig. 3.1. One is the homogeneously broken phase (HBP) at low T and low μ, where the homogeneous minimum of the effective action assumes a non-zero value $\bar{\Sigma}\neq 0$. It is this spontaneous breaking of the chiral symmetry that is used in the renormalization process that is carried out in vacuum (see Section 3.1.2). The other phase is the symmetric phase (SP), where $\bar{\Sigma}=0$ and thus chiral symmetry is restored. The two phases are separated at low chemical potential by a second order phase boundary that is located for vanishing chemical potential at $T_c/\bar{\Sigma}_0=\mathrm{e}^\gamma/\pi$. This phase boundary curves down for increasing chemical potential and ends in a critical endpoint (CP) at $(\mu,T)/\bar{\Sigma}_0\approx(0.6082,0.3183)$. The phase boundary continues as a first order phase and intersects the $T=0$ at $\mu_{c,\text{hom}}=1/\sqrt{2}$.

Apart from the homogeneous phase boundaries one finds so-called spinodal lines [94]. These separate the regions where the homogeneous effective potential exhibits only a single minimum (up to the minima that are connected by symmetry transformations) and the regions where there are multiple (local) minima.

If one relaxes the restriction of homogeneous field configurations and allows for a spatially dependent bosonic field, one finds the inhomogeneous phase (IP) as a third phase at low temperatures and large chemical potentials [28, 29]. The first order homogeneous phase boundary is completely engulfed by this new phase and all phase transitions in this phase diagram are of second order. The former CP coincides with the Lifshitz point (LP) from which the IP opens up. The phase boundary between HBP and IP meet

the $T = 0$ line at $\mu_c/\bar{\Sigma}_0 = 2/\pi$, while the IP↔SP phase boundary only reaches the $T = 0$ axis at $\mu \to \infty$.

Inside the IP one finds that the global minimum of the effective action Σ is a field configuration that has a spatial dependence. This condensate then does not only break the chiral symmetry, but also the translational symmetry is spontaneously broken. Some example configurations at $T = 0$ and various chemical potentials are shown in the upper plot in Fig. 3.2. The general behavior of the functional form of the condensate for increasing chemical potential is that

- the shape evolves from a kink-antikink shape to sin-like modulation,
- the amplitude decreases,
- the wavelength decreases.

The lower plot in Fig. 3.2 shows the baryon density $\langle\bar{\psi}\gamma_0\psi\rangle/N$ at the same chemical potentials. We notice that the baryon density is also inhomogeneous and it is peaked sharper at chemical potentials closer to the phase boundary. The maxima coincide with the zero crossings of the scalar field Σ, since it essentially acts as a potential for the baryons [28]. This localization of baryons is the most important phenomenological aspect of the IP. This behavior also gives rise to the alternative name "crystal phase" for the IP.

The mechanism that is responsible for such a condensate to be energetically favored is analogous [29, 92] to the Peierls instability that is known in similar models in condensed matter physics (see, e.g., Ref. [91]). The basic idea of the Peierls instability can be illustrated by considering a 1-dimensional lattice of atoms. It can be shown that applying a spatial perturbation of wave-number $2k_F$, where k_F is the Fermi wave-number of the electrons, lowers the energy of the system by creating a gap in the energy spectrum [34]. The result is a configuration of atoms with an inhomogeneous charge density . This concept can be applied to the $(1+1)$-dimensional GN model, where it results in an inhomogeneous chiral condensate with momentum $q = 2p_F = 2\mu$ [29, 92] (this is the same expectation as from the discussion in Chapter 1).

At this point it is important to comment on the relationship of this result and the Mermin-Wagner theorem [99, 100]. This theorem states that in $D \leq 2$ space-time dimensions there can be no breaking of a continuous symmetry, since the resulting Goldstone bosons would exhibit an infrared divergence. This protects the symmetry from being broken spontaneously. The translational symmetry, which is broken by the inhomogeneous condensate, is certainly a continuous symmetry at non-zero temperature. This apparent conflict is resolved by an analysis that is presented in Ref. [101], which was done for the $(1+1)$-dimensional Thirring model, but is also valid for other related models. This study analyzes the spatial dependence of correlators of fermionic condensates and finds $\langle\bar{\psi}(x)(1+\gamma_{\text{ch}})\psi(x)\bar{\psi}(0)(1-\gamma_{\text{ch}})\psi(0)\rangle \propto |x|^{-1/N}$. Thus, for finite N, one finds correlations of a finite range and thus no spontaneous breaking of the symmetry. However, in the limit of $N \to \infty$ one recovers infinite range correlations and thereby results in the spontaneous breaking of the symmetry.

$2+1$ Dimensions

The homogeneous phase diagram in $2+1$ dimensions features an HBP at low temperatures and chemical potentials and an SP in the rest of the (μ, T)-plane [95, 96] as illustrated by the minimizing homogeneous field configuration $\bar{\Sigma}$ depicted in Fig. 3.3. In contrast to $1+1$ dimensions, one finds only a second order phase transition between the two phases at finite temperature. The phase boundary starts at $\mu = 0$ at $T_c/\bar{\Sigma}_0 = 1/2\ln 2$ and extends to $\mu_{c,\text{hom}}/\bar{\Sigma}_0 = 1$ at $T = 0$. For low temperature, $\bar{\Sigma}$ changes more rapidly in the vicinity of the phase boundary. The phase transition at $T = 0$ is often described as a first order phase

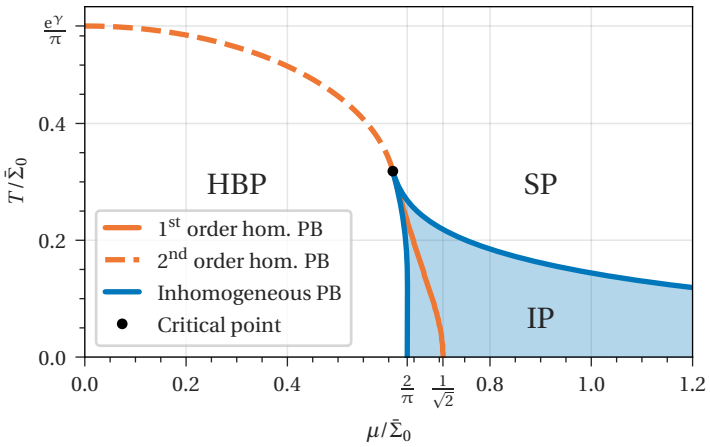

Figure 3.1: The phase diagram of the $(1+1)$-dimensional GN model in the (μ, T)-plane in units of the vacuum expectation value of the bosonic field σ. Adapted from Ref. [28, Fig. 8].

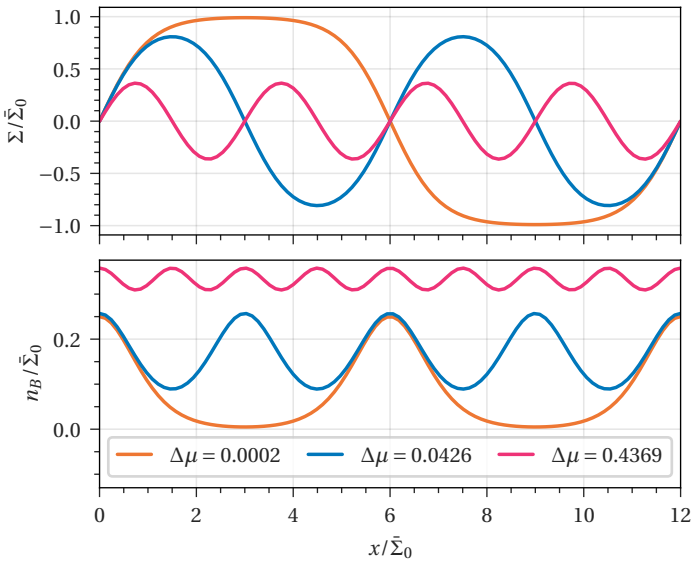

Figure 3.2: The minimizing field configuration Σ and the baryon density n_B as a function of space in units of the vacuum expectation value of the bosonic field σ for various chemical potentials μ with $\Delta\mu = (\mu - 2/\pi)/\bar{\Sigma}_0$. Produced with formulas from Refs. [28, 29].

transition. However, from the D-dimensional analysis in Ref. [64] (see also discussion in the next section), it is clear that this is the CP, which lies exactly at $T = 0$.

No study in the infinite volume and renormalized limit has found evidence for an IP at finite temperature. It was found that both a finite volume [85] or a finite regulator [49] can cause the CP to be located at a finite temperature and with it the existence of a first order phase transition. Similarly, one also finds that an IP exists for finite regulators [48, 49] at low temperatures and large chemical potential. In the renormalized limit, one finds only indications towards a degeneracy of homogeneous and inhomogeneous condensates at the phase transition at $T = 0$, which we discuss in Section 7.3.1.

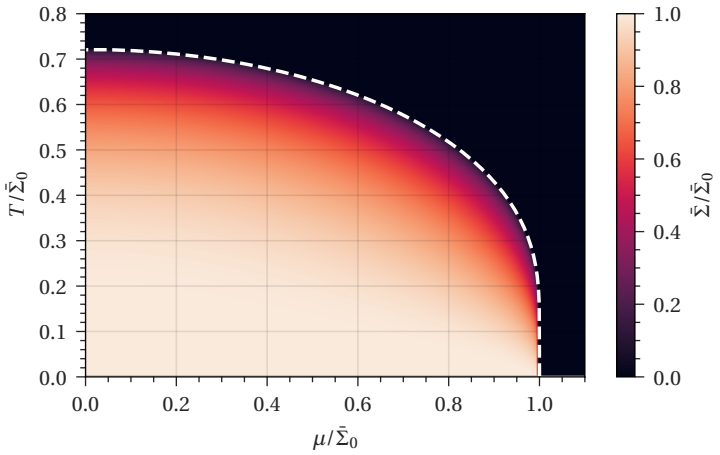

Figure 3.3: The value of the minimizing homogeneous field configuration $\bar{\Sigma}$ in the $(2+1)$-dimensional GN model in the (μ,T)-plane in units of the vacuum expectation value of the bosonic field σ. $\bar{\Sigma}$ and the white phase boundary are calculated by the respective formulas in Refs. [95, 96].

Homogeneous Phase Diagram in Non-Integer Spatial Dimensions d

Even though one finds an HBP both in $1+1$ and $2+1$ dimensions, their extent is different and the first order phase boundary vanishes. To understand the nature of these differences it is instructive to investigate the theory in non-integer spatial dimensions d, which serves to interpolate between the known integer dimensional results. We discuss the implications of non-integer d in more detail in Chapter 7. At this point, we only summarize the results about the homogeneous phase diagram that were originally presented in Ref. [64].

The left plot in Fig. 3.4 shows the phase diagram in the (μ,T)-plane for various spatial dimensions d. We observe that the phase diagram expands continuously for increasing d and that the CP evolves to lower temperatures between $d=1$ and $d=2$. The upper right plot in Fig. 3.4 shows that the critical chemical potential $\mu_{c,\mathrm{hom}}$ at $T=0$ diverges for $d\to 3$, which is not surprising as the model is not renormalizable anymore in $d=3$. The lower right plot in Fig. 3.4 illustrates how the CP meets the $T=0$ line exactly in $d=2$.

The evolution of the order of the phase boundary as a function of d can be illustrated by considering the homogeneous effective potential at $\mu_{c,\mathrm{hom}}$. Fig. 3.5 shows the normalized homogeneous effective potential $\overline{U}'_{\mathrm{eff}}(\bar{\sigma},\mu_{c,\mathrm{hom}}(d),d)=\overline{U}_{\mathrm{eff}}(\bar{\sigma},\mu_{c,\mathrm{hom}}(d),d)-\overline{U}_{\mathrm{eff}}(0,\mu_{c,\mathrm{hom}}(d),d)$ in the $(\bar{\sigma},d)$-plane at $T=0$. The red dashed lines indicates the minima. A first order phase transition is realized for $1\leq d<2$ due to the potential barrier that separates the two minima. In $d=2$, one finds an interval $[-\bar{\Sigma}_0,\bar{\Sigma}_0]$ of degenerate minima. Thus, all homogeneous field configurations corresponding to this interval have the same action, even though they are not connected by symmetry transformations. This degeneracy is likely a result of an interplay of the silver-blaze phenomenon at $T=0$ and the CP being located at this point $(\mu,T)=(\mu_{c,\mathrm{hom}},0)$ in $d=2$. In contrast, in $d=1$ the CP is located at a finite temperature, where one finds that the coefficients of the $\bar{\sigma}^2$ and $\bar{\sigma}^4$ contributions in the expanded homogeneous effective potential vanish [43, 94, 102]. This results in a nearly flat potential, but not exactly flat like in the situation in $d=2$. For $d>2$, we find a second order phase transition, which is reflected by the single minimum at $\bar{\sigma}=0$.

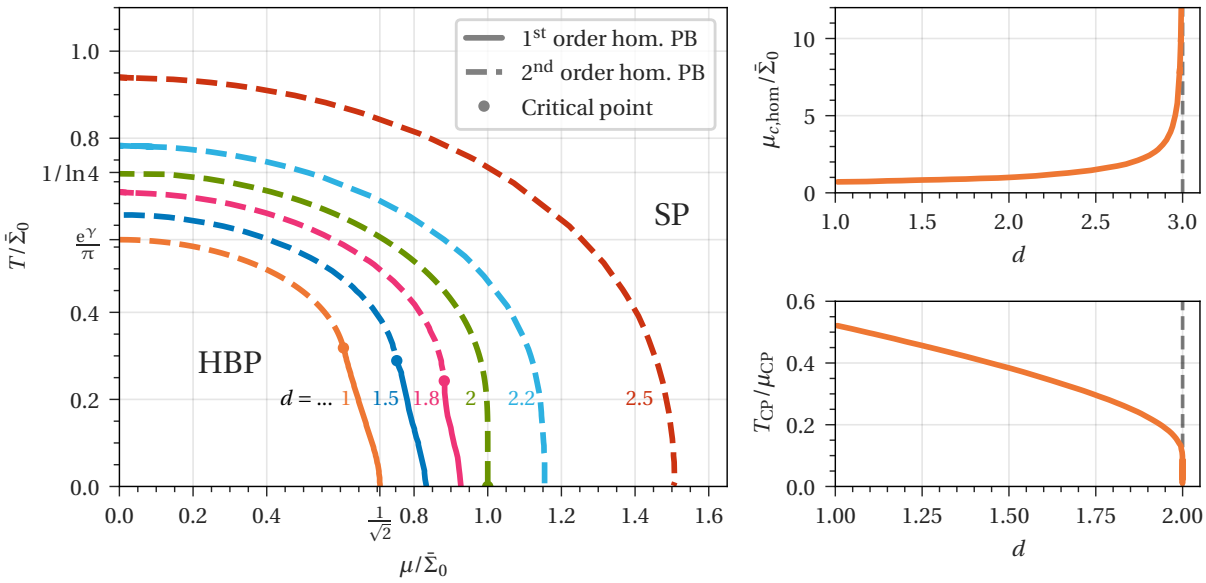

Figure 3.4: Left: The homogeneous phase diagram for various spatial dimensions in the (μ, T)-plane in units of the vacuum expectation value of the bosonic field σ. Adapted from Ref. [64, Fig. 8].
Upper right: The critical chemical potential $\mu_{c,\mathrm{hom}}$ at $T = 0$ as a function of the number of spatial dimensions. Adapted from Ref. [64, Fig. 11].
Lower right: The ratio T/μ of the position of the CP as a function of the number of spatial dimensions. Adapted from Ref. [64, Fig. 14].

3.1.4 Phase Diagram for Finite N

When we consider finite N instead of the limit $N \to \infty$, we find that bosonic quantum fluctuations for the field σ contribute to the path integral (see Section 2.2.1). These fluctuations are in general expected to weaken ordered phases (as observed in, e.g., Refs. [43, 44, 46, 52]). This could be just a shrunken extent of ordered phases in the phase diagram or could mean the vanishing of these phases altogether. Numerous studies are dedicated to the investigation of the phase diagram at finite N, which we summarize in this section.

$1+1$ Dimensions

In Section 3.1.3 we discussed that the spontaneous breaking of a continuous symmetry in $1+1$ dimensions at finite N is expected to be prevented by IR divergences of the would-be Goldstone boson. However, Ref. [103] presents a rather general argument for theories with discrete symmetries under the influence of fluctuations. In this setup, domains with different orientations have a domain wall, which is a single contact point and costs a constant amount of energy. It is then motivated that the free energy is decreased for an increasing density of domain walls. Thus, one ends up with a restored symmetry as there are no separated domains left. This is essentially an entropy versus energy argument: The finite energy cost of the domain wall is outweighed by the entropy gain of having more and more configurations. The exception is at zero temperature, where the energetically preferred, symmetry breaking configuration is realized, since entropy is weighted by temperature (TS) in thermodynamic potentials.

This is in line with calculations of an FRG study of the Yukawa-extended GN model [43] that found that

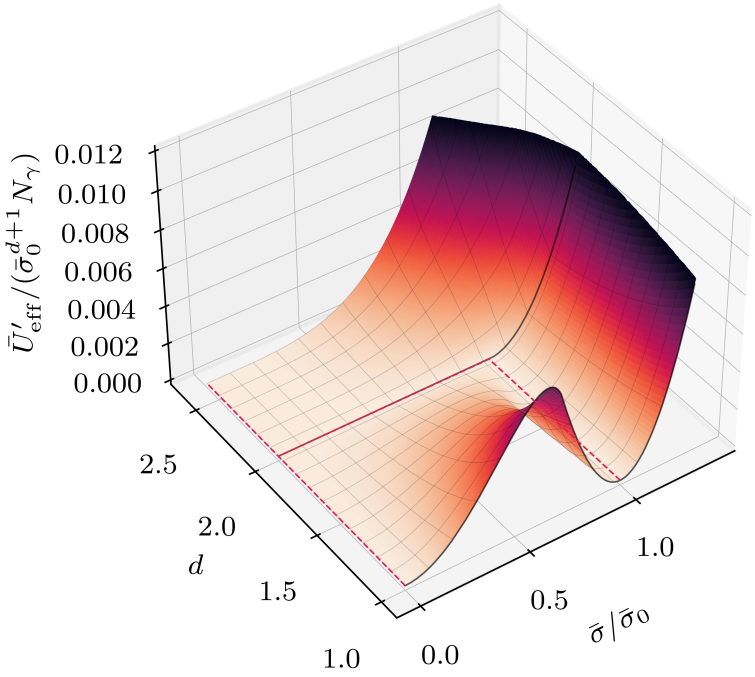

Figure 3.5: The normalized homogeneous effective potential $\overline{U}'_{\text{eff}}(\bar{\sigma},\mu_{c,\text{hom}}(d),d) = \overline{U}_{\text{eff}}(\bar{\sigma},\mu_{c,\text{hom}}(d),d) - \overline{U}_{\text{eff}}(0,\mu_{c,\text{hom}}(d),d)$ in the $(\bar{\sigma},d)$-plane at the critical chemical potential $\mu_{c,\text{hom}}(d)$, where the homogeneous phase transition occurs. The red dashed lines indicate the minima $\bar{\Sigma}$.

the chiral symmetry is unbroken at finite temperature for any finite N. Although the calculations at zero temperature are inconclusive, there are indications that the symmetry remains broken [43, 57].

In apparent contrast to these results and considerations are studies employing lattice Monte Carlo simulations [46, 47]. These calculations found results, which resemble the phase diagram in the limit of $N \to \infty$ with regimes that correspond to the three known phases. However, the observable that was used to identify the HBP might not have been suitable to detect whether the symmetry remains broken and the volume dependence was not investigated rigorously. This was not further explored, since the focus of these studies was the IP. However, even after a rather rigorous analysis of the correlation range inside the would-be IP, it was not possible to discern whether the found regime was an actual IP with broken translation symmetry or a regime with quasi-long order, i.e., ordering for all relevant large length scales. Thus, it is not clear whether these results are in direct conflict with the Mermin-Wagner theorem.

One could, however, argue that it is not relevant whether there is infinite range order or only quasi long-range order. The defining feature of the IP in the GN model within the $N \to \infty$ limit is that the baryon density is also inhomogeneous and gives rise to localized baryons (see Section 3.1.3). It was found that this feature is also present at finite N preserving the important phenomenological aspect of this phase [47].

2 + 1 **Dimensions**

In 2 + 1 dimensions, there are no arguments or theorems that prevent the homogeneous spontaneous breaking of the discrete chiral symmetry for a finite N. There are various studies that investigate the phase diagram of the GN model with different computational methods, e.g., Refs. [44, 73, 85, 86, 104–107]. In general, one finds a similar phase structure in the (μ, T)-plane as in the $N \to \infty$ limit with the HBP covering a smaller region in the phase diagram, which can be attributed to the bosonic fluctuations that weaken the ordered phase. If capable of detecting it, these studies find an absent IP with the exception of Ref. [73]. There the occurrence of the IP is, however, most likely a lattice artifact due to the small lattice spacings and large chemical potentials, which was observed in the $N \to \infty$ study in Ref. [49].

3.2 Nambu-Jona-Lasinio Model

By setting $G_S = G_{PSI} = G$, $N_f = 2$ and $N = N_c = 3$ in the Lagrangian of the gNJL model (2.1), we obtain the Lagrangian of what is commonly denoted as the NJL model in 3 + 1 dimensions [108, 109]

$$\mathcal{L}_{NJL} = \bar{\psi}(x)(\not{\partial} + \gamma_0 \mu)\psi(x) - G\left[\left(\bar{\psi}(x)\psi(x)\right)^2 + \left(\bar{\psi}(x) i\gamma_{ch}\vec{\tau}\psi(x)\right)^2\right], \tag{3.12}$$

where $\vec{\tau}$ is the vector of Pauli matrices. Moreover, in 3 + 1 dimensions one has to choose a 4×4 representation of the Clifford algebra. Thus, the spinors have $\overline{N} = N_f \times N_c \times N_\gamma = 2 \times 3 \times 4 = 24$ components. We use the term NJL model to refer to models characterized by this Lagrangian across all number of spacetime dimensions.[3]

In its original form, the NJL model was a nuclear model [108, 109], where the fermionic degrees of freedom represent baryons. It was, however, realized that this model was useful in describing the low-energy behavior of QCD in terms of quarks and the mesonic degrees of freedom [12]. In QCD, there are no fundamental quark-quark interactions, but an effective quark-quark interaction is induced by gluon exchanges, which becomes relevant in the effective action in the IR [112]. Essentially, in the NJL model all of these interactions mediated by gluons are effectively represented by the local FF vertex with the coupling G as sketched in Fig. 3.6.[4] While the scalar-pseudoscalar interaction channel, as present in the NJL model, is the dominant one in vacuum in QCD, other channels such as vector channels or even diquark channels might be more relevant at finite densities [113–115]. The description in terms of fermionic degrees of freedom interacting via FF interactions is a valid description for intermediate energies. At even lower energies, it is found that the mesons, which are the relevant degrees of freedom, can be described using the partially bosonized model (see Section 2.1.1) [112, 113]. Some variants of the NJL model also consider non-local FF interactions in order to describe more accurately the non-local nature of the effective quark-quark interactions in QCD [116]. Various conjectures and expectations of the behavior of QCD are based on results that are obtained in models and in particular in the NJL model [12, 13]. To this end, the NJL model is often considered with a bare quark mass for the fermions to better mimic the situation in QCD. We, however, consider the model with massless fermions to preserve chiral symmetry (see the next section) and investigate its dynamical breaking.

3 Note that in 1 + 1 dimensions sometimes the name NJL model refers to the model [110] that is also referred to as chiral Gross-Neveu model [111], which is invariant under $\mathrm{U}(1)_A$ transformations.

4 Note that the one-gluon exchange would not contribute to the effective FF coupling in a 1PI effective action and thus it is not listed in Fig. 3.6. In perturbative calculations, one finds that this one-gluon exchange is the leading order contribution.

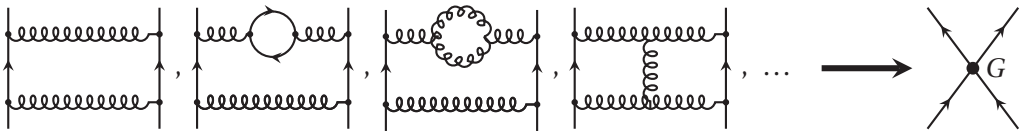

Figure 3.6: Schematic replacement of the effective quark-quark interactions mediated by gluon exchanges by the local FF interaction.

3.2.1 Symmetries

The following discussion assumes $N = 1$ as it eases notation. For arbitrary N all symmetry transformations are enhanced by species rotations in this space with the generalized Gell-Mann matrices as generators. The NJL model also shares most symmetries with free fermions that are briefly discussed in Appendix B.2 and we will only mention the differences regarding the chiral symmetry here as it is the most relevant for this work. As we are also interested in the spontaneous breaking of translation symmetry, we explicitly mention that the action of the NJL model just as the GN model in the continuum and infinite volume (or finite volume with appropriate boundary conditions) is invariant under translations.

Compared to the GN model, the pseudoscalar isovector interaction is present in the Lagrangian of the NJL model. The FF interaction terms explicitly break parts of the $\mathrm{U}(2)_V \times \mathrm{U}(2)_A$ chiral symmetry that we would expect from $N_f = 2$ free fermions down to a subgroup. We find that the model remains invariant under the vector symmetry (compare to Eq. (B.12))

$$\mathrm{U}(2)_V: \quad \psi \to \mathrm{e}^{\mathrm{i}(\alpha_0 \mathbb{1} + \theta_a \tau_a)} \psi, \quad \bar{\psi} \to \bar{\psi}\, \mathrm{e}^{-\mathrm{i}(\alpha_0 \mathbb{1} + \theta_a \tau_a)} \tag{3.13}$$

and the $\mathrm{U}(2)_A$ is broken down to (compare to Eq. (B.13))

$$\mathrm{SU}(2)_A: \quad \psi \to \mathrm{e}^{\mathrm{i}\phi_a \tau_a \gamma_{\mathrm{ch}}} \psi, \quad \bar{\psi} \to \bar{\psi}\, \mathrm{e}^{\mathrm{i}\phi_a \tau_a \gamma_{\mathrm{ch}}}. \tag{3.14}$$

Just as in the GN model, one finds that the auxiliary bosonic fields also transform under this chiral symmetry. Applying these transformations result in a rotation in field space as

$$\mathrm{O}(4): (\sigma, \vec{\pi}) \to R(\sigma, \vec{\pi}), \tag{3.15}$$

where R is a matrix of 4-dimensional rotations. In particular, for homogeneous field configurations, this allows to rotate the pseudoscalar fields into the scalar channel, i.e., the homogeneous field configurations $\left(\bar{\sigma}, \vec{\bar{\pi}}\right)$ and $(M,0) = \left(\sqrt{\bar{\sigma}^2 + \vec{\bar{\pi}}^2}, 0\right)$ have the same action.

We find that the action is not invariant under a $\mathrm{U}(1)_A$ axial transformation

$$\mathrm{U}(1)_A: \quad \psi \to \mathrm{e}^{\mathrm{i}\beta\gamma_{\mathrm{ch}}} \psi, \quad \bar{\psi} \to \bar{\psi}\, \mathrm{e}^{\mathrm{i}\beta\gamma_{\mathrm{ch}}}, \tag{3.16}$$

which we would expect from free fermions. Upon closer inspection, one finds that this symmetry would be realized, if we would include the FF interaction channels $(\bar{\psi}\vec{\tau}\psi)^2$ and $(\bar{\psi}\mathrm{i}\gamma_5\psi)^2$ in the action with the same coupling as the other channels. The channels are, however, chosen so that the symmetries of the model resemble the symmetries of QCD, where the $\mathrm{U}(1)_A$ symmetry is broken by a quantum anomaly. Thus, the absence of this symmetry is by design and not by accident.

There is also a variant of the NJL model with $N_f = 3$, in order to describe not only dynamics between up

and down quarks, but also strange quarks. In this case, the Lagrangian (2.1) (in this case of $N_f = 3$, $\vec{\tau}$ is the vector of the eight 3×3 Gell-Mann matrices) is modified by an additional six-point interaction term of the form (see, e.g., Ref. [12])

$$\mathcal{L}_6 = -K \left[\det_f \left(\bar{\psi}(1+\gamma_{\mathrm{ch}})\psi \right) - \det_f \left(\bar{\psi}(1-\gamma_{\mathrm{ch}})\psi \right) \right], \tag{3.17}$$

where $\det_f$ denotes the determinant in flavor space and K is the coupling constant that controls the strength of the six-point interaction. This additional term is needed, since the Lagrangian would exhibit the $\mathrm{U}(1)_A$ symmetry and this term breaks it explicitly again. We will, however, only consider the $N_f = 2$ variant.

3.2.2 Non-Renormalizability of the $(3+1)$-Dimensional Nambu-Jona-Lasinio Model

FF models like the NJL model are not renormalizable in $3+1$ dimensions, which is caused by the local nature of the FF interactions. While we can renormalize the model by an appropriate redefinition of the coupling constant in $d < 3$ (see Section 3.1.2), this non-renormalizable model would need an infinite number of counter terms to be introduced in order to tame the divergences [12]. Introducing that many regulators is neither computationally realizable nor does it seem sensible for a theory that is supposed to bear physical meaning.

Thus, the "standard" procedure in such cases is to use a single regulator to regulate the divergent contributions and keep this regulator at a finite value. The regularization scheme and the regulator then become an inseparable part of the theory. The model can be regarded as an effective theory that is the low-energy description of a more general theory, which is defined also at higher scales. In the case of the NJL model, this higher theory is believed to be QCD [117]. In this picture, the regulator determines the scale below which the gluon dynamics that mediate the interaction of quarks in QCD are effectively described by the contact FF interaction, i.e., the replacement shown in Fig. 3.6.[5]

The value of the regulator thus assumes the role of a parameter just as the bare coupling constant G. They are parameters without physical meaning that are tuned to give sensible physical observables. One typically uses the constituent quark[6] mass M_0 (the dynamically generated fermion mass in vacuum) and the pion decay constant f_π in vacuum to fix the values of the coupling and the regulator. For the pion decay constant we choose the value of 88 MeV [14, 27]. This differs from the experimentally observed 92 MeV [118][7], since we consider the chiral limit, which alters the value of the pion decay constant. The constituent quark mass is often chosen as $M_0 \approx 300$ MeV as it is roughly in line with QCD phenomenology. However, varying M_0 allows us to implicitly change the value of the regulator. We exploit this in Chapter 6 to investigate the regulator dependence and thus we often consider ranges of M_0 rather than specific values.

5 This interpretation only works with regularization schemes that feature a dimensionful regulator Λ. There is no analogous interpretation with dimensional regularization that one can also use in investigations of $(3+1)$-dimensional models (see Section 7.4).

6 The terminology and procedure is motivated by QCD. As such the fermionic fields that we introduced in Eq. (2.1) are also referred to as quarks.

7 Note that there are different conventions for f_π and such the given value in Ref. [118] is $f_\pi = 130.2$ MeV, which differs from our convention by a factor of $\sqrt{2}$.

Parameter Fitting

The "standard" way to fix the parameters in the NJL model was described in Ref. [12] and we follow this procedure, which we briefly summarize here. The major steps are:

1. Derive an expression for the dimensionless ratio f_π / M_0 from the vacuum-to-one-pion axial vector matrix element that depends on the pion-to-quark-quark coupling.
2. Derive an expression for the pion-to-quark-quark coupling that depends on the pion self polarization.
3. Use step 1 and 2 to give an expression, where f_π / M_0 solely depends on the dimensionless ratio M_0 / Λ and use this to determine the value of Λ.
4. Derive the gap-equation, which provides a self-consistent equation that relates the coupling G and M_0 / Λ.
5. Use the gap equation and the previously found value for Λ to obtain the value of the coupling G.

In the following, we go through each step and derive the respective quantities. This is done in a way that is largely independent of the regularization scheme. Consequently, we do not apply any regularization to the divergent quantities and only indicate when something needs regularization or depends on the regulator Λ. However, some steps might be different in some regularization schemes, which we discuss after the general derivation. In this fitting procedure we exclusively consider homogeneous bosonic fields $\bar{\sigma}$,$\vec{\pi}$ and use the chiral symmetry of the theory to rotate all bosonic fields into ($\bar{\sigma}$,0) (see Section 3.2.1). Thus, the dynamically generated fermion mass[8] is $M = \bar{\sigma}$ and $\vec{\pi} = 0$. Furthermore, we assume continuum dispersion relations[9] and thus the vacuum fermion propagator for homogeneous bosonic fields assumes the form

$$S(p) \coloneqq \widetilde{\widetilde{\mathrm{Q}}}^{-1}(p) = \frac{-\mathrm{i}\not{p} + M}{p^2 + M^2}. \tag{3.18}$$

The starting point is an expression for the pion decay constant, which is given by the vacuum-to-one-

8 We use M instead of $\bar{\sigma}$ in this section to align with the common terminology of the NJL model.
9 We discuss the peculiarities of lattice regularizations in Section 6.1.

pion axial vector matrix element

$$\mathrm{i}q_\mu f_\pi \delta_{i,j} = \quad \mathrm{i}\gamma_\mu\gamma_{\mathrm{ch}}\tfrac{\tau_j}{2}$$

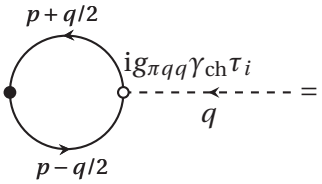

$$= \tfrac{1}{2} g_{\pi qq}\delta_{i,j}\int \tfrac{\mathrm{d}^4p}{(2\pi)^4}\,\mathrm{tr}\left[\gamma_\mu\gamma_{\mathrm{ch}}S\left(p+q/2\right)\gamma_{\mathrm{ch}}S\left(p-q/2\right)\right] =$$

$$= \tfrac{1}{2} g_{\pi qq}\overline{N}\delta_{i,j}Mq_\mu\int \tfrac{\mathrm{d}^4p}{(2\pi)^4}\,\frac{1}{\left[\left(p+\frac{1}{2}q\right)^2+M^2\right]\left[\left(p-\frac{1}{2}q\right)^2+M^2\right]} =$$

$$= \tfrac{1}{2} g_{\pi qq}\overline{N}\delta_{i,j}Mq_\mu I(q^2,M^2),$$

$$\Rightarrow \frac{f_\pi^2}{M^2} = \tfrac{1}{4} g_{\pi qq}^2\overline{N}^2 I^2(0,M^2), \tag{3.20}$$

where the dashed line is an external pion, $g_{\pi qq}$ is the pion-quark-quark coupling and the integral I is UV-divergent requiring regularization by some quantity Λ. We denote the regularized integral as I_Λ.

In order to evaluate the right-hand side of Eq. (3.20), we need an expression for the pion-quark-quark coupling $g_{\pi qq}$, which we can derive by considering the scattering of two quarks mediated by a pion exchange. This diagram is given in the random phase approximation[10] by a series of bubble diagrams, which can be evaluated as a geometric series [12]. It is expressed diagrammatically by Fig. 3.7, where the wide dashed line is an effective pion exchange given by the generic form

$$U_{ij}\left(q^2\right) = \mathrm{i}\gamma_{\mathrm{ch}}\tau_i g_{\pi qq}\frac{1}{q^2+m_\pi^2}g_{\pi qq}\mathrm{i}\gamma_{\mathrm{ch}}\tau_j, \tag{3.21}$$

where the choice of i,j sets which pion is exchanged and m_π is the pion mass, which we assume to be zero as we consider only the chiral limit.

10 This is an approximation beyond the MFA, which incorporates correlations between fluctuations [12].

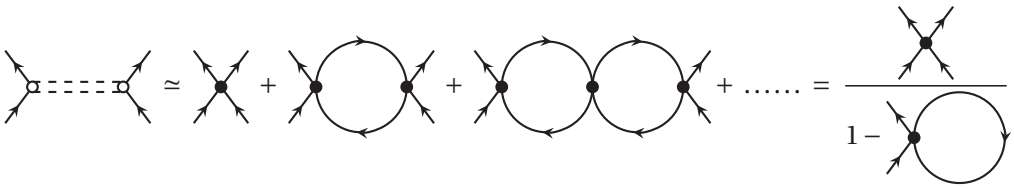

Figure 3.7: Diagrammatic expression of the quark-quark scattering via pion exchange in the random-phase approximation. The wide dashed line denotes the pion propagator and the solid black lines denote fermionic lines. The white vertices denote the quark-quark-pion vertex given by $g_{\pi qq}\mathrm{i}\gamma_{\mathrm{ch}}\tau_i$ and the black vertices denote the ordinary pseudoscalar four-fermion vertex. Adapted from Ref. [12, Fig. 5].

Translating the diagrammatic expression in Fig. 3.7 yields [12, 13]

$$\begin{aligned} U_{ij}\left(q^2\right) &= \mathrm{i}\gamma_{\mathrm{ch}}\tau_i\left[2G + 2G\Pi_{\mathrm{ps}}\left(q^2\right)2G + 2G\Pi_{\mathrm{ps}}\left(q^2\right)2G\Pi_{\mathrm{ps}}\left(q^2\right)2G + \ldots\right]\mathrm{i}\gamma_{\mathrm{ch}}\tau_j = \\ &= \mathrm{i}\gamma_{\mathrm{ch}}\tau_i\left[\frac{2G}{1+2G\Pi_{\mathrm{ps}}\left(q^2\right)}\right]\mathrm{i}\gamma_{\mathrm{ch}}\tau_j, \end{aligned} \tag{3.22}$$

where Π_{ps} denotes the vacuum polarization of the pion.

We expand the denominator in Eq. (3.22) in powers of q^2 about $q = 0$ and compare with Eq. (3.21) to obtain the expression

$$\frac{1+2G\Pi_{\mathrm{ps}}\left(q^2\right)}{G} = \frac{1+2G\Pi_{\mathrm{ps}}\left(0\right)+2G\frac{\partial\Pi_{\mathrm{ps}}\left(q^2\right)}{\partial q^2}\Big|_{q^2=0}q^2+\mathcal{O}\left(q^4\right)}{2G} \equiv \frac{q^2}{g_{\pi qq}^2}, \tag{3.23}$$

$$\Rightarrow g_{\pi qq}^{-2} = \frac{\partial\Pi_{\mathrm{ps}}\left(q^2\right)}{\partial q^2}\Big|_{q^2=0}. \tag{3.24}$$

Thus, we need to evaluate the pion vacuum polarization Π_{ps}, which is given by[11]

$$\begin{aligned} \Pi_{\mathrm{ps}}\left(q^2\right) &= \mathrm{Tr}\left[\mathrm{i}\gamma_{\mathrm{ch}}\tau_i S\mathrm{i}\gamma_{\mathrm{ch}}\tau_j S\right] = \\ &= \int\frac{\mathrm{d}^4p}{(2\pi)^4}\,\mathrm{tr}\left[\mathrm{i}\gamma_{\mathrm{ch}}\tau_i S\left(p+\tfrac{1}{2}q\right)\mathrm{i}\gamma_{\mathrm{ch}}\tau_j S\left(p-\tfrac{1}{2}q\right)\right] = \\ &= \overline{N}\delta_{i,j}\int\frac{\mathrm{d}^4p}{(2\pi)^4}\frac{p^2+\frac{1}{4}q^2-M^2}{\left[\left(p+\frac{1}{2}q\right)^2+M^2\right]\left[\left(p-\frac{1}{2}q\right)^2+M^2\right]} = \\ &= \frac{\overline{N}\delta_{i,j}}{2}\int\frac{\mathrm{d}^4p}{(2\pi)^4}\left[\frac{1}{\left(p+\frac{1}{2}q\right)^2+M^2}+\frac{1}{\left(p-\frac{1}{2}q\right)^2+M^2}\right] - \frac{\overline{N}\delta_{i,j}}{2}q^2I(q^2,M^2), \end{aligned} \tag{3.25}$$

where we applied a partial fraction decomposition to the integrand in the last step and we again find the integral $I(q^2,M^2)$. All three integrals are UV-divergent and thus need regularization. We apply shifts of $p+q\to p$ and $p-q\to p$ in the first two integrals. For some regularization schemes like SC at a finite regulator, this would lead to a modification of the integral boundaries. However, since we are only interested in Π_{ps} at infinitesimal q (as we evaluate Eq. (3.24) at $q^2=0$), we can neglect such contributions. We note that, if we would go away from the chiral limit and acquire a non-zero pion mass, we would need to evaluate Eq. (3.24) at finite q and would need to take greater care with the shifts. We evaluate Eq. (3.24) and find for the pion-to-quark-quark coupling

$$g_{\pi qq}^{-2} = \frac{\overline{N}}{2}I_\Lambda(0,M^2). \tag{3.26}$$

By inserting Eq. (3.26) into Eq. (3.20), we find the explicit form

$$\frac{f_\pi^2}{M^2} = \frac{1}{2}\overline{N}I_\Lambda(0,M^2). \tag{3.27}$$

11 Note that the matrices τ_i and τ_j set the corresponding isospin channel of the interaction vertices. We omit the explicit notation of i,j, since this polarization loop is diagonal in isospin and equal for all channels.

The left-hand side is given by the dimensionless ratio of f_π/M, which we give as an input into the parameter tuning, while the right hand-side depends only on the dimensionless ratio M^2/Λ^2. We set $M = M_0$, i.e., the constituent fermion mass that we impose in vacuum to tune the parameters of the theory, and then (numerically) determine the value of Λ that solves

$$\frac{f_\pi^2}{M_0^2} - \tfrac{1}{2}\overline{N} I_\Lambda(0, M_0^2) = 0. \tag{3.28}$$

In order to determine the coupling G, we consider the gap equation, which is the extremal condition of the effective potential (2.17).[12] The vacuum gap equation is given by

$$\begin{aligned} \left.\frac{\mathrm{d}\overline{U}_{\mathrm{eff}}}{\mathrm{d}M}\right|_{M=M_0} &= \left[\frac{M}{2G} - \mathrm{Tr}\,(S)\right]_{M=M_0} = 0 \\ \Rightarrow G &= \left[2\overline{N}\int \frac{\mathrm{d}^4p}{(2\pi)^4}\,\frac{1}{p^2+M_0^2}\right]^{-1}, \end{aligned} \tag{3.29}$$

where the integral is obviously UV-divergent again and needs to be regularized. Thus, the right-hand side depends only on the value of Λ that we already determined via Eq. (3.28) and inserting it yields the value for the coupling G.

The expressions for the relevant quantities of the parameter fitting procedure calculated with different regularization schemes are presented in Appendix C.2.

3.2.3 Phase Diagram in the Mean-Field Approximation

In the following, we discuss the phase diagram of the $(3+1)$-dimensional NJL model. As previously discussed the results might depend on the regularization scheme and at this point we limit this presentation to results as obtained with PV regularization, since it is the most common in the literature.

The inhomogeneous phase diagram of the NJL model has been discovered across several investigations among which are Refs. [14, 30, 31, 119]. Especially the earlier studies used a chiral density wave as an ansatz for the inhomogeneous field modulations. In this 1-dimensional modulation, the σ and π_3 fields oscillate with a phase shift as $(\sigma(z), \pi_3(z)) \propto (\cos(z), \sin(z))$. This modulation has the convenient property that the modulus is spatially constant. However, Ref. [14] offers the most complete picture, where the chiral condensate was restricted to arbitrary 1-dimensional modulations. It was then found that the problem reduces to solving the $(1+1)$-dimensional variant of the model for which the full solution is equivalent to the $(1+1)$-dimensional GN model that is shown in Fig. 3.2. This solution is energetically favored over the chiral density wave. In particular, this means that the pseudoscalar field vanishes, i.e., $\vec{\pi}(x) = 0$.

The inhomogeneous phase diagram as obtained in Ref. [14] is depicted in Fig. 3.8. One finds a phase diagram that strongly resembles the phase diagram of the $(1+1)$-dimensional GN model with a HBP, SP and IP, which, however, has a finite extent at $T = 0$. One also finds a first order phase boundary, when one restricts the model to homogeneous field configurations, which is completely covered by the IP. Moreover, the CP coincides with the LP, which is a feature that is observed in the $(1+1)$-dimensional GN model (see Section 3.1.3). The coincidence of these point breaks down when one uses cutoff regularization schemes, where surface terms that split these points appear, see e.g. Ref. [35].

12 We encountered the gap equation already in the renormalization of the GN model in Eq. (3.7).

It is important to note that this is the phase diagram for a single constituent quark mass M_0. As we will discuss in Section 6.3.1, the phase structure is sensitive to small changes in M_0 on this parameter.

3.2.4 Phase Diagram beyond the Mean-Field Approximation

An appropriate method to investigate the phase structure beyond the MFA would be lattice Monte-Carlo simulations. However, such simulations are relatively expensive due to the 4-dimensional space-time and the non-renormalizability prevents us from taking the continuum limit. Thus, it is often more attractive to directly consider QCD. One of the exceptions is given by the study in Refs. [45, 120], which performed lattice Monte-Carlo simulations with staggered fermions at non-zero chemical potential with a focus on the color superconducting phase. With respect to the chiral phase diagram, they find an HBP that has a smaller extent compared to the MFA results. The study did not consider the concept of IP and thus did not evaluate suitable observables to detect this.

The FRG is also an excellent tool for studies beyond the MFA, but it requires a kinetic term for the mesonic degrees of freedom. Even though, such a term is effectively generated during the RG-flow, one has to include it explicitly in the UV definition of the model [43]. Thus, formally one can only investigate the Yukawa extension of the corresponding NJL-type model, which is the QM model in case of the NJL model (see Section 3.3.2).

3.3 Other Models of Interest

In the following, we briefly mention the key features of some models that are relevant for the discussion of our investigations of the GN and NJL model in Chapters 6 and 7. There is a plethora of models more, but we omit them for brevity as they do not play a key role for our investigations.

3.3.1 The $(2+1)$-Dimensional Complete Lorentz-(Pseudo)Scalar Four-Fermion Model

A possibility for the absence of any IP in the $(2+1)$-dimensional GN model (see Section 3.1.3) could be the limited symmetry group, which only features the discrete chiral symmetry. To investigate this, the PSFF

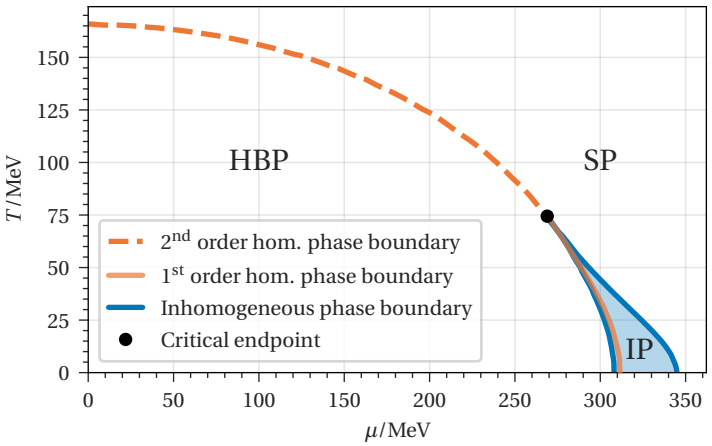

Figure 3.8: The phase diagram of the $(3+1)$-dimensional NJL model in the (μ,T)-plane obtained for 1-dimensional modulations at $M_0 = 300\,\text{MeV}$, $f_\pi = 88\,\text{MeV}$ with the PV regularization. Adapted from Ref. [14, Fig. 1].

model was considered with the Lagrangian [51]

$$\mathcal{L}_{\text{PSFF}} = \bar{\psi}\left(\partial\!\!\!/ + \gamma_0\mu\right)\psi - G\left[\sum_{j=1}^{16}\left(\bar{\psi}\, c_j\, \psi\right)^2\right], \tag{3.30}$$

where the interaction vertices c_j are 8×8 matrices in isospin and spin space and are elements of

$$C = \left(c_j\right)_{j=1,\dots,16} = \left(1, \mathrm{i}\gamma_4, \mathrm{i}\gamma_5, \gamma_{45}, \vec{\tau}, \mathrm{i}\vec{\tau}\gamma_4, \mathrm{i}\vec{\tau}\gamma_5, \vec{\tau}\gamma_{45}\right). \tag{3.31}$$

The matrices γ_4 and γ_{45} are additional Dirac matrices that arise when one considers the 4×4 reducible representation of the Clifford algebra in $2+1$ dimensions (see Appendix B.1 and, e.g., Ref. [93]). This model features the full chiral symmetry as one would find them for free fermions. A thorough investigation of this model and its Yukawa extensions as well as subsets of the interactions under the influence of additional chemical potentials showed no signal of an IP [51]. Thus, the absence of an IP in $(2+1)$-dimensional NJL-type models is a universal behavior, which is not limited to the GN model. This universal absence offers an advantage as we might be able to understand its causes already in the simple GN model and do not need to consider more complicated models.[13]

3.3.2 Quark-Meson Model

The QM model is the Yukawa extension of the $(3+1)$-dimensional NJL model with the common form of the Lagrangian given by

$$\mathcal{L}_{\text{QM}} = \tfrac{1}{2}\partial_\mu\sigma\partial_\mu\sigma + \tfrac{1}{2}\partial_\mu\vec{\pi}\partial_\mu\vec{\pi} + \lambda\left(\sigma^2 + \vec{\pi}^2 - v^2\right)^2 + \bar{\psi}\left(\partial\!\!\!/ + \gamma_0\mu + h\left(\sigma + \mathrm{i}\gamma_{\text{ch}}\vec{\tau}\cdot\vec{\pi}\right)\right)\psi, \tag{3.32}$$

where λ, v, h are the parameters of the theory. The bosonic kinetic term and the more complex bosonic potential render this theory renormalizable, which is the big advantage of this model over the NJL model. The traditional parameter fitting within the MFA is plagued by a parameter divergence that resembles a Landau pole and an unbounded effective action for large fields beyond this pole [35]. However, some of these issues can be circumvented by a better fitting strategy [121] and the unbounded effective action is conjectured to be an artifact of the MFA [35].

The phase diagram of the QM model in the MFA strongly resembles that of the NJL with the difference that the IP persists for large values of the regulator (see Section 6.3.1). The phase diagram of this model has been investigated beyond the MFA in FRG calculations, see Ref. [122] for a review that also discusses the QM model. A study with a simple local potential approximation truncation found an IP, where one would expect it from the MFA results [16]. However, unphysical effects like a back-bending of the phase boundary were observed, which some studies identify as a regularization artifact [123]. Moreover, it might be that the employed truncation is not sufficient as it does not take into account the flow of the Yukawa coupling or the wave-function renormalization, which were shown to have a non-negligible dynamic in such FRG calculations [39, 57].

3.3.3 Nambu-Jona-Lasinio-Type Models with Vector Interactions

In this work, we focus on NJL-type models as FF models that feature only Lorentz-(pseudo)scalar interaction channels. There are various studies, e.g., Refs. [66, 124–128], that considered extending the

13 This is the motivation to only consider the simple GN model in Chapter 7.

Lagrangian of such theories by vector interactions of the form $G_V(\bar{\psi}\gamma_\mu\psi)^2$, which give rise to bosonic vector fields via the HS transformation. When considering inhomogeneous condensation in such models, one finds that the CP splits from the LP by moving to lower temperatures for increasing vector coupling G_V while the LP remains at the same temperature [124]. These vector interactions break the coincidence of CP and LP that we observed in NJL-type models (see Sections 3.1.3 and 3.2.3). It was shown by analyzing effective FF interactions in FRG flows starting from fundamental quark-gluon interactions that, while being not the dominant interaction channel[14], vector interactions are expected to have a non-negligible contribution [115]. Thus, refining NJL-type models with such interactions seems like an appropriate step towards more realistic models [113, 114].

14 These are either the scalar-pseudoscalar interaction channel or diquark channels at larger chemical potential.

Chapter 4

Detection of Inhomogeneous Phases

Disclosure *This chapter discusses the common techniques for the investigation of inhomogeneous phases. All the presented ideas have been discussed in the literature and the relevant references are given at the appropriate positions. Especially the derivation of the stability analysis can be found in a similar form, e.g., in Refs. [39, 49, 67, 68, 129]*

If one restricts the bosonic fields in FF models to homogeneous field configurations within the MFA, it is in general easy to calculate the effective homogeneous potential. By minimizing this potential in the homogeneous value, one can find the energetically preferred field configuration. The assumption of homogeneous configurations is – as we have seen in the discussion of existing results in Chapter 2 – certainly not always justified. Therefore, to calculate the full phase diagram of such theories, we would have to minimize the effective action on the set of inhomogeneous field configurations of arbitrary shape and amplitude. As this is in general not possible, we want to present two strategies that allow us to gather insights about the IP.

The first one is composed of various ways to determine the functional shape of a preferred inhomogeneous condensate under various restrictions as presented in Section 4.1. The other being the stability analysis that detects, whether some inhomogeneous field configuration of unknown shape is energetically favored over a spatially homogeneous ground state as discussed in Section 4.2.

4.1 Determination of the Energetically Preferred Modulation

Within the MFA, one is exclusively concerned with the field configurations that minimizes the effective action, since it is the only relevant one. Thus, it seems natural to focus on finding this exact configuration to discern whether an IP is realized. The main difficulty is the evaluation of the effective action for a particular inhomogeneous modulation. There are several approaches to this and we mention the density of states approach, the Ginzburg-Landau (GL) expansion, and LFT regularizations. In principle, all of these approaches make it possible to evaluate the action using a certain ansatz for the modulation. One then minimizes the action with respect to the parameters of this ansatz.

4.1.1 Density of States Approach

The density of states approach is a powerful technique that allows one to evaluate the effective action for an inhomogeneous modulation. One expresses the effective action by the sum over the energy eigenvalues of the Hamilton operator of the theory, which in turn can be expressed by an integration over the eigenvalue density also called *density of states*.

For certain modulations such as the chiral density wave or the solution of the $(1+1)$-dimensional GN model (see Fig. 3.2), a closed form expression for the density of states is known [14, 29]. In this way, it is also possible to embed lower dimensional modulations in higher dimensional space. One then minimizes the effective action with respect to the parameters of the ansatz modulation, which appear in the density of states.

This technique (or related techniques) has been used in a wide range of models and investigations, e.g., in Refs. [28, 31, 110, 130–133].

4.1.2 Ginzburg-Landau Expansion

Within the framework of the GL expansion, one expands the effective action in powers of the fields and their derivatives. It is not limited to FF models or even high-energy physics as it is also commonly used in condensed matter calculations. Formally, this expansion in such NJL-type models is only valid in the vicinity of the CP and LP, where both the amplitude of the fields and their derivatives are small. It becomes straightforward to insert an ansatz for the modulation and to evaluate whether it is energetically favored over a homogeneous field configuration. This expansion was used in the investigation of the IP in, e.g., Refs. [35, 66, 67, 124, 129, 134].

4.1.3 Lattice Field Theory

Another possibility is to discretize the effective action via the methods of LFT, which also enables an evaluation of the effective action for non-uniform modulations. For finite lattice spacings, these modulations can also be regarded as an ansatz, albeit a very general one. The parameters of this ansatz are the field values at every lattice point. We can then minimize the effective action in these parameters just like with the other techniques. However, one also has to perform the infinite volume limit and the continuum limit (if one can take this limit), and thus, the minimization must be carried out across a range of lattice sizes and spacings. In order to reduce the parameters one can also consider a particular ansatz function and merely use the lattice approach as a means to evaluate the effective action for this modulation. Calculations using this approach without a specific ansatz were conducted, e.g., in Refs. [49, 50, 69, 71], and with a specific ansatz in Refs. [48, 65].

4.2 Stability Analysis

This section introduces the stability analysis technique, which we primarily use in the investigations in Chapters 5 to 7. This technique is highly versatile making it compatible with different regularization schemes in virtually any FF and Yukawa-type model[1] in various numbers of space-time dimensions. Moreover, it does not rely on a specific ansatz for the inhomogeneous field configuration, which greatly

1 Although some modifications and special care have to be taken when considering vector interactions as these can introduce an unbounded effective action and one has to potentially maximize the action instead of minimizing it [66, 124, 135, 136].

reduces the bias of the investigation. Due to this versatility it has been used in investigations of IPs in numerous studies, e.g., Refs. [39, 49–51, 65, 67–69, 71, 97, 129, 137, 138]. It can even be used within the FRG beyond the MFA in the search for IPs [16] and it is under development to be applied to studies of the IP in full QCD via Dyson-Schwinger equation (DSE) calculations [139]. This versatility comes with the drawback that we cannot use it to determine the functional form of the inhomogeneous chiral condensate. It is limited to detecting only, if an IP is favored over a homogeneous phase. There are scenarios where it fails to detect an IP; these scenarios are investigated, among other aspects, in Chapter 5.

Before we derive the stability analysis in detail in Section 4.2.1, we outline the central idea via the sketches in Fig. 4.1. In the NJL-type models with the MFA that we are interested in, it is often straightforward to calculate the effective action for homogeneous bosonic field configurations. In a theory with a single bosonic field, the effective action, as a function of the value of the homogeneous configuration $\bar{\phi}$, might resemble Fig. 4.1(a). As it is a function of a single variable, it is rather easy to determine the minimizing value of $\bar{\phi}$.

If we consider inhomogeneous field configurations, one would need to introduce additional axes for the values at every spacetime point or equivalently for the Fourier coefficients of the Fourier decomposed field as sketched in Fig. 4.1(b). Fig. 4.1(c) depicts a situation where we are able to calculate the functional dependence of $\mathcal{S}_{\text{eff}}$ on these coefficients and that there is a direction in which the effective action assumes even lower values. This would turn the homogeneous minimum into a saddle point, which is energetically not favored even though it appeared so when restricting the calculations to homogeneous fields. Minimizing the effective action in these Fourier coefficients, would yield the energetically preferred inhomogeneous field configuration. However, in most situations, it is impossible to calculate the dependence of the effective action on the Fourier coefficients of arbitrary magnitude.

In the stability analysis, one assumes only infinitesimal perturbations to the homogeneous field configurations and expands the effective action in powers of these perturbations. This does not allow us to calculate the functional dependence of the effective action on the Fourier coefficients, but its curvature in the inhomogeneous directions as suggested in Fig. 4.1(d). Thus, applying this expansion at the global minimum of the set of homogeneous field configurations allows us to detect if there is an inhomogeneous direction in which the effective action can assume even lower values. The condition for this to be successful is of course, that the inhomogeneous minimum is not separated from the homogeneous minimum by an energy barrier.

4.2.1 Derivation of the Stability Analysis in the $(d+1)$-Dimensional Nambu-Jona-Lasinio Model

We limit this derivation to the NJL model as defined by Eq. (3.12), but the relevant expressions for the GN model are recovered by neglecting any contributions that are generated by the presence of the pion fields and setting $N_f = 1$. Moreover, we restrict this discussion to integer spacetime dimensions D and we assume a Clifford algebra representation with an existing γ_{ch} (see Appendix B.1 for the implications of odd D). Although we do not specify the regularization scheme as of now, we assume a continuum representation of the fermionic propagator, i.e., this derivation deviates from the derivation for a lattice regularization. A detailed derivation of the lattice stability analysis in the context of the lattice discretized $(2+1)$-dimensional GN model is given in Ref. [49] and briefly outlined for the NJL model in Section 6.1.5 with explicit formulas given in Appendix C.4.3.

The generalization to theories with more interaction channels, Yukawa theories or other chemical potentials is mostly straightforward. Such a derivation for a general model in $2+1$ dimensions in the continuum is given in Ref. [51]. Furthermore, one can find detailed derivations for specific models such

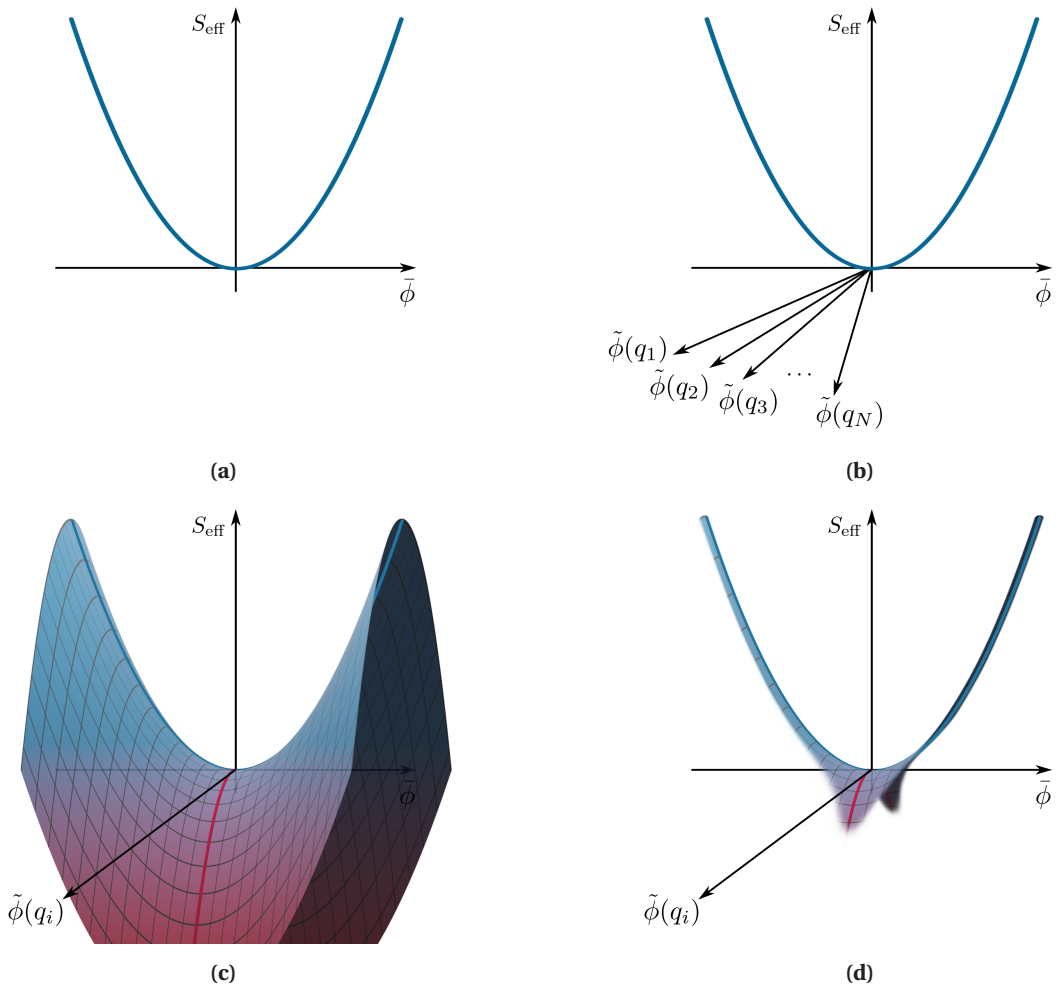

Figure 4.1: Four sketches to illustrate the general idea of the stability analysis.

as that for the $(1+1)$-dimensional GN model in Ref. [39], for the QM model in Ref. [68], and for the $(d+1)$-dimensional NJL model in Ref. [67]. Clearly the derivation of the stability analysis is something well discussed in the literature for various models and therefore this section serves as a more detailed recapitulation of such derivations at the example of the $(3+1)$-dimensional NJL model.

As a first step, we assume that only the last component of $\vec{\pi}$ condenses, since we do not consider an isospin imbalance (e.g., induced by an isospin chemical potential), i.e., $\pi_1 = \pi_2 = 0$ and $\pi_3 = \pi$. We split the bosonic fields into homogeneous parts and arbitrary spatial inhomogeneous perturbations

$$\sigma(x) = \bar{\sigma} + \delta\sigma(\mathbf{x}), \quad \pi(x) = \bar{\pi} + \delta\pi(\mathbf{x}). \tag{4.1}$$

We use the short-hand notation

$$\vec{\phi} = (\sigma, \pi) \quad \text{and} \quad \vec{c} = (\mathbb{1}, \mathrm{i}\gamma_{\text{ch}}\tau_3). \tag{4.2}$$

We then also split the Dirac operator (2.8)

$$\mathrm{Q}(x,y) = \bar{\mathrm{Q}}(x,y) + (2\pi)^D \delta^D(x-y)\,\delta\Phi(\mathbf{x}), \tag{4.3}$$

where $\bar{\mathrm{Q}}(x,y)$ is the Dirac operator with homogeneous bosonic fields and $\delta\Phi(\mathbf{x}) = c_i\,\delta\phi_i(\mathbf{x}) = \delta\sigma(\mathbf{x}) + \mathrm{i}\gamma_{\mathrm{ch}}\tau_3\delta\pi(\mathbf{x})$. Using this expression we can rewrite the ln Det term in Eq. (2.13) as

$$\ln\mathrm{Det}\,\beta\mathrm{Q} = \mathrm{Tr}\ln\beta\bar{\mathrm{Q}} + \mathrm{Tr}\ln\left(1+\delta\Phi\bar{\mathrm{Q}}^{-1}\right) = \mathrm{Tr}\ln\beta\bar{\mathrm{Q}} - \sum_{n=1}^{\infty}\tfrac{1}{n}\,\mathrm{Tr}\left[\left(-\delta\Phi\bar{\mathrm{Q}}^{-1}\right)^n\right], \tag{4.4}$$

where Tr denotes a functional trace of the operator over all spaces. This expansion allows us to rewrite $\mathcal{S}_{\mathrm{eff}}$ as a power series

$$\mathcal{S}_{\mathrm{eff}} = \sum_{n=0}^{\infty}\mathcal{S}_{\mathrm{eff}}^{(n)}, \tag{4.5}$$

with $\mathcal{S}_{\mathrm{eff}}^{(n)}$ being proportional to $\delta\Phi^n$. The first three terms of this power series are

$$\mathcal{S}_{\mathrm{eff}}^{(0)} = \tfrac{\beta V}{4G}\left[\bar{\sigma}^2+\bar{\pi}^2\right] - \ln\mathrm{Det}\,\beta\bar{\mathrm{Q}} \equiv \beta V\,\bar{U}_{\mathrm{eff}}, \tag{4.6}$$

$$\mathcal{S}_{\mathrm{eff}}^{(1)} = \tfrac{\beta}{2G}\int \mathrm{d}^dx\left[\bar{\sigma}\delta\sigma(\mathbf{x}) + \bar{\pi}\delta\pi(\mathbf{x})\right] - \mathrm{Tr}\left(-\delta\Phi\bar{\mathrm{Q}}^{-1}\right), \tag{4.7}$$

$$\mathcal{S}_{\mathrm{eff}}^{(2)} = \tfrac{\beta}{4G}\int \mathrm{d}^dx\left[\delta\sigma^2(\mathbf{x}) + \delta\pi^2(\mathbf{x})\right] - \mathrm{Tr}\left(\delta\Phi\bar{\mathrm{Q}}^{-1}\delta\Phi\bar{\mathrm{Q}}^{-1}\right), \tag{4.8}$$

where the leading contribution in this expansion is proportional to the homogeneous effective potential (see Eq. (2.17)).

The functional traces in Eqs. (4.7) and (4.8) are given by

$$\mathrm{Tr}\left[\left(\delta\Phi\bar{\mathrm{Q}}^{-1}\right)^n\right] = \int\prod_{j=1}^{n}\mathrm{d}^Dx^{(j)}\,\mathrm{tr}\left(\delta\Phi\left(\mathbf{x}^{(1)}\right)\bar{\mathrm{Q}}^{-1}\left(x^{(1)},x^{(2)}\right)\ldots\delta\Phi\left(\mathbf{x}^{(n)}\right)\bar{\mathrm{Q}}^{-1}\left(x^{(n)},x^{(1)}\right)\right), \tag{4.9}$$

where tr denotes the trace over all discrete spaces, e.g., flavor or Dirac space. The evaluation of these expressions is aided by considering the Fourier transformations of the quantities involved. The momentum representation of the propagator $\bar{\mathrm{Q}}^{-1}$ is given by

$$\bar{\mathrm{Q}}^{-1}(x,y) = \tfrac{1}{\beta}\sum_{n=-\infty}^{\infty}\int\tfrac{\mathrm{d}^dx}{(2\pi)^d}\,\mathrm{e}^{\mathrm{i}\nu_n(x_0-y_0)+\mathrm{i}\mathbf{p}\cdot(\mathbf{x}-\mathbf{y})}\,\widetilde{\bar{\mathrm{Q}}}^{-1}(\nu_n,\mathbf{p}) \tag{4.10}$$

with

$$\widetilde{\bar{\mathrm{Q}}}^{-1}(\nu_n,\mathbf{p}) = \frac{-\mathrm{i}\not{p}+\bar{\sigma}-\mathrm{i}\gamma_{\mathrm{ch}}\tau_3\bar{\pi}}{(\nu_n-\mathrm{i}\mu)^2+\mathbf{p}^2+\bar{\sigma}^2+\bar{\pi}^2} \tag{4.11}$$

and the inhomogeneous perturbation can be decomposed as

$$\delta\Phi(\mathbf{x}) = \int\tfrac{\mathrm{d}^dq}{(2\pi)^d}\,\mathrm{e}^{\mathrm{i}\mathbf{p}\cdot\mathbf{x}}\delta\tilde{\Phi}(\mathbf{q}) = \int\tfrac{\mathrm{d}^dq}{(2\pi)^d}\,\mathrm{e}^{\mathrm{i}\mathbf{q}\cdot\mathbf{x}}\left[\delta\tilde{\sigma}(\mathbf{q}) + \mathrm{i}\gamma_{\mathrm{ch}}\tau_3\delta\tilde{\pi}(\mathbf{q})\right]. \tag{4.12}$$

Using the Fourier representation for the propagator, $\mathcal{S}^{(1)}_{\text{eff}}$ assumes the form

$$\begin{aligned}\mathcal{S}^{(1)}_{\text{eff}} = &+\beta\left[\tfrac{\bar\sigma}{2G} - \tfrac{1}{\beta}\sum_{n=-\infty}^{\infty}\int\tfrac{\mathrm{d}^d p}{(2\pi)^d}\,\mathrm{tr}\left(\widetilde{\bar{\mathrm{Q}}}^{-1}(\nu_n,\mathbf{p})\right)\right]\int \mathrm{d}^d x\,\delta\sigma(\mathbf{x}) + \\ &+\beta\left[\tfrac{\bar\pi}{2G} - \tfrac{1}{\beta}\sum_{n=-\infty}^{\infty}\int\tfrac{\mathrm{d}^d p}{(2\pi)^d}\,\mathrm{tr}\left(\widetilde{\bar{\mathrm{Q}}}^{-1}(\nu_n,\mathbf{p})\,\mathrm{i}\tau_3\gamma_{\text{ch}}\right)\right]\int \mathrm{d}^d x\,\delta\pi(\mathbf{x}).\end{aligned} \tag{4.13}$$

The expressions in the square brackets are proportional to the homogeneous gap equations

$$\begin{aligned}\frac{\mathrm{d}\overline{U}_{\text{eff}}}{\mathrm{d}\bar\sigma} = \frac{\bar\sigma}{2G} - \tfrac{1}{\beta}\sum_{n=-\infty}^{\infty}\int\tfrac{\mathrm{d}^d p}{(2\pi)^d}\,\mathrm{tr}\left(\widetilde{\bar{\mathrm{Q}}}^{-1}(\nu_n,\mathbf{p})\right) &= \bar\sigma\left[\tfrac{1}{2G} - \overline{N}\tfrac{1}{\beta}\sum_{n=-\infty}^{\infty}\int\tfrac{\mathrm{d}^d p}{(2\pi)^d}\,\frac{1}{(\nu_n-\mathrm{i}\mu)^2+E^2}\right] = \\ &= \bar\sigma\left[\tfrac{1}{2G} - \overline{N} l_1\left(\bar\sigma^2+\bar\pi^2,\mu,T,d\right)\right], \end{aligned} \tag{4.14a}$$

$$\frac{\mathrm{d}\overline{U}_{\text{eff}}}{\mathrm{d}\bar\pi} = \frac{\bar\pi}{2G} - \tfrac{1}{\beta}\sum_{n=-\infty}^{\infty}\int\tfrac{\mathrm{d}^d p}{(2\pi)^d}\,\mathrm{tr}\left(\widetilde{\bar{\mathrm{Q}}}^{-1}(\nu_n,\mathbf{p})\,\mathrm{i}\tau_3\gamma_{\text{ch}}\right) = \bar\pi\left[\tfrac{1}{2G} - \overline{N} l_1\left(\bar\sigma^2+\bar\pi^2,\mu,T,d\right)\right], \tag{4.14b}$$

where $E^2 = \mathbf{p}^2+\bar\sigma^2+\bar\pi^2$. Thus $\mathcal{S}^{(1)}_{\text{eff}}$ vanishes, if $\bar\sigma,\bar\pi$ correspond to homogeneous extrema of the effective action.

Next, we insert the Fourier representations for the propagator and the inhomogeneous perturbations in $\mathcal{S}^{(2)}_{\text{eff}}$ to obtain

$$\mathcal{S}^{(2)}_{\text{eff}} = \tfrac{\beta}{2}\int\tfrac{\mathrm{d}^d q}{(2\pi)^d}\sum_{i,j=1}^{2}\delta\tilde\phi_i(\mathbf{q})\,\delta\tilde\phi_j(-\mathbf{q})\left[\tfrac{\delta_{i,j}}{2G} - \tfrac{1}{\beta}\sum_{n=-\infty}^{\infty}\int\tfrac{\mathrm{d}^d p}{(2\pi)^d}\,\mathrm{tr}\left(\widetilde{\bar{\mathrm{Q}}}^{-1}(\nu_n,\mathbf{p})\,c_i\,\widetilde{\bar{\mathrm{Q}}}^{-1}(\nu_n,\mathbf{p}+\mathbf{q})\,c_j\right)\right], \tag{4.15}$$

where the expression in the brackets are the elements of the Hessian of the effective action in field space. In order to identify a curvature, one would need to diagonalize this quantity via a basis transformation of $\delta\vec\phi$. We can circumvent this procedure by recognizing that the off-diagonal elements with $j\neq i$ are proportional to $\bar\sigma\times\bar\pi$ and that we can always use the chiral symmetry transformations to rotate the homogeneous part $\bar\pi$ into $\bar\sigma$. Thus, we assume $\bar\pi = 0$ from here on.

This simplifies $\mathcal{S}^{(2)}_{\text{eff}}$ to

$$\mathcal{S}^{(2)}_{\text{eff}} = \tfrac{\beta}{2}\int\tfrac{\mathrm{d}^d q}{(2\pi)^d}\left[|\delta\tilde\sigma(\mathbf{q})|^2\,\Gamma^{(2)}_{\sigma}(\mathbf{q},\bar\sigma,\mu,T) + |\delta\tilde\pi(\mathbf{q})|^2\,\Gamma^{(2)}_{\vec\pi}(\mathbf{q},\bar\sigma,\mu,T)\right] \tag{4.16}$$

with

$$\Gamma^{(2)}_{\phi_i}(\mathbf{q},\bar\sigma,\mu,T) = \frac{1}{2G} + \int\tfrac{\mathrm{d}^d p}{(2\pi)^d}\,\tfrac{1}{\beta}\sum_{n=-\infty}^{\infty}\mathrm{tr}\left[c_i\,\frac{-\mathrm{i}\tilde\nu_n\gamma_0 - \mathrm{i}(\mathbf{p}+\mathbf{q})_j\gamma_j+\bar\sigma}{\tilde\nu_n^2+E^2_{\mathbf{p}+\mathbf{q}}}\,c_i\,\frac{-\mathrm{i}\tilde\nu_n\gamma_0-\mathrm{i}\mathbf{p}_j\gamma_j+\bar\sigma}{\tilde\nu_n^2+E^2}\right] \tag{4.17}$$

and $\tilde\nu_n = \nu_n - \mathrm{i}\mu$, $E^2_{\mathbf{p}+\mathbf{q}} = (\mathbf{p}+\mathbf{q})^2+\bar\sigma^2$. Thus, we identify $\Gamma^{(2)}_{\phi_i}(\mathbf{q})$ as the curvature of the effective action for a perturbation of momentum $\mathbf{q}$ to $\bar\phi_i$. The calculation of the trace yields

$$\Gamma^{(2)}_{\phi_i}(\mathbf{q},\bar\sigma,\mu,T) = \frac{1}{2G} - \overline{N}\int\tfrac{\mathrm{d}^d p}{(2\pi)^d}\,\tfrac{1}{\beta}\sum_{n=-\infty}^{\infty}\frac{\tilde\nu_n^2+\mathbf{p}^2+\mathbf{p}\cdot\mathbf{q}-(-1)^{\delta_{i,1}}\bar\sigma^2}{\left(\tilde\nu_n^2+E^2_{\mathbf{p}+\mathbf{q}}\right)\left(\tilde\nu_n^2+E^2\right)}. \tag{4.18}$$

We proceed to split the integrand by completing the square,

$$\begin{aligned}\Gamma^{(2)}_{\phi_i}\left(\mathbf{q},\bar{\sigma},\mu,T\right) &= \frac{1}{2G} - \overline{N}\int \frac{\mathrm{d}^d p}{(2\pi)^d}\,\frac{1}{\beta}\sum_{n=-\infty}^{\infty} \frac{\tilde{\nu}_n^2 + (\mathbf{p}+\mathbf{q})^2 + \bar{\sigma}^2 - \mathbf{p}\cdot\mathbf{q} - \mathbf{q}^2 - 2\delta_{i,0}\bar{\sigma}^2}{\left(\tilde{\nu}_n^2 + E^2_{\mathbf{p}+\mathbf{q}}\right)\left(\tilde{\nu}_n^2 + E^2\right)} = \\ &= \frac{1}{2G} - \overline{N}\int \frac{\mathrm{d}^d p}{(2\pi)^d}\,\frac{1}{\beta}\sum_{n=-\infty}^{\infty}\left[\frac{1}{\tilde{\nu}_n^2 + E^2_{\mathbf{p}}} + \frac{-\mathbf{p}\cdot\mathbf{q} - \mathbf{q}^2 - 2\delta_{i,0}\bar{\sigma}^2}{\left(\tilde{\nu}_n^2 + E^2_{\mathbf{p}+\mathbf{q}}\right)\left(\tilde{\nu}_n^2 + E^2\right)}\right] = \\ &= \frac{1}{2G} - \overline{N} l_1\left(\bar{\sigma},\mu,T\right) + \overline{N}\int \frac{\mathrm{d}^d p}{(2\pi)^d}\,\frac{1}{\beta}\sum_{n=-\infty}^{\infty} \frac{+\mathbf{p}\cdot\mathbf{q} + \mathbf{q}^2 + 2\delta_{i,0}\bar{\sigma}^2}{\left(\tilde{\nu}_n^2 + E^2_{\mathbf{p}+\mathbf{q}}\right)\left(\tilde{\nu}_n^2 + E^2\right)},\end{aligned} \tag{4.19}$$

where we recognize that the first two terms are proportional to the gap equations (4.14a) and (4.14b). The further evaluation of the $\mathbf{q}$-dependent contribution depends on the the number of spatial dimensions d and the employed regularization scheme.[2] Explicit evaluations in the respective contexts can be found in Appendices C and D.

4.2.2 The Bosonic Wave-Function Renormalization

The bosonic wave function renormalization z_{ϕ_i} is the coefficient of the kinetic term quadratic in momentum within the effective action. Within the stability analysis, this is obtained by taking the double derivative of the bosonic two-point function [39], i.e.,

$$z_{\phi_i}\left(\bar{\sigma},\mu,T\right) = \left.\frac{\mathrm{d}^2\Gamma^{(2)}_{\phi_i}\left(q,\bar{\sigma},\mu,T\right)}{\mathrm{d}q^2}\right|_{q=0}. \tag{4.20}$$

If z is evaluated at the homogeneous minimum of the effective potential, we denote it as Z, i.e., $Z_{\phi_i}\left(\mu,T\right) \coloneqq z_{\phi_i}\left(\bar{\Sigma},\mu,T\right)$.

4.2.3 Detection of Inhomogeneous Phases and the Moat Regime

In this section, we discuss the different behaviors that we expect from the two-point function and their signals for the different phases. The bosonic two-point function $\Gamma^{(2)}_{\phi}$ measures the curvature of the effective action for an infinitesimal inhomogeneous perturbation $\delta\tilde{\phi}(\mathbf{q})$ of momentum $\mathbf{q}$. If we set the homogeneous field configurations $\bar{\sigma},\bar{\pi}$ to the global homogeneous minimum $\bar{\Sigma},\bar{\Pi}$, i.e., the configurations that minimize $\overline{U}_{\text{eff}}$, the gap equation and thus $\mathcal{S}^{(1)}_{\text{eff}}$ vanishes. This is the only relevant expansion point in the stability analysis, since its central object $\mathcal{S}^{(2)}_{\text{eff}}$ is then the leading order correction. The stability analysis performed at any other expansion point cannot provide information about the energetically preferred phase.[3] At this expansion point, $\Gamma^{(2)}(q=0)$ is positive or zero as this is the curvature for homogeneous perturbations, which is positive or zero[4] at the homogeneous minimum.

The traditionally expected behavior shown in Fig. 4.2(a) is that $\Gamma^{(2)}$ is a monotonically increasing function of q, since larger momenta should be associated to higher actions (e.g., given by a term $\propto \partial_\mu\phi\partial_\mu\phi$

2 Even some of the steps taken so far are not possible with lattice regularizations.

3 At some points in the discussion in Chapter 5, we also evaluate the two-point function at unphysical expansion points in an effort to study the structure of $\Gamma^{(2)}$.

4 We expect the curvature to vanish at a second order homogeneous phase transition.

in the action).

Negative values of $\Gamma^{(2)}$ indicate a negative curvature in the direction of an inhomogeneous perturbation and signal that an inhomogeneous field configuration is energetically favored. This is the situation depicted in Fig. 4.2(b), where the blue interval corresponds to the unstable momenta.

The moat regime (see Chapter 1) is characterized by a global minimum of $\Gamma^{(2)}$ at a finite q, which, however, is not necessarily negative. This shows that a point in the phase diagram that exhibits an instability is also part of a moat regime, but not vice versa. This minimum at a finite q is indicated by a negative curvature of $\Gamma^{(2)}$ at $q = 0$, which is given by Z. It is certainly possible to find $Z > 0$ and still a non-trivial global minimum. However, we restrict the detection of a moat regime to the sign of Z in the investigations in Chapters 5 to 7, but discuss the relevance of the cases where a moat regime is missed with this prescription (see Section 6.4).

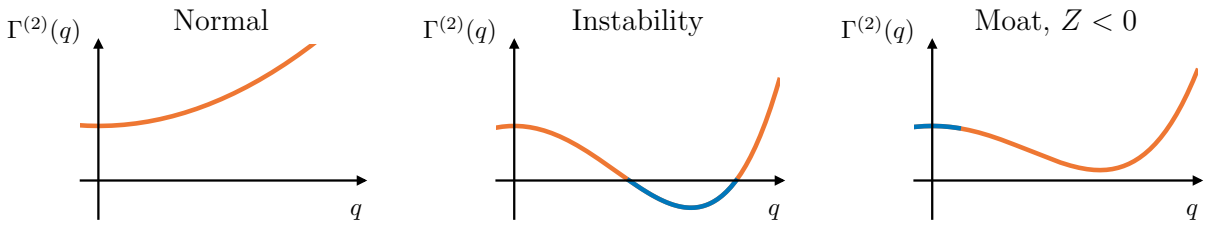

(a) **(b)** **(c)**

Figure 4.2: Sketches depicting the different scenarios that are expected from the two-point function $\Gamma^{(2)}$.

Chapter 5

Benchmarking the Stability Analysis in the (1 + 1)-Dimensional Gross-Neveu Model

Disclosure *This chapter discusses the results that were presented in Ref. [39], which was based on the preceding work in Ref. [140]. The work in Ref. [39] was not clearly divided between the authors and most calculations were carried out by multiple authors. All quantities that are presented here were calculated by me as well or exclusively calculated by me. These results were also discussed in a similar manner in Ref. [57] and, thus, there is overlap between the presentation here and in Ref. [57].*

In this chapter, we apply the stability analysis to the $(1+1)$-dimensional GN model, whose phase diagram can be calculated exactly [28] (see Section 3.1.3). Therefore, the goal of this investigation is not to explore unknown behavior in the phase diagram, but rather to benchmark the capabilities of the stability analysis against known results. Hence, this study presents an important step preceding the later investigations in Chapters 6 and 7, where we rely on the correctness of the stability analysis as an exact solution is not yet known.

The derivation of the stability analysis for the $(1+1)$-dimensional GN model can be obtained from the discussion in Section 4.2 by setting $N_f = 1$, $d = 1$ and neglecting all contributions that are generated by the existence of the pseudoscalar fields. An explicit derivation, and all relevant formulas for the two-point function and the wave-function renormalization in various limits of the arguments can be found in Ref. [39].

This chapter is organized as follows. Section 5.1 discusses the behavior of the two-point function for various parameter sets and investigates possible shortcomings of the stability analysis. In Section 5.2 it is analyzed how much we can deduce about the wavelength of the energetically preferred field configuration from analyzing the two-point function. The wave-function renormalization is examined for various parameters in Section 5.3 and the phase diagram as obtained from the stability analysis is discussed in Section 5.4. A brief summary is given in Section 5.5.

5.1 Behavior of the Two-Point Function

Fig. 5.1 shows the bosonic two-point function for various temperatures, chemical potentials and evaluation points $\bar{\sigma}$, i.e., the homogeneous field configuration used as an expansion point. Fig. 5.1(a) shows $\Gamma^{(2)}$ at $\mu = 0$ evaluated at the homogeneous minimum $\bar{\sigma} = \bar{\Sigma}$ for various temperatures. We exclusively find values

that are larger than zero and a monotonically rising behavior as a function of q. For $T/\bar{\Sigma}_0 = \mathrm{e}^{\gamma}/\pi = T_c/\bar{\Sigma}_0$, the model undergoes a second order phase transition from the HBP to the SP. Here, we expect that the curvature of the homogeneous potential at the homogeneous minimum vanishes, which is indicated by $\Gamma^{(2)}\left(q=0,\bar{\Sigma}=0,\mu=0,T_c\right)=0$.

Fig. 5.1(b) depicts the two-point function at $\mu/\bar{\Sigma}_0 = 0.6$ and $T = 0$ evaluated at a symmetric field configuration $\bar{\sigma} = 0$ and at the non-zero homogeneous minimum $\bar{\sigma} = \bar{\Sigma}$. The HBP is the energetically preferred phase at this point in the phase diagram (see Fig. 3.1). Nevertheless, by choosing the inappropriate expansion point $\bar{\sigma} = 0$, which is not the global homogeneous minimum, $\Gamma^{(2)}$ exhibits negative values at finite q. This signals an instability towards an inhomogeneous consideration, but it is not clear whether this is the globally favored configuration, since we used the wrong expansion point. Moreover, since these values for μ and T are in the region that is enclosed by the spinodals, the effective potential exhibits a positive curvature at the symmetric point $\bar{\sigma} = 0$. This illustrates that it is important to determine the correct homogeneous expansion point by properly minimizing the homogeneous effective potential.

Fig. 5.1(c) depicts $\Gamma^{(2)}$ at finite chemical potential and various temperatures, and evaluated at the respective homogeneous minimum $\bar{\sigma} = \bar{\Sigma}$. For low temperatures, this chemical potential corresponds to the IP in the full phase diagram of the GN model (compare to Fig. 3.1). This is reflected in the two-point function, which exhibits negative values for some momentum range. This is most evident for $T = 0$, where the two-point function diverges negatively at $q = 2\mu$, reflecting the discussion in Chapter 1 and Section 3.1.3. We denote the momentum corresponding to the minimum of $\Gamma^{(2)}$ as the characteristic momentum Q as , i.e.,

$$Q\left(\mu,T\right) = \min_{q} \Gamma^{(2)}\left(q,\bar{\Sigma},\mu,T\right). \tag{5.1}$$

The divergence at $q = 2\mu$ is nothing pathological, but merely reflects that the chemical potential at $T = 0$ can introduce non-analyticities in the effective action (see also the discussion Ref. [43]), which shows as a divergence in $\Gamma^{(2)}$ (as it is the curvature of the effective action). From the $T/\bar{\Sigma}_0 = 0.05$ curve, we see that a finite temperature smooths out this divergence. At $T/\bar{\Sigma}_0 = 0.2$ one finds that $\Gamma^{(2)}$ exhibits a single root, which signals the vanishing of the instability leaving only a moat regime. We find a monotonically increasing two-point function at large temperatures.

Fig. 5.1(d) depicts $\Gamma^{(2)}$ for fixed $T/\bar{\Sigma}_0 = 0.15$ for various chemical potentials at the homogeneous minimum $\bar{\sigma} = \bar{\Sigma}$. For $\mu/\bar{\Sigma}_0 = 0.0, 0.6$, we find monotonically increasing two-point functions. This behavior drastically changes at $\mu/\bar{\Sigma}_0 = 0.8$, which signals an instability by negative values of $\Gamma^{(2)}$. Increasing the chemical potential further weakens and eventually cancels the instability. We note that Q increases roughly following $Q = 2\mu$. Furthermore, we recognize that $\Gamma^{(2)}$ appears to retain its non-trivial minimum (and with it a negative wave-function renormalization, which we analyze more closely in Section 5.3) for increasing chemical potential. This is a qualitatively different (but not unexpected) effect than from increasing temperatures.

Fig. 5.2(a) depicts the two-point function in the plane of the homogeneous expansion point $\bar{\sigma}$ and the external momentum q at $(\mu,T)/\bar{\Sigma}_0 = (0.67, 0.1)$, which corresponds to the IP in the full phase diagram. If we restrict the field configurations to being homogeneous, this point belongs to the HBP. It is also enclosed by the spinodals meaning that the minimum of the homogeneous effective potential at finite $\bar{\Sigma}$ and the symmetric point are separated by a potential barrier as shown in Fig. 5.2(b). Fig. 5.2(a) reveals that the two-point function evaluated at $\bar{\Sigma}$ does not signal an instability towards an IP, which is in fact energetically favored. Only the evaluation points $\bar{\sigma}/\bar{\Sigma}_0 \lesssim 0.6$ exhibit a Q at a finite momentum. Since these evaluation points do not correspond to the homogeneous minimum, it is not clear whether this

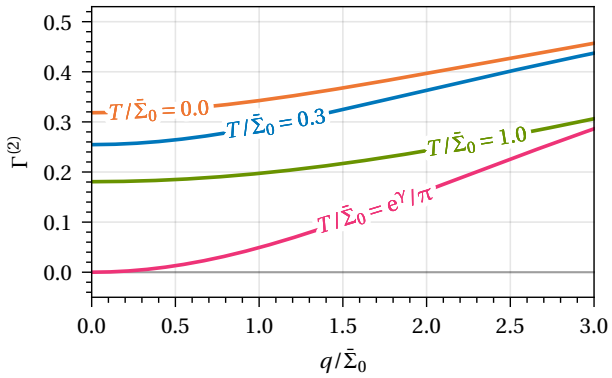

(a) $\Gamma^{(2)}$ at $\mu = 0$ and evaluated at the homogeneous minimum $\bar{\sigma} = \bar{\Sigma}$ for various temperatures. Reproduction of Ref. [39, Fig. 1].

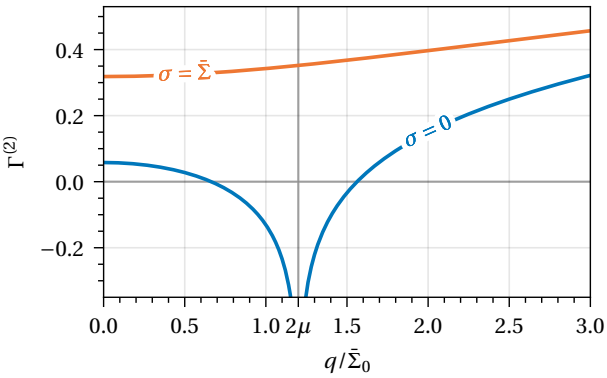

(b) $\Gamma^{(2)}$ at $\mu/\bar{\Sigma}_0 = 0.6$ and $T = 0$ for two homogeneous configurations $\bar{\sigma}$. Reproduction of Ref. [39, Fig. 2].

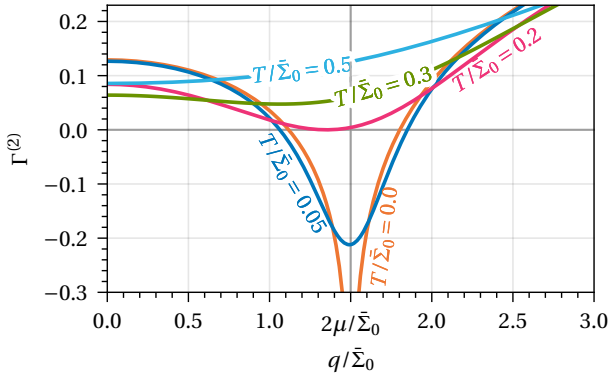

(c) $\Gamma^{(2)}$ at $\mu/\bar{\Sigma}_0 = 0.75$ and evaluated at the homogeneous minimum $\bar{\sigma} = \bar{\Sigma}$ for various temperatures. Reproduction of Ref. [39, Fig. 3].

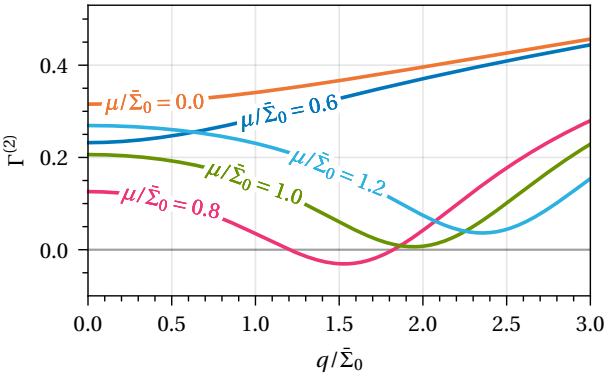

(d) $\Gamma^{(2)}$ at $T/\bar{\Sigma}_0 = 0.15$ and evaluated at the homogeneous minimum $\bar{\sigma} = \bar{\Sigma}$ for various chemical potentials. Reproduction of Ref. [39, Fig. 4].

Figure 5.1: The bosonic two-point function $\Gamma^{(2)}$ for various $\bar{\sigma}$, temperatures, and chemical potentials as a function of the external momentum q.

instability has any significance. Thus, at this point the stability analysis fails to detect the IP.

5.2 The Characteristic and the Dominant Momentum

The characteristic momentum Q is not necessarily the dominating momentum in the spectrum of the actual energetically preferred inhomogeneous chiral condensate, which we define as

$$q_\Sigma(\mu,T) = \arg\max_q \tilde{\Sigma}(q,\mu,T), \tag{5.2}$$

where $\tilde{\Sigma}$ is the Fourier transform of the energetically preferred field configuration Σ. Even though Q does not necessarily have to be equivalent to q_Σ, this "most unstable" momentum might provide a rough estimate.

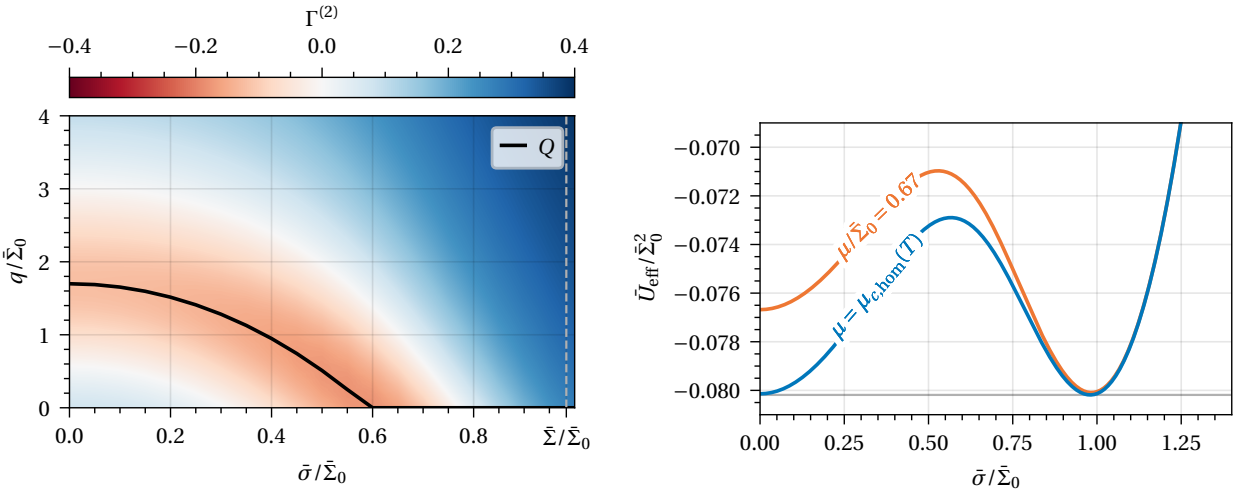

(a) The two-point function $\Gamma^{(2)}$ in the $(\bar{\sigma},q)$-plane at $T/\bar{\Sigma}_0 = 0.1$ and $\mu/\bar{\Sigma}_0 = 0.67$. The solid black line indicates the momentum that minimizes the two-point function at fixed $\bar{\sigma}$. Reproduction of Ref. [39, Fig. 8].

(b) The homogeneous effective potential at $T/\bar{\Sigma}_0 = 0.1$ for $\mu/\bar{\Sigma}_0 = 0.67$ and $\mu = \mu_{c,\mathrm{hom}}(T)$. Reproduction of Ref. [39, Fig. 7].

Figure 5.2: The effective potential and the two-point function illustrating the possible energy barrier between homogeneous expansion points and a possibly favored inhomogeneous configuration.

Fig. 5.3 depicts q_Σ and Q' given by[1]

$$Q'(\mu,T) = \begin{cases} Q(\mu,T) & \text{if } \Gamma^{(2)}\left(Q,\bar{\Sigma},\mu,T\right) < 0 \\ 0 & \text{otherwise} \end{cases}, \tag{5.3}$$

for two temperatures $T/\bar{\Sigma}_0 = 0, 0.15$ as a function of μ. For low chemical potentials Q' is zero while $q_\Sigma > 0$, which is caused by the finite homogeneous expansion point, which we discussed in Section 5.1. The characteristic momentum then jumps to a finite value as soon as $\bar{\Sigma} = 0$. The shaded region indicates the momenta that correspond to a negative $\Gamma^{(2)}$, i.e., momenta belonging to unstable directions of the effective action. Even though q_Σ is overestimated by Q', it is located within this range of unstable momenta. For increasing chemical potential the difference between q_Σ and Q' is decreasing. At $T/\bar{\Sigma}_0 = 0.15$, we find at the phase transition to the SP that both quantities are identical. This is not surprising as the amplitude of the energetically preferred configuration Σ vanishes at this transition. This renders the assumption of an inhomogeneous perturbation in the stability analysis exact.

Fig. 5.4 presents such a comparison in a more systematic way in the (μ,T)-plane. The left and the right plot show Q and q_Σ with their difference in the center plot. The region between the true phase transition from the HBP to the IP and the first order phase boundary HBP for a homogeneous order parameter differs maximally, because this is the region where the stability analysis fails. As we approach the phase transition from the IP to the SP, we find that the difference vanishes. The difference is again large beyond this transition, because Q is finite (but does not correspond to an instability) and q_Σ is zero in the SP.

1 This quantity indicates more clearly than Q whether an instability is present.

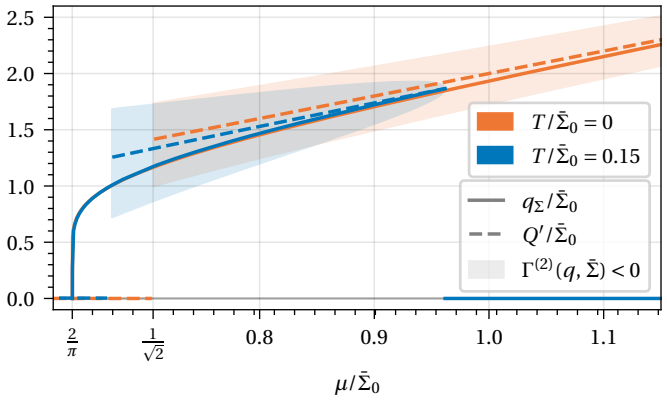

Figure 5.3: The dominant momentum q_Σ and the characteristic momentum Q at two temperatures $T = 0$ and $T/\bar{\Sigma}_0 = 0.15$ as a function of the chemical potential. The shaded regions indicate the range of momenta that correspond to a negative two-point function. Reproduction of Ref. [39, Fig. 10].

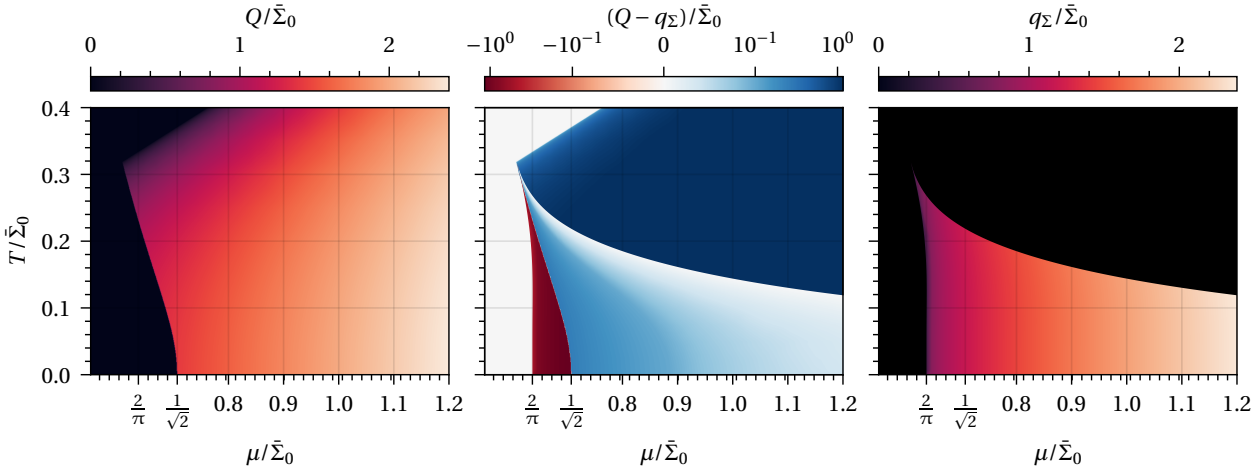

Figure 5.4: The dominant momentum q_Σ, the characteristic momentum Q and their difference in the (μ, T)-plane. Reproduction of Ref. [39, Fig. 11].

5.3 The Wave-Function Renormalization

As discussed in Section 4.2.2, one can extract the wave-function renormalization from the two-point function. Fig. 5.5 shows the wave-function renormalization Z evaluated at the homogeneous minimum for various temperatures as a function of μ and for various chemical potentials as a function of T.

In Fig. 5.5(a), the wave-function renormalization at low temperatures $T/\bar{\Sigma}_0 = 0.0, 0.2$ exhibits a jump at the homogeneous phase boundary, which is the drastic change in behavior that we have already seen on the level of the two-point function. This is caused by the first-order homogeneous phase transition, which causes a large change in the homogeneous expansion point. Z is negative for large chemical potentials signaling the moat regime for all depicted temperature curves. At higher temperatures, Z does not jump (as there is only a second-order homogeneous phase transition).

Fig. 5.5(b) depicts Z as a function of T for various chemical potentials. At $\mu/\bar{\Sigma}_0 = 0.7$, one crosses from the HBP into the SP via a first order transition in the homogeneous phase diagram. This is seen in the

wave-function renormalization as it exhibits a jump similarly as in Fig. 5.5(a). We find that Z assumes positive values for large enough temperatures at all depicted chemical potentials.

5.4 The Phase Diagram from the Stability Analysis

Fig. 5.6 summarizes the results of the preceding sections in a plot of the phase diagram in the (μ, T)-plane as obtained from the stability analysis. Inside the hatched region, one finds negative values of $\Gamma^{(2)}(q)$ for some finite q, which signals an IP. By comparing with Fig. 3.1, we notice that a part of the IP is not detected. In this region, which is located between the HBP ↔ IP boundary and the first order homogeneous phase transition, the homogeneous minimum is at a finite value. We found that it is separated by an energy barrier from the energetically preferred inhomogeneous minimum. Thus, one does not find a negative curvature for inhomogeneous perturbations, even though an inhomogeneous chiral condensate is energetically favored. The IP ↔ SP phase boundary is correctly reproduced, which is where the amplitude of the inhomogeneous condensate vanishes. This renders the expansion in the stability analysis exact.

The colormap indicates the value of the bosonic wave-function renormalization Z, where negative values correspond to the so-called moat regime. In the SP, one finds starting from the LP below the line given by $T \approx \mu/1.910669$ a negative Z [39, 43, 102]. Thus, the moat regime is present in a region, which is considerably larger than the IP itself.

5.5 Summary

The investigations in this chapter show that the stability analysis can be a formidable tool to detect the IP in FF models. The extent of the IP in the exactly solvable (1 + 1)-dimensional GN model is correctly reproduced up to a region in the vicinity of the homogeneous first order phase transition. Here, an energy barrier in the action separates the finite homogeneous expansion point and the inhomogeneous minimum in the effective action. Moreover, we observe that the characteristic momentum that corresponds to the minimum of the two-point function provides a good estimate for the dominating momentum of the

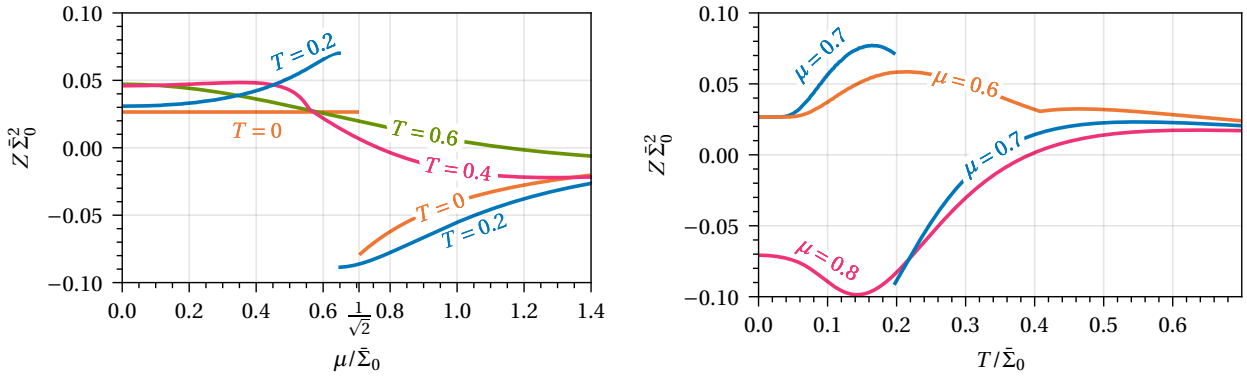

(a) The bosonic wave-function renormalization Z at various temperatures as a function of the chemical potential. Reproduction of Ref. [39, Fig. 12].

(b) The bosonic wave-function renormalization Z at various chemical potentials as a function of the temperature. Reproduction of Ref. [39, Fig. 13].

Figure 5.5: The bosonic wave-function renormalization Z at various temperatures and chemical potentials.

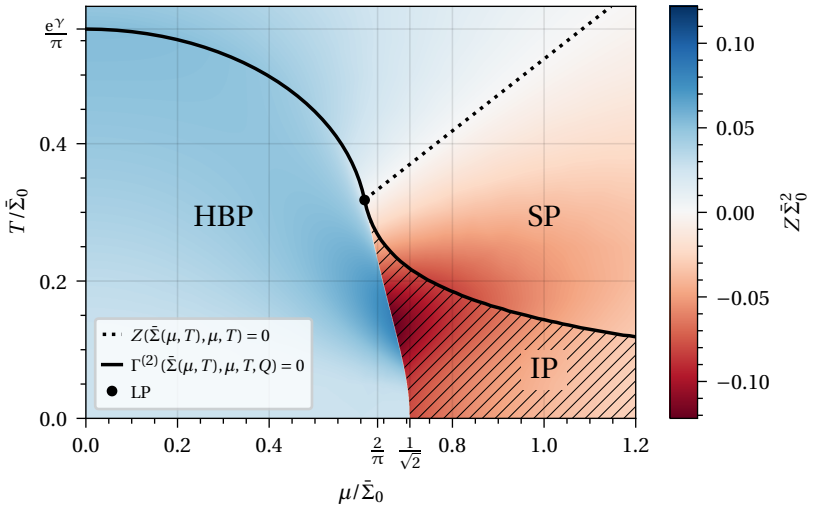

Figure 5.6: The phase diagram of the $(1+1)$-dimensional GN model as obtained from the stability analysis in the (μ,T)-plane. At the solid lines, one finds a single root in the two-point function $\Gamma^{(2)}$. The hatched region is the region of instability where one finds negative values of the two-point function at finite q. The colorbar indicates the value of the bosonic wave-function renormalization Z. Reproduction of Ref. [39, Fig. 9].

energetically favored inhomogeneous field configuration. Lastly, we mapped out the moat regime in this model and found that it covers a large portion of the (μ,T)-plane.

Chapter 6

Regularization Scheme Dependence of the Inhomogeneous Phase and the Moat Regime in the (3 + 1)-Dimensional Nambu-Jona-Lasinio Model

Disclosure *Some of the results that are discussed in this chapter were already presented in Ref. [71]. All calculations presented in this work were either also calculated by me or exclusively calculated by me. In particular, the lattice calculations in the infinite space-time volume were only carried out by me. Moreover, all results in Sections 6.3.5 and 6.4 were exclusively calculated by me and have not been published elsewhere. As of the writing of this thesis, a publication, which presents the results of this chapter, is in preparation [141].*

Within calculations of NJL-type models in the MFA, one encounters UV-divergent fermionic loop integrals, whose divergences are regulated by some regulator Λ and then absorbed by an appropriate coupling term. This process is called renormalization and allows us to remove the regulator from the theory. In the $(3+1)$-dimensional NJL model, the form of these divergences is such that one cannot absorb it by a coupling. Thus, one has to keep the regulator at a finite value and treat it as a parameter of the theory (see Section 3.2). There are many possible schemes to implement this regularization (see Section 2.3.1). Even though the schemes are expected to approach the same result in the renormalized limit, they tend to break some fundamental properties of the theory at finite regulators, e.g., translational invariance for lattice regularizations. Therefore, in models such as the $(3+1)$-dimensional NJL model these effects become part of the theory (see the discussion in Section 3.2.2). Unless we can discard all but one regularization scheme as unsuited for such an investigation, it is not clear which scheme to use. Therefore, we can only trust the results of a particular scheme, if they qualitatively agree with the results from other regularization schemes.

The scheme dependence in the $(3+1)$-dimensional NJL has been investigated with regard to the homogeneous phase diagram [55] and even with a focus on the IP [54]. These studies only considered continuum regularization schemes and disregarded lattice regularizations. However, for studies of the IP beyond the MFA lattice Monte-Carlo simulations are an excellent tool, which complement the capabilities of other methods in investigations beyond the MFA such as the FRG. Such simulations have already been used to investigate the inhomogeneous phase diagram of the $(1+1)$-dimensional GN model [46, 47] and of the related chiral GN model [111] at finite N. In the $(3+1)$-dimensional NJL model, Monte-Carlo simulations were employed to study the homogeneous phase diagram beyond the MFA [45, 142]. Thus, as

a preceding investigation to a possible Monte-Carlo study of the IP in the (3 + 1)-dimensional NJL model aiming to answer research question Q1, it is important to investigate the scheme dependence of the IP when using lattice regularizations within the MFA. This seeks to answer research question Q2 and is the first goal of this chapter.

Moreover, these aforementioned studies mostly compare individual parameter sets with one another, where it is difficult to analyze a general difference between schemes. Thus, by comparing the $T = 0$ phase diagram for the PV, SC and lattice schemes for a whole range of parameters, we search to achieve a more complete analysis of the scheme dependence. This seeks to answer research question Q3 and is the second goal of this chapter.

Lastly, recent studies [38, 42] emphasized the importance of the so-called moat regime (see the discussion in Chapter 1), which is closely related to the IP. As the last goal of this chapter, we analyze the dependence of this moat regime on the PV and SC scheme to provide an answer to research question Q4.

This chapter is organized as follows. Sections 6.1 and 6.2 discuss the particularities of this procedure when using lattice regularizations and the considered parameter sets respectively. The scheme dependence of the IP at $T = 0$ is investigated in Section 6.3. Section 6.4 analyzes the scheme dependence of the moat regime for the PV and SC scheme in the (μ, T)-plane. A short summary of these results is given in Section 6.5.

6.1 Parameter Fitting and Stability Analysis with Lattice Regularizations

While we presented the general parameter fitting strategy and the relevant formulas for continuum regularizations in Section 3.2.2, we also have to implement the analogous expressions for the lattice calculations. Moreover, the stability analysis, which was derived in Section 4.2 under the assumption of a continuum regularization, has to be adapted to lattice discretizations. This section aims to introduce the used lattice discretizations, the needed modifications of the parameter fitting as well as the modified stability analysis in a compact way. Some of these aspects have in part be discussed in the literature and we refer to them at the appropriate points.

6.1.1 Momentum Integration on the Lattice

The way that momentum integration is done on the lattice is significantly different from the continuum regularization schemes. A discretized space-time with lattice spacing a introduces an upper limit for the realizable momenta on this lattice given by $\Lambda_{\mathrm{LFT}} = \pi/a$. Moreover, a finite physical extent of the space-time $\frac{1}{T} \times V$ discretizes the momentum spectrum. Thus, in general the Matsubara summation and integration over spatial momenta in the continuum is replaced as

$$\sum_{n=-\infty}^{\infty} \int \frac{\mathrm{d}^3 p}{(2\pi)^3} \xrightarrow{\text{Lattice}} \frac{1}{a^4} \sum_{p \in \tilde{\Gamma}}, \tag{6.1}$$

where $\tilde{\Gamma}$ is the reciprocal lattice that holds all momenta available on the lattice. If we consider an infinite spatial volume, we recover a continuous spatial spectrum

$$\frac{1}{a^4} \sum_{p \in \tilde{\Gamma}} \xrightarrow{V \to \infty} \frac{1}{a} \sum_{p_0 \in \tilde{\Gamma}_0} \int_{-\frac{\pi}{a}}^{\frac{\pi}{a}} \frac{\mathrm{d}p_1}{2\pi} \int_{-\frac{\pi}{a}}^{\frac{\pi}{a}} \frac{\mathrm{d}p_2}{2\pi} \int_{-\frac{\pi}{a}}^{\frac{\pi}{a}} \frac{\mathrm{d}p_3}{2\pi} \tag{6.2}$$

and at zero temperature the sum over temporal momenta also becomes an integral (just like for the continuum at $T = 0$)

$$\frac{1}{a}\sum_{p_0\in\tilde{\Gamma}_0}\int_{-\frac{\pi}{a}}^{\frac{\pi}{a}}\frac{\mathrm{d}p_1}{2\pi}\int_{-\frac{\pi}{a}}^{\frac{\pi}{a}}\frac{\mathrm{d}p_2}{2\pi}\int_{-\frac{\pi}{a}}^{\frac{\pi}{a}}\frac{\mathrm{d}p_3}{2\pi}\xrightarrow{T\to 0}\int_{-\frac{\pi}{a}}^{\frac{\pi}{a}}\frac{\mathrm{d}p_0}{2\pi}\int_{-\frac{\pi}{a}}^{\frac{\pi}{a}}\frac{\mathrm{d}p_1}{2\pi}\int_{-\frac{\pi}{a}}^{\frac{\pi}{a}}\frac{\mathrm{d}p_2}{2\pi}\int_{-\frac{\pi}{a}}^{\frac{\pi}{a}}\frac{\mathrm{d}p_3}{2\pi}\,. \tag{6.3}$$

In terms of momentum integration, the only difference left between a momentum cutoff regularization (either SC or STC) and lattice regularizations is the geometry of the region of integration ((hyper)spherical vs. hypercubic). Thus, there is no spherical symmetry realized, which would allow us to simplify the integrals by going into spherical coordinates. We only consider the case of $T = 1/V = 0$ in the investigations with lattice regularization (with the exception of the results in Section 6.3.4) and as such only the integration as given by Eq. (6.3) is relevant for this work.

6.1.2 Lattice Regularizations

In LFT, fermionic and bosonic matter fields exist on the lattice points (contrary to gauge fields, which are described by the link variables). Thus, the discretization of local interaction terms involving only the fields is as straightforward as replacing the spatial integration with a sum over lattice sites.[1] For terms involving space-time derivatives, one might be inclined to represent these derivatives acting on these fields by a finite difference of neighboring lattice points such as

$$\partial\phi(x) \to \frac{\phi(x+a)-\phi(x-a)}{2a}, \tag{6.4}$$

where ϕ is some 1-dimensional scalar field. One can suppress discretization artifacts by introducing additional contributions from lattice sites that are further away. Nevertheless, a lattice derivative as in Eq. (6.4) is feasible for scalar bosonic fields in theories that feature only an even number of derivatives of the fields in the action.

The fermionic theories that we are interested in contain a single derivative acting on the fermionic fields in the Dirac operator, which appears in the action. This has some profound consequences, which are described by the Nielsen-Ninomiya theorem [143]. This theorem implies that any fermion discretization that is local, translational invariant, hermitian, and preserves chiral symmetry suffers from so-called fermion doublers. These are additional species of fermions that exist due to additional poles in the inverse Dirac operator, which are introduced by the discretization.

As a consequence there is a plethora of fermion discretizations all of which sacrifice one or more of the five incompatible properties given by the Nielsen-Ninomiya theorem. Therefore, there is not a single optimal way of discretizing fermionic theories and it depends on the application which schemes are appropriate.

We consider two kinds of lattice discretizations in this chapter:

1. SLAC[2] fermions [144, 145] for all four space-time directions,

1 This is not entirely true for some specific fermion discretization schemes, which is discussed in the section about Hybrid fermions.

2 This fermion discretization was developed by researchers at the Stanford Linear Accelerator Center (SLAC) – thus the name.

2. a Hybrid discretization, where the temporal dimension is discretized with SLAC fermions and the spatial dimensions are discretized with naive fermions.[3]

SLAC Fermions

The main idea of the SLAC discretization is to correctly reproduce the continuum dispersion relation of the fermionic fields, thus preserving chiral symmetry and avoiding fermion doublers [144, 145]. To understand its construction, we consider the fermion kinetic term in momentum space in the continuum

$$\int \mathrm{d}^D x\, \bar{\psi}(x)\partial\!\!\!/\psi(x) = \int \frac{\mathrm{d}^D p}{(2\pi)^D}\, \tilde{\bar{\psi}}(p)\mathrm{i}p\!\!\!/\tilde{\psi}(p), \tag{6.5}$$

where $\tilde{\bar{\psi}},\tilde{\psi}$ are the Fourier coefficients of the fermionic fields $\bar{\psi},\psi$. Here the momentum representation of the derivative operator is a term $\mathrm{i}p\!\!\!/$ that is linear in momentum.

The SLAC derivative operator $\mathrm{D}_{\mathrm{SLAC}}$ is then constructed such that

$$\int \mathrm{d}^D x\, \bar{\psi}(x)\mathbb{D}_{\mathrm{SLAC}}\psi(x) = \# \int \frac{\mathrm{d}^D p}{(2\pi)^D}\, \tilde{\bar{\psi}}(p)\mathrm{i}\gamma_\mu \mathcal{P}_{\mathrm{SLAC}}\left(p_\mu\right)\tilde{\psi}(p), \tag{6.6}$$

where # is some irrelevant constant resulting from the Fourier transformation on the lattice and $\mathcal{P}_{\mathrm{SLAC}}$ is the SLAC dispersion relation

$$\mathcal{P}_{\mathrm{SLAC}}\left(p_\mu\right) = 2\Lambda_{\mathrm{LFT}}\left(\frac{p_\mu}{2\Lambda_{\mathrm{LFT}}} - \left\lfloor \frac{1}{2} + \frac{p_\mu}{2\Lambda_{\mathrm{LFT}}} \right\rfloor\right), \tag{6.7}$$

where $\lfloor\cdot\rfloor$ denotes the floor function. Fig. 6.1 shows $\mathcal{P}_{\mathrm{SLAC}}$ as a function of p_μ. It is exactly linear for momenta inside the first Brillouin zone, i.e., $|p_\mu| < \Lambda_{\mathrm{LFT}}$ and this behavior is periodically continued for larger momenta. This causes a discontinuity at the edge of the Brillouin zone, which results in non-locality in position space. Chiral symmetry is, however, preserved exactly and there are no fermion doublers in the spectrum.[4] The non-locality is the reason why this discretization cannot be used in gauge theories and thus is not commonly used in LFT in general. However, it has been used successfully in various investigations of FF models such as the GN model [46, 47, 65, 104], the chiral GN model [111], the Thirring model [146, 147], and the NJL model [65].

The Dirac operator of the NJL model in momentum space at $T = 0$ with the SLAC regularization is given by

$$\mathrm{Q}\left(p,q\right) = (2\pi)^D \delta^D\left(p-q\right)\left[\mathrm{i}\gamma_\mu \mathcal{P}_{\mathrm{SLAC}}\left(p_\mu\right) + \gamma_0\mu\right] + \tilde{\sigma}\left(p-q\right) + \mathrm{i}\gamma_{\mathrm{ch}}\vec{\tau}\cdot\tilde{\vec{\pi}}\left(p-q\right). \tag{6.8}$$

Hybrid Fermions

In the Hybrid discretization, we apply a SLAC derivative in the temporal direction and discretize the spatial directions with the so-called naive discretization. It is called 'naive' as one uses the simple finite

3 The choice of a Hybrid discretization instead of a purely naive discretization is caused by technical issues, which we illustrate below.

4 One could argue that the SLAC fermions still exhibit doublers by the would-be zero crossing at the edge of the Brillouin zone, where the slope of the dispersion relation is infinite.

difference for the discretization

$$\partial_\mu \psi(x_\mu) \to \frac{\psi(x_\mu + a) - \psi(x_\mu - a)}{2a}, \tag{6.9}$$

which is how one might intuitively discretize such a derivative using Taylor expansions of $\psi(x_\mu + a)$ and $\psi(x_\mu - a)$. We find a dispersion relation

$$\mathcal{P}_{\text{naive}}\left(p_\mu\right) = \sin(p_\mu a), \tag{6.10}$$

for the naive discretization. This discretization is local, translational invariant, hermitian, and preserves chiral symmetry. True to the Nielsen-Ninomiya theorem, one finds that such a discretization is plagued by 2^n fermion doublers, where n is the number of spacetime directions discretized naively. The poles of the inverse Dirac operator that correspond to these doublers are located at the edge of the first Brillouin zone, which are generated by the zero crossings of the dispersion relation at $p_\mu = \Lambda_{\text{LFT}}$ as shown in Fig. 6.1.

These doublers cause additional artifacts in theories with a Yukawa interaction term, i.e., terms $\propto \bar{\psi}(x)\Gamma\phi(x)\psi(x)$ with ϕ being some bosonic field and Γ being some arbitrary matrix in spinor space. In momentum space, one finds that this term is proportional to

$$\sim \tilde{\bar{\psi}}(p)\Gamma\tilde{\phi}(p-q)\tilde{\psi}(q), \tag{6.11}$$

i.e., the interaction of the fermionic fields at different momenta is mediated by the bosonic field with the momentum equivalent to the difference of the fermionic momenta. Thus, the bosonic field at large momenta can mediate interactions of fermionic fields from the vicinity of different poles, i.e., different doubler fields (the poles of the doublers have a minimum distance of π/a in momentum space). These interactions are problematic for two main reasons [46, 58, 148]. Firstly, if one considers doublers as additional fermion species, these introduce incorrect interactions as there are no interactions between different fermion species in bosonized NJL-type models (compare to Eqs. (2.7) and (2.8)). The other problem is that these interactions do not only contain the original Dirac structure Γ. One finds that they effectively contain additional Dirac matrices, thus generating also vector and other interactions, which are also not realized in the NJL-type models that we are interested in.

These incorrect doubler-doubler interactions can partly be cured by a modification of the Yukawa interaction. In the momentum space form of Eq. (6.11), one introduces a so-called weight function $\tilde{W}(\mathbf{p}-\mathbf{q}) = \prod_{i=1}^{D-1} \tilde{w}(p_i - q_i)$ into the Yukawa interaction in the Dirac operator at $T = 0$ in momentum space

$$\begin{aligned} \mathrm{Q}\left(p,q\right) = (2\pi)^D \delta^D\left(p-q\right)\left[\mathrm{i}\gamma_0 \mathcal{P}_{\text{SLAC}}\left(p_0\right) + \gamma_0\mu + \mathrm{i}\gamma_i \sin\left(p_i a\right)\right] + \\ + \tilde{W}\left(\mathbf{p}-\mathbf{q}\right)\left[\tilde{\sigma}\left(p-q\right) + \mathrm{i}\gamma_{\text{ch}}\vec{\tau}\cdot\vec{\tilde{\pi}}\left(p-q\right)\right]. \end{aligned} \tag{6.12}$$

The weighting function should fulfill two properties:

1. $\tilde{w}(0) = 1$, i.e., interactions of fields at the same momentum should not be changed,
2. $\tilde{w}(\pi/a) = 0$, i.e., interactions of fields with a momentum difference of π/a in any direction should be completely suppressed.

One expects that in the continuum limit, any weight function, which fulfills these quantities, to effectively suppress doubler-doubler interactions as the relevant fermionic modes are located at the poles.

We consider two possible functional forms for the weight function:

- A smooth weighting based on a cosine function of the form

$$\tilde{w}_{\cos} = \frac{1+\cos(p_\mu)}{2}. \tag{6.13}$$

  We refer to the Hybrid discretization with this weighting function as $\text{Hybrid}_{\cos}$.

- A sharp complete suppression of momenta larger than $\pi/(2a)$ [5] of the form

$$\tilde{w}_{\Theta} = \Theta\left(1 - |p_\mu| \frac{2a}{\pi}\right). \tag{6.14}$$

  We refer to the Hybrid discretization with this weighting function as Hybrid_{Θ}.

If we restrict the bosonic fields to being homogeneous, calculations with both weighting functions yield identical results. Only the $\tilde{\phi}(0)$ Fourier coefficient is then non-zero for which both weighting functions are identical $\tilde{w}_{\cos} = \tilde{w}_{\Theta} = 1$. We refer for a more in-depth discussion of the doubler mixing and the weighting procedure to the Refs. [46, 58, 148].

In our calculations, we assume that the fermion doublers act as additional fermion species (as we expect that there are effectively no interactions between them due to the weighting). This means that, for $N_c = 3$, the calculations with the Hybrid fermions would contain $N = 8N_c$ fermion species compared to the $N = N_c = 3$ for the regularization schemes without fermion doublers. To account for this, we set $N_c = 3/8$ to obtain $N = 3$ for the Hybrid fermions.[6]

6.1.3 Lattice Fermion Propagators for Homogeneous Bosonic Fields

Due to the different fermion dispersion relations realized in the Dirac operator (see Section 6.1.2), we find different form of the fermion propagators for the different lattice regularization. For the SLAC discretization, the fermion propagator at finite chemical potential and for a homogeneous bosonic field

5 This is the hypothetical border between the two momentum areas associated with different doublers.

6 A non-integer number of colors appears pathological, but since there are no Gauge fields in this model, N_c enters only as a prefactor in integrals.

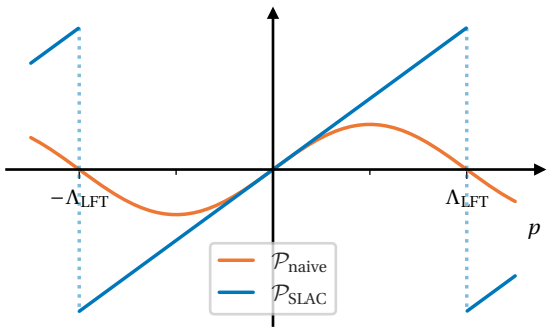

Figure 6.1: A sketch illustrating the two fermionic dispersion relations $\mathcal{P}_{\text{naive}}$ and $\mathcal{P}_{\text{SLAC}}$.

configuration $(\sigma,\vec{\pi}) = (\bar{\sigma},0)$ is given by

$$S_{\mathrm{SLAC}}(p) = \frac{-\mathrm{i}\gamma_\mu \mathcal{P}_{\mathrm{SLAC}}(p_\mu) - \gamma_0\mu + \bar{\sigma}}{\left(\mathcal{P}_{\mathrm{SLAC}}(p_0) - \mathrm{i}\mu\right)^2 + \sum_{i=1}^{3}\left(\mathcal{P}_{\mathrm{SLAC}}(\mathbf{p}_i)\right)^2 + \bar{\sigma}^2}, \tag{6.15}$$

with the dispersion relation $\mathcal{P}_{\mathrm{SLAC}}$ given by Eq. (6.7). Note that even though the propagator looks in form similar to the continuum propagator, the discontinuous dispersion relation introduces discontinuities in the propagator itself.

For the Hybrid discretization, the fermion propagator at finite chemical potential is given by

$$S_{\mathrm{Hybrid}}(p) = \frac{-\mathrm{i}\gamma_0\left[\mathcal{P}_{\mathrm{SLAC}}(p_0) - \mathrm{i}\mu\right] - \mathrm{i}\sum_{i=1}^{3}\gamma_i \sin(a\mathbf{p}_i) + \bar{\sigma}}{\left(\mathcal{P}_{\mathrm{SLAC}}(p_0) - \mathrm{i}\mu\right)^2 + \sum_{i=1}^{3}\sin^2(a\mathbf{p}_i) + \bar{\sigma}^2}. \tag{6.16}$$

For both discretizations, the altered dispersion relations have severe impact on our ability to carry out analytic computations with these regularization. In particular, in expressions with fermion propagators that have sums of momenta as argument, e.g., $S(p+q)$, one cannot easily separate the momenta as we have done in the continuum derivation of the stability analysis in Section 4.2.

6.1.4 Parameter Fitting

We discussed the parameter fitting process of the NJL model for continuum regularization schemes in Section 3.2.2. For the used SLAC and Hybrid lattice regularizations some of the steps are fundamentally different.[7]

The first major difference is that on the left-hand side of Eq. (3.19) the momentum q_μ has to be replaced by the respective fermion dispersion relation $\mathcal{P}_X(q_\mu)$ [45, 120]. The right-hand side expression is obviously different due to the momentum integration and general form of the fermion propagator. Furthermore, if we choose to orient q in the direction of a naive discretization, the expression evaluates to zero due to the additional poles of the doublers. Thus, one has to choose $\mu = 0$ with the Hybrid discretization and this is the main reason why we cannot choose a naive discretization in every space-time direction. Another difference is in Eq. (3.25), where one does not arrive at an expression, which can be simplified with a partial fraction decomposition. This immensely complicates taking the derivative of Π_{ps}.

The final expressions for the parameter fitting as they are found with the lattice discretizations are given in Appendix C.2.3.

6.1.5 Stability Analysis

The stability analysis for the Hybrid discretization has been derived for the (2 + 1)-dimensional GN model in Ref. [49]. The derivation for the NJL model is almost identical due to the similarities of the models. Therefore, we present only the final expressions of the two-point functions for the Hybrid and SLAC discretizations, and refer for details to the discussion in Refs. [49, 50].

As with the continuum regularizations in Section 4.2, one has to calculate the trace over a product of

7 A discussion for the parameter fitting with staggered fermions can be found in Refs. [45, 120].

propagators. For the matrix trace we find

$$\begin{aligned}&\operatorname{tr}\left[c_i S_X\left(p+(0,\mathbf{q})\right) c_i S_X\left(p\right)\right] = \\ &= \overline{N}\frac{-\left(\mathcal{P}_{\mathrm{SLAC}}\left(p_0\right)-\mathrm{i}\mu\right)^2-\sum_{i=1}^{3}\mathcal{P}_X\left(p_i\right)\mathcal{P}_X\left(p_i+\mathbf{q}_i\right)+(-1)^{\delta_{i,1}}\bar{\sigma}^2}{\left[\left(\mathcal{P}_{\mathrm{SLAC}}(p_0)-\mathrm{i}\mu\right)^2+\sum_{i=1}^{3}\left(\mathcal{P}_X(\mathbf{p}_i)\right)^2+\bar{\sigma}^2\right]\left[\left(\mathcal{P}_{\mathrm{SLAC}}(p_0)-\mathrm{i}\mu\right)^2+\sum_{i=1}^{3}\left(\mathcal{P}_X(\mathbf{p}_i+\mathbf{q}_i)\right)^2+\bar{\sigma}^2\right]},\end{aligned} \tag{6.17}$$

where S_X,$\mathcal{P}_X$ are either the corresponding Hybrid (Eqs. (6.10) and (6.16)) or SLAC expressions (Eqs. (6.7) and (6.15)). The largest difference to the continuum regularizations is that one cannot separate this into a q-independent and a q-dependent part anymore.

In contrast to the continuum calculations, the orientation of $\mathbf{q}$ is not entirely arbitrary as the lattice breaks the rotational symmetry. We choose to $\mathbf{q}$ orient along one of the Cartesian axes, e.g., $\mathbf{q} = (0,0,q)$, but other orientations could also be plausible.

SLAC Fermions

In the infinite volume at $T = 0$, one finds for the two-point function (see Section 4.2 for the notation of regarding the two-point function)

$$\Gamma^{(2)}_{\phi_i}\left(q,\bar{\sigma},\mu,T=0\right) = \frac{1}{2G} + \int_{-\Lambda_{\mathrm{LFT}}}^{\Lambda_{\mathrm{LFT}}}\frac{\mathrm{d}p_0}{2\pi}\int_{-\Lambda_{\mathrm{LFT}}}^{\Lambda_{\mathrm{LFT}}}\frac{\mathrm{d}p_1}{2\pi}\int_{-\Lambda_{\mathrm{LFT}}}^{\Lambda_{\mathrm{LFT}}}\frac{\mathrm{d}p_2}{2\pi}\int_{-\Lambda_{\mathrm{LFT}}}^{\Lambda_{\mathrm{LFT}}}\frac{\mathrm{d}p_3}{2\pi}\operatorname{tr}\left[c_i S_{\mathrm{SLAC}}\left(p\right) c_i S_{\mathrm{SLAC}}\left(p+(0,\mathbf{q})\right)\right]. \tag{6.18}$$

One can carry out the integration over the temporal momenta to obtain Eqs. (C.50) and (C.51).

Hybrid Fermions

With the Hybrid fermions, one finds that the weight function that we had to introduce to the Yukawa interaction (see Section 6.1.2) contributes in the two-point function (compare Refs. [49, 50]). Thus, we find for the two-point function in the infinite volume at $T = 0$

$$\begin{aligned}&\Gamma^{(2)}_{\phi_i}\left(q,\bar{\sigma},\mu,T=0\right) = \\ &= \frac{1}{2G} + \tilde{W}_X\left(\mathbf{q}\right)\tilde{W}_X\left(-\mathbf{q}\right)\int_{-\Lambda_{\mathrm{LFT}}}^{\Lambda_{\mathrm{LFT}}}\frac{\mathrm{d}p_0}{2\pi}\int_{-\Lambda_{\mathrm{LFT}}}^{\Lambda_{\mathrm{LFT}}}\frac{\mathrm{d}p_1}{2\pi}\int_{-\Lambda_{\mathrm{LFT}}}^{\Lambda_{\mathrm{LFT}}}\frac{\mathrm{d}p_2}{2\pi}\int_{-\Lambda_{\mathrm{LFT}}}^{\Lambda_{\mathrm{LFT}}}\frac{\mathrm{d}p_3}{2\pi}\operatorname{tr}\left[c_i S_{\mathrm{Hybrid}}\left(p\right) c_i S_{\mathrm{Hybrid}}\left(p+(0,\mathbf{q})\right)\right],\end{aligned} \tag{6.19}$$

where the weight function $\tilde{W}_X$ is either chosen to be $\tilde{W}_{\cos}$ or $\tilde{W}_\Theta$ (see Section 6.1.2). One can carry out the integration over the temporal momenta to obtain Eqs. (C.50) and (C.52).

6.2 Parameter Scans

Fig. 6.2 summarizes the results of the parameter fitting procedure (see Section 3.2.2 for the parameter fitting strategy and Appendix C.2 for explicit formulas for the parameter fitting). Note that the results for the Hybrid$_\Theta$ and Hybrid$_{\cos}$ regularization are identical as the parameter fitting is done with homogeneous fields, where both discretizations are identical. All results with the PV regularization in this chapter are obtained with $N_{\mathrm{PV}} = 3$ with $\vec{c} = (1,-3,3,-1)$ and $\vec{\alpha} = (0,1,2,3)$. Fig. 6.2(a) depicts the regulator Λ as a

function of the constituent fermion mass M_0, which is an input into the parameter fitting. The regulator is a bare quantity, which is special to the different regularization schemes, but its role as the largest defining scale is universal. Here we recognize that across the regularization schemes Λ increases for decreasing M_0. The regulator increases slightly both with the PV and Hybrid regularization for increasing M_0 at large values.

Fig. 6.2(b) depicts the values of the regulator as in Fig. 6.2(a), but in units of the largest regulator Λ_{PV}. This shows that except for the Hybrid regularization the ratios between the regulators remain relatively constant.

Fig. 6.2(c) shows the coupling as a function of the constituent fermion mass M_0. The coupling is a bare quantity, whose value can wildly differ between the regularization schemes. However, the order of magnitude in units of Λ and the trend as function of M_0 agree between the schemes. Fig. 6.2(d) shows the regulator as a function of the coupling, which serves mainly as a reference to depict which parts of the parameter space are covered by the different regularization schemes.

In general we find that the parameters of the SLAC fermions and the SC regularization, and the ones of the PV and Hybrid regularization are pairwise quite similar. For the former, this stems from the fact that for homogeneous fields in vacuum (the situation in the tuning process), the two schemes regulate the theory almost identically. There are only two differences. The first one is that the SLAC fermions also regulate the temporal direction, and the second one is the discrepancy in the region of momentum integration, which has a hypergeometric shape for the SLAC fermions, while for the SC regularization, it possesses a spherical geometry (compare with the discussion in Section 6.1.1). The PV and Hybrid regularization both introduce additional fermion species during regularization. This likely has a significant impact on the parameters, which sets it off from the other regularization schemes.

6.3 Regularization Scheme Dependence of the Inhomogeneous Phase at Zero Temperature

In this section, we discuss the regularization scheme dependence of the IP at $T = 0$ for the PV, SC, SLAC, Hybrid$_\Theta$ and Hybrid$_{\cos}$ regularization schemes. We start by presenting the principal result of this investigation in Section 6.3.1, which is the inhomogeneous phase diagram as obtained from the stability analysis. This leads to more detailed discussions of various aspects in an effort to understand the large discrepancies between the regularization schemes in the subsequent sections.

Whenever we show two-point functions in the rest of this chapter, they are evaluated at the physical expansion point, i.e., the homogeneous field configuration that minimizes the homogeneous effective potential, unless explicitly stated otherwise.

6.3.1 General Phase Structure

Fig. 6.3 depicts the results of the stability analysis at $T = 0$ in the (M_0,μ)-plane for different regularization schemes, which represent the central results of this chapter. The upper plot shows the chemical potential μ in units of MeV, while the lower plot shows μ in units of the respective regulator Λ. We recall from Fig. 6.2 that the regulator is a function of M_0 and in general small values of M_0 correspond to large values of the regulator. The results are presented at $T = 0$ as this greatly facilitates calculations and suffices to illustrate the possible regulator dependence.

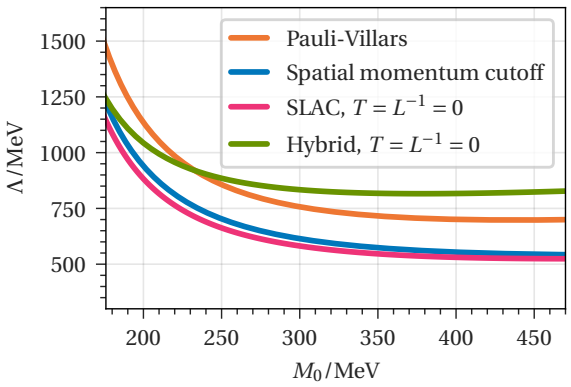

(a) The regulator Λ as a function of M_0. Note the respective definitions of Λ for the different schemes.

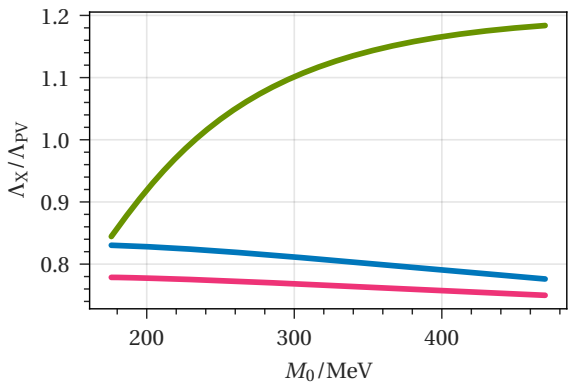

(b) The value of the regulators in units of Λ_{PV} as a function of M_0 .

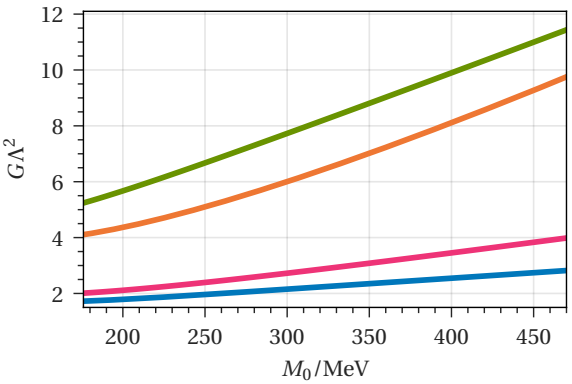

(c) The coupling G in units of Λ as a function of M_0.

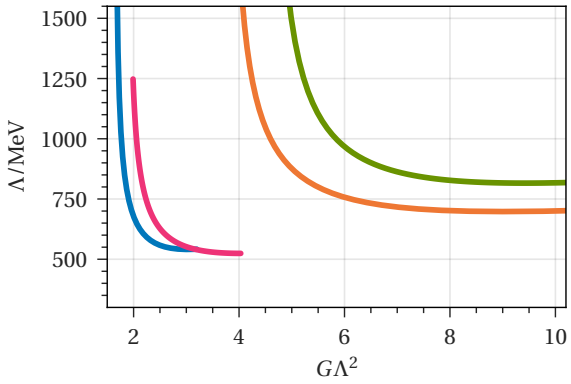

(d) The lines in the G,Λ-plane which are covered by the regularization schemes.

Figure 6.2: Various quantities involved in the parameter fitting process of the NJL model for PV, SC, SLAC and Hybrid regularization (the parameters are identical for Hybrid_Θ and $\text{Hybrid}_{\cos}$).

Homogeneous Phase Boundaries

We determine the homogeneous phase boundaries as presented in Fig. 6.3 by minimization of the homogeneous effective potential (2.17) and subsequent root finding (see Appendix C.3 for explicit expressions for the effective potential with the different regularization schemes). The knowledge of the homogeneous phase structure is important, since the physically relevant expansion point for the stability analysis is given by the minimum of the effective potential $\bar{\Sigma}$.

We note that the homogeneous phase boundaries agree comparatively well – noteworthy are the almost indistinguishable boundaries for the SC and PV regularization (the orange and blue lines). Interestingly, while the SC and SLAC regularization behave rather similar in the parameter tuning, we find a larger discrepancy between the homogeneous phase boundaries. This can be traced back to the regularization of the temporal direction with the lattice regularization, which alters the way that the chemical potential acts on the system compared to the SC regularization. The homogeneous phase boundaries of all regularization schemes converge for small M_0, i.e., large values of Λ. Moreover, we find that the position of the critical endpoint largely agrees between the regularization schemes.

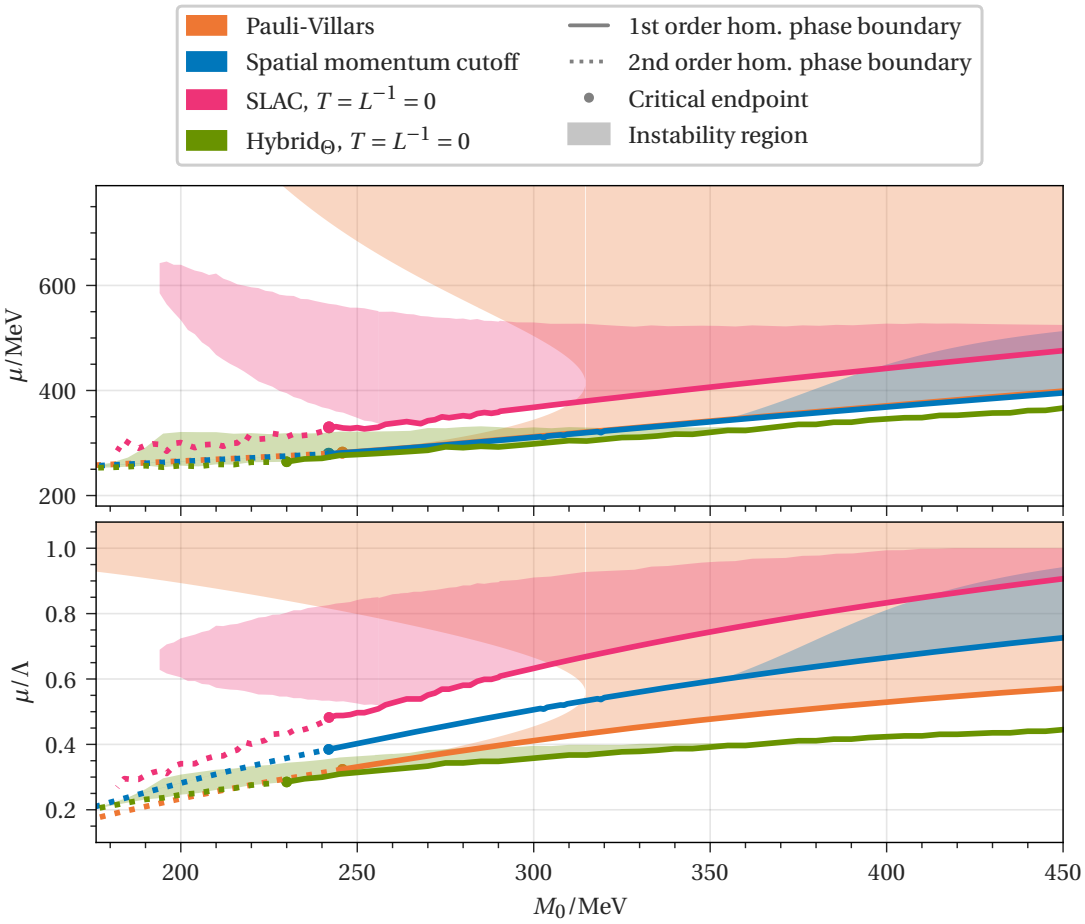

Figure 6.3: The phase diagram from the stability analysis in the (M_0,μ)-plane-plane at $T = 0$ for the PV, SC, SLAC and Hybrid$_\Theta$ regularization. In the upper plot, μ is given in MeV and in the lower plot the same data is given for μ/Λ, where Λ assumes the respective values for the different regularizations. The solid lines represent the first order phase boundary and the dotted lines the second order phase boundary, when the fields are restricted to homogeneous field configurations. The circle indicates the CP. The shaded regions are the regions of instability where the bosonic two-point functions $\Gamma^{(2)}$ exhibit negative values for some bosonic momenta q.

The boundaries for the two lattice discretization schemes are noisy at small M_0 as the underlying integrals are evaluated with stochastic integration techniques (essentially a Monte-Carlo integration). In the regions of small M_0 the required number of samples is beyond the numerical capabilities and the integration routines would require further improvements. However, this mostly affects the homogeneous phase boundary and since this is not the focus of our investigation, the current state suffices. As we are mainly interested in qualitative results, these errors in the phase boundary do not pose a severe problem.

Instability Regions

The instability regions are the regions where the bosonic two-point function $\Gamma^{(2)}$ exhibits negative values for some finite momentum q.[8] This signals that at this point in the phase diagram an energetically preferred inhomogeneous field configuration exists. However, as we have seen in Chapter 5, it can happen that parts of the IP are not correctly detected by the stability analysis. This is evidently also the case in some parts of the phase diagram as shown in Fig. 6.3. Similar to the results in Chapter 5, we only detect an instability when $\bar{\Sigma} = 0$. From the investigations in Ref. [14] we know that parts of the IP can be located within the HBP that one finds for homogeneous field configurations (see Fig. 3.8). Explicit expressions for the two-point function for the different regularization schemes for various limits of the parameters are presented Appendix C.4.

The most striking feature of the instability regions in Fig. 6.3 is the total disagreement between the regularization schemes with regard to the region of instability. There is not a single point in the (μ, M_0)-plane where all schemes exhibit an instability simultaneously. In the following we go through the different regularization schemes one by one and highlight important features.

The PV regularization This regularization exhibits the largest instability region as it extends to infinity in the direction of the chemical potential. For M_0 smaller than $\approx 315\,\mathrm{MeV}$, we find that the instability region splits into a small part that is connected to the HBP, which is commonly denoted as "inhomogeneous island", and a larger, disconnected region called "inhomogeneous continent". The continent was discussed in detail in Ref. [149] with inconclusive results about the reliability of the results regarding the IP in this region. Although rather obscured in the plot, we find that the LP and CP agree as it is generally observed for the renormalizable low-dimensional models (see Section 3.1.3) and the PV regularization in (3 + 1)-dimensional models (see e.g. Refs. [14, 35]).

The SC regularization The instability region of this regularization is considerably smaller and lacks any sort of inhomogeneous continent and has a finite extent in μ-direction. We note that the LP does not coincide with the CP, which was already observed in Refs. [14, 35, 49, 132].

The SLAC regularization This lattice regularization shows a rather different behavior with the instability region splitting off, while no inhomogeneous island connected to the HBP is retained. Just as with the SC, one observes the split of LP and CP.

The Hybrid regularization Only one of the two discretization schemes Hybrid_Θ and $\mathrm{Hybrid}_{\cos}$ is depicted. The $\mathrm{Hybrid}_{\cos}$ discretization does not exhibit any instability at all, which we investigate in Section 6.3.2 while their homogeneous phase boundary is identical (see the discussion in Section 6.1.2). The Hybrid_Θ discretization has yet another shape of the instability region compared to the other regularization schemes with the Hybrid region being the smallest of all schemes. Unlike with the other regularization schemes, the instability region is also connected to the HBP in regions where the homogeneous phase transition is of second order. This implies that the LP is located at a higher temperature than the CP. A similar behavior can be observed in the NJL model, when vector interactions are included [66] (see the discussion in Section 3.3.3). In the present situation, it is a regularization artifact of the naive fermion discretization. We recall the discussion in Section 6.1.2 of the discretization of the Yukawa interaction

8 We do not restrict the search interval in q and also allow (unphysical) bosonic momenta $q > \Lambda$.

when using the naive fermions. Here, we mentioned that large momenta components of the bosonic fields mediate interactions between the doublers. This warrants a modification of the interaction term that suppresses the interactions for high momenta of the bosonic fields. For finite lattice spacing, this is only an approximate suppression and we expect some residual interactions between the doublers. The important aspect is that these interactions contain different additional combinations of Dirac matrices. Thus, for finite Λ_{LFT} we expect some vector interactions to contribute, which appear to separate the LP and CP in such a way that the LP is located at a higher temperature.

We note that like with the homogeneous phase boundary we find agreement between the regularization schemes for small M_0 corresponding to large Λ, as the IP vanishes for all of them in this region. The lower plot, where μ is given in units of the regulator Λ, reveals that the homogeneous phase boundaries as well as the instability regions are located at chemical potentials that are in the order of the regulator Λ. This is obviously problematic since Λ should serve as the largest defining scale in our system. By applying such large chemical potentials, this clear separation of scales is no longer present. Taking this into account, it is remarkable that the homogeneous phase boundaries agree that well. This then poses the question of why the IP exhibits such an inconsistent behavior between the regularization schemes at essentially the same chemical potentials as the HBP boundary. We recall the discussions in Chapter 1 and Section 3.1.3, that motivate that the momentum of the inhomogeneous condensate q is set by the chemical potential to be $q = 2\mu$. This is also what we observed in the stability analysis of the $(1+1)$-dimensional GN model in Chapter 5. Thus, by comparison with Fig. 6.3, we recognize that the relevant momenta in the inhomogeneous phase are mostly equal or larger than Λ. This already indicates that we are confronted with severe regulator artifacts providing a preliminary answer to research question Q3.

6.3.2 Two-Point Functions

In an effort to understand the vastly different instability regions, we examine individual two-point functions for different regularization schemes in this section. This gives as an insight on how exactly the peculiarities of the regularization schemes influence the two-point functions and consequently the results of the stability analysis.

Fig. 6.4 shows $\Gamma^{(2)}_{\sigma}$ at $M_0 = 300\,\text{MeV}$ for two chemical potentials as a function of q/Λ. We note that the PV and SC results are similar, even though the SC results exhibit a shallower minimum at finite q or no non-trivial minimum at all. The SC regularization suppresses contributions from large momenta in the integrals completely, which are important at larger chemical potentials. This might the reason why the SC results are in general more shallow with less deep minima.

Even though they are very different in shape, all lattice regularizations exhibit a periodicity of $\Gamma^{(2)}$ with period $q = 2\Lambda$ and an even reflection symmetry at $q = \Lambda$. This is due to the periodicity of the fermionic dispersion relations on the lattice, which translates into the periodicity of the two-point function.

The SLAC regularization exhibits the HBP at $\mu = 311.6\,\text{MeV}$, which is why one does not observe an instability and a large, positive offset at $q = 0$. At $\mu = 450\,\text{MeV}$ it is the only regularization that exhibits an instability. It is also the only regularization scheme that exhibits a non-zero slope at $q = 0$. This is a lattice discretization artifact of the SLAC discretization, which generates a contribution $\propto +|q|$ from the fermionic determinant. This contribution would vanish in the continuum limit, which of course we cannot perform in this model. Since the two-point function is symmetric in q, this creates a non-analytic point at $q = 0$. Therefore, quantities like the bosonic wave-function renormalization are spoiled by this regularization artifact.

The Hybrid_{Θ} discretization exhibits a constant region, which is due to the weighting function in the

Yukawa interaction (see Section 6.1.2 and Section 6.1.5) that also contributes to the two-point function (see Eqs. (6.19) and (C.52)). This suppresses any momentum dependent contribution in the two-point functions. For $\mu = 311.6\,\text{MeV}$, the two-point function exhibits even an instability for a small range in q. For the larger chemical potential, $\Gamma_\sigma^{(2)}$ is approximately constant for all momenta, but drops in the suppressed region. The constant behavior in the non-suppressed region is due to the large chemical potential, which completely saturates the lattice.

The $\text{Hybrid}_{\cos}$ discretization on the other hand has a smooth functional form. For the lower chemical potential, it exhibits a shallow, positive minimum. For larger q it rises and is equal to the result of the Hybrid_Θ regularization at $q = \Lambda$, which is due to the way the weighting functions are constructed. This behavior is caused by the smooth suppression realized in the Yukawa interaction, which contributes starting from $q = 0$. This is the reason why this discretization does not exhibit an instability, since the weak instability that is still present in Hybrid_Θ is completely spoiled by the weighting.

We note two things from Fig. 6.4 that we investigate further in the following sections:

1. If the lattice regularization schemes show an instability, the minimum of $\Gamma_\sigma^{(2)}$ is at the maximal realizable momentum (Λ_{LFT} in case of SLAC and $\Lambda_{\text{LFT}}/2$ in case of Hybrid_Θ due to the weighting). This certainly invites discretization artifacts and might occur in a large portion of the phase diagram and calls for a detailed analysis. These aspects are investigated more closely in Sections 6.3.3 and 6.3.4.
2. The PV and SC schemes exhibit two-point functions that are qualitatively similar, but with quantitative differences that could cause large differences in the extent of the instability regions. This might be due to the different ways that medium contributions are taken into account and quantitative differences between the schemes might be less severe if we do not regulate the medium parts (see Section 2.3.3). This aspect is investigated more closely in Section 6.3.5.

6.3.3 The Characteristic Momentum

Fig. 6.5(a) shows the bosonic two-point as a function of the external momentum q for various chemical potentials at $T = 0$ as obtained with the PV regularization. We recognize that Q as defined in Eq. (5.1) increases with chemical potential and roughly follows $Q \approx 2\mu$. This dependence of the preferred momentum is what we would expect from the considerations in Chapter 1 and Section 3.1.3 and from what we observed with the stability analysis in the (1 + 1)-dimensional GN model in Section 5.2. This results in $Q > \Lambda$ even though the applied chemical potential is smaller than Λ_{PV}.[9] This is in principle no problem with continuum regularizations and the PV in particular, since the bosonic momentum q is not regularized. From a computational point of view all values of q are valid. However, it is certainly questionable to consider bosonic momenta which are much larger than any fermionic momentum that contributes significantly.

For the lattice discretizations, this problem is far more evident. Fig. 6.5(b) shows the two-point function as a function of the external momentum q for various chemical potentials at $T = 0$ as obtained with the SLAC discretization. Due to the periodicity of $\Gamma^{(2)}$ in q with period 2Λ and its even symmetry about $q = \Lambda$, bosonic momenta $q > \Lambda$ do not contribute any different than $q < \Lambda$ (up to reflection). If we now take this

9 At this point, it should be noted once again that the regulator is some potentially arbitrary value as nothing prevents us to redefine the PV regularization as $\Lambda'_{\text{PV}} = \alpha\Lambda_{\text{PV}}$ with some multiplicative constant α. However, we chose the definition of the regulators in such a way that their value has some significance, e.g., Λ_{SC} is chosen such that it reflects the largest momentum in the loop integration.

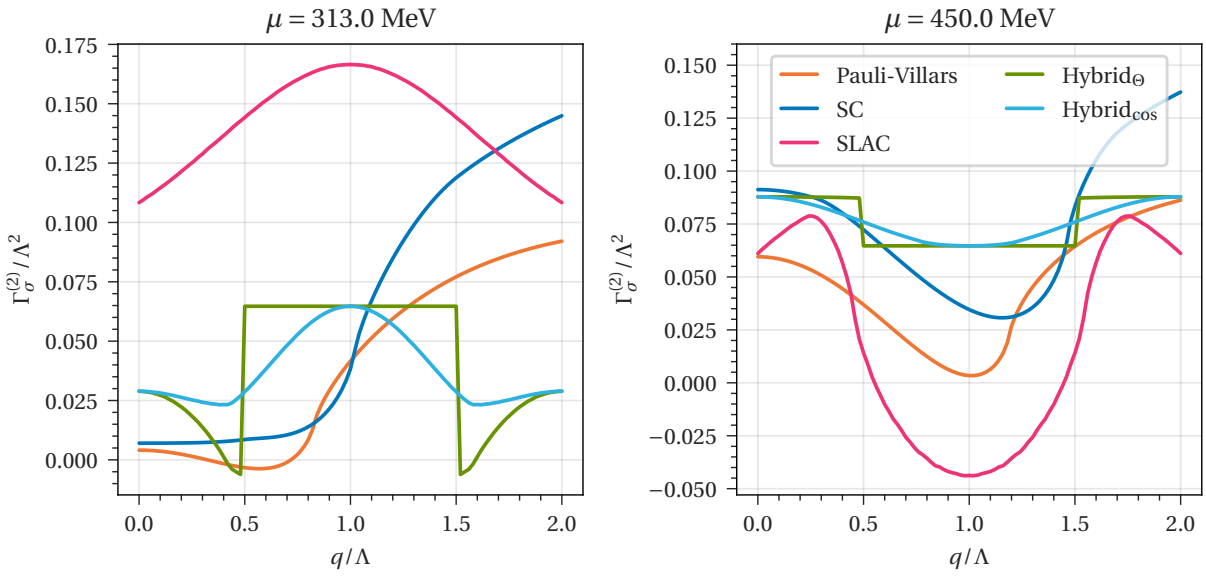

Figure 6.4: Two-point functions $\Gamma_\sigma^{(2)}$ for various regularization schemes at $T = 0$, $M_0 = 300\,\text{MeV}$, $\mu = 450\,\text{MeV}$ and $\mu = 313\,\text{MeV} \gtrapprox \mu_{c,\text{hom}}^{(\text{PV})}$, i.e., slightly larger than the critical chemical potential of the homogeneous phase transition for the PV regularization.

circumstance, the expectation of $Q = 2\mu$, and realize by inspection of Fig. 6.3 that the IP is solely located at $\mu > \Lambda/2$, we understand why $\Gamma_\sigma^{(2)}$ exhibits this peculiar shape. Essentially, the chemical potential would imply a $Q > \Lambda$, but since this cannot be realized by the lattice regularization, Q is located at Λ. Increasing μ cannot give any further reasonable evolution of Q as it is already at its maximum value.

Fig. 6.6 depicts Q' (see Eq. (5.3)) in the (M_0,μ)-plane for various regularization schemes. This shows that the observed problems for the SLAC regularization in Fig. 6.5(b) actually occur inside the entire IP. While the continuum regularization schemes exhibit the expected dependence of Q on μ, we find for the lattice regularization that Q assumes its maximally realizable value in the entire IP (except for a small part for the Hybrid$_\Theta$ regularization). Note that for Hybrid$_\Theta$ that – except for the small portion shown by the inset – the characteristic momentum is fixed $Q' = \Lambda/2$ within the instability region, since any higher momentum is suppressed by the Θ-weighting (see the discussion in Section 6.3.2). This constant behavior of Q should not be interpreted as a shortcoming of the lattice regularizations, but rather as a clear signal that something problematic occurs. Considering bosonic momenta above Λ violates the hierarchy of scales that the initial parameter tuning is based on – regardless of the regularization scheme.

6.3.4 The Characteristic Momentum and the Energetically Preferred Field Configuration

We noted previously that the characteristic momentum Q is not necessarily the dominant momentum q_Σ (see Section 5.2) of the energetically preferred, inhomogeneous chiral condensate. Thus, it might be possible that for the lattice discretizations one finds an inhomogeneous chiral condensate with a dominant wave-number, which is not fixed at the maximal value of $q_\Sigma = \Lambda$ (or $q_\Sigma = \Lambda/2$ for the Hybrid$_\Theta$ discretization) and that might show a dependence on μ as we would expect. To investigate this, we consider the SLAC discretized effective action on a finite lattice and minimize it in the values of the field at the lattice points (see the discussion in Section 4.1.3). Hereby, we restrict the fields to a 1-dimensional

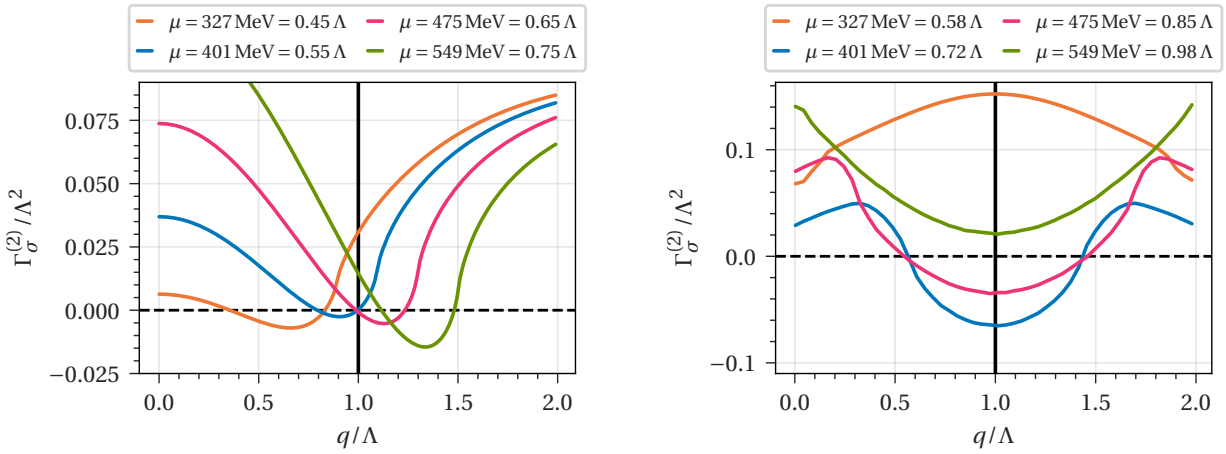

(a) PV regularization

(b) SLAC regularization

Figure 6.5: $\Gamma^{(2)}_\sigma$ as a function of q for various chemical potentials for the PV and SLAC regularization at $T = 0$ and $M_0 = 325\,\text{MeV}$.

spatial dependence, but consider no further restrictions on the possible modulations. This is in part motivated by Refs. [14, 133], which found that 1-dimensional condensates are favored in this region of the phase diagram and to greatly reduce the numerical cost of the minimization. The minimization and calculation of the two-point function in the finite space-time volume in this section is carried out with a lattice code that was developed for the specific task of minimizing lattice discretized actions of FF models. It has also been used in the production of the results in Refs. [47, 50, 150].

Fig. 6.7(a) shows the two-point function for $T = L^{-1} \approx 7.4\,\text{MeV}$ and $T = L^{-1} = 0$ at $\mu = 379.7\,\text{MeV}$, $M_0 = 287.0\,\text{MeV}$ obtained with the SLAC discretization. It agrees very well with the infinite volume and $T = 0$ result, and thus from the two-point function, we would expect a chiral condensate with a dominant momentum of the maximally realizable value. Fig. 6.7(b) depicts the field configurations that minimize the effective action for this T,μ,L when the fields are restricted to a 1-dimensional spatial dependence. We notice that the π field is constant zero, which was also observed in Ref. [14]. The σ field oscillates with the minimal available wavelength (also shown by Fig. 6.7(c)), which confirms our expectations. The extreme chemical potentials inside the IP favor a wavelength of the chiral condensate which cannot be fulfilled by the lattice regularization. This is solely due to the chemical potential being in the order of the regulator, which is questionable in the first place regardless of the employed regularization scheme.

6.3.5 Impact of the No Medium Regularization

In this section we want to investigate the impact that the regularization of the medium contribution has on the two-point function and on the instability regions when using the SC and PV regularization.

Two-point Functions with Unregularized Medium Contributions

Fig. 6.8 shows the two-point functions for various chemical potentials using the SC and PV scheme both with and without NMR (see Section 2.3.3) at $T = 0$ and $M_0 = 350\,\text{MeV}$.

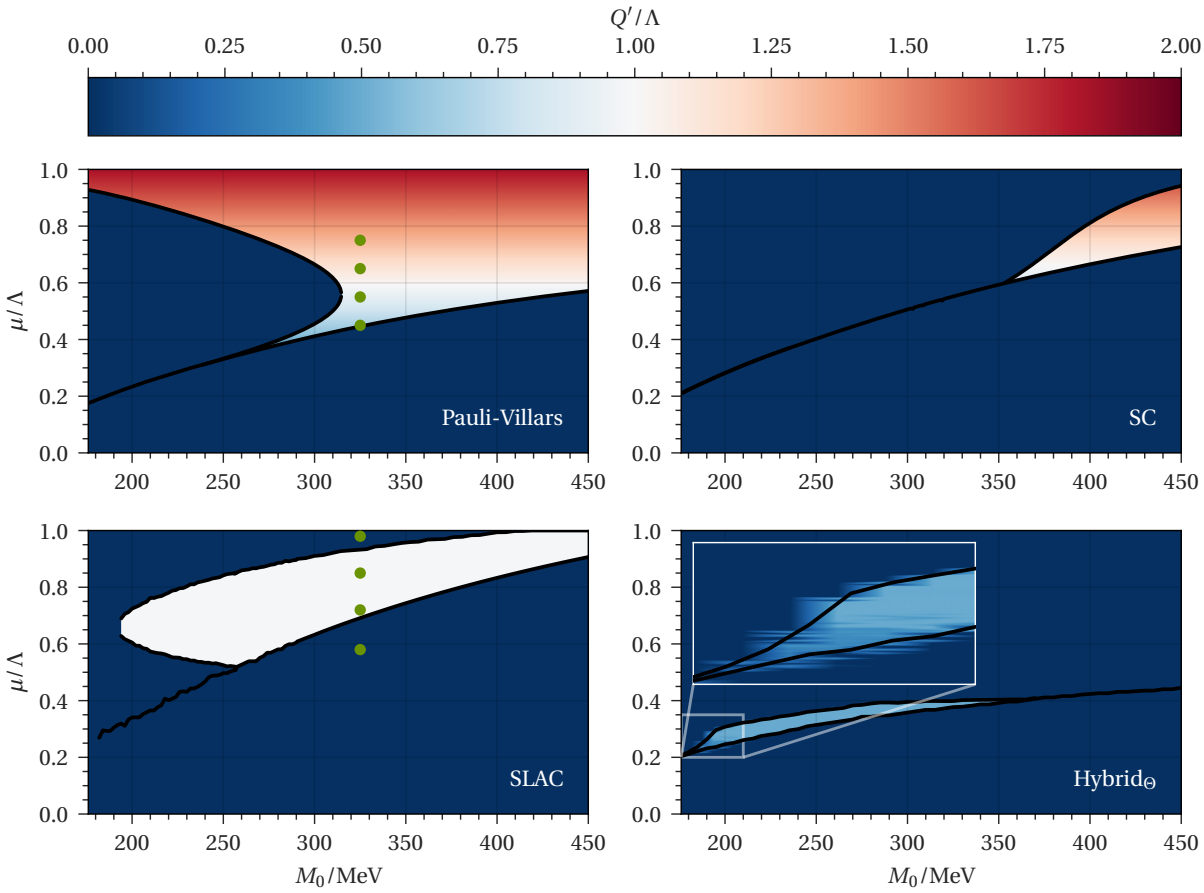

Figure 6.6: Q' in the (M_0,μ)-plane at $T = 0$ for various regularizations. The green dots correspond to the chemical potentials of the two-point functions in Figs. 6.5(a) and 6.5(b).

With the smallest chemical potential $\mu = 358.10\,\text{MeV}$ there is little change when applying NMR to the SC. Notably the minimum of $\Gamma_\sigma^{(2)}$ assumes a higher value. For the PV, there is no change at all, which can be understood when considering Eq. (C.36). At zero temperature, the Θ-function that appears in the medium contribution of the PV regulator terms suppresses any contributions for $\mu < \alpha_1 \Lambda_{\text{PV}} = 1 \times \Lambda_{\text{PV}}$ (see Section 6.2 for our choice of the other PV parameters).

At $\mu = 537.15\,\text{MeV}$, the result for SC changes from a two-point function, which does not show an instability, without NMR to one that exhibits negative values with NMR. The same change can be observed at $\mu = 859.44\,\text{MeV}$, which is above the value of Λ for both schemes. In addition, the SC scheme without NMR exhibits a completely flat region at low bosonic momenta q, which completely vanishes with NMR. The standard PV result shows a positive curvature at low q, but exhibits a non-trivial negative minimum at large q. This local maximum in between vanishes completely with NMR.

In general, we note that for lower chemical potentials the impact of NMR is not substantial, but gets significant for large chemical potentials. This is expected as regulator artifacts should become more severe when the external quantities such as μ are in the order of the regulator. One also finds that the relative differences between the two-point function of the PV and SC scheme with NMR become smaller for increasing μ. Here the result is dominated by the medium contributions, which are free of regulator

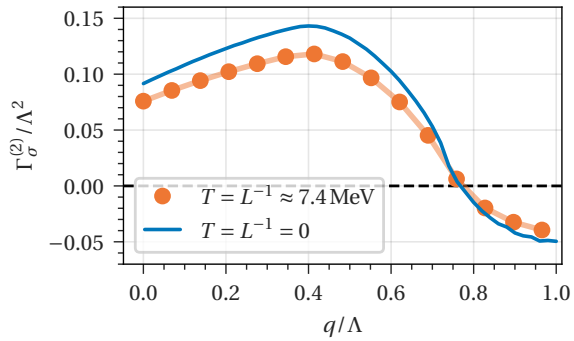

(a) The two-point function $\Gamma_\sigma^{(2)}$ for $T = L^{-1} \approx 7.4\,\mathrm{MeV}$ and $T = L^{-1} = 0$.

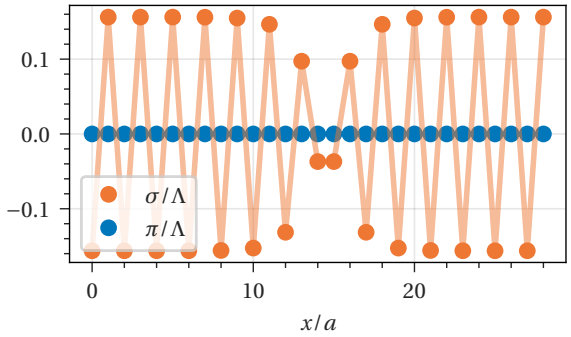

(b) The energetically preferred field configuration in position space for $T = L^{-1} \approx 7.4\,\mathrm{MeV}$ for fields restricted to one spatial dimension.

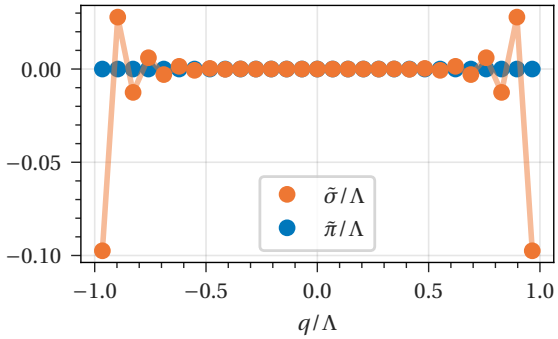

(c) The energetically preferred field configuration in momentum space for $T = L^{-1} \approx 7.4\,\mathrm{MeV}$ for fields restricted to one spatial dimension.

Figure 6.7: The two-point function and the energetically preferred field configuration at $\mu = 2\Lambda/\pi = 0.6366\Lambda = 379.7\,\mathrm{MeV}$, $M_0 = 287.0\,\mathrm{MeV}$ for the SLAC regularization.

artifacts with the NMR procedure. As such the two-point functions between regularization schemes appear to approach one another. On the contrast, we find that at lower chemical potentials close to the HBP, there is not much impact and the change of the phase structure might not be substantial in this region.

The Phase Structure at Zero Temperature with no Medium Regularization

Fig. 6.9 shows the IP as obtained from the stability analysis for the PV and SC scheme with and without NMR similar to Fig. 6.3. The PV scheme is not depicted in its NMR version as it does not impact the phase structure (and would only clutter the plot). Going from the standard result with the SC to its NMR version, we find that the changes of the homogeneous phase boundary too small to be visible, but the instability region exhibits a vastly different behavior. An inhomogeneous continent splits off just as with the PV regularization, which is enabled by the effect that we saw in Fig. 6.8, where an instability for large chemical potential was recovered with NMR. However, the most peculiar result is that there is a small region that exhibits an instability in the standard case, but no instability with NMR. Such effects can be seen in the

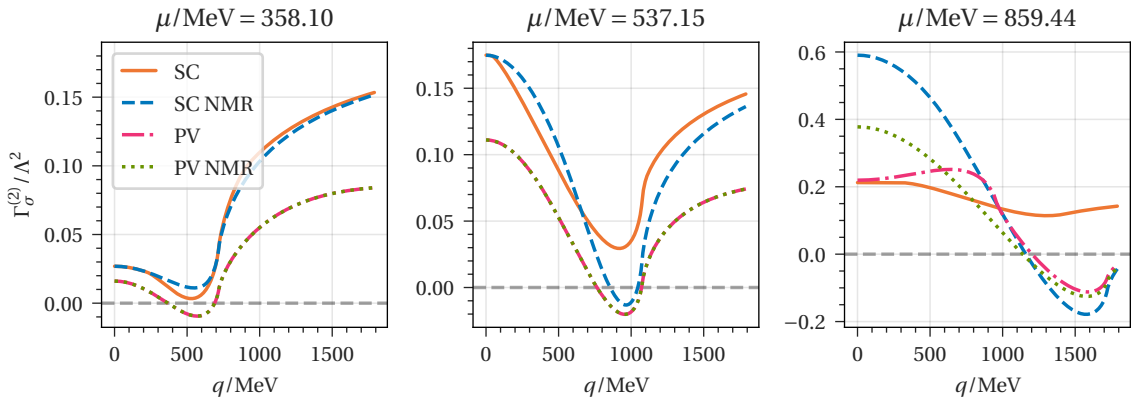

Figure 6.8: The two-point function $\Gamma_\sigma^{(2)}$ as a function of the bosonic momentum q at various chemical potentials, $T = 0$, and $M_0 = 350\,\text{MeV}$ for the PV and SC regularization with and without NMR. The regulators assume the value $\Lambda_{\text{PV}} = 716.20\,\text{MeV}$ and $\Lambda_{\text{SC}} = 573.77\,\text{MeV}$.

left panel of Fig. 6.8, where the value of the minimum of the two-point function with the SC regularization with NMR increases and becomes more shallow compared to the standard SC scheme.

Even though the instability regions of the PV scheme and SC scheme with NMR regularization are somewhat similar in shape, there is still a shift in M_0 between the two. This is likely due to effects of the vacuum parts of the involved quantities which are independent of the NMR procedure. This is an important aspect for answering research question Q3: It is not only the medium contributions that introduce regularization artifacts via large chemical potentials, but the favored large bosonic momenta that contribute to the vacuum part, which causes a regulator dependence.

No Medium Regularization and Lattice Regularizations

The two-point function for the lattice regularizations in Eqs. (C.50) to (C.52) do not offer a separation of vacuum and medium contributions. This is caused by the finite lattice spacing in the temporal direction. Therefore, we cannot apply the NMR procedure to the lattice calculations.

In principle, it is possible to implement RG consistency [79] (see Section 2.3.3) in the calculations with the lattice regularizations to achieve a comparable effect as with the NMR procedure. However, it is questionable whether it would make sense for the lattice regularizations. The major problem of the lattice results in Section 6.3.1 is the periodic structure of $\Gamma^{(2)}$ and as a result $Q = \Lambda$ being constant within IP (or $Q = \Lambda/2$ for the Hybrid$_\Theta$ discretization). The periodic behavior of $\Gamma^{(2)}$ is caused by the periodic dispersion relation of the fermions. While the period of this dispersion relation that contributes in the medium part would be infinite with RG consistency, it would remain unchanged in the vacuum part. Thus, some residual periodic structure would remain, which might result in even more questionable results.

6.4 Regularization Scheme Dependence of the Moat Regime

In Section 6.3.3, it is shown how the large chemical potentials favor characteristic momenta Q that are larger than the respective regulators, which introduces yet another scale in the order of the regulator. This leads to a severe regularization scheme dependence of the IP, since multiple scales now compete with the regulator. At the same time, the phase boundary of the HBP is located at similar chemical potentials

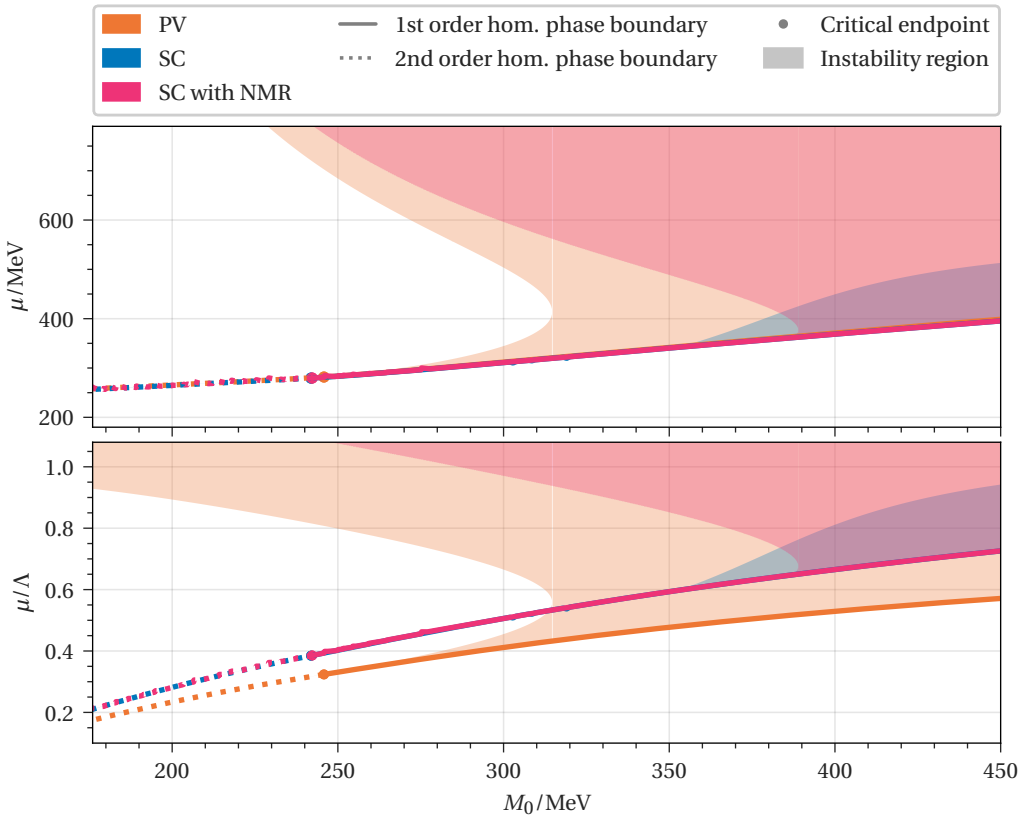

Figure 6.9: The phase diagram from the stability analysis in the (M_0,μ)-plane at $T = 0$ for the PV and SC regularization with and without NMR. In the upper plot, μ is given in MeV and in the lower plot the same data is given for μ/Λ, where Λ assumes the respective values for the different regularizations. The solid lines represent the first order phase boundary and the dotted lines the second order phase boundary, when the fields are restricted to homogeneous field configurations. The circle indicates the critical endpoint. The shaded regions are the regions of instability where the bosonic two-point functions $\Gamma^{(2)}$ exhibit negative values for some bosonic momenta q.

and does not change too drastically when switching the regularization schemes. This suggests that the corresponding chemical potential by itself is small enough compared to the regulator to avoid a large regularization scheme dependence of the phase structure even without NMR.

This suggests that the moat regime also might not be as dependent on the regularization scheme as the IP. An indicator for the moat regime is the bosonic wave-function renormalization (4.20), which is the curvature of the bosonic two-point function $\Gamma^{(2)}$ at $q = 0$. Since it is evaluated at $q = 0$, no additional energy scales are introduced and the only large scale that remains is the chemical potential.

To investigate this, we restrict the calculations to the PV and SC schemes as their results for the IP already showed large discrepancies. Moreover, they are numerically considerably less expensive, which further favors them as a first investigation point. If one would also study this on the lattice, it would only be sensible to conduct such an investigation with the Hybrid regularizations. The plots of the two-point

functions with the SLAC fermions in Section 6.3.3 reveal that there is a positive contribution $\propto |q|$ within $\Gamma^{(2)}$, which is an artifact of finite lattice spacing. This leads to a diverging wave-function renormalization completely invalidating the wave-function renormalization as an indicator for the moat regime. One would again have to investigate $\Gamma^{(2)}$ at a finite q to check whether it exhibits a non-trivial minimum, which negates the original reasoning to investigate the moat regime via the wave-function renormalization.

Whenever we mention the wave-function renormalization in the following, we are referring to Z_σ, i.e., the wave-function renormalization of the σ field evaluated at the homogeneous minimum. In the SP, z_σ and z_π are equal as their two-point functions are identical (see Eq. (4.19)). In the HBP, they differ, but are both positive and therefore not relevant for the discussion of the moat regime. Thus, we can restrict our discussion to Z_σ without any loss of information regarding the moat regime, which is characterized by at least one of the wave-function renormalizations being negative.

The explicit expressions for the wave-function renormalization in the SC and PV scheme are given in Appendix C.5.

6.4.1 The Moat Regime at Zero Temperature

Fig. 6.10 shows the moat regime and the HBP for the PV and SC scheme at $T = 0$ in the (M_0,μ)-plane. The agreement between the regularization schemes is considerably better than with the IP, which is shown by the dashed lines. We find a similar shape of the moat regimes with a significantly larger overlap between the schemes. Moreover, the moat regime is found in a larger region than the IP. It is a more persistent feature, which is present for a larger range of M_0 with a considerable extent in the μ direction.

One finds upper boundaries in μ for the moat regime above which it vanishes. This is due to strong regularization artifacts which appear for $\mu \geq \Lambda$. As illustrated by Fig. 6.8, one observes that a plateau develops in $\Gamma^{(2)}_\sigma$ for the SC scheme for $\mu > \Lambda$ yielding $Z_\sigma = 0$. Nevertheless, one finds a non-trivial minimum for some large q. The PV regularization on the other hand, exhibits even a positive curvature in $\Gamma^{(2)}$ at $q = 0$ for large enough μ. Both behaviors lead to $Z_\sigma \geq 0$ and thus to an apparent disappearance of the moat regime. These artifacts are fixed if we carry out the calculations with the NMR (see Fig. 6.8).[10]

For low M_0, one finds that the moat regime splits from the HBP at the CP for the PV regularization and at larger M_0 for the SC scheme. The missing coincidence of these points for the SC scheme was reported in Ref. [35] and is due to surface terms that contribute with the SC regularization.

6.4.2 The Moat Regime at Finite Temperature

The results at $T = 0$ seem to confirm our expectations that the regularization scheme dependence is less severe. We proceed to calculate Z_σ in the (μ,T)-plane to study whether an additional finite temperature introduces larger discrepancies between the regularization schemes. Figs. 6.11 and 6.12 show the minimum of the homogeneous effective potential $\bar{\Sigma}$, which serves as the evaluation point of Z, and Z_σ as well as HBP and moat regime for different $M_0 = 400\,\text{MeV}, 300\,\text{MeV}$ for the PV and SC regularization schemes. Both regularization schemes exhibit as expected a positive Z_σ within the HBP, and at lower T and larger chemical potential a moat regime with $Z_\sigma < 0$. The boundary of the moat regime evolves to higher temperatures for increasing chemical potential, where the line of $Z_\sigma = 0$ (indicated by the dotted line) is of a slightly different shape and slope between the two schemes. The shape of this moat regime resembles the moat regime in the (1 + 1)-dimensional GN model shown in Fig. 5.6.

10 The lower bound in μ for the moat regime is not affected by NMR and thus we omitted the NMR from Fig. 6.8 to keep the figure readable.

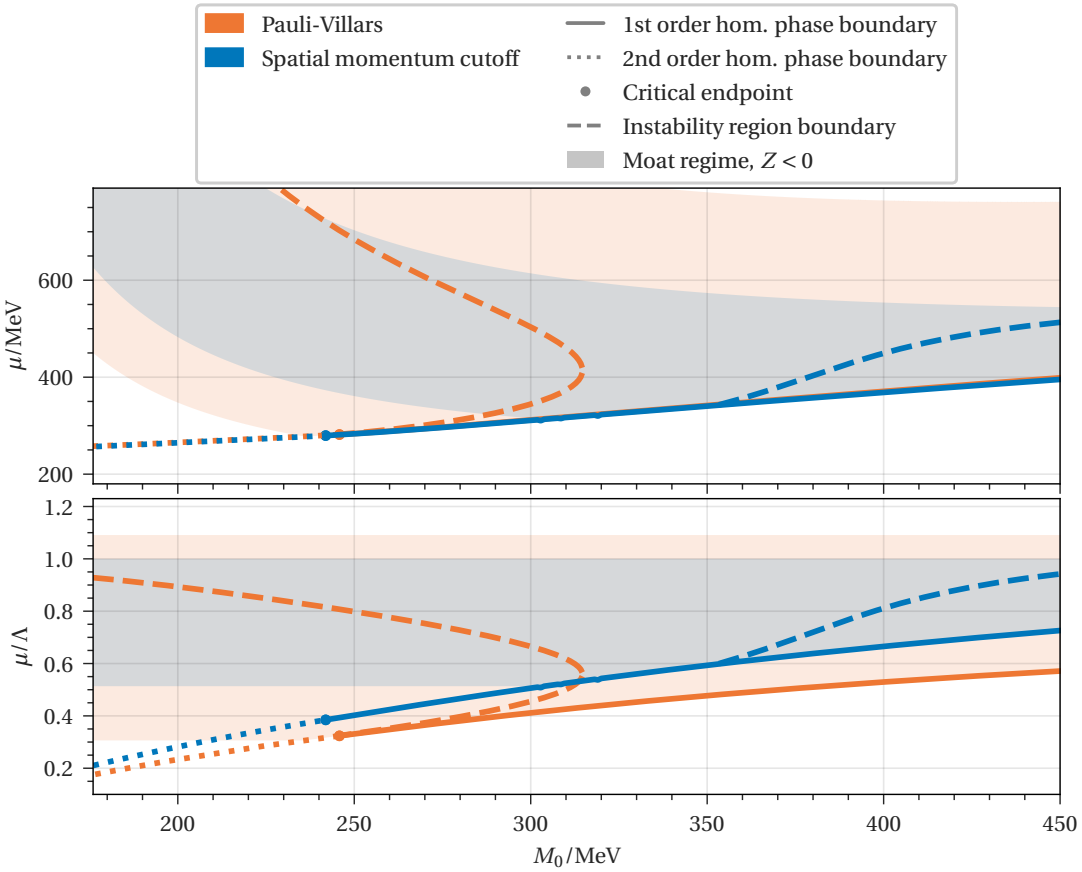

Figure 6.10: The phase diagram and the moat regime from the stability analysis in the (M_0,μ)-plane at $T = 0$ for the PV and SC regularization. In the upper plot, μ is given in MeV and in the lower plot the same data is given for μ/Λ, where Λ assumes the respective values for the different regularizations. The solid lines represent the first order phase boundary and the dotted lines the second order phase boundary, when the fields are restricted to homogeneous field configurations. The circle indicates the critical endpoint. The dashed lines mark the regions of instability as shown in Fig. 6.3. The shaded regions are the regions where the wave-function renormalization Z exhibits negative values for some bosonic momenta indicating the existence of the moat regime at this point.

For $M_0 = 300\,\text{MeV}$, one observes a divergence of the wave-function renormalization at $T = 0$ and $\mu = M_0$ that radiates to higher temperatures. This peak can be understood by considering the formulas for the two-point function at $T = 0$ given in Eqs. (C.35) and (C.47) that exhibit a non-analytic point at $q^2 = 4(\mu^2 - \bar{\sigma}^2)$. This is the same non-analyticity, as the one that we observed in the two-point functions of the (1 + 1)-dimensional GN model in Chapter 5, albeit in higher dimensions it is not a divergence. The non-analytic point is then located at $q = 0$ for $\mu = \bar{\Sigma}$, which causes the wave-function renormalization – being the curvature of the two-point function – to diverge (compare to Eq. (C.54)).

The results from both regularizations seem to agree sufficiently well as shown by the comparison done in Figs. 6.11(c) and 6.12(c). The moat regime calculated with the SC scheme starts at a lower temperature along the phase boundary of the HBP, which we can attribute to the splitting of the CP and LP that we observed in Sections 6.3.1 and 6.4.1. For the results at $M_0 = 300\,\text{MeV}$ this splitting of CP and LP actually

causes the moat regime for the SC to be barely disconnected from the HBP. Thus, even though the qualitative behavior of the moat regime agrees more than that of the IP, one finds that the regularization scheme specific effects are still highly relevant.

The pseudoscalar wave-function renormalization of Z_π is identical to Z_σ when $\bar{\Sigma} = 0$. Within the HBP, it is smaller in magnitude, but exhibits the same positive sign. Therefore, we omit a separate plot of Z_π as it does not grant additional information about the moat regime.

While the coupling G appeared in the two-point function, it does not contribute to the wave-function renormalization as it was removed by the double derivative with respect to q (compare to Eq. (4.20)). Therefore, if we evaluate the wave-function renormalization z_σ at the symmetric point $\bar{\sigma} = 0$, we are able to plot the wave-function renormalization in the plane of μ/Λ and T/Λ as no other quantities contribute in z_σ, i.e., the results are independent M_0. This allows us to depict z_σ in the SP independent of parameter sets as done in Fig. 6.13. We find a very similar behavior of z_σ for both regularization schemes. Of course the region in the (μ, T)-plane, where the homogeneous minimum is indeed at $\bar{\Sigma} = 0$ and the SP is realized, depends on the parameter set, but the behavior within this region is universal. Thus, when considering an individual parameter set, we can immediately calculate the behavior of Z in the SP by rescaling the independent result of Fig. 6.13 by the respective value of Λ. This illustrates how the moat disconnects from the HBP for parameter sets with larger Λ due to different scaling of the SP result.

6.5 Summary

In this chapter, we analyzed the regulator scheme dependence of the IP at zero temperature for the PV, SC, SLAC and Hybrid regularization schemes as well as the moat regime in the (μ, T)-plane for the PV and SC schemes. We found that the IP strongly depends on the regularization scheme and for the $\text{Hybrid}_{\cos}$ discretization one does not find an IP at all. This occurs because the parameter regions where the IP is present correspond to small regulators and quantities such as the chemical potential or the characteristic momentum of the instability being in the order of the regulator. This facilitates strong regularization artifacts causing this discrepancy between the results. Moreover, we found that even the SC and PV schemes with NMR exhibit large differences in the phase diagram. This leads to the conclusion that the fundamental characteristics of the schemes are the cause for the disagreement of the results between them. This provides the answer to research question Q6 that there is in fact a severe regularization scheme dependence.

We also have found that the IP vanishes in all regularization schemes for large regulators. The fact that an IP is found in the $(2 + 1)$-dimensional GN model – despite its absence in the renormalized model – alongside this result, sparked the question raised in research question Q5: whether the IP is an inherent feature of the $(3 + 1)$-dimensional NJL or if it is driven by the regulator. This is studied in Chapter 7.

The lattice regularization schemes, which were the initial motivation for this study, suffer the most from these problems. Characteristic momenta that are larger than the resolvable momenta ($q > \Lambda_{\text{LFT}}$ for SLAC and $q > \Lambda_{\text{LFT}}/2$ for Hybrid_Θ) are favored. This results in an independence of the inhomogeneous condensate on the chemical potential within the instability region as it always oscillates with the shortest available wave-length, which is a clear discretization artifact. The lattice regularization schemes that we employed exhibited individual problems. The two-point function obtained with the SLAC regularization contains a contribution $\propto +|q|$, which might severely influence the momentum dependence of $\Gamma^{(2)}$ and results in a non-analytic point at $q = 0$. The naive fermions on the other hand are plagued by fermion doublers that can interact among each other via vector interactions and more complicated Dirac structures. While the weighting functions suppress these interactions, they contribute at a finite lattice

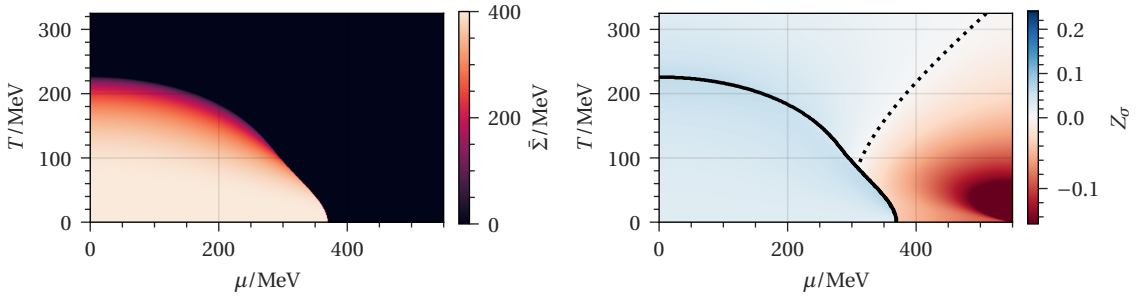

(a) SC regularization, $M_0 = 400\,\text{MeV}$, $\Lambda_{\text{SC}} = 553.98\,\text{MeV}$.

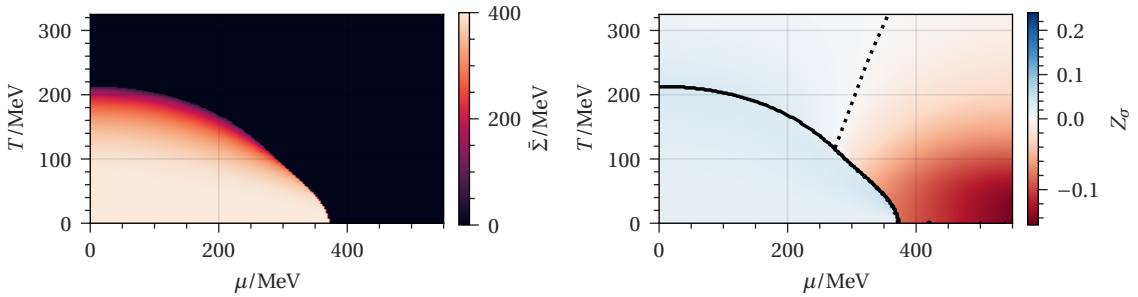

(b) PV regularization, $M_0 = 400\,\text{MeV}$, $\Lambda_{\text{PV}} = 700.71\,\text{MeV}$.

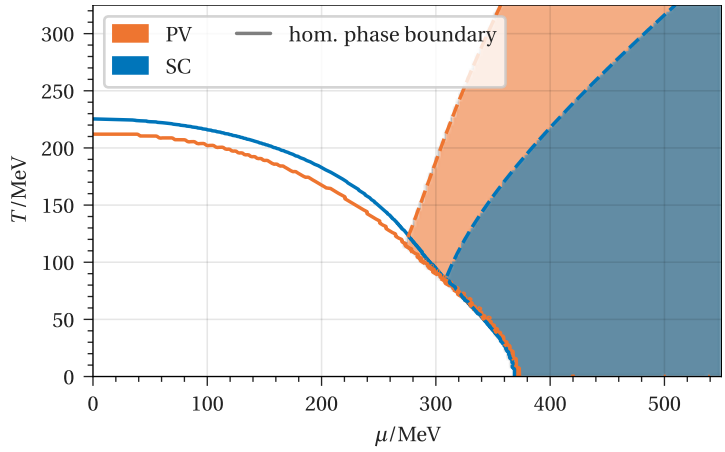

(c) Boundaries of the HBP and the moat regime for the data sets above.

Figure 6.11: The minimizing field configuration of the homogeneous effective potential $\bar{\Sigma}$ and the scalar wave-function renormalization Z_σ in the (μ, T)-plane with the SC and PV regularization for $M_0 = 400\,\text{MeV}$ are shown in **(a)** and **(b)**. In the right plot, the dotted line indicates the $Z_\sigma = 0$ line and the solid line the homogeneous phase boundary. The boundaries of the HBP and the moat regime for the respective regularization schemes are shown in **(c)**.

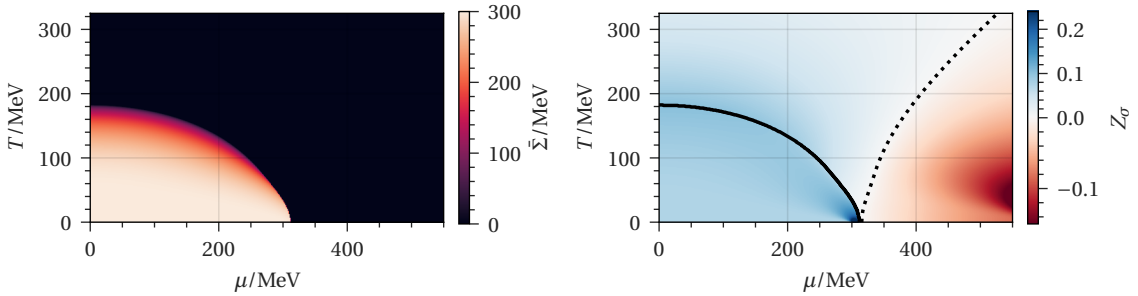

(a) SC regularization, $M_0 = 300\,\text{MeV}$, $\Lambda_{\text{SC}} = 614.27\,\text{MeV}$.

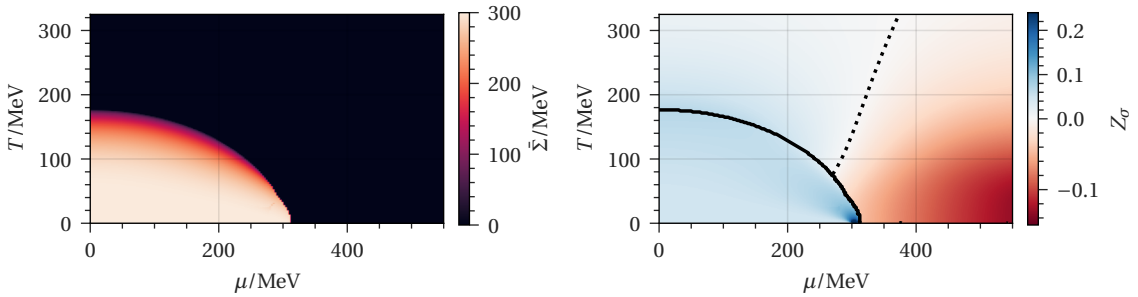

(b) PV regularization, $M_0 = 300\,\text{MeV}$, $\Lambda_{\text{PV}} = 757.05\,\text{MeV}$.

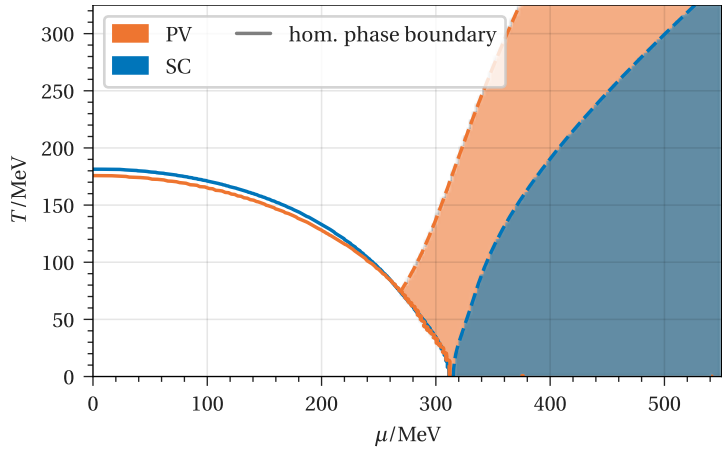

(c) Boundaries of the HBP and the moat regime for the data sets above.

Figure 6.12: The minimizing field configuration of the homogeneous effective potential $\bar{\Sigma}$ and the scalar wave-function renormalization Z_σ in the (μ, T)-plane with the SC and PV regularization for $M_0 = 300\,\text{MeV}$ are shown in **(a)** and **(b)**. In the right plot, the dotted line indicates the $Z_\sigma = 0$ line and the solid line the homogeneous phase boundary. The boundaries of the HBP and the moat regime for the respective regularization schemes are shown in **(c)**.

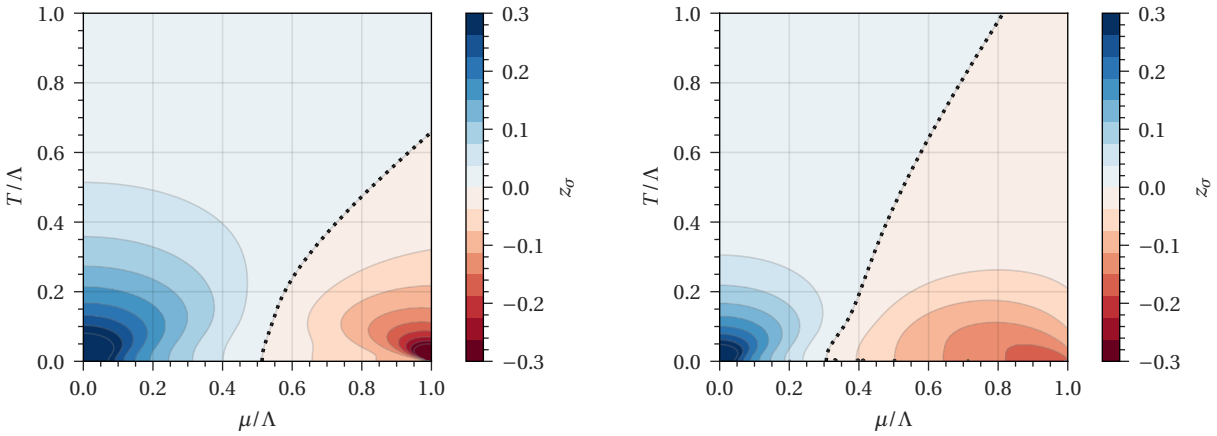

(a) Result for the SC regularization.

(b) Result for the PV regularization.

Figure 6.13: The wave-function renormalization z_σ evaluated at $\bar{\sigma} = 0$ in the (μ, T)-plane with the SC and PV regularization. As G does not appear in the expressions for z_σ, the results in this plot are independent of M_0.

spacing nonetheless. This results in a splitting of the CP and the LP that is known from models with vector interactions (see the discussion in Section 3.3.3 and e.g. Ref. [124]). Thus, answering research question Q2 in general lattice discretizations are not suitable to investigate the IP in the (3 + 1)-dimensional NJL model due to the large relevant bosonic momenta. Moreover, we found that both the Hybrid and the SLAC discretizations exhibit individual discretization artifacts, which might also spoil the investigation of the IP in other non-renormalizable models.

In the second half of the investigation, we turned to the moat regime for the SC and PV schemes. Its detection does not rely on large bosonic momenta and thus the only quantity in the scale of the regulator is the chemical potential. In providing a first answer to research question Q4, we found that the agreement between the schemes regarding the moat regime is substantially better and the moat regime covers a large portion of the (μ, T)-plane.

Chapter 7

The Gross-Neveu Model in Non-Integer Spatial Dimensions $1 \leq d < 3$

Disclosure *This chapter discusses results that were presented in Ref. [97], for which I was the sole author.*

As discussed in Section 3.1.3, the GN model exhibits an IP in $1+1$ dimensions in the $N \to \infty$ limit [28], while the phase is entirely absent at non-zero temperature in $2+1$ dimensions [48–51] (see Section 3.1.3). This absence is not restricted to the GN model, but occurs in the same way in other FF models and their Yukawa-type extensions that feature Lorentz-(pseudo)scalar interaction channels [51]. Therefore, understanding the reason for the absence of IPs in $2+1$ dimensions would benefit not only our understanding of the GN model, but an entire class of these FF models.

In $3+1$ dimensions, the GN model is rarely considered as most investigations of FF models there focus on the NJL model. However, it turns out that the two models exhibit the same phase diagram. This is rather obvious, if the bosonic fields are restricted to homogeneous field configurations as one can rotate the pseudoscalar fields into the scalar channel (see Section 3.2.1). In addition, it was found that their phase diagram and preferred ground states are also identical when inhomogeneous field configurations are considered [14]. Therefore, studying the GN model gives reasonable insight into the phase diagram of the NJL model as well.

As analyzed in great detail in Chapter 6, this phase diagram has a strong dependence on the regularization scheme and on the value of the finite regulator. Therefore, it seems unclear whether the IP is a robust feature of the $(3+1)$-dimensional NJL-type models or if it is a regulator driven effect.

The primary goal of this chapter is to understand the reason why the GN model (and the NJL model) exhibits vastly different phase diagrams in $d = 1, 2, 3$ spatial dimensions. Studying this behavior is intended to provide appropriate answers to the research questions Q5 and Q6. To do so, we consider the GN model in non-integer spatial dimensions $1 \leq d < 3$, where the model is fully renormalizable [59, 64]. In Section 3.1.3, we discussed the homogeneous phase structure, which was already investigated in-depth in Ref. [64]. We carry out the stability analysis as introduced in Section 4.2 for arbitrary non-integer spatial dimensions $1 \leq d < 3$ to investigate the existence of an IP. In this setup, the number of spatial dimensions enters only as a numerical parameter, which allows us to study the effect of the number of spatial dimensions isolated from other effects like fermion representations that usually change when modifying the number of spatial dimensions. It is important to state that the consideration of non-integer dimensions is merely a tool to understand the change in behavior when switching between integer number of dimensions. Therefore,

the results for some particular non-integer value of the number of spatial dimensions d is not important, but the trend for varying d is.

7.1 Considerations in Non-Integer Dimensions

Before we begin with this investigation, we have to consider the implications of a non-integer number of spatial dimensions. The biggest concern is the Clifford algebra, which is a central concept in fermionic theories and its properties are frequently used in the calculations of the stability analysis (see Appendix B.1 for general remarks about the Clifford algebra in various space-time dimensions). Its role in non-integer dimensions has been thoroughly discussed in Ref. [74]. One finds that in any number of dimensions the central anti-commutation relation

$$\{\gamma_\mu, \gamma_\nu\} = 2\delta_{\mu,\nu}\mathbb{1} \tag{7.1}$$

holds.

However, the definition of γ_{ch} cannot be extended to non-integer dimensions without ambiguities. As such γ_{ch} is ill-defined and we avoid anything that depends on it to keep consistency. This is particular true for the anti-commutation relation

$$\{\gamma_{\text{ch}}, \gamma_\nu\} = 0. \tag{7.2}$$

This also causes the discrete chiral symmetry (3.3) to be present only in integer number of dimensions. In non-integer dimensions, we still observe the symmetry (3.4) of the action as $\sigma \to -\sigma$, but it is not connected to chiral symmetry anymore. We, however, continue to use the terminology HBP, SP, IP to refer to the phases with the corresponding behavior of the field σ.

Apart from the Clifford algebra, expressions that depend on the angle between non-integer dimensional vectors are problematic. These appear in expressions of the stability analysis (compare Eq. (4.19)) and we need to devise strategies to circumvent such expressions.

7.2 The Stability Analysis in Non-Integer Spatial Dimensions

Even though, we introduced the stability analysis at the example of the NJL model in integer spatial dimensions d in Section 4.2, the derivation for non-integer d requires some greater care. Therefore, we recapitulate some central steps that deviate from the standard discussion. For the remainder of the derivation, we mostly refer to the steps presented in Section 4.2.

7.2.1 The Bosonic Two-Point Function

We start with the GN model equivalent of Eq. (4.18), which is given by

$$\Gamma^{(2)}\left(\mathbf{q}, \bar{\sigma}, \mu, T, d\right) = \frac{1}{2G} - N_\gamma \int \frac{\mathrm{d}^d p}{(2\pi)^d} \frac{1}{\beta} \sum_{n=-\infty}^{\infty} \frac{\tilde{\nu}_n^2 + \mathbf{p}^2 + \mathbf{p}\cdot\mathbf{q} - \bar{\sigma}^2}{\left(\tilde{\nu}_n^2 + E_{\mathbf{p}+\mathbf{q}}^2\right)\left(\tilde{\nu}_n^2 + E_{\mathbf{p}}^2\right)}. \tag{7.3}$$

Instead of completing the square as done in Eq. (4.19), it is more instructive in this case to perform a partial fraction decomposition of the form

$$\frac{1}{\left(\tilde{\nu}_n^2 + E_{\mathbf{p}+\mathbf{q}}^2\right)\left(\tilde{\nu}_n^2 + E_{\mathbf{p}}^2\right)} = \frac{1}{2\left(\tilde{\nu}_n^2 + \left(\mathbf{p}+\frac{\mathbf{q}}{2}\right)^2 + \frac{\mathbf{q}^2}{4} + \bar{\sigma}^2\right)}\left(\frac{1}{\tilde{\nu}_n^2 + E_{\mathbf{p}+\mathbf{q}}^2} + \frac{1}{\tilde{\nu}_n^2 + E_{\mathbf{p}}^2}\right), \tag{7.4}$$

which we can use to transform Eq. (7.3) into

$$\Gamma^{(2)}\left(\mathbf{q},\bar{\sigma},\mu,T,d\right) = \frac{1}{2G} - N_\gamma \int \frac{\mathrm{d}^d p}{(2\pi)^d}\, \frac{1}{\beta} \sum_{n=-\infty}^{\infty} \left[\frac{1}{2\left(\tilde{p}_0^2 + E_{\mathbf{p}+\mathbf{q}}^2\right)} + \frac{1}{2\left(\tilde{p}_0^2 + E_{\mathbf{p}}^2\right)} - \frac{\frac{\mathbf{q}^2}{2} + 2\bar{\sigma}^2}{\left(\tilde{p}_0^2 + E_{\mathbf{p}+\mathbf{q}}^2\right)\left(\tilde{p}_0^2 + E_{\mathbf{p}}^2\right)}\right]. \tag{7.5}$$

Since we consider the model only in $1 \leq d < 3$, where it is fully renormalizable, it is possible to take the limit $\Lambda_{\mathrm{SC}} \to \infty$. Thus, we regain translational invariance in the momentum integrals and can apply a shift $\mathbf{p}+\mathbf{q} \to \mathbf{p}$ in the first integral in Eq. (7.5) without adjusting the integral boundaries. This shift yields

$$\Gamma^{(2)}\left(\mathbf{q},\bar{\sigma},\mu,T,d\right) = \frac{1}{2G} - N_\gamma l_1\left(\bar{\sigma}^2,\mu,T,d\right) + N_\gamma L_2(\mathbf{q},\bar{\sigma},\mu,T,d), \tag{7.6}$$

where l_1 is given by Eq. (3.8), $L_2 = \frac{1}{2}\left(\mathbf{q}^2 + 4\bar{\sigma}^2\right) l_2$ and l_2 is given by (compare to Eq. (4.19))

$$l_2\left(\mathbf{q},\bar{\sigma},\mu,T,d\right) = \frac{1}{\beta} \sum_{n=-\infty}^{\infty} \int \frac{\mathrm{d}^d p}{(2\pi)^d} \frac{1}{\left(\tilde{\nu}_n^2 + E_{\mathbf{p}+\mathbf{q}}^2\right)\left(\tilde{\nu}_n^2 + E_{\mathbf{p}}^2\right)}. \tag{7.7}$$

The constant contribution $1/(2G) - N_\gamma l_1$ is straightforward to compute (except for the complications from d-dimensional integrals) and the derivation of these quantities is presented in Appendix D.3. The integral l_2, however, needs some refinement treatment in non-integer d spatial dimensions compared to integer d. The first step is to get rid of any contributions that depend on the angle between the loop momentum $\mathbf{p}$ and the external bosonic momentum $\mathbf{q}$. We can achieve this by applying a Feynman parametrization of the integrand in Eq. (7.7) resulting in

$$\begin{aligned}
l_2 &= \frac{1}{\beta} \sum_{n=-\infty}^{\infty} \int \frac{\mathrm{d}^d p}{(2\pi)^d} \int_0^1 \mathrm{d}x\, \frac{1}{\left[(\mathbf{p}+\mathbf{q})^2 x + \Delta^2 x + (1-x)\mathbf{p}^2 + (1-x)\Delta^2\right]^2} = \\
&= \frac{1}{\beta} \sum_{n=-\infty}^{\infty} \int \frac{\mathrm{d}^d p}{(2\pi)^d} \int_0^1 \mathrm{d}x\, \frac{1}{\left[(\mathbf{p}+\mathbf{q}x)^2 + \Delta^2 + \mathbf{q}^2 x(1-x)\right]^2} = \\
&= \frac{1}{\beta} \sum_{n=-\infty}^{\infty} \int \frac{\mathrm{d}^d p}{(2\pi)^d} \int_0^1 \mathrm{d}x\, \frac{1}{\left[\mathbf{p}^2 + \Delta^2 + \mathbf{q}^2 x(1-x)\right]^2},
\end{aligned} \tag{7.8}$$

where $\Delta^2 = \tilde{\nu}_n^2 + \bar{\sigma}^2$ and we applied a shift $\mathbf{p}+\mathbf{q}x \to \mathbf{p}$ in the last step. This procedure exchanges the problematic angle contribution between $\mathbf{p}$ and $\mathbf{q}$ with the 1-dimensional Feynman parameter integral over x. In this form we can carry out the summation over the Matsubara frequencies and transform the

momentum integral into d-dimensional spherical coordinates to obtain the expression

$$l_2 = \int_0^1 \mathrm{d}x \int \frac{\mathrm{d}^d p}{(2\pi)^d} \frac{1}{\beta} \sum_{n=-\infty}^{\infty} \frac{1}{\left[\tilde{\nu}_n^2 + \bar{\sigma}^2 + p^2 + q^2 x(1-x)\right]^2} =$$
$$= \frac{S_d}{(2\pi)^d} \int_0^1 \mathrm{d}x \int_0^\infty \mathrm{d}p\, p^{d-1} \left[\frac{1}{2}\tanh\left(\frac{\tilde{E}+\mu}{2T}\right) + \frac{1}{2}\tanh\left(\frac{\tilde{E}-\mu}{2T}\right) - \frac{\tilde{E}}{T}\left(\frac{1}{4\cosh^2\left(\frac{\tilde{E}+\mu}{2T}\right)} + \frac{1}{4\cosh^2\left(\frac{\tilde{E}-\mu}{2T}\right)} \right) \right], \tag{7.9}$$

where $S_d = \frac{2\pi^{d/2}}{\Gamma(d/2)}$ and $\tilde{E}^2 = \bar{\sigma}^2 + p^2 + q^2 x(1-x)$. For arbitrary $q, \bar{\sigma}, \mu, d$, one can only evaluate the integral over the momentum p in a closed form when $T = 0$. The corresponding calculations are presented in Appendix D.3.

In total, we find for the two-point function at zero temperature (see Appendix D.3 for details of the derivation)

$$\Gamma^{(2)}\left(q,\bar{\sigma},\mu,T=0,d\right) =$$
$$= \frac{N_\gamma}{2^d \pi^{\frac{d}{2}} \Gamma\left(\frac{d}{2}\right)} \left[\frac{1}{d\sqrt{\pi}} \Gamma\left(\frac{1-d}{2}\right) \Gamma\left(\frac{d+2}{2}\right) \left(|\bar{\Sigma}_0|^{d-1} - |\bar{\sigma}|^{d-1} \right) + \right.$$
$$+ \begin{cases} \frac{|\mu|^{d-1}}{(d-1)} & \text{if } \bar{\sigma} = 0, \mu \neq 0 \\ \frac{|\bar{\sigma}|^{d-1}}{d} \left|\frac{\bar{\mu}}{\bar{\sigma}}\right|^d {}_2F_1\left(\frac{1}{2}, \frac{d}{2}; \frac{d+2}{2}; -\frac{\bar{\mu}^2}{\bar{\sigma}^2}\right) & \text{if } \bar{\sigma} \neq 0, \bar{\mu}^2 > 0 \\ 0 & \text{otherwise} \end{cases} + \tag{7.10}$$
$$\left. + \left(\frac{q^2}{4} + \bar{\sigma}^2\right) \int_0^1 \mathrm{d}x \begin{cases} \frac{\tilde{\mu}^{d-3}}{(3-d)} {}_2F_1\left(\frac{3}{2}, \frac{3-d}{2}; \frac{3-d}{2}+1; -\frac{\tilde{\Delta}^2}{\tilde{\mu}^2}\right) - \frac{\tilde{\mu}^{d-2}}{|\mu|} & \text{if } \tilde{\mu}^2 > 0 \\ \frac{\tilde{\Delta}^{d-3}}{2} B\left(\frac{d}{2}, \frac{3-d}{2}\right) & \text{otherwise} \end{cases} \right],$$

where $\bar{\mu}^2 = \mu^2 - \bar{\sigma}^2$, $\tilde{\Delta}^2 = \bar{\sigma}^2 + q^2 x(1-x)$ and $\tilde{\mu}^2 = \mu^2 - \tilde{\Delta}^2$. The remaining integral over x is calculated numerically since no closed form can be given for the integral for arbitrary parameters $q, \bar{\sigma}, \mu, d$.

7.2.2 The Wave-Function Renormalization

We evaluate the wave-function renormalization according to Eq. (4.20). We apply the double derivative with respect to q to L_2 with l_2 given by Eq. (7.8).[1] After carrying out the derivative, evaluating at $q = 0$ and performing the integral over x (see Appendix D.4 for details), one finds the simple expression

$$z\left(\bar{\sigma},\mu,T,d\right) = \frac{N_\gamma}{4} \int \frac{\mathrm{d}^d p}{(2\pi)^d} \frac{1}{\beta} \sum_{n=-\infty}^{\infty} \left(\frac{2}{\left[\tilde{\nu}_n^2 + E^2\right]^2} - \frac{8\bar{\sigma}^2}{3\left[\tilde{\nu}_n^2 + E^2\right]^3} \right). \tag{7.11}$$

The steps of carrying out the Matsubara summation, taking the $T \to 0$ limit and performing the mo-

1 It is certainly possible to apply the derivative to the final expression of $\Gamma^{(2)}$. However, due to the complicated functional dependence on q, it is a lot easier to carry out the derivative before performing the momentum integrals.

mentum integration are presented in Appendix D.4. One then arrives at the closed form expression of the wave-function renormalization for zero temperature

$$z\left(\bar{\sigma},\mu,T=0,d\right) = \frac{N_\gamma}{2^{d+2}\pi^{\frac{d}{2}}\,\Gamma\left(\frac{d}{2}\right)} \begin{cases} \frac{1}{(3-d)\bar{\mu}^{3-d}}\,{}_2F_1\left(\frac{3}{2},\frac{3-d}{2};\frac{5-d}{2};-\frac{\bar{\sigma}^2}{\bar{\mu}^2}\right) + \\ -\frac{1}{(5-d)}\frac{\bar{\sigma}^2}{\bar{\mu}^2}\frac{1}{\bar{\mu}^{3-d}}\,{}_2F_1\left(\frac{5}{2},\frac{5-d}{2};\frac{7-d}{2};-\frac{\bar{\sigma}^2}{\bar{\mu}^2}\right) + \\ +\frac{\bar{\mu}^{d-2}}{|\mu|}\left[\frac{\bar{\sigma}^2}{\mu^2}\left(1+\frac{1}{3\bar{\mu}^2}\left(2\bar{\sigma}^2-(4-d)\mu^2\right)\right)-1\right] & \text{if } \bar{\mu}^2>0, \\ \frac{1}{2|\bar{\sigma}|^{3-d}}\left[B\left(\frac{d}{2},\frac{3-d}{2}\right)-B\left(\frac{d}{2},\frac{5-d}{2}\right)\right] & \text{otherwise} \end{cases} . \tag{7.12}$$

7.3 Results of the Stability Analysis at Zero Temperature

This section discusses the results of the stability analysis at zero temperature as derived in Section 7.2.2 and Appendices D.3 and D.4. The discussion is split among the number of dimensions in $1 \leq d \leq 2$ in Section 7.3.1 and $2 \leq d < 3$ in Section 7.3.2. This is done due to the different implications of the results and the respective conclusions we can draw from them. All results presented in this section are obtained at $T = 0$. We abstain from indicating this in the following.

7.3.1 Results for $1 \leq d \leq 2$

Fig. 7.1(a) shows the two-point function evaluated at the expansion point $\bar{\sigma} = \bar{\Sigma} = 0$ for various numbers of spatial dimensions $1 \leq d \leq 2$ at $\mu = \mu^+_{c,\text{hom}}$ as a function of q, where $\mu^+_{c,\text{hom}}$ is the critical chemical potential of the homogeneous phase transition with an infinitesimal positive shift to ensure that the homogeneous expansion point is $\bar{\Sigma} = 0$.

The result for $d = 1$ is the familiar result as observed in Section 5.1, where $\Gamma^{(2)}$ diverges negatively at $q = 2\mu$. For non-integer d, one cannot solve the integral over x in Eq. (7.10) in a closed form and we have to resort to a numerical integration. For $q = 2\mu$ and $\bar{\sigma} = 0$, one finds that the integrand is divergent at $x = 1/2$ and, thus, it is not immediately clear, whether the two-point function after performing the x-integration is divergent as in $d = 1$. We can, however, expand the integrand around $2x = 1$ and find that the most divergent contribution is

$$\frac{(2x-1)^{d-2}}{|\mu|^{3-d}}. \tag{7.13}$$

Since the most divergent contribution is proportional to $(2x-1)^{d-2}$, the integral is finite for any $d > 1$. Accordingly, the divergence of the two-point function in $d = 1$ turns into a finite cusp for $d > 1$. The value of $\Gamma^{(2)}$ at this cusp remains negative for any $d < 2$ and with this the instability towards an IP remains.

At $d = 2$, the two-point function vanishes for $|q| < 2\mu$, which signals an energetical degeneracy between the homogeneous expansion point and the same homogeneous configuration with inhomogeneous perturbations of these momenta. This has some similarities to the effective homogeneous potential (see Fig. 3.4), which exhibits an interval of minimizing homogeneous field configurations in $d = 2$ at $\mu_{c,\text{hom}}$. Yet another form of degeneracy at this point in $d = 2$ was documented in Ref. [151], where 1-dimensional inhomogeneous solutions from the GN model in $d = 1$ were embedded in the 2-dimensional space. These configurations were energetically degenerate to the homogeneous field configurations. Although far

from conclusive evidence, this hints towards a general degenerate behavior of the effective action at this (d,μ,T)-point.

It is important to note that the instability for $1 < d < 2$ is always present at $\mu^{+}_{c,\mathrm{hom}}$. For larger chemical potentials, one finds that the offset at $q = 0$ increases. For chemical potentials larger than some critical chemical potential, $\Gamma^{(2)}$ is strictly positive for all q. This is shown in Fig. 7.1(b) at $\mu/\bar{\Sigma}_0 = 3.0$. For d closer to $d = 1$, we still find an instability, but for larger d it is completely gone. Even though, the instability vanishes for some spatial dimensions, one always finds a global minimum of $\Gamma^{(2)}$ at a finite q for $d < 2$.

This results in a wave-function renormalization that is negative for all $\mu > \mu_{c,\mathrm{hom}}$ for $d > 2$ as shown in Fig. 7.2. The wave-function renormalization is constant and positive for $\mu < \mu_{c,\mathrm{hom}}$. At the homogeneous phase transition which is indicated by the circular marker, it jumps to a negative value and remains negative for any μ. In contrast, we find $Z = 0$ in $d = 2$ for $\mu > \mu_{c,\mathrm{hom}}$.

These results show that solely the increase of the number of spatial dimensions, which enters as a numerical parameter, weakens the instability towards an IP and causes its disappearance in $d = 2$. Thus, we can provide a partial answer to research question Q5 by identifying d as the determining property whether an IP exists, albeit we still lack the understanding why the IP only exists in integer dimensions $d = 1$.

7.3.2 Results for $2 \leq d \leq 3$

Fig. 7.3(a) shows the two-point function $\Gamma^{(2)}$ evaluated at the physical expansion point $\bar{\sigma} = \bar{\Sigma} = 0$ for various number of spatial dimensions $2 \leq d < 3$ at $\mu = \mu^{+}_{c,\mathrm{hom}}$ as a function of q. For $d > 2$, we find that $\Gamma^{(2)}$ is a strictly monotonically increasing function of q, which is the case for any chemical potential. Thus, there is no instability towards an IP for any $2 < d < 3$. The function continues to exhibit a non-analytic point at $q = 2\mu$, whose vicinity is increasingly smoothed out for increasing d.

Fig. 7.3(b) shows the wave-function renormalization, which is positive and constant for $\mu < \mu_{c,\mathrm{hom}}$ as in $1 \leq d < 2$. At $\mu/\bar{\Sigma}_0 = 1$, we find that Z diverges positively, which is also observed in the results of the moat regime of the $(3+1)$-dimensional NJL model in Section 6.4. We reiterate the argument made there and

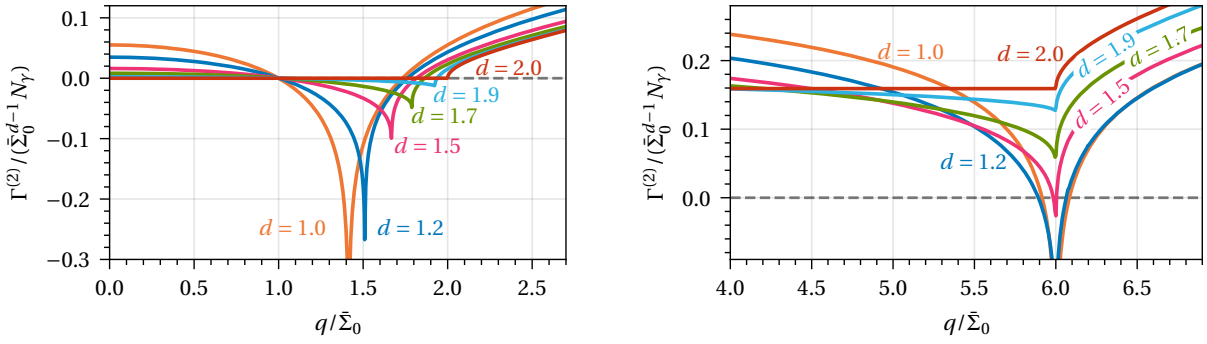

(a) At $\mu^{+}_{c,\mathrm{hom}}(d)$, which is the critical chemical potential of the homogeneous phase transition with an infinitesimal positive shift to ensure that the homogeneous expansion point is $\bar{\Sigma} = 0$. Reproduction of Ref. [51, Fig. 2].

(b) At $\mu/\bar{\Sigma}_0 = 3.0$.

Figure 7.1: The two-point function $\Gamma^{(2)}$ as a function of the bosonic momentum q for various spatial dimensions $1 \leq d \leq 2$ at $T = 0$ and various chemical potentials.

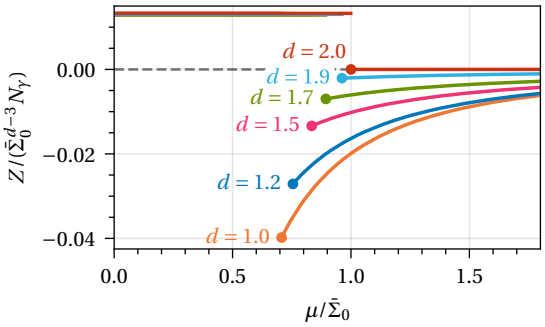

Figure 7.2: The bosonic wave-function renormalization Z at $T = 0$ as a function of the chemical potential for various spatial dimensions $1 \leq d \leq 2$. The circles indicate the critical chemical potential of the homogeneous phase transition. Reproduction of Ref. [51, Fig. 3].

explain this in a graphical manner. The non-analytic point in $\Gamma^{(2)}$ is for finite $\bar{\sigma}$ located at $q^2 = 4(\mu^2 - \bar{\sigma}^2)$,[2] which means that this point is located at $q = 0$ for $\mu = \bar{\sigma}$. If we only consider the relevant expansion point of $\bar{\sigma} = \bar{\Sigma}$, one finds only $\mu \neq \bar{\Sigma}$ for $1 \leq d < 2$. For $d > 2$, the homogeneous phase transition is however located at $\mu/\bar{\Sigma}_0 > 1$, which enables the occurrence of $\mu = \bar{\Sigma} = \bar{\Sigma}_0$. This causes the non-analytic point in the two-point function to be located at $q = 0$ and subsequently causes Z – being the second derivative of $\Gamma^{(2)}$ – to diverge. The wave-function renormalization remains positive for $\mu/\bar{\Sigma}_0 > 1$ and thus is positive for any μ, resulting in the absence of a moat regime.

These results are in stark contrast to the results that one obtains from calculations in $(3+1)$-dimensional models such as the NJL model that we discussed in Chapter 6. For any $2 < d < 3$, we do not find traces of an instability or a moat regime in the renormalized GN model, while the calculations of non-renormalizable models in $d = 3$ show instabilities in large parts of the parameter space and phase diagram. Two differences between these results remain, with the first one being the infinitesimal difference between $d < 3$ and $d = 3$. Since we observe a smooth evolution of the results for increasing d for $1 \leq d < 3$, we would not expect a fundamental change by going from $d < 3$ to $d = 3$. Thus, the second difference is the only significant one, which is the fact that the calculations in $d = 3$ have to be carried out in the presence of a finite regulator, while we considered the renormalized model in $d < 3$. Thus, we conclude that the results of an IP and the moat regime as we documented them in Chapter 6 are solely due to the presence of such a finite regulator. This is clearly answering research question Q6.

This does not necessarily mean that the IP in these models is a regularization "artifact". It might be that the regulator is an important part for the ability of effective models such as the NJL model to mimic QCD. This, however, gives the choice of the regularization scheme even more importance as this is evidently the origin of the IP. Especially, one should not base the choice solely on convenience or numerical feasibility.

7.3.3 Phase Structure in the (μ,d)-Plane

Fig. 7.4 shows the phase structure in the (μ,d)-plane as obtained from a homogeneous minimization and the stability analysis. For $d < 2$, we find an IP in some range of μ, which turns into a moat regime for larger chemical potentials. For $d > 2$, we only find the HBP and SP, but no indication of a moat regime or an

2 This can be seen in Eq. (D.24), where the single non-analytic point $\tilde{\mu}^2 = 0$ in the integrand is probed for $q^2 = 4(\mu^2 - \bar{\sigma}^2)$ at $x = 1/2$.

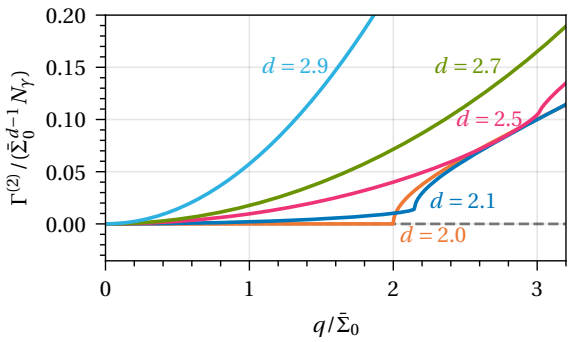

(a) The two-point function $\Gamma^{(2)}$ as a function of the bosonic momentum q at $T = 0$ and $\mu = \mu^{+}_{c,\mathrm{hom}}(d)$. Reproduction of Ref. [51, Fig. 4].

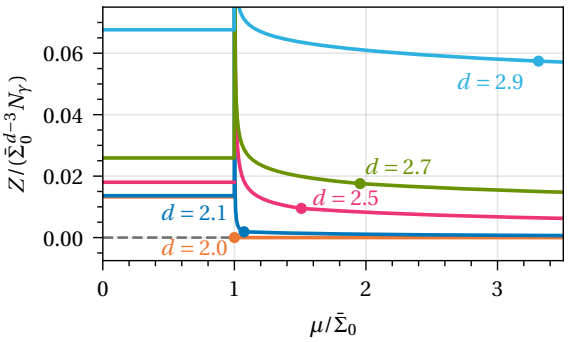

(b) The bosonic wave-function renormalization Z at $T = 0$ as a function of the chemical potential. The circles indicate the critical chemical potential of the homogeneous phase transition. Reproduction of Ref. [51, Fig. 5].

Figure 7.3: The two-point function and the wave-function renormalization for $d \geq 2$.

instability towards an IP.

We note that one exclusively finds an IP or moat regime in spatial dimensions d, where there is also a first order homogeneous phase transition at $T = 0$ or equivalently a CP at a finite temperature. This is in agreement with the observation from calculations of the GN model and related models where the CP and LP coincide [14, 28, 29, 35, 39].

We recall that our analysis in Chapter 5 revealed that the stability analysis is unable to detect a portion of the IP. This occurred for chemical potentials, which are smaller than the critical chemical potential associated to the the first order homogeneous phase transition. This is most likely also the case for $1 < d < 2$, but we lack an exact solution for the inhomogeneous condensate to check for this shortcoming of the stability analysis.

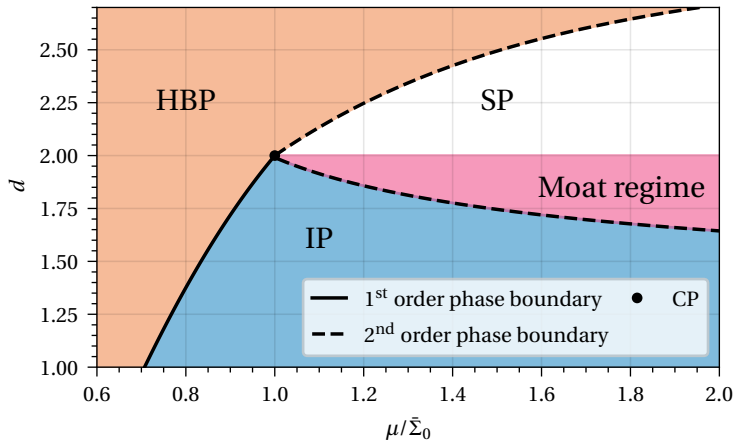

Figure 7.4: The phase structure of the GN model in the (μ,d)-plane at $T = 0$ as obtained from our stability analysis. The homogeneous phase boundaries are calculated by Ref. [64, Eq. (3.33) and Eq. (3.35)]. Reproduction of Ref. [51, Fig. 6].

7.4 The $(3+1)$-Dimensional Gross-Neveu Model with Dimensional Regularization

This section gives an alternative interpretation of the results that are discussed in Section 7.3. We considered in our study of the $(3+1)$-dimensional NJL model in Chapter 6 only regularization schemes that suppress UV-modes in divergent integrals at large momenta by some dimensional quantity Λ to render the integrals UV-finite. This is, however, not the only approach. Dimensional regularization (see Section 2.3.1) renders the integrals finite by considering a D-dimensional space-time, which one sends to the desired integer result during renormalization. In studies of non-renormalizable $(3+1)$-dimensional NJL-type models using this regularization scheme, one then keeps $D < 4$ [55, 75, 152, 153] instead of keeping the regulator at a finite value. Smaller D corresponds to a stronger regularization just like a small regulator does.

Considering this, our analysis of the $(d+1)$-dimensional GN model can be viewed as a study of the $(3+1)$-dimensional GN model with dimensional regularization. By scanning d, we effectively studied the regulator dependence of the phase diagram similar to the study of the NJL model in Chapter 6. In this picture, stronger regularization just procures the phase diagram of a lower dimensional version of the model.

With the dimensional regularization, this is very intuitive since one directly alters the dimensionality to regulate the UV divergence. Graphically speaking, one controls the dimensions such that the integrand falls off faster than the integration volume grows. However, e.g., the PV regularization works similarly: introducing additional terms in the integrand such that it falls off faster than the integration volume grows.[3] Even though there is certainly not a one to one correspondence in the form of the regularized integrand, one could argue that this effectively reduces the dimensions of the problem carrying over the concept of strong regularization being equivalent to a lower dimensional problem. This might explain why the $(3+1)$-dimensional NJL model under strong regularization exhibits phenomena like a CP and the IP, which are found in the low-dimensional models for $1 \leq d < 2$.

7.5 Summary

In this chapter, we performed the stability analysis of the GN model in non-integer spatial dimensions d, where the model is fully renormalizable. This resulted in a setup, where the number of spatial dimensions enters only as a continuous parameter and reveals that d is the driver of the disappearance of the IP when going from $1+1$ to $2+1$ dimensions. Moreover, we did not find any sign for an instability for $2 < d < 3$. This suggests that the IP that is found in $(3+1)$-dimensional FF models such as the NJL model is solely enabled by the presence of a finite regulator. Finally, we presented an alternative interpretation of these results as a study of the regularization scheme dependence in the $(3+1)$-dimensional GN model with dimensional regularization. This gave rise to the conjecture that the regularization of models such as the NJL model effectively reduces the dimensionality of the theory, yielding features characteristic of lower-dimensional versions of the model.

3 One can make the exact same argument, e.g., for the Schwinger proper time regularization (see the discussion in Section 2.3.1).

7.6 Possible Extensions

While the present investigation proved to be fruitful with regard to the important conclusion that we were able to draw from it, it is far from complete. There are many possible extensions of this d-dimensional approach, which could shed light on further aspects of the phase structure of NJL-type models.

7.6.1 Extension to the Nambu-Jona-Lasinio Model

Applying the stability analysis to the NJL model in arbitrary spatial dimensions forces us to consider the role of γ_{ch}. In $D = 4$ space-time dimensions one might define

$$\gamma_{\text{ch}} \equiv \gamma_5 \coloneqq \frac{1}{4!}\varepsilon^{\mu\nu\lambda\kappa}\gamma_\mu\gamma_\nu\gamma_\lambda\gamma_\kappa. \tag{7.14}$$

However, such a definition fails for arbitrary spacetime dimensions D, where the ε symbol is not defined. Instead one might define

$$\gamma_{\text{ch}} \equiv \gamma_5 \coloneqq \gamma_0\gamma_1\gamma_2\gamma_3, \tag{7.15}$$

that is equivalent to Eq. (7.14) in $D = 4$, since such a γ_5 anti-commutes with γ_μ for $\mu = 0,1,2,3$. It, however, commutes for all other values of μ, which is relevant in non-integer spacetime dimensions D, where μ might assume non-integer values [60, 74] (see also the short comment in Appendix B.1.3). Thus, considering the NJL model in non-integer dimensions requires special care. Not only the derivation of the stability analysis would deviate significantly from the GN model, but also the renormalization since we would have two independent gap equations due to the lack of chiral symmetry. Consequently, two independent couplings as realized in the original Lagrangian of the gNJL Eq. (2.1) should be considered.

7.6.2 Finite Temperature

We limited this analysis to $T = 0$ as it enabled us to give analytic or heavily simplified expressions for most quantities. While this was enough to draw the fundamental conclusions about the role of the number of dimensions and the regulator in $d = 3$, it only gave us a glimpse of the full phase structure. Thus, an obvious extension is the consideration of finite temperature, which would allow us to draw the full phase diagram in μ, T, d-space. This would illuminate the full evolution of the IP and the moat regime between the integer dimensions. Calculations are already in preparation and results will be published soon.

7.6.3 Finite Regulators

One of the main conclusion was that the IP is generated by a finite regulator in calculations in $d = 3$. Thus, in order to connect to these results smoothly, it would be interesting to perform the calculations at a finite regulator. This allows to demonstrate the recovery of the absent IP and extend our analysis to $1 \leq d \leq 3$ number of spatial dimensions.

7.6.4 Ansatz for the Inhomogeneous Condensate

Various investigations (e.g,. [14, 31, 151, 154]) have embedded 1-dimensional modulations in higher dimensional space in an effort to determine an inhomogeneous field configuration that is energetically preferred over the homogeneous one. In these calculations using the density of states approach (see Section 4.1.1), one splits space into the direction where the modulation lies in and the perpendicular

space. This perpendicular space can be treated in such a way that allows for generalization to non-integer d spatial dimensions.

Carrying out such an investigation allows us to detect parts of the IP, which are not detectable for the stability analysis, e.g., in the vicinity of a homogeneous, first order phase transition as it occurs in the $(1+1)$-dimensional GN model (see Chapter 5). Moreover, one could observe how the dimensionality of the perpendicular space favors or disfavors particular inhomogeneous modulations.

Chapter 8

Summary, Conclusion, and Outlook

8.1 Summary

In this thesis, we investigated the chiral inhomogeneous condensation in several NJL-type models and in a varying number of dimensions within the MFA. We mainly relied on the stability analysis based on the bosonic two-point function to detect the existence of an IP and the moat regime.

We introduced NJL-type models and the most important aspects of calculations in these models, e.g., the MFA and regularization schemes, in Chapter 2 in a general manner. Specific NJL-models with a focus on the GN and NJL model were discussed in Chapter 3. We covered the most important results from the literature regarding the phase diagram of these models as these form the basis for our investigations. The stability analysis, which is the principal technique for our studies of the IP, was introduced and derived in Chapter 4.

As a preceding step to our main investigations with the stability analysis, we rigorously tested its capabilities in the $(1+1)$-dimensional GN model in Chapter 5. The exact phase diagram and the functional shape of the inhomogeneous condensate in the IP of this model is known [28, 29] (see Section 3.1). Thus, this model posed the ideal testing ground to benchmark the stability analysis. We found that the stability analysis is able to correctly reproduce the phase boundary between the IP and the SP. Moreover, it can provide a useful estimate for the wavelength of the energetically preferred inhomogeneous field configuration. A deficit is that it failed to detect parts of the IP in the vicinity of the first order homogeneous phase boundary, which was partially expected. This study was a necessary step in the preparation of the investigation of models, where we do not have access to the exact solution, e.g., the $(3+1)$-dimensional NJL model.

In Chapter 6, we thoroughly studied the regularization scheme dependence of the IP and the moat regime of the non-renormalizable $(3+1)$-dimensional NJL model. There, the stability analysis proved to be extremely versatile as we could apply it with the PV, SC, SLAC, and Hybrid regularization. The latter two are lattice regularization that were the original main focus of this investigation. Guided by research question Q2, this investigation was supposed to clarify whether full lattice Monte-Carlo simulations of this model are feasible as a preceding step to answering research question Q1 with such simulations. We found that the IP changes drastically when switching regularization schemes. The identified reason for this behavior is that the parameter ranges in which the IP occurs correspond to large chemical potentials in the order of the regulator. This favors inhomogeneous condensates with momenta that can be even larger than the regulator. Especially the results of the lattice regularizations are heavily influenced by this, as these are not able to resolve bosonic momenta that are larger than the regulator. We argued that this is not a deficit of the lattice regularizations, but rather of the problematic parameter regions. For the continuum regularization, we analyzed the impact on the extent of the IP that NMR has, i.e., the removal

of regularization of the medium contributions. While it did not impact the PV results at $T = 0$, it drastically enlarged the instability region for the SC regularization and resulted in a similar shaped region as the one obtained with the PV regularization. Lastly, we analyzed the moat regime for the PV and SC regularization. Its indicator – the wave-function renormalization – is evaluated at zero bosonic momentum and the only large parameter is the chemical potential. Thus, it might be that the regularization scheme dependence is less severe as fewer quantities compete with the regulator. This conjecture appears to be correct as we found a considerably better agreement between the PV and SC regularization than for the IP.

Motivated by the severe regulator dependence of the IP in the $(3+1)$-dimensional NJL model and the disappearance of the IP when going from the $(1+1)$-dimensional GN model to the $(2+1)$-dimensional version, we set out to understand how the existence of the IP depends on the number of dimensions. To this end, we considered the GN model in non-integer spatial dimensions $1 \leq d < 3$ and applied the stability analysis to it in Chapter 7. This resulted in a renormalized setup, where the number of spatial dimensions entered only as a continuous parameter. We did not observe any instability or moat regime for $2 \leq d < 3$.

8.2 Conclusion and Outlook

One of the central conclusions that we can draw from the results of this thesis is that the choice of the regularization scheme in the investigation of $(3+1)$-dimensional models is not arbitrary. We saw that there is a strong dependence on the scheme and that the regularization is the generator of the IP in these models. Thus, if we are to give the results obtained with these models any physical relevance, the regularization scheme should be chosen carefully. It should be based on the fact which scheme renders the $(3+1)$-dimensional NJL model as an effective model for QCD the best and not on, e.g., ease of calculations. Thus, the answer to research question Q3 is that the regulator scheme dependence is significant up to the point that there is no overlap between the results for the IP of different regularization schemes.

Furthermore, we learned that it is not sensible to investigate the IP in the $(3+1)$-dimensional NJL model beyond the MFA with lattice Monte-Carlo simulations. Our results within the MFA showed that the extreme chemical potentials introduce severe regularization artifacts, which completely spoil the phenomenology of the IP when using lattice regularizations. These would also be present in the full simulations. Thus, the answer to research question Q2 is that one should not use lattice regularizations in studies of the IP in the $(3+1)$-dimensional NJL model.

This negative finding makes it clear that we cannot answer research question Q1 by performing lattice Monte-Carlo simulations of the $(3+1)$-dimensional NJL model.[1] One could, however, consider the QM model, which is the Yukawa extension of the NJL model. This model is renormalizable in contrast to the NJL model and still exhibits an IP for large regulators Λ [14, 35]. Thus, one could carry out lattice simulations at small lattice spacing with an IP that would likely be free of severe regularization artifacts. One should, however, conduct an investigation of the IP in the QM model within the MFA using a lattice regularization similar to the study in the NJL model. This should already give clear indications about regularization artifacts and is considerable less expensive than the full Monte-Carlo simulations from a computational point of view. Moreover, from a technical point of view the calculations are barely different from the calculations of the NJL model as the models differ only by a quartic potential term and kinetic term for the bosons. This direction was not pursued within this thesis solely due to time constraints,

1 Due to the severe regularization scheme dependence, one should also be careful with respect to results obtained with other techniques.

but should be the next step in future investigations seeking to answer research question Q1 with lattice methods.

The severe regularization scheme dependence of the IP could also be an indication that this phase is in fact not physically relevant in QCD. The moat regime appears relatively robust when changing the regularization scheme (at least between the SC and PV scheme) and covers a large portion of the phase diagram similarly to what we observed in the $(1+1)$-dimensional GN model. This answers research question Q4. Thus, it might be that it is a more relevant phenomenon than the IP and future investigations could focus on the moat regime, which also has clear experimental signals [38, 40–42].

Moreover, in Chapter 7, we observed that the number of spatial dimensions profoundly impacts the existence of the IP. From the results of the stability analysis, we could conclude that the disappearance of the IP and the moat regime when going from $d = 1$ to $d = 2$ is solely caused by the number of spatial dimensions. This provides a first answer to research question Q5, but we still lack the insight why the number of spatial dimensions causes the disappearance. Moreover, we did not find any instability or tendency towards an IP for $2 < d < 3$ in our renormalized setup. This led to the conclusion that the IP in $d = 3$, e.g., as in the $(3+1)$-dimensional NJL model (as we found it in Chapter 6), is solely enabled by the presence of a finite regulator. This is a clear answer to research question Q6. Thus, we can generally conclude that without regularization [14, 30, 31, 48, 49], one does not observe an IP or a moat regime in NJL-type models for any integer number of spatial dimensions other than $d = 1$. The exclusivity of this phenomenon to that specific number of spatial dimensions needs to be investigated further. A first step might be to explore the phase structure in the full μ, T, d-space, which we also discussed in Section 7.6 among other possible extensions. Here, one could study the position of the CP in the (μ, T)-plane as a function of d. As this point coincides with the LP, its existence at a finite temperature indirectly signals the existence of an IP. Thus, understanding why this point vanishes for $d > 2$, could give further hints about the d-dependence of the IP. Corresponding work is already in preparation.

Lastly, the reinterpretation of the study of the $(d+1)$-dimensional GN model as the $(3+1)$-dimensional GN model with dimensional regularization in Section 7.4, suggested that a strong regularization in a $(3+1)$-dimensional model corresponds to procuring a lower dimensional version of the model.[2] While this is obvious with the dimensional regularization, we argued that other regularization schemes like the PV effectively reduce the dimensionality of the problem in their own way. This falls in line with the conclusion that phenomena like the IP are confined to $(1+1)$-dimensional NJL-type models and a strong regularization merely gives access to this phase structure in higher dimensions. The relationship between regularization and *effective dimensionality* of the theory appears to be an important part in understanding the nature of results in $(3+1)$-dimensional NJL-type models. A rigorous study of the phenomenon of effective dimensionality could be conducted in the $(2+1)$-dimensional GN model building on the investigations in Ref. [49]. This model has the advantage that it is renormalizable avoiding problematic parameter regions as in the $(3+1)$-dimensional NJL model and it is "close" to dimensions that exhibit an IP as shown in Section 7.3.1. Thus, one would not have to apply a severe regularization to lower the dimensions enough to observe the CP at finite temperature, an IP or the moat regime. By comparing with the d-dimensional results of Chapter 7, one could map out the effective dimension for finite regulators in different regularization schemes.

Evidently, there are numerous aspects of the IP and the moat regime in these NJL-type models that are not yet fully understood. The nature of these appear to be profound enough such that they arise in these

2 This argumentation is certainly not restricted to $(3+1)$-dimensional models and would also explain why a finite regulator in $(2+1)$-dimensional models gives rise to an IP (see Section 3.1.3 and, e.g., Ref. [49]).

comparatively primitive calculations in the MFA. Therefore, their simplicity should be regarded as an advantage, since it enables a less obstructed path to studying central aspects of the IP in fermionic theories than full-fledged simulations of complicated models beyond the MFA. In any case, such investigations can only provide a general understanding of the IP and the moat regime, but ultimately only first-principle calculations will unambiguously confirm whether these phenomena are actually realized in QCD.

A Notation and Common Definitions

This Appendix serves as a general reference for certain notation, conventions and definitions to avoid repeated definitions. The following is a loose list of default conventions and notation, which can be assumed to hold unless stated otherwise.

General

- To organize equations and expressions, we use not only parentheses (, but also brackets [and braces { mostly in that order.
- We do not always list all arguments of a given quantity, if it is clear from the respective context which values the different parameters assume.
- The region of integration of multidimensional integrals such as

$$\int \mathrm{d}^n x \tag{A.1}$$

  spans the whole $\mathbb{R}^n$.
- $\langle\cdot\rangle$ denotes expectation values of the path integral.

Space-Time Quantities

- D always denotes the number of space-time dimensions and d the number of spatial dimensions.
- Spatial vectors are denoted in bold, e.g., $\mathbf{p}$.
- Space-time vectors are slanted in default font, e.g., p, but depending on the context this can also be the absolute value of a spatial vector $p = |\mathbf{p}|$.
- Repeated indices imply a summation over these indices with the boundaries of the summation given by the context.
- We use Greek letters such as μ,ν for space-time indices that run from 0 to $D-1$ and roman letters such as i,j for spatial indices that run from 1 to $D-1$.

Fermions

- In fermionic bilinears, we omit unit matrices of the spaces in which the matrix in the bilinear is diagonal and we do not explicitly denote in which space the matrices acts. For example, for spinors with N_f flavors and a N_γ-dimensional Dirac space, we write $\bar{\psi}\gamma_0\psi$ instead of $\bar{\psi}\gamma_0\mathbb{1}_{N_f}\psi$ or the absurd $\sum_{a=1}^{N_f}\sum_{\alpha=1}^{N_\gamma}\sum_{b=1}^{N_f}\sum_{\beta=1}^{N_\gamma}\bar{\psi}_{a,\alpha}(\gamma_0)_{\alpha,\beta}(\mathbb{1}_{N_f})_{a,b}\psi_{b,\beta}$.
- The fermionic Matsubara frequencies are denoted as $\nu_n = (2n+1)\pi T$ and the shifted frequencies $\tilde{\nu}_n = \nu_n - \mathrm{i}\mu$.

- The Fermi-Dirac distribution is denoted by

$$n(E) = \frac{1}{\exp\left(\beta(x+\mu)\right)+1}, \quad \bar{n}(E) = \frac{1}{\exp\left(\beta(x-\mu)\right)+1}. \tag{A.2}$$

Bosons

- We denote homogeneous bosonic configurations with a bar, e.g., a homogeneous configuration of the field ϕ is denoted by $\bar{\phi}$.
- We denote field configurations that correspond to minima of the effective action by the corresponding capital letters, e.g., the minimizing field configuration of σ is denoted by Σ and an explicitly homogeneous minimizing field configuration would be $\bar{\Sigma}$.

B Various Remarks on the Clifford Algebra and Chiral Symmetry of Fermions

B.1 Clifford Algebra and Fermion Representations

We shortly present central aspects of the Clifford algebra and fermion representations in various number of space-time dimensions. As this is an exhaustive topic, this discussion merely scratches the surface and we refer to Refs. [74, 155, 156] for more details.

The Euclidean Clifford algebra in D space-time dimensions contains the matrices γ_μ that fulfill the anti-commutation relation

$$\{\gamma_\mu,\gamma_\nu\} = 2\delta_{\mu,\nu}, \quad \mu,\nu = 0,\ldots,D-1, \tag{B.1}$$

where γ_μ are matrices of dimension $N_\gamma \times N_\gamma$, where N_γ is being referred to as dimension of the respective representation of the Clifford algebra. The dimensions N_γ is closely tied to number of space-time dimensions.

B.1.1 Even Space-Time Dimensions

In even space-time dimensions $D = 2k$ one finds only equivalent irreducible representations of dimension $N_\gamma = 2^k$ [155]. The $2k$ Dirac matrices $\gamma_0,\gamma_1,\ldots,\gamma_{2k-1}$ can be constructed systematically each with k direct products of the Pauli matrices. Then one finds an additional matrix γ_{2k}[1], which anti-commutes with all space-time Dirac matrices γ_μ, i.e, $\{\gamma_{2k},\gamma_\mu\} = 0$. We denote this matrix as γ_{ch}.

B.1.2 Odd Space-Time Dimensions

For odd space-time dimensions $D = 2k+1$ there is an ambiguity in the definition of the Dirac matrices. One finds in general two inequivalent, irreducible representations of dimension $N_\gamma = 2^k$. In this representation, however, we do not find an extra matrix that anti-commutes with the space-time Dirac matrices as γ_{2k} is part of them. One can, however, construct a reducible representation of dimension $N_\gamma = 2^{k+1}$ out of the two inequivalent, irreducible representations. This results in two extra matrices γ_{2k+1} and γ_{2k+2}, which anti-commute with the space-time Dirac matrices.

In $D = 3$ this amounts to the fact that we consider 4×4 Dirac matrices. One finds the three space-time matrices $\gamma_0,\gamma_1,\gamma_2$ and two additional Dirac matrices that are often denoted as γ_4 and γ_5 [93], which fulfill $\{\gamma_{4/5},\gamma_\mu\} = 0$. This enlarges the chiral symmetry for fermionic actions, see Appendix B.2.

B.1.3 Non-integer Space-Time Dimensions

The following is a short summary of the corresponding discussions in Refs. [60, 74]. We mention these aspects also in Sections 7.1 and 7.6.1 and thus this discussion is given here only for completeness. The

1 This is the matrix that is commonly denoted as γ_5 in $D = 4$.

topic of the Clifford algebra in non-integer space-time dimensions is peculiar as one would expect that the concept is only sensible in integer space-time dimensions. However, in the context of dimensional regularization one is forced to carry out this generalization [74].

Essentially one finds that one can safely generalize the fundamental anti-commutation relation

$$\{\gamma_\mu,\gamma_\nu\} = 2\delta_{\mu,\nu} \tag{B.2}$$

to non-integer μ,ν. However, one cannot rigorously define γ_{ch} as it is usually defined via an ε-symbol, e.g., in $D = 4$ one would define

$$\gamma_{\text{ch}} \equiv \gamma_5 := \frac{1}{4!}\varepsilon^{\mu\nu\lambda\kappa}\gamma_\mu\gamma_\nu\gamma_\lambda\gamma_\kappa. \tag{B.3}$$

This symbol is not generalizable to non-integer dimensions. There are various other definitions that are ambiguous in non-integer dimensions. Since results would possibly depend on this, we refrain from assuming the existence of γ_{ch} and the anti-commutation relation

$$\{\gamma_{\text{ch}},\gamma_\mu\} = 0. \tag{B.4}$$

B.2 Chiral Symmetry of Free Fermions

In this section we discuss the chiral symmetry transformations under which the action of free fermions are invariant. Of course there are other various symmetries, but these are – except for translational invariance – not relevant for this work. We refer to Refs. [57, 60] for a detailed discussion of chiral and further symmetries.

The Lagrange density of N_f degenerate flavors of free fermions is given by

$$\mathcal{L} = \sum_{a=1}^{N_f} \bar{\psi}_a(\partial\!\!\!/ + m)\psi_a, \tag{B.5}$$

where $\bar{\psi}_a,\psi_a$ are fermion spinors with N_γ degrees of freedom and m is the fermion mass. N_γ is the dimension of the representation of the Clifford algebra, i.e., the dimensions of the γ-matrices.

We start the discussion of the chiral symmetries by considering a single fermion flavor $N_f = 1$, in order to ease the notation and will generalize our findings to arbitrary N_f. Furthermore, we consider an irreducible representation of the Clifford algebra in an even number of integer space-time dimensions, i.e., γ_{ch} exists and there are no additional Dirac matrices that anti-commute with the space-time Dirac matrices. We recognize that the Lagrangian (B.5) is invariant under a global vector $\mathrm{U}(1)_V$ transformation

$$\mathrm{U}(1)_V: \quad \psi \to \mathrm{e}^{\mathrm{i}\alpha\,\mathbb{1}_{N_\gamma}}\psi, \quad \bar{\psi} \to \bar{\psi}\,\mathrm{e}^{-\mathrm{i}\alpha\,\mathbb{1}_{N_\gamma}}, \tag{B.6}$$

where $\mathbb{1}_{N_\gamma}$ is the $N_\gamma \times N_\gamma$ unit matrix acting in spinor space. The associated conserved current to this symmetry is

$$\mathcal{J}_\mu = \bar{\psi}\gamma_\mu\psi, \tag{B.7}$$

and the conserved charge is the fermion number

$$N = \int \mathrm{d}^d x\,\mathcal{J}_0 = \int \mathrm{d}^d x\,\psi^\dagger\psi. \tag{B.8}$$

This is the charge whose expectation value is fixed by introducing $\exp\left(\bar{\psi}\mu\gamma_0\psi\right)$ to the path integral.

For massless fermions, i.e., $m = 0$, the Lagrangian is also invariant under an axial $\mathrm{U}(1)_A$ symmetry

$$\mathrm{U}(1)_A: \quad \psi \to \mathrm{e}^{\mathrm{i}\beta\gamma_{\mathrm{ch}}}\psi, \quad \bar{\psi} \to \bar{\psi}\,\mathrm{e}^{\mathrm{i}\beta\gamma_{\mathrm{ch}}}, \tag{B.9}$$

which transforms the left- and right-handed fermions oppositely in contrast to the $\mathrm{U}(1)_V$, which transforms both equally. We can see the behavior by inspecting the individual transformations on left- and right-handed fermions

$$\psi_L = \frac{1-\gamma_{\mathrm{ch}}}{2}\psi \to \frac{1-\gamma_{\mathrm{ch}}}{2}\,\mathrm{e}^{\mathrm{i}\beta\gamma_{\mathrm{ch}}}\psi = \mathrm{e}^{-\mathrm{i}\beta}\psi_L, \quad \psi_R = \frac{1+\gamma_{\mathrm{ch}}}{2}\psi \to \frac{1+\gamma_{\mathrm{ch}}}{2}\,\mathrm{e}^{\mathrm{i}\beta\gamma_{\mathrm{ch}}}\psi = \mathrm{e}^{\mathrm{i}\beta}\psi_R. \tag{B.10}$$

The associated current of the symmetry is

$$\mathcal{J}_A^\mu = \bar{\psi}\gamma_\mu\gamma_{\mathrm{ch}}\psi. \tag{B.11}$$

If we now consider arbitrary N_f, we find additional symmetries with flavor rotations

$$\mathrm{SU}\left(N_f\right)_V: \quad \psi \to \mathrm{e}^{\mathrm{i}\theta_a\tau_a\mathbb{1}_{N_\gamma}}\psi, \quad \bar{\psi} \to \bar{\psi}\,\mathrm{e}^{-\mathrm{i}\theta_a\tau_a\mathbb{1}_{N_\gamma}}, \tag{B.12}$$

$$\mathrm{SU}\left(N_f\right)_A: \quad \psi \to \mathrm{e}^{\mathrm{i}\phi_a\tau_a\gamma_{\mathrm{ch}}}\psi, \quad \bar{\psi} \to \bar{\psi}\,\mathrm{e}^{\mathrm{i}\phi_a\tau_a\gamma_{\mathrm{ch}}}, \tag{B.13}$$

where τ_a are the $N_f^2 - 1$ generalized Gell-Mann matrices of size $N_f \times N_f$ [56]. These are the Pauli matrices for $N_f = 2$ and the ordinary Gell-Mann matrices for $N_f = 3$. These two symmetries generate independent $\mathrm{SU}\left(N_f\right)$ transformations for left- and right-handed fermions $\mathrm{SU}\left(N_f\right)_L, \mathrm{SU}\left(N_f\right)_R$. The whole symmetry group for N_f flavors is then $\mathrm{U}(1)_V \times \mathrm{U}(1)_A \times \mathrm{SU}\left(N_f\right)_L \times \mathrm{SU}\left(N_f\right)_R$. A mass term then breaks the chiral symmetry, thus reducing the symmetry group as $\mathrm{U}(1)_{\mathbb{1}} \times \mathrm{U}(1)_A \times \mathrm{SU}\left(N_f\right)_L \times \mathrm{SU}\left(N_f\right)_R \to \mathrm{U}(1)_V \times \mathrm{SU}\left(N_f\right)_V$

In odd space-time dimensions, one finds in a reducible fermion representation additional chiral symmetry transformations generated by γ_4 and $\gamma_{45} = \mathrm{i}\gamma_4\gamma_{\mathrm{ch}}$ (see, e.g., Refs. [51, 93]). For $N_f = 1$, these are the vector transformation

$$\mathrm{U}(1)_{V,\gamma_{45}}: \quad \psi \to \mathrm{e}^{\mathrm{i}\delta\gamma_{45}}\psi, \quad \bar{\psi} \to \bar{\psi}\,\mathrm{e}^{-\mathrm{i}\delta\gamma_{45}}, \tag{B.14}$$

and the axial transformation

$$\mathrm{U}(1)_{A,\gamma_4}: \quad \psi \to \mathrm{e}^{\mathrm{i}\eta\gamma_4}\psi, \quad \bar{\psi} \to \bar{\psi}\,\mathrm{e}^{\mathrm{i}\eta\gamma_4}. \tag{B.15}$$

We, however, do not consider odd integer number of space-time dimensions and thus do not need to consider these transformations further.

C Formulas for the (3 + 1)-Dimensional Nambu-Jona-Lasinio Model

In this appendix, we present the formulas that the results in Chapter 6 are obtained with. We mainly present the final results and consequently this Appendix serves more as a collection of formulas than a documentation of their derivation. We do not present the expressions for parameter limits that are trivial to obtain from preceding formulas.

C.1 General Expressions and Preceding Remarks

In this section, we give some expressions that occur frequently in this Appendix so that we do not have to introduce them at the corresponding positions. We also introduce regularization scheme specific expressions, which are then used in the corresponding formulas even though we do not necessarily mark this.

Energies

We frequently use two expressions for the energies of the loop fermions

$$E = \sqrt{\mathbf{p}^2 + \bar{\sigma}^2}, \quad E_{\mathbf{p}+\mathbf{q}} = \sqrt{(\mathbf{p}+\mathbf{q})^2 + \bar{\sigma}^2}. \tag{C.1}$$

The version for the additional particles in the PV scheme are denoted by

$$E_k = \sqrt{\mathbf{p}^2 + M_k^2}, \quad E_{\mathbf{p}+\mathbf{q},k} = \sqrt{(\mathbf{p}+\mathbf{q})^2 + M_k^2}, \tag{C.2}$$

see Section 2.3.1 for the PV notation. For the Lattice regularizations the energies take the form

$$E = \sqrt{\sum_{i=1}^{3} \mathcal{P}_X^2(\mathbf{p_i}) + \bar{\sigma}^2}, \quad E_{\mathbf{p}+\mathbf{q}} = \sqrt{\sum_{i=1}^{3} \mathcal{P}_X^2(\mathbf{p_i}+\mathbf{q_i}) + \bar{\sigma}^2}, \tag{C.3}$$

where $\mathcal{P}_X$ is the corresponding fermion dispersion relation of the used regularization scheme (see Section 6.1.2).

Chemical potentials

In general, we assume a positive chemical potential $\mu > 0$ to ease notation. However, the results do not depend on the sign of μ. In order to render the expressions insensitive to this, one can just exchange every $\mu \to |\mu|$.

The shifted chemical potential

$$\bar{\mu} = \sqrt{\mu^2 - \bar{\sigma}^2} \tag{C.4}$$

is frequently used and its PV variant is given by

$$\bar{\mu}_k = \sqrt{\mu^2 - M_k^2}. \tag{C.5}$$

C.2 Formulas for the Parameter Fitting

The central formulas for the parameter fitting are an expression for f_π^2/M_0^2 and the coupling G. These are calculated according to Section 3.2.2 and the final results are given in the following.

C.2.1 Pauli-Villars

$$\frac{f_\pi^2}{M_0^2} = -\frac{\overline{N}}{8\pi^2}\sum_{k=0}^{N_{\mathrm{PV}}} c_k \ln\left(\frac{M_{0,k}^2}{\Lambda_{\mathrm{PV}}^2}\right), \tag{C.6}$$

$$\frac{1}{G} = \frac{\overline{N}}{8\pi^2}\sum_{k=0}^{N_{\mathrm{PV}}} c_k M_{0,k}^2 \ln\left(\frac{M_{0,k}^2}{\Lambda_{\mathrm{PV}}^2}\right), \tag{C.7}$$

where $M_{0,k}^2 = M_0^2 + \alpha_k \Lambda_{\mathrm{PV}}^2$.

C.2.2 Spatial Momentum Cutoff

$$\frac{f_\pi^2}{M_0^2} = \frac{\overline{N}}{16\pi^2}\left[\operatorname{arsinh}\left(\frac{\Lambda_{\mathrm{SC}}}{|M_0|}\right) - \left(\frac{M_0^2}{\Lambda_{\mathrm{SC}}^2}+1\right)^{-\frac{1}{2}}\right], \tag{C.8}$$

$$\frac{1}{G} = \frac{\overline{N}}{4\pi^2}\left[\Lambda_{\mathrm{SC}}\sqrt{M_0^2+\Lambda_{\mathrm{SC}}^2} - \operatorname{arsinh}\left(\frac{\Lambda_{\mathrm{SC}}}{|M_0|}\right)M_0^2\right]. \tag{C.9}$$

C.2.3 Lattice Regularization

The formulas for the lattice regularizations only differ in their expression for the energy E (see Eq. (C.3)) and thus we do not differentiate here between SLAC and Hybrid discretization. The resulting formulas for the parameter fitting are

$$\frac{f_\pi^2}{M_0^2} = \frac{\overline{N}}{4\pi^4}\int_0^{\Lambda_{\mathrm{LFT}}}\mathrm{d}p_1\int_0^{\Lambda_{\mathrm{LFT}}}\mathrm{d}p_2\int_0^{\Lambda_{\mathrm{LFT}}}\mathrm{d}p_3\left[\frac{\arctan\left(\frac{\Lambda_{\mathrm{LFT}}}{E}\right)}{E^3} + \frac{\Lambda_{\mathrm{LFT}}}{E^2(E^2+\Lambda_{\mathrm{LFT}}^2)}\right] \tag{C.10}$$

and

$$\frac{1}{G} = \frac{2\overline{N}}{\pi^4}\int_0^{\Lambda_{\mathrm{LFT}}}\mathrm{d}p_1\int_0^{\Lambda_{\mathrm{LFT}}}\mathrm{d}p_2\int_0^{\Lambda_{\mathrm{LFT}}}\mathrm{d}p_3\,\frac{1}{E}\arctan\left(\frac{E}{\Lambda_{\mathrm{LFT}}}\right). \tag{C.11}$$

C.3 Formulas for the Homogeneous Effective Potential

The homogeneous effective potential has the general form

$$\overline{U}_{\text{eff}}\left(\bar{\sigma},T,\mu\right)=\frac{\bar{\sigma}^2}{4G}-\frac{\overline{N}}{2}l_0\left(\bar{\sigma},T,\mu\right), \tag{C.12}$$

where l_0 is the only regularization scheme dependent quantity (except for the coupling, which is determined by the corresponding formula in Appendix C.2). Therefore, we will only give the various expressions for l_0 in the following.

C.3.1 Pauli-Villars

With the PV regularization, one finds for arbitrary $\bar{\sigma},T,\mu$

$$\begin{aligned} l_0\left(\bar{\sigma},T,\mu\right)&=\frac{1}{2\pi^2}\int_0^\infty \mathrm{d}p\, p^2\sum_{k=0}^{N_{\text{PV}}}c_k\left[E_k+\tfrac{1}{\beta}\ln\left(1+\mathrm{e}^{-\beta(E_k+\mu)}\right)+\tfrac{1}{\beta}\ln\left(1+\mathrm{e}^{-\beta(E_k-\mu)}\right)\right]= \\ &=\frac{1}{32\pi^2}\left\{\sum_{k=0}^{N_{\text{PV}}}c_kM_k^4\ln\left(\frac{M_k^2}{\Lambda_{\text{PV}}^2}\right)+16\int_0^\infty \mathrm{d}p\,\frac{p^4}{3}\sum_{k=0}^{N_{\text{PV}}}c_k\frac{n\left(E_k\right)+\bar{n}\left(E_k\right)}{E_k}\right\}, \end{aligned} \tag{C.13}$$

where we performed a partial integration of the medium part.
The vacuum contribution to l_0 is

$$l_0\left(\bar{\sigma},T=0,\mu=0\right)=\frac{1}{32\pi^2}\sum_{k=0}^{N_{\text{PV}}}c_kM_k^4\ln\left(\frac{M_k^2}{\Lambda_{\text{PV}}^2}\right) \tag{C.14}$$

and in the symmetric case $\bar{\sigma}=0$ one finds

$$l_0\left(\bar{\sigma}=0,T=0,\mu=0\right)=\frac{\Lambda_{\text{PV}}^4}{32\pi^2}\sum_{k=1}^{N_{\text{PV}}}c_k\alpha_k^2\ln\left(\alpha_k\right). \tag{C.15}$$

For $T=0$ at arbitrary other parameters, one can give the closed form expression

$$l_0\left(\bar{\sigma},T=0,\mu\right)=\frac{1}{32\pi^2}\sum_{k=0}^{N_{\text{PV}}}c_k\left\{M_k^4\ln\left(\frac{M_k^2}{\Lambda_{\text{PV}}^2}\right)+\Theta\left(\bar{\mu}_k^2\right)\frac{2}{3}\left[3M_k^2\operatorname{arsinh}\left(\frac{\bar{\mu}_k}{|M_k|}\right)+\bar{\mu}_k\left(2\left|\mu\right|^3-5M_k^2\left|\mu\right|\right)\right]\right\}, \tag{C.16}$$

which reduces for $\bar{\sigma}=0$ to

$$\begin{aligned} l_0\left(\bar{\sigma}=0,T=0,\mu\right)=\frac{1}{32\pi^2}\Bigg\{&\Lambda_{\text{PV}}^4\sum_{k=1}^{N_{\text{PV}}}c_k\alpha_k^2\ln\left(\alpha_k\right)+\Theta\left(\mu^2\right)\frac{4\mu^4}{3}+ \\ &+\sum_{k=1}^{N_{\text{PV}}}c_k\Theta\left(\bar{\mu}_k^2\right)\frac{2}{3}\left[3M_k^2\operatorname{arsinh}\left(\frac{\bar{\mu}_k}{|M_k|}\right)+\bar{\mu}_k\left(2\left|\mu\right|^3-5M_k^2\mu\right)\right]\Bigg\}. \end{aligned} \tag{C.17}$$

C.3.2 Spatial Momentum Cutoff

With the SC regularization, one finds for arbitrary $\bar{\sigma}, T, \mu$

$$\begin{aligned} l_0(\bar{\sigma},T,\mu) &= \frac{1}{2\pi^2}\int_0^{\Lambda_{\mathrm{SC}}} \mathrm{d}p\, p^2 \left[E + \tfrac{1}{\beta}\ln\left(1+\mathrm{e}^{-\beta(E+\mu)}\right) + \tfrac{1}{\beta}\ln\left(1+\mathrm{e}^{-\beta(E-\mu)}\right)\right] = \\ &= \frac{1}{16\pi^2}\Bigg\{\Lambda_{\mathrm{SC}}\sqrt{\Lambda_{\mathrm{SC}}^2+\bar{\sigma}^2}\left(2\Lambda_{\mathrm{SC}}^2+\bar{\sigma}^2\right) - \bar{\sigma}^4 \operatorname{arsinh}\left(\frac{\Lambda_{\mathrm{SC}}}{|\bar{\sigma}|}\right) + \\ &\qquad + 8\int_0^{\Lambda_{\mathrm{SC}}} \mathrm{d}p\, p^2 \left[\tfrac{1}{\beta}\ln\left(1+\mathrm{e}^{-\beta(E+\mu)}\right) + \tfrac{1}{\beta}\ln\left(1+\mathrm{e}^{-\beta(E-\mu)}\right)\right]\Bigg\}. \end{aligned} \tag{C.18}$$

The vacuum contribution to l_0 is

$$l_0(\bar{\sigma},T=0,\mu=0) = \frac{1}{16\pi^2}\left[\Lambda_{\mathrm{SC}}\sqrt{\Lambda_{\mathrm{SC}}^2+\bar{\sigma}^2}\left(2\Lambda_{\mathrm{SC}}^2+\bar{\sigma}^2\right) - \bar{\sigma}^4\operatorname{arsinh}\left(\frac{\Lambda_{\mathrm{SC}}}{|\bar{\sigma}|}\right)\right] \tag{C.19}$$

and in the symmetric case $\bar{\sigma}=0$ one finds

$$l_0(\bar{\sigma}=0,T=0,\mu=0) = \frac{\Lambda_{\mathrm{SC}}^4}{8\pi^2}. \tag{C.20}$$

For $T=0$ at arbitrary other parameters, one can give the closed form expression

$$\begin{aligned} & l_0(\bar{\sigma},T=0,\mu) = \\ &= l_0(\bar{\sigma},T=0,\mu=0) - \frac{\Theta(\bar{\mu}^2)}{16\pi^2}\int_0^{P=\min(\Lambda_{\mathrm{SC}},\bar{\mu})} \mathrm{d}p\, p^2\left(E-|\mu|\right) = \\ &= l_0(\bar{\sigma},T=0,\mu=0) - \frac{\Theta(\bar{\mu}^2)}{16\pi^2}\left[P\sqrt{P^2+\bar{\sigma}^2}\left(2P^2+\bar{\sigma}^2\right) - \bar{\sigma}^4\operatorname{arsinh}\left(\frac{P}{|\bar{\sigma}|}\right) - \frac{|\mu|P^3}{3}\right] = \\ &= \frac{1}{16\pi^2}\begin{cases} \Lambda_{\mathrm{SC}}\sqrt{\Lambda_{\mathrm{SC}}^2+\bar{\sigma}^2}\left(2\Lambda_{\mathrm{SC}}^2+\bar{\sigma}^2\right) - \bar{\sigma}^4\operatorname{arsinh}\left(\frac{\Lambda_{\mathrm{SC}}}{|\bar{\sigma}|}\right) & \text{if } \bar{\mu}=0, \\ \Lambda_{\mathrm{SC}}\sqrt{\Lambda_{\mathrm{SC}}^2+\bar{\sigma}^2}\left(2\Lambda_{\mathrm{SC}}^2+\bar{\sigma}^2\right) - \bar{\sigma}^4\operatorname{arsinh}\left(\frac{\Lambda_{\mathrm{SC}}}{|\bar{\sigma}|}\right) & \\ -\bar{\mu}|\mu|^3 + \bar{\sigma}^4\operatorname{arsinh}\left(\frac{\bar{\mu}}{|\bar{\sigma}|}\right) + \frac{2}{3}|\mu|\bar{\mu}^3 & \text{if } 0<\bar{\mu}^2<\Lambda_{\mathrm{SC}}^2, \\ \frac{|\mu|\Lambda_{\mathrm{SC}}^3}{3} & \text{if } \bar{\mu}^2>\Lambda_{\mathrm{SC}}^2. \end{cases} \end{aligned} \tag{C.21}$$

which reduces for $\bar{\sigma} = 0$ to

$$\begin{aligned} l_0\left(\bar{\sigma}=0,T=0,\mu\right) &= \frac{\Lambda_{\mathrm{SC}}^4}{8\pi^2} - \frac{\Theta\left(\mu^2\right)}{16\pi^2} \int_0^{P=\min\left(\Lambda_{\mathrm{SC}},|\mu|\right)} \mathrm{d}p\, p^2\left(p-|\mu|\right) = \\ &= \frac{1}{8\pi^2}\left\{\Lambda_{\mathrm{SC}}^4 - \Theta\left(\mu^2\right)\left[P^4 - \frac{4}{3}|\mu| P^3\right]\right\} = \\ &= \frac{1}{8\pi^2}\begin{cases} \Lambda_{\mathrm{SC}}^4 & \text{if } \mu = 0, \\ \Lambda_{\mathrm{SC}}^4 + \frac{1}{3}\mu^4 & 0 < \mu^2 \leq \Lambda_{\mathrm{SC}}^2, \\ \frac{4}{3}|\mu|\Lambda_{\mathrm{SC}}^3 & \mu^2 > \Lambda_{\mathrm{SC}}^2. \end{cases} \end{aligned} \tag{C.22}$$

C.3.3 Lattice Regularization

The formulas for the lattice regularizations only differ in their expression for the energy E (see Eq. (C.3)) and thus we do not differentiate here between SLAC and Hybrid discretization. The resulting expressions for l_0 at $T = 0$ is

$$\begin{aligned} l_0\left(\bar{\sigma},T=0,\mu\right) = \frac{8}{(2\pi)^4} \int_0^{\Lambda_{\mathrm{LFT}}} \mathrm{d}p_1 \int_0^{\Lambda_{\mathrm{LFT}}} \mathrm{d}p_2 \int_0^{\Lambda_{\mathrm{LFT}}} \mathrm{d}p_3 \Big[&-4\Lambda_{\mathrm{LFT}} - 2|\mu| \operatorname{arctan2}\left(2|\mu|\Lambda_{\mathrm{LFT}}, E^2-\mu^2+\Lambda_{\mathrm{LFT}}^2\right) + \\ &+ 2E \operatorname{arctan2}\left(2E\Lambda_{\mathrm{LFT}}, E^2-\mu^2-\Lambda_{\mathrm{LFT}}^2\right) + \Lambda_{\mathrm{LFT}} \ln\left(4\mu^2\Lambda_{\mathrm{LFT}}^2 + \left(E^2-\mu^2+\Lambda_{\mathrm{LFT}}^2\right)^2\right) + \\ &- \Theta(\mu^2-E^2) 2\pi(E-|\mu|)\Big], \end{aligned} \tag{C.23}$$

where

$$\operatorname{arctan2}(y,x) = \begin{cases} \arctan\left(\frac{y}{x}\right) & \text{if } x > 0, \\ \arctan\left(\frac{y}{x}\right) + \pi & \text{if } x < 0 \text{ and } y \geq 0, \\ \arctan\left(\frac{y}{x}\right) - \pi & \text{if } x < 0 \text{ and } y < 0, \\ +\frac{\pi}{2} & \text{if } x = 0 \text{ and } y > 0, \\ -\frac{\pi}{2} & \text{if } x = 0 \text{ and } y < 0, \\ \text{undefined} & \text{if } x = 0 \text{ and } y = 0. \end{cases} \tag{C.24}$$

C.4 Formulas for the Stability Analysis

For the continuum regularizations SC and PV, one can split the two-point function $\Gamma^{(2)}$ into a q-independent part l_1 and a q-dependent part L_2 to obtain the form (compare to Eq. (4.19))

$$\Gamma_{\phi_i}^{(2)}\left(\mathbf{q},\bar{\sigma},\mu,T\right) = \frac{1}{2G} - \overline{N} l_1\left(\bar{\sigma},\mu,T\right) + \overline{N} L_{2,\phi_i}\left(\mathbf{q},\bar{\sigma},\mu,T\right) \tag{C.25}$$

with

$$l_1\left(\bar{\sigma},\mu,T\right) = \int \frac{\mathrm{d}^3p}{(2\pi)^3} \frac{1}{\beta} \sum_{n=-\infty}^{\infty} \frac{1}{\tilde{\nu}_n^2 + E^2} = \int \frac{\mathrm{d}^3p}{(2\pi)^3} \frac{1 - n\left(E\right) - \bar{n}\left(E\right)}{2E} \tag{C.26}$$

and

$$L_{2,\phi_i}\left(\mathbf{q},\bar{\sigma},\mu,T\right) = \int \frac{\mathrm{d}^3p}{(2\pi)^3}\,\frac{1}{\beta}\sum_{n=-\infty}^{\infty}\frac{\mathbf{p}\cdot\mathbf{q}+\mathbf{q}^2+2\delta_{i,0}\bar{\sigma}^2}{\left(\tilde{\nu}_n^2+E_{\mathbf{p}+\mathbf{q}}^2\right)\left(\tilde{\nu}_n^2+E_{\mathbf{p}}^2\right)} = \tag{C.27}$$

$$= \int \frac{\mathrm{d}^3p}{(2\pi)^3}\,\frac{\mathbf{p}\cdot\mathbf{q}+\mathbf{q}^2+2\delta_{i,0}\bar{\sigma}^2}{2\mathbf{p}\cdot\mathbf{q}+q^2}\times\left[\frac{1-n\left(E\right)-\bar{n}\left(E\right)}{2E}-\frac{1-n\left(E_{\mathbf{p}+\mathbf{q}}\right)-\bar{n}\left(E_{\mathbf{p}+\mathbf{q}}\right)}{2E_{\mathbf{p}+\mathbf{q}}}\right]. \tag{C.28}$$

We orient the bosonic momentum as $\mathbf{q} = (0,0,q)$ with $q > 0$ without loss of generality as the considered regularization schemes preserved the full spatial rotation symmetry.

C.4.1 Pauli-Villars

The momentum independent integral l_1

One finds for l_1 for arbitrary $\bar{\sigma},T,\mu$ the expression

$$l_1\left(\bar{\sigma},\mu,T\right) = \frac{1}{4\pi^2}\sum_{k=0}^{N_{\mathrm{PV}}}c_k\left\{M_k^2\ln\left(\frac{M_k^2}{\Lambda_{\mathrm{PV}}^2}\right)-\int_0^{\infty}\mathrm{d}p\,p^2\,\frac{n\left(E_k\right)+\bar{n}\left(E_k\right)}{2E_k}\right\}. \tag{C.29}$$

The vacuum contribution to l_1 is

$$l_1\left(\bar{\sigma},\mu=0,T=0\right) = \frac{1}{4\pi^2}\sum_{k=0}^{N_{\mathrm{PV}}}c_kM_k^2\ln\left(\frac{M_k^2}{\Lambda_{\mathrm{PV}}^2}\right), \tag{C.30}$$

which reduces for $\bar{\sigma} = 0$ to

$$l_1\left(\bar{\sigma}=0,\mu=0,T=0\right) = \frac{\Lambda_{\mathrm{PV}}^2}{4\pi^2}\sum_{k=1}^{N_{\mathrm{PV}}}c_k\alpha_k\ln\left(\alpha_k\right). \tag{C.31}$$

For $T = 0$ at arbitrary other parameters, one can give the closed form expression

$$l_1\left(\bar{\sigma},\mu,T=0\right) = \frac{1}{4\pi^2}\sum_{k=0}^{N_{\mathrm{PV}}}c_k\left\{M_k^2\ln\left(\frac{M_k^2}{\Lambda_{\mathrm{PV}}^2}\right)-\frac{\Theta\left(\bar{\mu}_k^2\right)}{2}\left[\left|\mu\right|\bar{\mu}_k-M_k^2\,\mathrm{arsinh}\left(\frac{\bar{\mu}_k}{|M_k|}\right)\right]\right\} \tag{C.32}$$

and for additional $\bar{\sigma} = 0$

$$l_1\left(\bar{\sigma}=0,\mu,T=0\right) = \frac{1}{4\pi^2}\left\{\sum_{k=1}^{N_{\mathrm{PV}}}c_k\alpha_k\ln\left(\alpha_k\right)-\Theta\left(\mu^2\right)\frac{\mu^2}{2}-\sum_{k=1}^{N_{\mathrm{PV}}}c_k\frac{\Theta\left(\bar{\mu}_k^2\right)}{2}\left[\left|\mu\right|\bar{\mu}_k-M_k^2\,\mathrm{arsinh}\left(\frac{\bar{\mu}_k}{|M_k|}\right)\right]\right\}. \tag{C.33}$$

The Momentum Dependent Integral l_2

With the PV regularization, we can shift the integration variable $\mathbf{p}$ without changing the integral boundary (as the spatial momentum integration covers the whole $\mathbb{R}^3$). This allows us to obtain

$$L_{2,\phi_i}\left(\mathbf{q},\bar{\sigma},\mu,T\right)=\left(\mathbf{q}^2+\delta_{i,1}4\bar{\sigma}^2\right)\int\frac{\mathrm{d}^3p}{(2\pi)^3}\frac{1}{2\mathbf{p}\cdot\mathbf{q}-q^2}\frac{1-n\left(E\right)-\bar{n}\left(E\right)}{2E}.$$

Carrying out the angle integration and applying the regularization results in

$$\begin{aligned}L_{2,\phi_i}\left(q,\bar{\sigma},\mu,T\right)=-\frac{\left(q^2+\delta_{i,0}4\bar{\sigma}^2\right)}{(4\pi)^2}\sum_{k=0}^{N_{\mathrm{PV}}}c_k\Bigg\{\left[\frac{1}{2}\ln\left(\frac{M_k^2}{\Lambda_{\mathrm{PV}}^2}\right)+\sqrt{1+\frac{4M_k^2}{q^2}}\,\mathrm{arcoth}\left(\sqrt{1+\frac{4M_k^2}{q^2}}\right)\right]+\\-\int_0^\infty\mathrm{d}p\,\frac{p}{q}\,\frac{n\left(E_k\right)+\bar{n}\left(E_k\right)}{E_k}\ln\left|\frac{2p-q}{2p+q}\right|\Bigg\}.\end{aligned}\tag{C.34}$$

Taking the $T=0$ limit allows us to give a closed form expression

$$\begin{aligned}&L_{2,\phi_i}\left(q,\bar{\sigma},\mu,T=0\right)=\\&=-\frac{\left(q^2+\delta_{i,0}4\bar{\sigma}^2\right)}{(4\pi)^2}\sum_{k=0}^{N_{\mathrm{PV}}}c_k\Bigg\{\left[\frac{1}{2}\ln\left(\frac{M_k^2}{\Lambda_{\mathrm{PV}}^2}\right)+\sqrt{1+\frac{4M_k^2}{q^2}}\,\mathrm{arcoth}\left(\sqrt{1+\frac{4M_k^2}{q^2}}\right)\right]+\\&-\Theta\left(\bar{\mu}_k^2\right)\left[-\operatorname{artanh}\left(\frac{\bar{\mu}_k}{|\mu|}\right)+\frac{1}{2}\sqrt{1+\frac{4M_k^2}{q^2}}\ln\left|\frac{q|\mu|+\bar{\mu}_k\sqrt{q^2+4M_k^2}}{q|\mu|-\bar{\mu}_k\sqrt{q^2+4M_k^2}}\right|-\frac{|\mu|}{q}\ln\left|\frac{2\bar{\mu}_k+q}{2\bar{\mu}_k-q}\right|\right]\Bigg\}.\end{aligned}\tag{C.35}$$

By setting additional $\bar{\sigma}=0$ we obtain

$$\begin{aligned}&L_{2,\phi_i}\left(q,\bar{\sigma}=0,\mu,T=0\right)=\\&=-\frac{q^2}{(4\pi)^2}\Bigg\{\ln\left|\frac{q}{\Lambda_{\mathrm{PV}}}\right|+\sum_{k=1}^{N_{\mathrm{PV}}}\left[\frac{1}{2}\ln\left(\frac{M_k^2}{\Lambda_{\mathrm{PV}}^2}\right)+\sqrt{1+\frac{4M_k^2}{q^2}}\,\mathrm{arcoth}\left(\sqrt{1+\frac{4M_k^2}{q^2}}\right)\right]+\\&-\frac{1}{2q}\left[\left(2\left|\mu\right|+q\right)\ln\left|\frac{2\left|\mu\right|+q}{\Lambda_{\mathrm{PV}}}\right|+\left(2\left|\mu\right|-q\right)\ln\left|\frac{2\left|\mu\right|-q}{\Lambda_{\mathrm{PV}}}\right|\right]+\\&-\sum_{k=1}^{N_{\mathrm{PV}}}\Theta\left(\bar{\mu}_k^2\right)\left[-\operatorname{artanh}\left(\frac{\bar{\mu}_k}{|\mu|}\right)+\frac{1}{2}\sqrt{1+\frac{4M_k^2}{q^2}}\ln\left|\frac{|q\mu|+\bar{\mu}_k\sqrt{q^2+4M_k^2}}{|q\mu|-\bar{\mu}_k\sqrt{q^2+4M_k^2}}\right|-\frac{|\mu|}{q}\ln\left|\frac{2\bar{\mu}_k+q}{2\bar{\mu}_k-q}\right|\right]\Bigg\}.\end{aligned}\tag{C.36}$$

One other hand, taking the $q\to 0$ limit in Eq. (C.34) results in

$$L_{2,\phi_i}\left(q=0,\bar{\sigma},\mu,T\right)=-\frac{\delta_{i,0}4\bar{\sigma}^2}{(4\pi)^2}\sum_{k=0}^{N_{\mathrm{PV}}}c_k\left\{\frac{1}{2}\ln\left(\frac{M_k^2}{\Lambda_{\mathrm{PV}}^2}\right)-\int_0^\infty\mathrm{d}p\,\frac{n\left(E_k\right)+\bar{n}\left(E_k\right)}{E_k}\right\}.\tag{C.37}$$

This yields the closed form expression at $T = 0$

$$L_{2,\phi_i}\left(q=0,\bar{\sigma},\mu,T=0\right) = -\frac{\delta_{i,0}4\bar{\sigma}^2}{(4\pi)^2}\sum_{k=0}^{N_{\mathrm{PV}}} c_k \left\{\frac{1}{2}\ln\left(\frac{M_k^2}{\Lambda_{\mathrm{PV}}^2}\right) - \Theta\left(\bar{\mu}_k^2\right)\operatorname{arsinh}\left(\frac{\bar{\mu}_k}{|\bar{\sigma}|}\right)\right\}, \tag{C.38}$$

which reduces in the symmetric limit to

$$L_{2,\phi_i}\left(q=0,\bar{\sigma}=0,\mu,T\right) = 0. \tag{C.39}$$

C.4.2 Spatial Momentum Cutoff

The Momentum Independent Integral l_1

One finds for l_1 for arbitrary $\bar{\sigma},T,\mu$ the expression

$$l_1\left(\bar{\sigma},\mu,T\right) = \frac{1}{8\pi^2}\left\{\Lambda_{\mathrm{SC}}\sqrt{\bar{\sigma}^2+\Lambda_{\mathrm{SC}}^2} - \operatorname{arsinh}\left(\tfrac{\Lambda_{\mathrm{SC}}}{|\bar{\sigma}|}\right)\bar{\sigma}^2 - \int_0^{\Lambda_{\mathrm{SC}}} \mathrm{d}p\, p^2 \frac{n(E)+\bar{n}(E)}{E}\right\}. \tag{C.40}$$

The vacuum contribution to l_1 is

$$l_1\left(\bar{\sigma},\mu=0,T=0\right) = \frac{1}{8\pi^2}\left\{\Lambda_{\mathrm{SC}}\sqrt{\bar{\sigma}^2+\Lambda_{\mathrm{SC}}^2} - \operatorname{arsinh}\left(\tfrac{\Lambda_{\mathrm{SC}}}{|\bar{\sigma}|}\right)\bar{\sigma}^2\right\}, \tag{C.41}$$

which reduces for $\bar{\sigma} = 0$ to

$$l_1\left(\bar{\sigma}=0,\mu=0,T=0\right) = \frac{\Lambda_{\mathrm{SC}}^2}{8\pi^2}. \tag{C.42}$$

For $T = 0$ at arbitrary other parameters, one can give the closed form expression

$$\begin{aligned} l_1\left(\bar{\sigma},\mu,T=0\right) &= \frac{1}{8\pi^2}\left\{\Lambda_{\mathrm{SC}}\sqrt{\bar{\sigma}^2+\Lambda_{\mathrm{SC}}^2} - \operatorname{arsinh}\left(\tfrac{\Lambda_{\mathrm{SC}}}{|\bar{\sigma}|}\right)\bar{\sigma}^2 - \int_0^{\Lambda_{\mathrm{SC}}} \mathrm{d}p\, \frac{p^2}{E}\,\Theta\left(\mu^2-E^2\right)\right\} = \\ &= \tfrac{1}{8\pi^2}\Big\{\Lambda_{\mathrm{SC}}\sqrt{\bar{\sigma}^2+\Lambda_{\mathrm{SC}}^2} - \operatorname{arsinh}\left(\tfrac{\Lambda_{\mathrm{SC}}}{|\bar{\sigma}|}\right)\bar{\sigma}^2 + \\ &\qquad - \Theta\left(\bar{\mu}^2\right)\left[P\sqrt{\bar{\sigma}^2+P^2} - \operatorname{arsinh}\left(\tfrac{P}{|\bar{\sigma}|}\right)\bar{\sigma}^2\right]^{P=\min(\Lambda_{\mathrm{SC}},\bar{\mu})}\Big\} = \\ &= \frac{1}{8\pi^2}\begin{cases} \Lambda_{\mathrm{SC}}\sqrt{\bar{\sigma}^2+\Lambda_{\mathrm{SC}}^2} - \operatorname{arsinh}\left(\tfrac{\Lambda_{\mathrm{SC}}}{|\bar{\sigma}|}\right)\bar{\sigma}^2 & \text{if } \bar{\mu}^2 = 0, \\ \Lambda_{\mathrm{SC}}\sqrt{\bar{\sigma}^2+\Lambda_{\mathrm{SC}}^2} - \operatorname{arsinh}\left(\tfrac{\Lambda_{\mathrm{SC}}}{|\bar{\sigma}|}\right)\bar{\sigma}^2 - \bar{\mu}|\mu| + \operatorname{arsinh}\left(\tfrac{\bar{\mu}}{|\bar{\sigma}|}\right)\bar{\sigma}^2 & \text{if } 0 < \bar{\mu}^2 < \Lambda_{\mathrm{SC}}^2, \\ 0 & \text{if } \bar{\mu}^2 > \Lambda_{\mathrm{SC}}^2 \end{cases} \end{aligned} \tag{C.43}$$

and for additional $\bar{\sigma} = 0$

$$l_1\left(\bar{\sigma}=0,\mu,T=0\right) = \tfrac{1}{8\pi^2}\left\{\Lambda_{\mathrm{SC}}^2 - \Theta\left(\mu^2\right)\left[P^2\right]^{P=\min\left(\Lambda_{\mathrm{SC}},|\mu|\right)}\right\} = \tag{C.44}$$

$$= \frac{1}{8\pi^2}\begin{cases}\Lambda_{\mathrm{SC}}^2 & \text{if } \mu^2 = 0,\\ \Lambda_{\mathrm{SC}}^2 - \mu^2 & \text{if } 0 < \mu^2 < \Lambda_{\mathrm{SC}}^2,\\ 0 & \text{if } \mu^2 > \Lambda_{\mathrm{SC}}^2.\end{cases} \tag{C.45}$$

The Momentum Dependent Integral l_2

With the SC regularization, we cannot shift the integral variables without modifying the integral bounds. Thus, in Eq. (C.28) it is more sensible to directly calculate the expressions. We only present the $T = 0$ as we do not need the finite temperature expressions. First, we are performing the angle integration to obtain

$$\begin{aligned} L_{2,\phi_i}\left(q,\bar{\sigma},\mu,T=0\right) &= \frac{1}{(2\pi)^2}\int_0^{\Lambda_{\mathrm{SC}}} \mathrm{d}p\, p^2 \int_0^{\pi} \mathrm{d}\theta\, \sin\theta \frac{pq\cos\theta + q^2 + 2\delta_{i,0}\bar{\sigma}^2}{2pq\cos\theta + q^2} \times \\ &\times \left[\frac{1 - n\left(E\right) - \bar{n}\left(E\right)}{2E} - \frac{1 - n\left(E_{\mathbf{p+q}}\right) - \bar{n}\left(E_{\mathbf{p+q}}\right)}{2E_{\mathbf{p+q}}}\right] = \\ &= \frac{1}{8\pi^2}\int_0^{\Lambda_{\mathrm{SC}}} \mathrm{d}p\, p \left\{\frac{\Theta(E^2-\mu^2)}{E}\left[\frac{q^2 + \delta_{i,0}4\bar{\sigma}^2}{4q}\ln\left(\left|\frac{q+2p}{q-2p}\right|\right) + p\right] + \right. \\ &+ \Theta\left(E_{p+q}^2 - \mu^2\right)\left[\frac{-1}{2q}\begin{cases}\left(E_{p+q} - \mu\right) & \text{if } \mu^2 \geq E_{p-q}^2,\\ \left(E_{p+q} - E_{p-q}\right) & \text{otherwise .}\end{cases}\right. + \\ &\left.\left. + \frac{q^2 + \delta_{i,0}4\bar{\sigma}^2}{4qE}\begin{cases}\ln\left|\frac{\mu^2-E^2}{2pq+q^2}\frac{(E_{p+q}+E)^2}{(|\mu|+E)^2}\right| & \text{if } \mu^2 \geq E_{p-q}^2,\\ \ln\left|\frac{2p-q}{2p+q}\frac{(E_{p+q}+E)^2}{(E_{p-q}+E)^2}\right| & \text{otherwise .}\end{cases}\right]\right\}. \end{aligned} \tag{C.46}$$

The next step is to perform the momentum integration. The Heaviside functions Θ give a lower bound to the integral. These are $P_{\mathrm{L},0} = \max(0, \mathrm{Re}(\bar{\mu}))$ for the part with $\Theta(E^2 - \mu^2)$ and $P_{\mathrm{L,q}} = \max(0, \mathrm{Re}(\bar{\mu}) - q)$ for

the part with $\Theta\left(E_{p+q}^2-\mu^2\right)$. We then find the final form

$$
\begin{aligned}
&L_{2,\phi_i}\left(q,\bar{\sigma},\mu,T=0\right)= \\
&=\tfrac{1}{8\pi^2}\Bigg[\left(q^2+\delta_{i,0}4\bar{\sigma}^2\right)\left(\frac{E}{4q}\ln\left|\tfrac{2p+q}{2p-q}\right|+\tfrac{1}{8}\ln\left|\tfrac{p+E}{p-E}\right|-\frac{\sqrt{4\bar{\sigma}^2+q^2}}{8q}\ln\left|\frac{qE+p\sqrt{4\bar{\sigma}^2+q^2}}{qE-p\sqrt{4\bar{\sigma}^2+q^2}}\right|\right)+ \\
&\quad-\tfrac{1}{2}\left(pE-\bar{\sigma}^2\ln|\bar{\sigma}p+\bar{\sigma}E|\right)\Bigg]_{p=P_{\mathrm{L},0}}^{p=\Lambda_{\mathrm{SC}}}+ \\
&+\tfrac{1}{8\pi^2}\Bigg[\frac{1}{2q}\begin{cases}-\frac{q\bar{\sigma}^2\,\mathrm{arsinh}\left(\frac{p+q}{|\bar{\sigma}|}\right)+q(p+q)E_{p+q}}{2}-\frac{\mu p^2}{2}+\frac{E_{p+q}^3}{3} & \text{if } \mu^2\geq E_{p-q}^2,\\ -\frac{q\bar{\sigma}^2}{2}\left[\mathrm{arsinh}\left(\frac{p+q}{|\bar{\sigma}|}\right)+\mathrm{arsinh}\left(\frac{p-q}{|\bar{\sigma}|}\right)\right]+ & \\ +\frac{2p^2-q^2+2\bar{\sigma}^2}{6}\left(E_{p+q}-E_{p-q}\right)+\frac{qp}{6}\left(E_{p+q}+E_{p-q}\right) & \text{otherwise}\end{cases}+ \\
&+\frac{q^2+\delta_{i,0}4\bar{\sigma}^2}{4}\times \\
&\times\begin{cases}0 & \text{if } \mu^2\geq E_{p-q}^2,\\ \mathrm{artanh}\left(\frac{p}{E}\right)+\frac{E}{q}\ln\left|\frac{2p-q}{2p+q}\right|+\frac{\sqrt{q^2+4\bar{\sigma}^2}}{2q}\ln\left|\frac{qE+\sqrt{q^2+4\bar{\sigma}^2}p}{qE-\sqrt{q^2+4\bar{\sigma}^2}p}\right| & \text{otherwise}\end{cases}\Bigg]_{p=P_{\mathrm{L,q}}}^{p=\Lambda_{\mathrm{SC}}}+ \\
&+\tfrac{1}{8\pi^2}\int_{P_{\mathrm{L,q}}}^{\Lambda_{\mathrm{SC}}}\mathrm{d}p\,p\,\frac{q^2+\delta_{i,0}4\bar{\sigma}^2}{E4q}\begin{cases}\ln\left|\frac{\mu^2-E^2}{2pq+q^2}\,\frac{(E_{p+q}+E)^2}{(|\mu|+E)^2}\right| & \text{if } \mu^2\geq E_{p-q}^2,\\ \ln\left(\frac{(E_{p+q}+E)^2}{(E_{p-q}+E)^2}\right), & \text{otherwise}\end{cases}
\end{aligned}
\tag{C.47}
$$

where the solution to the integral in the last line cannot be given in a closed form and has to be obtained numerically.

When considering the symmetric limit $\bar{\sigma} = 0$, the expressions simplify considerably and we find

$$
\begin{aligned}
&L_{2,\phi_i}\left(q,\bar{\sigma}=0,\mu,T=0\right) = \qquad\qquad (C.48)\\
&= \frac{1}{8\pi^2}\left[\frac{q}{8}f(2p,q)+4p^2\right]_{p=|\mu|}^{p=\Lambda_{\mathrm{SC}}} + \\
&-\frac{1}{16\pi^2 q}\left[\begin{cases} \frac{2}{3}p^3 & \text{if } p \le q-|\mu| \\ \frac{p^3}{3}+\frac{p^2}{2}(|\mu|+q)-\frac{(|\mu|-q)^2(5|\mu|+q)}{6} & \text{if } q-|\mu|<p<q+|\mu| \\ p^2 q+3\mu^2 q-\frac{q^3}{3} & \text{if } p \ge q+|\mu| \end{cases}\right]_{p=\max(0,\mu-q)}^{p=\Lambda_{\mathrm{SC}}} + \\
&+\frac{q}{32\pi^2}\left[\begin{cases} \frac{1}{2}\left[f(2p,q)-4p\left(\ln q+1\right)\right] & \text{if } p \le q-|\mu|, \\ \frac{q\ln|2p+q|}{2}-f(p,|\mu|)+p\left(\ln\left(\frac{2p+q}{q}\right)-1\right)+ & \\ +\frac{1}{2}\left[f(2(q-|\mu|),q)-4(q-|\mu|)\left(\ln q+1\right)\right]+ & \\ -\frac{q\ln|3q-|\mu||}{2}+f(q-|\mu|,|\mu|)-(q-|\mu|)\left(\ln\left(\frac{3q-|\mu|}{q}\right)-1\right) & \text{if } q-|\mu|<p<q+|\mu|, \\ \frac{f(2p,q)}{2}-\frac{f(2(q+|\mu|),q)}{2} & \\ +\frac{1}{2}\left[f(2(q-|\mu|),q)-4(q-|\mu|)\left(\ln q+1\right)\right]+ & \\ +\frac{q\ln|3q+|\mu||}{2}-f(q+|\mu|,\mu)+(q+|\mu|)\left(\ln\left(\frac{3q+|\mu|}{q}\right)-1\right)+ & \\ -\frac{q\ln|3q-|\mu||}{2}+f(q-|\mu|,|\mu|)-(q-|\mu|)\left(\ln\left(\frac{3q-|\mu|}{q}\right)-1\right) & \text{if } p \ge q+|\mu| \end{cases}\right]_{p=\max(0,\mu-q)}^{p=\Lambda_{\mathrm{SC}}},
\end{aligned}
$$

where we introduced the auxiliary function

$$f(x,y) = (x+y)\ln|x+y| - (x-y)\ln|x-y|. \qquad (C.49)$$

C.4.3 Lattice Regularization

As detailed in Section 6.1.5, one cannot separate the lattice two-point function into an l_1 and L_2. While we can integrate over the temporal momenta in Eqs. (6.18) and (6.19) at $T = 0$, we cannot carry out the spatial momentum integrals analytically, due to the lack of rotational symmetry and the lattice dispersion relations.

Performing the integration over the temporal momenta of propagator trace (6.17) yields

$$
\begin{aligned}
I\left(\mathbf{p},q,\bar{\sigma},\mu\right) &= \int_{-\Lambda_{\mathrm{LFT}}}^{\Lambda_{\mathrm{LFT}}} \frac{\mathrm{d}p_0}{2\pi}\, \mathrm{tr}\left[c_i S_X\left(p+(0,\mathbf{q})\right) c_i S_X\left(p\right)\right] = \\
&= \frac{\overline{N}}{\sum_{i=1}^{3}\left(\mathcal{P}_X^2\left(\mathbf{p_i}\right)-\mathcal{P}_X^2\left(\mathbf{p_i}+\mathbf{q_i}\right)\right)} \times \\
&\quad \times \left[\frac{E^2-\sum_{i=1}^{3}\mathcal{P}_X\left(\mathbf{p_i}+\mathbf{q_i}\right)\mathcal{P}_X\left(\mathbf{p_i}\right)+\bar{\sigma}^2}{E}\left[\arctan\left(\frac{\Lambda_{\mathrm{LFT}}}{E-|\mu|}\right)+\arctan\left(\frac{\Lambda_{\mathrm{LFT}}}{E+|\mu|}\right)\right]+\right. \\
&\quad \left.-\frac{E_{\mathbf{p}+\mathbf{q}}^2-\sum_{i=1}^{3}\mathcal{P}_X\left(\mathbf{p_i}+\mathbf{q_i}\right)\mathcal{P}_X\left(\mathbf{p_i}\right)+\bar{\sigma}^2}{E_{\mathbf{p}+\mathbf{q}}}\left[\arctan\left(\frac{\Lambda_{\mathrm{LFT}}}{E_{\mathbf{p}+\mathbf{q}}-|\mu|}\right)+\arctan\left(\frac{\Lambda_{\mathrm{LFT}}}{E_{\mathbf{p}+\mathbf{q}}+|\mu|}\right)\right]\right],
\end{aligned}
\tag{C.50}
$$

where S_X,$\mathcal{P}_X$ are either the corresponding Hybrid (Eqs. (6.10) and (6.16)) or SLAC expressions (Eqs. (6.7) and (6.15)).

SLAC Fermions

$$
\Gamma^{(2)}\left(q,\bar{\sigma},\mu,T=0\right) = \frac{1}{2G} - \frac{1}{2\pi}\int_{-\Lambda_{\mathrm{LFT}}}^{\Lambda_{\mathrm{LFT}}}\frac{\mathrm{d}p_1}{2\pi}\int_{-\Lambda_{\mathrm{LFT}}}^{\Lambda_{\mathrm{LFT}}}\frac{\mathrm{d}p_2}{2\pi}\int_{-\Lambda_{\mathrm{LFT}}}^{\Lambda_{\mathrm{LFT}}}\frac{\mathrm{d}p_3}{2\pi}\, I\left(\mathbf{p},q,\bar{\sigma}^2,\mu\right) \tag{C.51}
$$

Hybrid Fermions

$$
\Gamma^{(2)}\left(q,\bar{\sigma},\mu,T=0\right) = \frac{1}{2G} - \tilde{W}_X\left(\mathbf{q}\right)\tilde{W}_X\left(-\mathbf{q}\right)\frac{1}{2\pi}\int_{-\Lambda_{\mathrm{LFT}}}^{\Lambda_{\mathrm{LFT}}}\frac{\mathrm{d}p_1}{2\pi}\int_{-\Lambda_{\mathrm{LFT}}}^{\Lambda_{\mathrm{LFT}}}\frac{\mathrm{d}p_2}{2\pi}\int_{-\Lambda_{\mathrm{LFT}}}^{\Lambda_{\mathrm{LFT}}}\frac{\mathrm{d}p_3}{2\pi}\, I\left(\mathbf{p},q,\bar{\sigma}^2,\mu\right) \tag{C.52}
$$

C.5 Formulas for the Wave-Function Renormalization

The calculation of the wave-function renormalization (4.20) involves taking the double derivative with respect to q of $\Gamma^{(2)}$ and evaluating it at vanishing momentum. Even though one can apply this derivative to the final form of $\Gamma^{(2)}$, it is considerably easier to apply it to Eq. (C.27), i.e., before the Matsubara summation and the momentum integration. The results for z with the PV and SC scheme are given in the following.

C.5.1 Pauli-Villars

The wave-function renormalization with the SC scheme for general parameters is given by

$$\begin{aligned} & z_{\phi_i}\left(\bar{\sigma},\mu,T\right) = \\ & = \frac{\bar{N}}{16\pi^2}\sum_{k=0}^{N_{\mathrm{PV}}} c_k \Bigg\{ -\frac{1}{3}\frac{\delta_{i,0}\bar{\sigma}^2}{M_k^2} - \frac{1}{2}\ln\left(\frac{M_k^2}{\Lambda_{\mathrm{PV}}^2}\right) - \int_0^\infty \mathrm{d}p\, \frac{n\left(E_k\right)+\bar{n}\left(E_k\right)}{E_k} + \\ & \qquad - \frac{\bar{\sigma}^2}{3}\int_0^\infty \mathrm{d}p\, \frac{1}{E_k^3}\left[-n\left(E_k\right)-\bar{n}\left(E_k\right)+\tfrac{E_k}{T}\left[n^2\left(E_k\right)+\bar{n}^2\left(E_k\right)-n\left(E_k\right)-\bar{n}\left(E_k\right)\right]\right] \Bigg\}, \end{aligned} \tag{C.53}$$

which reduces for $T \to 0$ to the closed form

$$\begin{aligned} & z_{\phi_i}\left(\bar{\sigma},\mu,T=0\right) = \\ & = \frac{\bar{N}}{16\pi^2}\sum_{k=0}^{N_{\mathrm{PV}}} c_k \Bigg\{ -\frac{1}{3}\frac{\delta_{i,0}\bar{\sigma}^2}{M_k^2} - \frac{1}{2}\ln\left(\frac{M_k^2}{\Lambda_{\mathrm{PV}}^2}\right) + \\ & \qquad - \int_0^\infty \mathrm{d}p\, \frac{\Theta\left(\mu^2-E_k^2\right)}{E_k} - \frac{\bar{\sigma}^2}{3}\int_0^\infty \mathrm{d}p\, \frac{1}{E_k^3}\left[\Theta\left(\mu^2-E_k^2\right)+\frac{E_k}{|\mu|}\delta\left(\tfrac{E_k}{\mu}-1\right)\right] \Bigg\} = \\ & = \frac{\bar{N}}{16\pi^2}\sum_{k=0}^{N_{\mathrm{PV}}} c_k \Bigg\{ -\frac{1}{3}\frac{\delta_{i,0}\bar{\sigma}^2}{M_k^2} - \frac{1}{2}\ln\left(\frac{M_k^2}{\Lambda_{\mathrm{PV}}^2}\right) - \frac{\Theta\left(\bar{\mu}_k^2\right)}{3}\left[3\,\mathrm{arsinh}\left(\frac{\bar{\mu}_k}{M_k}\right)+\frac{\bar{\sigma}^2}{M_k^2}\left|\frac{\bar{\mu}_k}{\mu}\right|+\frac{\bar{\sigma}^2}{\mu\bar{\mu}_k}\right] \Bigg\}. \end{aligned} \tag{C.54}$$

On the other hand, the symmetric case $\bar{\sigma} = 0$ yields

$$\begin{aligned} & z_{\phi_i}\left(\bar{\sigma}=0,\mu,T\right) = \\ & = \frac{\bar{N}}{16\pi^2}\Bigg\{ \int_0^\infty \mathrm{d}p\, \frac{1}{p}\left[1-n\left(p\right)-\bar{n}\left(p\right)+\tfrac{p}{T}\left(n^2\left(p\right)+\bar{n}^2\left(p\right)-n\left(p\right)-\bar{n}\left(p\right)\right)\right] + \\ & \qquad + \sum_{k=1}^{N_{\mathrm{PV}}} c_k \int_0^\infty \mathrm{d}p\, \frac{p^2}{E_k^3}\left[1-n\left(E_k\right)-\bar{n}\left(E_k\right)+\tfrac{E_k}{T}\left(n^2\left(E_k\right)+\bar{n}^2\left(E_k\right)-n\left(E_k\right)-\bar{n}\left(E_k\right)\right)\right] \Bigg\}, \end{aligned} \tag{C.55}$$

which reduces for $T = 0, \mu \neq 0$

$$\begin{aligned} & z_{\phi_i}\left(\bar{\sigma}=0,\mu\neq 0,T=0\right) = \\ & = \frac{\bar{N}}{16\pi^2}\Bigg\{ \tfrac{1}{2}\ln(4) - \frac{1}{3} - \frac{\delta_{i,0}}{3} - \frac{1}{2}\ln\left(\frac{\mu^2}{\Lambda_{\mathrm{PV}}^2}\right) + \\ & \qquad + \sum_{k=1}^{N_{\mathrm{PV}}} c_k \left[-\frac{1}{3}\frac{\delta_{i,0}\bar{\sigma}^2}{M_k^2} - \frac{1}{2}\ln\left(\frac{M_k^2}{\Lambda_{\mathrm{PV}}^2}\right) - \frac{\Theta\left(\bar{\mu}_k^2\right)}{3}\left[3\,\mathrm{arsinh}\left(\frac{\bar{\mu}_k}{M_k}\right)+\frac{\bar{\sigma}^2}{M_k^2}\left|\frac{\bar{\mu}_k}{\mu}\right|+\frac{\bar{\sigma}^2}{\mu\bar{\mu}_k}\right]\right] \Bigg\}. \end{aligned} \tag{C.56}$$

C.5.2 Spatial Momentum Cutoff

The wave-function renormalization with the PV scheme for general parameters is given by

$$
\begin{aligned}
&z_{\phi_i}\left(\bar{\sigma},\mu,T\right) = \qquad \text{(C.57)}\\
&= \frac{\bar{N}}{16\pi^2}\left\{ 2\int_0^{\Lambda_{\mathrm{SC}}} \mathrm{d}p\, p^2 \frac{1}{E^3}\Big[1 - n(E) - \bar{n}(E) + \tfrac{E}{T}\left(n^2(E) + \bar{n}^2(E) - n(E) - \bar{n}(E)\right)\Big] + \right.\\
&\quad - 3\int_0^{\Lambda_{\mathrm{SC}}} \mathrm{d}p\, \frac{\bar{\sigma}^2 p^2 + \frac{p^4}{3}}{E^5}\Big[1 - n(E) - \bar{n}(E) + \tfrac{E}{T}\left[n^2(E) + \bar{n}^2(E) - n(E) - \bar{n}(E)\right] + \\
&\qquad\qquad - \tfrac{E^2}{3T^2}\left[2n^3(E) + 2\bar{n}^3(E) - 3n^2(E) - 3\bar{n}^2(E) + n(E) + \bar{n}(E)\right]\Big] + \\
&\quad + \frac{2}{3}\int_0^{\Lambda_{\mathrm{SC}}} \mathrm{d}p\, \tfrac{5\bar{\sigma}^2 p^4}{E^7}\Big[1 - n(E) - \bar{n}(E) + \tfrac{E}{T}\left[n^2(E) + \bar{n}^2(E) - n(E) - \bar{n}(E)\right] + \\
&\qquad - \tfrac{2E^2}{15T^2}\left[2n^3(E) + 2\bar{n}^3(E) - 3n^2(E) - 3\bar{n}^2(E) + n(E) + \bar{n}(E)\right] + \\
&\qquad \left. + \tfrac{E^3}{15T^3}\left[6n^4(E) + 6\bar{n}^4(E) - 12n^3(E) - 12\bar{n}^3(E) + 7n^2(E) + 7\bar{n}^2(E) - n(E) - \bar{n}(E)\right]\Big]\right\}
\end{aligned}
$$

and the symmetric limit $\bar{\sigma} \to 0$ results in

$$
\begin{aligned}
&z_{\phi_i}\left(\bar{\sigma} = 0,\mu,T\right) = \\
&= \frac{\bar{N}}{16\pi^2}\left\{ \int_0^{\Lambda_{\mathrm{SC}}} \mathrm{d}p\, \frac{1}{p}\Big[1 - n(p) - \bar{n}(p) + + \tfrac{p}{T}\left[n^2(p) + \bar{n}^2(p) - n(p) - \bar{n}(p)\right]\Big] + \right.\\
&\quad \left. + \int_0^{\Lambda_{\mathrm{SC}}} \mathrm{d}p\, \tfrac{p}{3T^2}\left[2n^3(p) + 2\bar{n}^3(p) - 3n^2(p) - 3\bar{n}^2(p) + n(p) + \bar{n}(p)\right] \right\}. \qquad \text{(C.58)}
\end{aligned}
$$

D Calculations for the Gross-Neveu Model in Non-Integer Spatial Dimensions $1 \leq d < 3$

We outline the calculations of the renormalization and the stability analysis in the $(d+1)$-dimensional GN model. For the $T = 0$ results, we will present all non-trivial limits in $\bar{\sigma}, \mu, q$. For explicit expressions in integer dimension $d = 1$ we refer to Ref. [57] for the homogeneous effective potential and to Ref. [39] for the two-point function and the wave-function renormalization. For expressions in $d = 2$, we refer to Refs. [49, 51, 157].

D.1 Auxiliary Formulas

Throughout this Appendix, we encounter various integrals that can be evaluated in a closed form. We want to present them here, such that we can refer to them during the actual calculations to keep the derivation uninterrupted. Multiple of these formulas rely on the Gaussian hypergeometric function ${}_2F_1$ that we define via the integral representation

$$ {}_2F_1\left(\alpha,\beta;\gamma;z\right) = \frac{1}{B(\beta,\gamma-\beta)} \int_0^1 \mathrm{d}t\, t^{\beta-1}(1-t)^{\gamma-\beta-1}(1-tz)^{-\alpha} \tag{D.1} $$

with B being the Beta function. The central integral identities that we use are [158, 3.194 1.-3.]

$$ \int_0^u \frac{\mathrm{d}x\, x^{\mu-1}}{(1+\beta x)^\nu} = \frac{u^\mu}{\mu} {}_2F_1\left(\nu,\mu;1+\mu;-\beta u\right) \qquad \text{with} \quad |\arg(1+\beta u)| < \pi,\ \mathrm{Re}\,\mu > 0, \tag{D.2} $$

$$ \int_u^\infty \frac{\mathrm{d}x\, x^{\mu-1}}{(1+\beta x)^\nu} = \frac{u^{\mu-\nu}}{\beta^\nu(\nu-\mu)} {}_2F_1\left(\nu,\nu-\mu;\nu-\mu+1;-\frac{1}{\beta u}\right) \qquad \text{with} \quad \mathrm{Re}\,\nu > \mathrm{Re}\,\mu, \tag{D.3} $$

$$ \int_0^\infty \frac{\mathrm{d}x\, x^{\mu-1}}{(1+\beta x)^\nu} = \beta^{-\mu} B\left(\mu,\nu-\mu\right) \qquad \text{with} \quad \mathrm{Re}\,\nu > \mathrm{Re}\,\mu,\ |\arg\beta| < \pi. \tag{D.4} $$

Using Eqs. (D.2) to (D.4), we can solve some of these often encountered integrals that occur in the

medium parts such as

$$\int_0^\infty \mathrm{d}p\, \frac{p^{d-1}}{E^n}\Theta\left(\tfrac{p^2}{\bar{\mu}^2}-1\right) = \frac{1}{2|\bar{\sigma}|^n}\int_{R(\bar{\mu}^2)}^\infty \mathrm{d}x\, \frac{x^{\frac{d}{2}-1}}{\left(1+\frac{x}{\bar{\sigma}^2}\right)^{n/2}} = \\ = \begin{cases} \frac{|\bar{\sigma}|^{d-n}}{2} B\left(\frac{d}{2},\frac{n-d}{2}\right) & \text{if } \bar{\mu}^2 \leq 0 \\ \frac{1}{(n-d)}|\bar{\mu}|^{d-n}\, {}_2F_1\left(\frac{n}{2},\frac{n-d}{2};\frac{n-d}{2}+1;-\frac{\bar{\sigma}^2}{\bar{\mu}^2}\right) & \text{otherwise} \end{cases} \tag{D.5}$$

and the version with an inverted Θ-function

$$\int_0^\infty \mathrm{d}p\, \frac{p^{d-1}}{E^n}\Theta\left(1-\tfrac{p^2}{\bar{\mu}^2}\right) = \frac{1}{2|\bar{\sigma}|^n}\int_0^{R(\bar{\mu}^2)} \mathrm{d}x\, \frac{x^{\frac{d}{2}-1}}{\left(1+\frac{x}{\bar{\sigma}^2}\right)^{n/2}} = \\ = \begin{cases} 0 & \text{if } \bar{\mu}^2 \leq 0 \\ \frac{1}{d}\frac{|\bar{\mu}|^d}{|\bar{\sigma}|^n}\, {}_2F_1\left(\frac{n}{2},\frac{d}{2};\frac{d}{2}+1;-\frac{\bar{\mu}^2}{\bar{\sigma}^2}\right) & \text{otherwise} \end{cases} \tag{D.6}$$

with $E = \sqrt{p^2+\bar{\sigma}^2}$, the ramp function $R(x) = x\Theta(x)$ and $\bar{\mu}^2 = \mu^2 - \bar{\sigma}^2$.

Further integrals involving δ-distributions

$$\int_0^\infty \mathrm{d}p\, \frac{p^{d-1}}{E^n}\delta\left(\frac{E}{|\mu|}-1\right) = \int_{\left|\frac{\bar{\sigma}}{\mu}\right|}^\infty \mathrm{d}x\, \frac{\left(x^2\mu^2-\bar{\sigma}^2\right)^{\frac{d-2}{2}}}{|\mu|^{n-2}x^{n-1}}\delta(x-1) = \begin{cases} \frac{|\bar{\mu}|^{d-2}}{|\mu|^{n-2}} & \text{if } \bar{\mu}^2 \geq 0 \\ 0 & \text{otherwise} \end{cases} \tag{D.7}$$

and

$$\int_0^\infty \mathrm{d}p\, \frac{p^{d-1}}{E^n}\delta'\left(\frac{E}{|\mu|}-1\right) = \int_{\left|\frac{\bar{\sigma}}{\mu}\right|}^\infty \mathrm{d}x\, \frac{\left(x^2\mu^2-\bar{\sigma}^2\right)^{\frac{d-2}{2}}}{|\mu|^{n-2}x^{n-1}}\delta'(x-1) = \\ = \begin{cases} -\frac{|\bar{\mu}|^{d-4}}{|\mu|^{n-2}}\left(\mu^2(d-2)-\bar{\mu}^2(n-1)\right) & \text{if } \bar{\mu}^2 \geq 0 \\ 0 & \text{otherwise} \end{cases} \tag{D.8}$$

are straightforward to evaluate.

D.2 Derivation of the Renormalized, Homogeneous Effective Potential

In this section, we outline the steps to obtain the renormalized, homogeneous effective potential $\overline{U}_{\text{eff, ren}}$ for spatial dimensions $1 \leq d < 3$ as given by Eq. (3.10). Moreover, we present several limiting cases of this general result.

The generic form of the homogeneous effective potential is

$$\overline{U}_{\text{eff}}(\bar{\sigma},T,\mu,d) = \frac{\bar{\sigma}^2}{4G} - \frac{1}{\beta V}\ln\mathrm{Det}\,\beta\overline{\mathrm{Q}}, \tag{D.9}$$

where $\bar{\mathrm{Q}}$ is the Dirac operator for a homogeneous field $\bar{\sigma}$.

The first step is to provide an expression for the $\frac{1}{\beta V}\ln\mathrm{Det}\,\beta\bar{\mathrm{Q}}$ term in the effective potential. The eigenvalues of $\bar{\mathrm{Q}}$ are identical to the ones of the Dirac operator of free fermions with mass $m=\bar{\sigma}$ allowing us to easily express the term in question by a momentum integration as (see, e.g., Ref. [58, Appendix A and B] for a step-by-step derivation in the context of the $(1+1)$-dimensional GN model)

$$\frac{1}{\beta V}\ln\mathrm{Det}\,\beta\bar{\mathrm{Q}} = \frac{N_\gamma}{2}\int\frac{\mathrm{d}^d p}{(2\pi)^d}\frac{1}{\beta}\sum_{n=-\infty}^{\infty}\ln\left[\beta\left((\nu_n-\mathrm{i}\mu)^2+E^2\right)\right] \equiv \frac{N_\gamma}{2}l_0, \tag{D.10}$$

with the energy $E^2=\mathbf{p}^2+\bar{\sigma}^2$ and the fermionic Matsubara frequencies $\nu_n=(2n+1)\pi/\beta$. Performing the Matsubara summation and carrying out the angle integration of the momentum integral yields

$$\begin{aligned} l_0 &= \int\frac{\mathrm{d}^d p}{(2\pi)^d}\left[E+\tfrac{1}{\beta}\ln\left(1+\exp\left(-\beta(E+\mu)\right)\right)+\tfrac{1}{\beta}\ln\left(1+\exp\left(-\beta(E-\mu)\right)\right)\right] = \\ &= \frac{S_d}{(2\pi)^d}\int_0^\infty \mathrm{d}p\,p^{d-1}\left[E+\tfrac{1}{\beta}\ln\left(1+\exp\left(-\beta(E+\mu)\right)\right)+\tfrac{1}{\beta}\ln\left(1+\exp\left(-\beta(E-\mu)\right)\right)\right], \end{aligned} \tag{D.11}$$

where $S_d=2\pi^{d/2}/\Gamma(d/2)$. The vacuum part of this integral is clearly UV-divergent for any number of spatial dimensions $d>0$. To extract and handle this divergence, we apply a SC scheme (see Section 2.3.1) and carry out the integration of the vacuum part using Eq. (D.2) to obtain

$$\begin{aligned} l_{0,\Lambda_{\mathrm{SC}}}\left(\mu=0,T=0\right) &= \frac{S_d}{(2\pi)^d}\int_0^{\Lambda_{\mathrm{SC}}}\mathrm{d}p\,p^{d-1}E = \frac{S_d}{(2\pi)^d}\frac{\Lambda_{\mathrm{SC}}^d}{d}|\bar{\sigma}|_2F_1\left(-\tfrac{1}{2},\tfrac{d}{2};\tfrac{d+2}{2};-\left(\tfrac{\Lambda_{\mathrm{SC}}}{\bar{\sigma}}\right)^2\right) = \\ &= \frac{S_d}{(2\pi)^d}\frac{1}{2}\left[-\frac{|\bar{\sigma}|^{d+1}\Gamma\left(-\frac{d}{2}-\frac{1}{2}\right)\Gamma\left(\frac{d}{2}+1\right)}{d\sqrt{\pi}}+\Lambda_{\mathrm{SC}}^d\left(\frac{2\Lambda_{\mathrm{SC}}}{d+1}+\frac{\bar{\sigma}^2}{(d-1)\Lambda_{\mathrm{SC}}}+\frac{\bar{\sigma}^4}{4(3-d)\Lambda_{\mathrm{SC}}^3}+\mathcal{O}\left(\Lambda_{\mathrm{SC}}^{-5}\right)\right)\right], \end{aligned} \tag{D.12}$$

where we expanded for $|\Lambda_{\mathrm{SC}}/\bar{\sigma}|\gg 1$ in the last step.

As stated in Section 3.1.2, we renormalize the theory by requiring that $\bar{\sigma}$ assumes a non-zero value $\bar{\Sigma}_0$ in vacuum, i.e., $\langle\sigma\rangle_{T=\mu=0}=\bar{\Sigma}_0$. This condition is expressed via the gap-equation

$$\left.\frac{\mathrm{d}\bar{U}_{\mathrm{eff}}}{\mathrm{d}\bar{\sigma}}\right|_{T=\mu=0,\bar{\sigma}=\bar{\Sigma}_0} = \left.\left[\frac{\bar{\sigma}}{2G}-\bar{\sigma}N_\gamma l_1\left(\bar{\sigma},\mu,T,d\right)\right]\right|_{T=\mu=0,\bar{\sigma}=\bar{\Sigma}_0} \overset{!}{=} 0, \tag{D.13}$$

where

$$l_1\left(\bar{\sigma},\mu,T,d\right) = \int\frac{\mathrm{d}^d p}{(2\pi)^d}\frac{1}{\beta}\sum_{n=-\infty}^{\infty}\frac{1}{(\nu_n-\mathrm{i}\mu)^2+E^2} = \frac{S_d}{(2\pi)^d}\int_0^\infty\mathrm{d}p\,p^{d-1}\frac{1-n\left(E\right)-\bar{n}\left(E\right)}{2E}, \tag{D.14}$$

with the Fermi-Dirac distribution

$$n\left(E\right)=\frac{1}{\exp\left(\beta(x+\mu)\right)+1}, \quad \bar{n}\left(E\right)=\frac{1}{\exp\left(\beta(x-\mu)\right)+1}. \tag{D.15}$$

Taking the zero temperature limit of Eq. (D.14) yields

$$l_1(\bar{\sigma},\mu,T=0,d) = \int \frac{\mathrm{d}^d p}{(2\pi)^d} \frac{1}{\beta} \sum_{n=-\infty}^{\infty} \frac{1}{(\nu_n - \mathrm{i}\mu)^2 + E^2} = \frac{S_d}{(2\pi)^d} \int_0^\infty \mathrm{d}p\, p^{d-2} \frac{1-\Theta\left(1-\frac{E^2}{\mu^2}\right)}{2E}. \tag{D.16}$$

The vacuum part of the unregularized l_1 is divergent for $d \geq 1$. After regularization we can perform the integral with the identity Eq. (D.2) to obtain

$$\begin{aligned}
&l_{1,\Lambda_{\mathrm{SC}}}(\bar{\sigma},\mu=0,T=0,d) = \\
&= \tfrac{S_d}{(2\pi)^d} \int_0^{\Lambda_{\mathrm{SC}}} \mathrm{d}p\, \frac{p^{d-1}}{2E} = \\
&= \frac{S_d}{(2\pi)^d} \frac{\Lambda_{\mathrm{SC}}^d}{2d|\bar{\sigma}|} {}_2F_1\left(\tfrac{1}{2},\tfrac{d}{2};\tfrac{d+2}{2};-\tfrac{\Lambda_{\mathrm{SC}}^2}{\bar{\sigma}^2}\right) = \\
&= \frac{S_d}{(2\pi)^d} \frac{1}{2} \left[\frac{\bar{\sigma}^{d-1}}{d\sqrt{\pi}} \Gamma\left(\tfrac{d}{2}+1\right) \Gamma\left(\tfrac{1}{2}-\tfrac{d}{2}\right) + \Lambda_{\mathrm{SC}}^d \left(\frac{1}{(d-1)\Lambda_{\mathrm{SC}}} + \frac{\bar{\sigma}^2}{2(3-d)\Lambda_{\mathrm{SC}}^3} + \mathcal{O}\left(\Lambda_{\mathrm{SC}}^{-5}\right) \right) \right],
\end{aligned} \tag{D.17}$$

where we expanded for $|\Lambda_{\mathrm{SC}}/\bar{\sigma}| \gg 1$ in the last step. By inserting this result into the gap-equation (D.13), we obtain for the coupling G

$$\frac{1}{G} = N_\gamma \frac{S_d}{(2\pi)^d} \left[\frac{\bar{\Sigma}_0^{d-1} \Gamma\left(\frac{d}{2}+1\right) \Gamma\left(\frac{1}{2}-\frac{d}{2}\right)}{d\sqrt{\pi}} + \Lambda_{\mathrm{SC}}^d \left(\frac{1}{(d-1)\Lambda_{\mathrm{SC}}} + \frac{\bar{\Sigma}_0^2}{2(3-d)\Lambda_{\mathrm{SC}}^3} + \mathcal{O}\left(\Lambda_{\mathrm{SC}}^{-5}\right) \right) \right]. \tag{D.18}$$

We insert this expression and the regularized $l_{0,\Lambda_{\mathrm{SC}}}$ into Eq. (D.9), and send $\Lambda_{\mathrm{SC}} \to \infty$, to obtain the renormalized, homogeneous effective potential

$$\begin{aligned}
\bar{U}_{\text{eff, ren}}(\bar{\sigma},T,\mu,d) = &\frac{N_\gamma}{2^{d-1}\pi^{\frac{d}{2}}} \frac{(d+1)\Gamma\left(-\frac{d+1}{2}\right)}{8\sqrt{\pi}} \left(-\frac{\bar{\Sigma}_0^{d-1}\bar{\sigma}^2}{2} + \frac{|\bar{\sigma}|^{d+1}}{d+1} \right) + \\
&+ \frac{N_\gamma}{2} \frac{S_d}{(2\pi)^d} \int_0^\infty \mathrm{d}p\, p^{d-1} \left[\tfrac{1}{\beta} \ln\left(1+\mathrm{e}^{-\beta(E+\mu)}\right) + \tfrac{1}{\beta} \ln\left(1+\mathrm{e}^{-\beta(E-\mu)}\right) \right],
\end{aligned} \tag{D.19}$$

where we neglected a divergent, thermodynamically irrelevant $\bar{\sigma}$-independent term. The medium part of this expression can be further evaluated for certain combinations of $\mu,\bar{\sigma},d$. However, within the present context we are interested in the $T = 0$ results, which allow complete closed form expressions.

Thus, we take the $T \to 0$ limit of Eq. (D.19) to obtain

$$\begin{aligned}
&\overline{U}_{\text{eff, ren}}(\bar{\sigma}, T=0, \mu, d) = \qquad\qquad (D.20)\\
&= \frac{N_\gamma}{2^{d-1}\pi^{\frac{d}{2}}} \frac{(d+1)}{8\sqrt{\pi}} \Gamma\left(-\tfrac{d+1}{2}\right)\left(-\frac{\bar{\Sigma}_0^{d-1}\bar{\sigma}^2}{2} + \frac{|\bar{\sigma}|^{d+1}}{d+1}\right) + \frac{N_\gamma}{2}\frac{S_d}{(2\pi)^d}\int_0^\infty \mathrm{d}p\, p^{d-1}\Theta\left(\mu^2 - E^2\right)\left(E - |\mu|\right) = \\
&= \frac{N_\gamma}{2^d\pi^{\frac{d}{2}}}\left[\frac{(d+1)}{4\sqrt{\pi}}\Gamma\left(-\tfrac{d+1}{2}\right)\left(-\frac{\bar{\Sigma}_0^{d-1}\bar{\sigma}^2}{2} + \frac{|\bar{\sigma}|^{d+1}}{d+1}\right) + \frac{\Theta\left(\bar{\mu}^2\right)}{d}|\bar{\sigma}|^{d+1}\left|\frac{\bar{\mu}}{\bar{\sigma}}\right|^d \left({}_2F_1\left(-\tfrac{1}{2}, \tfrac{d}{2}; \tfrac{d+2}{2}; -\tfrac{\bar{\mu}^2}{\bar{\sigma}^2}\right) - \left|\frac{\mu}{\bar{\sigma}}\right|\right)\right],
\end{aligned}$$

where we used Eq. (D.6) to solve the integral. We find that that the symmetric limit $\bar{\sigma} \to 0$ of this expression reduces to

$$\overline{U}_{\text{eff}}(\bar{\sigma}=0, T=0, \mu, d) = -\frac{N_\gamma}{2^d\pi^{\frac{d}{2}}}\frac{|\mu|^{d+1}}{\Gamma\left(\frac{d}{2}\right)d(d+1)}. \qquad (D.21)$$

D.3 The Two-Point Function at Zero Temperature

In this section, we want to give some intermediary steps for the final formula of the two-point function at $T = 0$ that was presented in Eq. (7.10).

We start with the calculation of the constant contribution $1/(2G) - N_\gamma l_1$ at zero temperature and finite chemical potential. By inserting Eqs. (D.17) and (D.18) and using Eq. (D.6), we obtain for the constant contribution

$$\begin{aligned}
&\frac{1}{2G} - N_\gamma l_1\left(\bar{\sigma}, \mu, T=0, d\right) = \qquad\qquad (D.22)\\
&= \frac{N_\gamma}{2^d\pi^{\frac{d}{2}}\Gamma\left(\frac{d}{2}\right)}\left[\frac{\Gamma\left(\frac{d}{2}+1\right)\Gamma\left(\frac{1}{2}-\frac{d}{2}\right)}{d\sqrt{\pi}}\left(\left|\bar{\Sigma}_0\right|^{d-1} - \left|\bar{\sigma}\right|^{d-1}\right) + \int_0^\infty \mathrm{d}p\,\frac{p^{d-1}}{E}\Theta\left(1 - \tfrac{E^2}{\mu^2}\right)\right] = \\
&= \frac{N_\gamma}{2^d\pi^{\frac{d}{2}}\Gamma\left(\frac{d}{2}\right)}\left[\frac{\Gamma\left(\frac{d}{2}+1\right)\Gamma\left(\frac{1}{2}-\frac{d}{2}\right)}{d\sqrt{\pi}}\left(\left|\bar{\Sigma}_0\right|^{d-1} - \left|\bar{\sigma}\right|^{d-1}\right) + \begin{cases} 0 & \text{if } \bar{\mu}^2 < 0 \\ \frac{|\mu|^{d-1}}{d-1} & \text{if } \mu^2 \geq 0 \text{ and } \bar{\sigma} = 0 \\ \frac{1}{d}\frac{|\bar{\mu}|^d}{|\bar{\sigma}|}{}_2F_1\left(\frac{1}{2}, \frac{d}{2}; \frac{d}{2}+1; -\frac{\bar{\mu}^2}{\bar{\sigma}^2}\right) & \text{otherwise} \end{cases}\right].
\end{aligned}$$

For the q-dependent l_2, we start from Eq. (7.9) and take the limit $T \to 0$, which results in

$$\begin{aligned}
l_2\left(q^2, \bar{\sigma}, \mu, T=0, d\right) &= \frac{S_d}{(2\pi)^d}\int_0^1 \mathrm{d}x \int_0^\infty \mathrm{d}p\, p^{d-1}\frac{1}{4\tilde{E}^3}\left[\Theta\left(\frac{\tilde{E}}{|\mu|} - 1\right) - \frac{\tilde{E}}{|\mu|}\delta\left(\frac{\tilde{E}}{|\mu|} - 1\right)\right] = \qquad (D.23)\\
&= \frac{1}{2^{d+1}\pi^{d/2}\Gamma\left(\frac{d}{2}\right)}\int_0^1 \mathrm{d}x \begin{cases} \frac{\tilde{\mu}^{d-3}}{(3-d)}{}_2F_1\left(\frac{3}{2}, \frac{3-d}{2}; \frac{3-d}{2}+1; -\frac{\tilde{\Delta}^2}{\tilde{\mu}^2}\right) - \frac{\tilde{\mu}^{d-2}}{|\mu|} & \text{if } \tilde{\mu}^2 > 0 \\ \frac{\tilde{\Delta}^{d-3}}{2}B\left(\frac{d}{2}, \frac{3-d}{2}\right) & \text{otherwise} \end{cases},
\end{aligned}$$

where $\tilde{E}^2 = p^2 + \tilde{\Delta}^2$, $\tilde{\mu}^2 = \mu^2 - \tilde{\Delta}^2$, $\tilde{\Delta}^2 = \bar{\sigma}^2 + q^2x(1-x)$ and we used Eqs. (D.5) and (D.7).

By combining the results for the constant contribution and l_2, we can give the full expression for the

two-point function at $T = 0$

$$\begin{aligned}
&\Gamma^{(2)}\left(q^2,\bar{\sigma},\mu,T=0,d\right) = \\
&= \frac{N_\gamma}{2^d \pi^{\frac{d}{2}} \Gamma\left(\frac{d}{2}\right)} \left[\frac{\Gamma\left(\frac{d}{2}+1\right)\Gamma\left(\frac{1}{2}-\frac{d}{2}\right)}{d\sqrt{\pi}} \left(\left|\bar{\Sigma}_0\right|^{d-1} - \left|\bar{\sigma}\right|^{d-1} \right) + \right. \\
&\qquad + \left\{ \begin{array}{ll} \frac{|\mu|^{d-1}}{(d-1)} & \text{if } \bar{\sigma}=0, \mu \neq 0 \\ \frac{|\bar{\sigma}|^{d-1}}{d} \left|\frac{\bar{\mu}}{\bar{\sigma}}\right|^d {}_2F_1\left(\frac{1}{2},\frac{d}{2};\frac{d+2}{2};-\frac{\bar{\mu}^2}{\bar{\sigma}^2}\right) & \text{if } \bar{\sigma}\neq 0, \bar{\mu}^2 > 0 \\ 0 & \text{otherwise} \end{array} \right\} + \\
&\qquad \left. + \left(\frac{q^2}{4} + \bar{\sigma}^2\right) \int_0^1 \mathrm{d}x \left\{ \begin{array}{ll} \frac{\tilde{\mu}^{d-3}}{(3-d)} {}_2F_1\left(\frac{3}{2},\frac{3-d}{2};\frac{3-d}{2}+1;-\frac{\tilde{\Delta}^2}{\tilde{\mu}^2}\right) - \frac{\tilde{\mu}^{d-2}}{|\mu|} & \text{if } \tilde{\mu}^2 > 0 \\ \frac{\tilde{\Delta}^{d-3}}{2} B\left(\frac{d}{2},\frac{3-d}{2}\right) & \text{otherwise} \end{array} \right\} \right].
\end{aligned} \tag{D.24}$$

The integral over x is trivial in the limit of $q \to 0$ and we obtain the closed form

$$\begin{aligned}
&\Gamma^{(2)}\left(q^2=0,\bar{\sigma},\mu,T=0,d\right) = \frac{N_\gamma}{2^d \pi^{\frac{d}{2}} \Gamma\left(\frac{d}{2}\right)} \left[\frac{\Gamma\left(\frac{d}{2}+1\right)\Gamma\left(\frac{1}{2}-\frac{d}{2}\right)}{d\sqrt{\pi}} \left(\left|\bar{\Sigma}_0\right|^{d-1} - \left|\bar{\sigma}\right|^{d-1} \right) + \right. \\
&\left. + |\bar{\sigma}|^{d-1} \times \left\{ \begin{array}{ll} \frac{1}{d} \left|\frac{\bar{\mu}}{\bar{\sigma}}\right|^d {}_2F_1\left(\frac{1}{2},\frac{d}{2};\frac{d+2}{2};-\frac{\bar{\mu}^2}{\bar{\sigma}^2}\right) + \frac{1}{3-d} \left|\frac{\bar{\mu}}{\bar{\sigma}}\right|^{d-3} {}_2F_1\left(\frac{3}{2},\frac{3-d}{2};\frac{5-d}{2};-\frac{\bar{\sigma}^2}{\bar{\mu}^2}\right) - \frac{|\bar{\mu}|^{d-2}}{|\mu|} & \text{if } \bar{\mu}^2 > 0 \\ \frac{1}{2} B\left(\frac{d}{2},\frac{3-d}{2}\right) & \text{otherwise} \end{array} \right\} \right].
\end{aligned} \tag{D.25}$$

On the other hand, if we take the symmetric limit $\bar{\sigma} \to 0$ of Eq. (D.24), we find for the two-point function

$$\begin{aligned}
&\Gamma^{(2)}\left(q^2,\bar{\sigma}=0,\mu,T=0,d\right) = \\
&= \frac{N_\gamma}{2^d \pi^{\frac{d}{2}} \Gamma\left(\frac{d}{2}\right)} \left[\frac{\Gamma\left(\frac{d}{2}+1\right)\Gamma\left(\frac{1}{2}-\frac{d}{2}\right)}{d\sqrt{\pi}} \left|\bar{\Sigma}_0\right|^{d-1} + \frac{|\mu|^{d-1}}{(d-1)} + \right. \\
&\qquad \left. + \frac{q^2}{4} \int_0^1 \mathrm{d}x \left\{ \begin{array}{ll} \frac{|\tilde{\mu}_0|^{d-3}}{(3-d)} {}_2F_1\left(\frac{3}{2},\frac{3-d}{2};\frac{3-d}{2}+1;-\frac{(q^2 x(1-x))^2}{\tilde{\mu}_0^2}\right) - \frac{|\tilde{\mu}_0|^{d-2}}{|\mu|} & \text{if } \tilde{\mu}_0^2 > 0 \\ \frac{|q^2 x(1-x)|^{d-3}}{2} B\left(\frac{d}{2},\frac{3-d}{2}\right) & \text{otherwise} \end{array} \right\} \right],
\end{aligned} \tag{D.26}$$

where $\tilde{\mu}_0^2 = \mu^2 - q^2 x(1-x)$.

The limit of both $q = 0$ and $\bar{\sigma} = 0$ results in

$$\Gamma^{(2)}\left(q^2=0,\bar{\sigma}=0,\mu,T=0,d\right) = \frac{N_\gamma}{2^d \pi^{\frac{d}{2}} \Gamma\left(\frac{d}{2}\right)} \left[\frac{\Gamma\left(\frac{d}{2}+1\right)\Gamma\left(\frac{1}{2}-\frac{d}{2}\right)}{d\sqrt{\pi}} \left|\bar{\Sigma}_0\right|^{d-1} + \frac{|\mu|^{d-1}}{(d-1)} \right]. \tag{D.27}$$

D.4 The Wave-Function Renormalization

In this section, we want to give some intermediary steps for the derivation of the wave-function renormalization.

We start the derivation of the wave-function renormalization by taking the double derivative with respect to q of $\Gamma^{(2)}$ with l_2 given by Eq. (7.8) and obtain

$$\begin{aligned} z\left(\bar{\sigma},\mu,T,d\right) &= \frac{1}{2}\frac{\mathrm{d}^2}{\mathrm{d}q^2}\left[\frac{N_\gamma}{2}(q^2+4\bar{\sigma}^2)\tfrac{1}{\beta}\sum_{n=-\infty}^{\infty}\int\frac{\mathrm{d}^d p}{(2\pi)^d}\int_0^1 \mathrm{d}x\,\frac{1}{\left[p^2+\Delta^2+q^2x(1-x)\right]^2}\right]\Bigg|_{q=0} = \\ &= \frac{N_\gamma}{2}\tfrac{1}{\beta}\sum_{n=-\infty}^{\infty}\int\frac{\mathrm{d}^d p}{(2\pi)^d}\int_0^1 \mathrm{d}x\,\frac{\Delta^4+p^4+8\bar{\sigma}^2p^2(x-1)x+2\Delta^2(p^2+4\bar{\sigma}^2(x-1)x)}{\left(\Delta^2+p^2\right)^4} = \\ &= \frac{N_\gamma}{2}\tfrac{1}{\beta}\sum_{n=-\infty}^{\infty}\int\frac{\mathrm{d}^d p}{(2\pi)^d}\left[\frac{1}{\left(\Delta^2+p^2\right)^2}-\frac{8\bar{\sigma}^2}{3}\frac{1}{\left(\Delta^2+p^2\right)^3}\right]. \end{aligned} \tag{D.28}$$

Carrying out the Matsubara summation and transforming the momentum integral to d-dimensional spherical coordinates yields

$$\begin{aligned} z = \tfrac{N_\gamma}{4}\tfrac{S_d}{(2\pi)^d}\int_0^\infty \mathrm{d}p\,p^{d-1}\Bigg\{ &\frac{1}{2E^3}\left[\tfrac{1}{2}\tanh\left(\tfrac{E+\mu}{2T}\right)+\tfrac{1}{2}\tanh\left(\tfrac{E-\mu}{2T}\right)-\frac{E}{T}\left(\frac{1}{4\cosh^2\left(\tfrac{E+\mu}{2T}\right)}+\frac{1}{4\cosh^2\left(\tfrac{E-\mu}{2T}\right)}\right)\right]+ \\ &-\frac{\bar{\sigma}^2}{2E^5}\left[\tfrac{1}{2}\tanh\left(\tfrac{E+\mu}{2T}\right)+\tfrac{1}{2}\tanh\left(\tfrac{E-\mu}{2T}\right)-\frac{E}{T}\left(\frac{1}{4\cosh^2\left(\tfrac{E+\mu}{2T}\right)}+\frac{1}{4\cosh^2\left(\tfrac{E-\mu}{2T}\right)}\right)+\right. \\ &\left.-\frac{E^2}{T^2}\left(\frac{\sinh\left(\tfrac{E+\mu}{2T}\right)}{12\cosh^3\left(\tfrac{E+\mu}{2T}\right)}+\frac{\sinh\left(\tfrac{E-\mu}{2T}\right)}{12\cosh^3\left(\tfrac{E-\mu}{2T}\right)}\right)\right]\Bigg\}, \end{aligned} \tag{D.29}$$

where we used standard Matsubara summation formulas, see, e.g., Ref. [57]. While we cannot perform the remaining momentum integral for arbitrary $q,\bar{\sigma},\mu,d,T$ analytically, it is possible to obtain closed form expressions at $T=0$.

Taking the zero temperature limit of Eq. (D.29), we find the form

$$
\begin{aligned}
& z\left(\bar{\sigma},\mu,T=0,d\right) = \\
&= \frac{N_\gamma}{2}\frac{S_d}{(2\pi)^d}\int_0^\infty \mathrm{d}p\, p^{d-1}\left\{\frac{1}{2E^3}\left[\Theta\left(\tfrac{E^2}{\mu^2}-1\right)-\frac{E}{|\mu|}\left(\delta\left(\tfrac{E}{|\mu|}+1\right)+\delta\left(\tfrac{E}{|\mu|}-1\right)\right)\right]+\right. \\
&\left. -\frac{\bar{\sigma}^2}{2}\left[\frac{\Theta\left(\frac{E^2}{\mu^2}-1\right)}{E^5}-\frac{1}{E^4|\mu|}\left(\delta\left(\tfrac{E}{|\mu|}+1\right)+\delta\left(\tfrac{E}{|\mu|}-1\right)\right)+\frac{1}{3E^3\mu^2}\left(\delta'\left(\tfrac{E}{|\mu|}+1\right)+\delta'\left(\tfrac{E}{|\mu|}-1\right)\right)\right]\right\} \\
&= \frac{N_\gamma}{2^{d+2}\pi^{\frac{d}{2}}\Gamma\left(\frac{d}{2}\right)}\begin{cases}
\frac{1}{(3-d)\tilde{\mu}^{3-d}}\,{}_2F_1\left(\frac{3}{2},\frac{3-d}{2};\frac{5-d}{2};-\frac{\bar{\sigma}^2}{\tilde{\mu}^2}\right)+ \\
-\frac{1}{(5-d)}\frac{\bar{\sigma}^2}{\tilde{\mu}^2}\frac{1}{\tilde{\mu}^{3-d}}\,{}_2F_1\left(\frac{5}{2},\frac{5-d}{2};\frac{7-d}{2};-\frac{\bar{\sigma}^2}{\tilde{\mu}^2}\right)+ \\
+\frac{\tilde{\mu}^{d-2}}{|\mu|}\left[\frac{\bar{\sigma}^2}{\mu^2}\left(1+\frac{1}{3\tilde{\mu}^2}\left(2\bar{\sigma}^2-(4-d)\mu^2\right)\right)-1\right] & \text{if } \tilde{\mu}^2>0 \\
\frac{1}{2|\bar{\sigma}|^{3-d}}\left[B\left(\frac{d}{2},\frac{3-d}{2}\right)-B\left(\frac{d}{2},\frac{5-d}{2}\right)\right] & \text{otherwise}
\end{cases},
\end{aligned}
\tag{D.30}
$$

where we evaluated the momentum integrals with Eqs. (D.5), (D.7) and (D.8). The symmetric limit $\bar{\sigma} \to 0$ of this expression amounts to

$$
z\left(\bar{\sigma}=0,\mu,T=0,d\right) = \frac{N_\gamma}{2^{d+2}\pi^{\frac{d}{2}}\Gamma\left(\frac{d}{2}\right)}\frac{d-2}{d-3}\left|\mu\right|^{d-3}. \tag{D.31}
$$

Bibliography

1. Gross, David J. and Frank Wilczek: 'Ultraviolet Behavior of Nonabelian Gauge Theories'. *Phys. Rev. Lett.* (1973), vol. 30. Ed. by Taylor, J. C.: pp. 1343–1346 (cit. on p. 1).
2. Politzer, H. David: 'Reliable Perturbative Results for Strong Interactions?' *Phys. Rev. Lett.* (1973), vol. 30. Ed. by Taylor, J. C.: pp. 1346–1349 (cit. on p. 1).
3. Alford, M., K. Rajagopal, and F. Wilczek: 'QCD at Finite Baryon Density: Nucleon Droplets and Color Superconductivity'. *Physics Letters B* (1998), vol. 422(1-4): pp. 247–256 (cit. on p. 1).
4. Glozman, Leonid Ya, Owe Philipsen, and Robert D. Pisarski: 'Chiral spin symmetry and the QCD phase diagram'. *The European Physical Journal A* (2022), vol. 58(12): p. 247 (cit. on p. 1).
5. Glozman, L. Ya: 'Chiral spin symmetry and hot/dense QCD'. *Progress in Particle and Nuclear Physics* (2023), vol. 131: p. 104049 (cit. on p. 1).
6. Aoki, Y., G. Endrodi, Z. Fodor, S. D. Katz, and K. K. Szabo: 'The order of the quantum chromodynamics transition predicted by the standard model of particle physics'. *Nature* (2006), vol. 443(7112): pp. 675–678 (cit. on p. 1).
7. Borsanyi, Szabolcs, Zoltan Fodor, Jana N. Guenther, Ruben Kara, Sandor D. Katz, Paolo Parotto, Attila Pasztor, Claudia Ratti, and Kalman K. Szabo: 'The QCD crossover at finite chemical potential from lattice simulations'. *Physical Review Letters* (2020), vol. 125(5): p. 052001 (cit. on pp. 1, 2).
8. Bazavov, A. et al.: 'Chiral crossover in QCD at zero and non-zero chemical potentials'. *Physics Letters B* (2019), vol. 795: pp. 15–21 (cit. on pp. 1, 2).
9. Fu, Wei-jie, Jan M. Pawlowski, and Fabian Rennecke: 'The QCD phase structure at finite temperature and density'. *Physical Review D* (2020), vol. 101(5): p. 054032 (cit. on pp. 1, 2, 4).
10. Gao, Fei and Jan M. Pawlowski: 'Chiral phase structure and critical end point in QCD'. *Physics Letters B* (2021), vol. 820: p. 136584 (cit. on pp. 1, 2).
11. Fischer, Christian S.: 'QCD at finite temperature and chemical potential from Dyson-Schwinger equations'. *Progress in Particle and Nuclear Physics* (2019), vol. 105: pp. 1–60 (cit. on pp. 1, 2).
12. Klevansky, S. P.: 'The Nambu-Jona-Lasinio model of quantum chromodynamics'. *Reviews of Modern Physics* (1992), vol. 64(3): pp. 649–708 (cit. on pp. 2, 14, 15, 27, 29–32).
13. Buballa, Michael: 'NJL model analysis of quark matter at large density'. *Phys. Rept.* (2005), vol. 407: pp. 205–376 (cit. on pp. 2, 10, 13, 27, 32).
14. Nickel, Dominik: 'Inhomogeneous phases in the Nambu-Jona-Lasino and quark-meson model'. *Physical Review D* (2009), vol. 80(7): p. 074025 (cit. on pp. 2–4, 14, 29, 33, 34, 38, 63, 67, 78, 85, 87, 90, 91).
15. Schaefer, Bernd-Jochen and Jochen Wambach: 'The Phase Diagram of the Quark-Meson Model'. *Nuclear Physics A* (2005), vol. 757(3-4): pp. 479–492 (cit. on p. 2).

16. Tripolt, Ralf-Arno, Bernd-Jochen Schaefer, Lorenz von Smekal, and Jochen Wambach: 'The low-temperature behavior of the quark-meson model'. *Physical Review D* (2018), vol. 97(3): p. 034022 (cit. on pp. 2, 4, 16, 35, 39).

17. Schaefer, Bernd-Jochen, Jan M. Pawlowski, and Jochen Wambach: 'The Phase Structure of the Polyakov–Quark-Meson Model'. *Physical Review D* (2007), vol. 76(7): p. 074023 (cit. on p. 2).

18. Fu, Wei-jie, Zhao Zhang, and Yu-xin Liu: '2+1 Flavor Polyakov–Nambu–Jona-Lasinio Model at Finite Temperature and Nonzero Chemical Potential'. *Physical Review D* (2008), vol. 77(1): p. 014006 (cit. on p. 2).

19. Fukushima, Kenji: 'Phase diagrams in the three-flavor Nambu–Jona-Lasinio model with the Polyakov loop'. *Physical Review D* (2008), vol. 78(3): p. 039902 (cit. on p. 2).

20. Halasz, M. A., A. D. Jackson, R. E. Shrock, M. A. Stephanov, and J. J. M. Verbaarschot: 'On the Phase Diagram of QCD'. *Physical Review D* (1998), vol. 58(9): p. 096007 (cit. on p. 2).

21. Odyniec, Grazyna: 'RHIC Beam Energy Scan Program: Phase I and II'. *PoS* (2013), vol. CPOD2013: p. 043 (cit. on p. 2).

22. Bhaduri, Partha Pratim: 'The physics goals of the CBM experiment at FAIR'. *PoS* (2022), vol. CPOD2021: p. 031 (cit. on p. 2).

23. An, Xin et al.: 'The BEST framework for the search for the QCD critical point and the chiral magnetic effect'. *Nuclear Physics A* (2022), vol. 1017: p. 122343 (cit. on p. 2).

24. Fu, Wei-jie, Xiaofeng Luo, Jan M. Pawlowski, Fabian Rennecke, and Shi Yin: 'Ripples of the QCD Critical Point'. (2023), vol. preprint (cit. on p. 2).

25. Borsanyi, Szabolcs, Zoltan Fodor, Matteo Giordano, Jana N. Guenther, Kornél Kapás, Sandor K. Katz, Kalman K. Szabó, Attila Pasztor, Israel Portillo, and Claudia Ratti: 'Searching the QCD critical endpoint with lattice simulations'. *EPJ Web Conf.* (2020), vol. 235. Ed. by Vitev, I., C. da Silva, S. Mioduszewski, C. Ratti, I. Sarcevic, and M. Schlegel: p. 02004 (cit. on p. 2).

26. Zambello, Kevin, David A. Clarke, Petros Dimopoulos, Francesco Di Renzo, Jishnu Goswami, Guido Nicotra, Christian Schmidt, and Simran Singh: 'Determination of Lee-Yang edge singularities in QCD by rational approximations'. (2023), vol. preprint (cit. on p. 2).

27. Buballa, Michael and Stefano Carignano: 'Inhomogeneous chiral condensates'. *Progress in Particle and Nuclear Physics* (2015), vol. 81: pp. 39–96 (cit. on pp. 3, 4, 10, 29).

28. Thies, Michael and Konrad Urlichs: 'Revised phase diagram of the Gross-Neveu model'. *Physical Review D* (2003), vol. 67: p. 125015 (cit. on pp. 3, 21–23, 38, 45, 78, 85, 89).

29. Schnetz, Oliver, Michael Thies, and Konrad Urlichs: 'Phase diagram of the Gross-Neveu model: Exact results and condensed matter precursors'. *Annals Phys.* (2004), vol. 314: pp. 425–447 (cit. on pp. 3, 11, 21–23, 38, 85, 89).

30. Sadzikowski, Mariusz and Wojciech Broniowski: 'Non-uniform chiral phase in effective chiral quark models'. *Physics Letters B* (2000), vol. 488(1): pp. 63–67 (cit. on pp. 3, 4, 13, 33, 91).

31. Nakano, E. and T. Tatsumi: 'Chiral symmetry and density wave in quark matter'. *Physical Review D* (2005), vol. 71(11): p. 114006 (cit. on pp. 3, 4, 15, 33, 38, 87, 91).

32. Müller, Daniel, Michael Buballa, and Jochen Wambach: 'Dyson-Schwinger study of chiral density waves in QCD'. *Physics Letters B* (2013), vol. 727(1-3): pp. 240–243 (cit. on p. 3).

33. KOJO, TORU, YOSHIMASA HIDAKA, LARRY MCLERRAN, and ROBERT D. PISARSKI: 'Quarkyonic Chiral Spirals'. *Nucl. Phys. A* (2010), vol. 843: pp. 37–58 (cit. on p. 3).

34. PEIERLS, RUDOLF: *More Surprises in Theoretical Physics*. Vol. 105. Princeton University Press, 1991 (cit. on pp. 3, 22).

35. CARIGNANO, STEFANO, MICHAEL BUBALLA, and BERND-JOCHEN SCHAEFER: 'Inhomogeneous phases in the quark-meson model with vacuum fluctuations'. *Physical Review D* (2014), vol. 90(1): p. 014033 (cit. on pp. 3, 9, 14, 16, 33, 35, 38, 63, 72, 85, 90).

36. LAKASCHUS, PHILLIP, MICHAEL BUBALLA, and DIRK H. RISCHKE: 'Competition of inhomogeneous chiral phases and two-flavor color superconductivity in the NJL model'. *Physical Review D* (2021), vol. 103(3): p. 034030 (cit. on p. 3).

37. BUBALLA, MICHAEL and STEFANO CARIGNANO: 'Inhomogeneous chiral symmetry breaking in dense neutron-star matter'. *The European Physical Journal A* (2016), vol. 52(3): p. 57 (cit. on p. 3).

38. PISARSKI, ROBERT D. and FABIAN RENNECKE: 'Signatures of Moat Regimes in Heavy-Ion Collisions'. *Physical Review Letters* (2021), vol. 127(15): p. 152302 (cit. on pp. 3, 4, 53, 91).

39. KOENIGSTEIN, ADRIAN, LAURIN PANNULLO, STEFAN RECHENBERGER, MARC WINSTEL, and MARTIN J. STEIL: 'Detecting inhomogeneous chiral condensation from the bosonic two-point function in the (1 + 1)-dimensional Gross-Neveu model in the mean-field approximation'. *Journal of Physics A: Mathematical and Theoretical* (2022), vol. 55(37): p. 375402 (cit. on pp. 3, 4, 12, 13, 19, 35, 37, 39, 40, 43, 45, 47–51, 85, 112).

40. PISARSKI, R. D., F. RENNECKE, A. TSVELIK, and S. VALGUSHEV: 'The Lifshitz Regime and its Experimental Signals'. *Nuclear Physics A* (2021), vol. 1005: p. 121910 (cit. on pp. 4, 91).

41. RENNECKE, FABIAN and ROBERT D. PISARSKI: 'Moat Regimes in QCD and their Signatures in Heavy-Ion Collisions'. *PoS* (2022), vol. CPOD2021: p. 016 (cit. on pp. 4, 91).

42. RENNECKE, FABIAN, ROBERT D. PISARSKI, and DIRK H. RISCHKE: 'Particle Interferometry in a Moat Regime'. (2023), vol. preprint (cit. on pp. 4, 53, 91).

43. STOLL, JONAS, NIKLAS ZORBACH, ADRIAN KOENIGSTEIN, MARTIN J. STEIL, and STEFAN RECHENBERGER: 'Bosonic fluctuations in the (1 + 1)-dimensional Gross-Neveu(-Yukawa) model at varying μ and T and finite N'. 2021 (cit. on pp. 4, 16, 24–26, 34, 46, 50).

44. SCHERER, DANIEL D., JENS BRAUN, and HOLGER GIES: 'Many-flavor Phase Diagram of the (2+1)d Gross-Neveu Model at Finite Temperature'. *Journal of Physics A: Mathematical and Theoretical* (2013), vol. 46(28): p. 285002 (cit. on pp. 4, 16, 25, 27).

45. HANDS, SIMON and DAVID N. WALTERS: 'Numerical Portrait of a Relativistic BCS Gapped Superfluid'. *Physical Review D* (2004), vol. 69(7): p. 076011 (cit. on pp. 4, 14, 34, 52, 58).

46. LENZ, JULIAN, LAURIN PANNULLO, MARC WAGNER, BJÖRN WELLEGEHAUSEN, and ANDREAS WIPF: 'Inhomogeneous phases in the Gross-Neveu model in 1+1 dimensions at finite number of flavors'. *Physical Review D* (2020), vol. 101(9): p. 094512 (cit. on pp. 4, 14, 25, 26, 52, 55–57).

47. LENZ, JULIAN J., LAURIN PANNULLO, MARC WAGNER, BJÖRN WELLEGEHAUSEN, and ANDREAS WIPF: 'Baryons in the Gross-Neveu model in 1+1 dimensions at finite number of flavors'. *Physical Review D* (2020), vol. 102(11): p. 114501 (cit. on pp. 4, 14, 26, 52, 55, 67).

48. NARAYANAN, RAJAMANI: *Phase diagram of the large N Gross-Neveu model in a finite periodic box*. 2020 (cit. on pp. 4, 5, 23, 38, 78, 91).

49. Buballa, Michael, Lennart Kurth, Marc Wagner, and Marc Winstel: 'Regulator dependence of inhomogeneous phases in the 2+1-dimensional Gross-Neveu model'. *Physical Review D* (2021), vol. 103(3): p. 034503 (cit. on pp. 4, 5, 14, 19, 21, 23, 27, 37–39, 58, 59, 63, 78, 91, 112).

50. Pannullo, Laurin, Marc Wagner, and Marc Winstel: 'Inhomogeneous phases in the chirally imbalanced 2+1-dimensional Gross-Neveu model and their absence in the continuum limit'. *Symmetry* (2022), vol. 14(2): p. 265 (cit. on pp. 4, 14, 19, 38, 39, 58, 59, 67, 78).

51. Pannullo, Laurin and Marc Winstel: 'Absence of inhomogeneous chiral phases in 2+1-dimensional four-fermion and Yukawa models'. *Physical Review D* (2023), vol. 108(3): p. 036011 (cit. on pp. 4, 5, 35, 39, 78, 83–85, 97, 112).

52. Karsch, F., John B. Kogut, and H. W. Wyld: 'The Gross-Neveu model at finite temperature and density'. *Nuclear Physics B* (1987), vol. 280: pp. 289–303 (cit. on pp. 4, 25).

53. Broniowski, Wojciech and Marek Kutschera: 'Ambiguities in effective chiral models with cut-off'. *Physics Letters B* (1990), vol. 242(2): pp. 133–138 (cit. on p. 4).

54. Partyka, Tomasz L. and Mariusz Sadzikowski: 'Phase diagram of the non-uniform chiral condensate in different regularization schemes at T=0'. *Journal of Physics G: Nuclear and Particle Physics* (2009), vol. 36(2): p. 025004 (cit. on pp. 4, 15, 52).

55. Kohyama, H., D. Kimura, and T. Inagaki: 'Regularization dependence on phase diagram in Nambu–Jona-Lasinio model'. *Nucl. Phys. B* (2015), vol. 896: pp. 682–715 (cit. on pp. 4, 13, 15, 16, 52, 86).

56. Narison, Stephan: *QCD Spectral Sum Rules*. Vol. 26. World Scientific Lecture Notes in Physics. WORLD SCIENTIFIC, 1990 (cit. on pp. 7, 97).

57. Koenigstein, Adrian: 'Non-perturbative aspects of (low-dimensional) quantum field theories'. PhD thesis. Frankfurt am Main: Goethe University Frankfurt am Main, 2023 (cit. on pp. 8, 12, 16, 21, 26, 35, 45, 96, 112, 118).

58. Pannullo, Laurin: 'Inhomogeneous Phases in the 1 + 1-Dimensional Gross-Neveu Model at Finite Number of Fermion Flavors'. Master's thesis. Frankfurt am Main: Goethe-Universität Frankfurt am Main, 2020 (cit. on pp. 8, 19, 56, 57, 114).

59. Hands, Simon, Aleksandar Kocic, and John B. Kogut: 'Four - Fermi Theories in Fewer Than Four Dimensions'. *Annals of Physics* (1993), vol. 224(1): pp. 29–89 (cit. on pp. 9, 78).

60. Peskin, Michael Edward and Daniel V. Schroeder: *An introduction to quantum field theory*. Reading, Mass: Addison-Wesley Pub. Co, 1995. 842 pp. (cit. on pp. 9, 19, 87, 95, 96).

61. Masayuki, Asakawa and Yazaki Koichi: 'Chiral restoration at finite density and temperature'. *Nuclear Physics A* (1989), vol. 504(4): pp. 668–684 (cit. on p. 10).

62. 't Hooft, G.: 'A planar diagram theory for strong interactions'. *Nuclear Physics B* (1974), vol. 72(3): pp. 461–473 (cit. on p. 11).

63. Pasqualotto, Arthur E. B., Ricardo L. S. Farias, William R. Tavares, Sidney S. Avancini, and Gastão Krein: 'Causality violation and the speed of sound of hot and dense quark matter in the Nambu–Jona-Lasinio model'. *Physical Review D* (2023), vol. 107(9): p. 096017 (cit. on pp. 13, 16).

64. Inagaki, T., T. Kouno, and T. Muta: 'Phase structure of four-fermion theories at finite temperature and chemical potential in arbitrary dimensions'. *International Journal of Modern Physics A* (1995), vol. 10(15): pp. 2241–2268 (cit. on pp. 13, 19, 23–25, 78, 85).

65. Heinz, Achim, Francesco Giacosa, Marc Wagner, and Dirk H. Rischke: 'Inhomogeneous condensation in effective models for QCD using the finite-mode approach'. *Physical Review D* (2016), vol. 93(1): p. 014007 (cit. on pp. 14, 38, 39, 55).

66. Carignano, Stefano, Marco Schramm, and Michael Buballa: 'Influence of vector interactions on the favored shape of inhomogeneous chiral condensates'. *Physical Review D* (2018), vol. 98(1): p. 014033 (cit. on pp. 14, 35, 38, 63).

67. Buballa, Michael and Stefano Carignano: 'Inhomogeneous chiral phases away from the chiral limit'. *Physics Letters* (2019), vol. B791: pp. 361–366 (cit. on pp. 14, 37–40).

68. Buballa, Michael, Stefano Carignano, and Lennart Kurth: 'Inhomogeneous phases in the quark-meson model with explicit chiral-symmetry breaking'. *The European Physical Journal Special Topics* (2020), vol. 229(22-23): pp. 3371–3385 (cit. on pp. 14, 37, 39, 40).

69. Wagner, Marc: 'Fermions in the pseudoparticle approach'. *Physical Review D* (2007), vol. 76(7): p. 076002 (cit. on pp. 14, 38, 39).

70. De Forcrand, Philippe and Urs Wenger: 'New baryon matter in the lattice Gross-Neveu model'. *PoS* (2006), vol. LAT2006. Ed. by Blum, Tom, Michael Creutz, Carleton DeTar, Frithjof Karsch, Andreas Kronfeld, Colin Morningstar, David Richards, Junko Shigemitsu, and Doug Toussaint: p. 152 (cit. on p. 14).

71. Pannullo, Laurin, Marc Wagner, and Marc Winstel: 'Inhomogeneous phases in the 3+1-dimensional Nambu-Jona-Lasinio model and their dependence on the regularization scheme'. *PoS* (2023), vol. LATTICE2022: p. 156 (cit. on pp. 14, 38, 39, 52).

72. Bitar, K. M. and P. M. Vranas: 'A Study of the Nambu–Jona-Lasinio Model on the Lattice'. *Physical Review D* (1994), vol. 50(5): pp. 3406–3421 (cit. on p. 14).

73. Hands, Simon, John B. Kogut, Costas G. Strouthos, and Thao N. Tran: 'Fermi surface phenomena in the (2+1)D four-Fermi model'. *Physical Review D* (2003), vol. 68(1): p. 016005 (cit. on pp. 14, 27).

74. 't Hooft, G. and M. Veltman: 'Regularization and renormalization of gauge fields'. *Nuclear Physics B* (1972), vol. 44(1): pp. 189–213 (cit. on pp. 15, 19, 79, 87, 95, 96).

75. Adhikari, Prabal and Jens O. Andersen: 'Consistent regularization and renormalization in models with inhomogeneous phases'. *Physical Review D* (2017), vol. 95(3): p. 036009 (cit. on pp. 15, 86).

76. Bruschke, Tobias: 'Inhomogene Kondensate im Gross-Neveu Modell'. BA thesis. Jena, Germany: Friedrich-Schiller-Universität Jena, 2022 (cit. on p. 15).

77. Wetterich, Christof: 'Exact evolution equation for the effective potential'. *Physics Letters B* (1993), vol. 301(1): pp. 90–94 (cit. on p. 15).

78. Janssen, Lukas and Holger Gies: 'Critical behavior of the (2+1)-dimensional Thirring model'. *Physical Review D* (2012), vol. 86(10): p. 105007 (cit. on p. 16).

79. Braun, Jens, Marc Leonhardt, and Jan M. Pawlowski: 'Renormalization group consistency and low-energy effective theories'. *SciPost Phys.* (2019), vol. 6(5): p. 056 (cit. on pp. 16, 70).

80. Skokov, V., B. Friman, E. Nakano, K. Redlich, and B.-J. Schaefer: 'Vacuum fluctuations and the thermodynamics of chiral models'. *Physical Review D* (2010), vol. 82(3): p. 034029 (cit. on p. 16).

81. GUPTA, UMA SHANKAR and VIVEK KUMAR TIWARI: 'Revisiting the Phase Structure of the Polyakov-quark-meson Model in the presence of Vacuum Fermion Fluctuation'. *Physical Review D* (2012), vol. 85(1): p. 014010 (cit. on p. 16).

82. ANDERSEN, JENS O., RASHID KHAN, and LARS T. KYLLINGSTAD: 'The chiral phase transition and the role of vacuum fluctuations'. (2011), vol. preprint (cit. on p. 16).

83. SCHAEFER, BERND-JOCHEN and MATHIAS WAGNER: 'QCD critical region and higher moments for three flavor models'. *Physical Review D* (2012), vol. 85(3): p. 034027 (cit. on p. 16).

84. GROSS, DAVID J. and ANDRE NEVEU: 'Dynamical symmetry breaking in asymptotically free field theories'. *Physical Review D* (1974), vol. 10: p. 3235 (cit. on p. 18).

85. LENZ, JULIAN J., MICHAEL MANDL, and ANDREAS WIPF: 'The magnetized (2+1)-dimensional Gross-Neveu model at finite density'. (2023), vol. preprint (cit. on pp. 19, 23, 27).

86. LENZ, JULIAN J., MICHAEL MANDL, and ANDREAS WIPF: 'Magnetic catalysis in the (2+1)-dimensional Gross-Neveu model'. *Physical Review D* (2023), vol. 107(9): p. 094505 (cit. on pp. 19, 27).

87. SCHERER, DANIEL D. and HOLGER GIES: 'Renormalization Group Study of Magnetic Catalysis in the 3d Gross-Neveu Model'. *Physical Review B* (2012), vol. 85(19): p. 195417 (cit. on p. 19).

88. KLIMENKO, K. G., R. N. ZHOKHOV, and V. CH ZHUKOVSKY: 'Superconductivity phenomenon induced by external in-plane magnetic field in (2+1)-dimensional Gross–Neveu type model'. *Modern Physics Letters A* (2013), vol. 28(23): p. 1350096 (cit. on p. 19).

89. KLIMENKO, K. G.: 'Three-dimensional Gross-Neveu model in external electric field'. *Teor. Mat. Fiz.* (1991), vol. 89: pp. 388–394 (cit. on p. 19).

90. KARBSTEIN, FELIX and MICHAEL THIES: 'How to get from imaginary to real chemical potential'. *Physical Review D* (2007), vol. 75(2): p. 025003 (cit. on p. 19).

91. MERTSCHING, J. and H. J. FISCHBECK: 'The Incommensurate Peierls Phase of the Quasi-One-Dimensional Fröhlich Model with a Nearly Half-Filled Band'. *physica status solidi (b)* (1981), vol. 103(2): pp. 783–795 (cit. on pp. 19, 22).

92. THIES, MICHAEL: 'From relativistic quantum fields to condensed matter and back again: Updating the Gross-Neveu phase diagram'. *Journal of Physics A: Mathematical and General* (2006), vol. 39(41): pp. 12707–12734 (cit. on pp. 19, 22).

93. GIES, HOLGER, LUKAS JANSSEN, STEFAN RECHENBERGER, and MICHAEL M. SCHERER: 'Phase transition and critical behavior of d=3 chiral fermion models with left/right asymmetry'. *Physical Review D* (2010), vol. 81(2): p. 025009 (cit. on pp. 19, 35, 95, 97).

94. WOLFF, U.: 'The phase diagram of the infinite N Gross-Neveu model at finite temperature and chemical potential'. *Physics Letters* (1985), vol. 157B: pp. 303–308 (cit. on pp. 19, 21, 24).

95. KLIMENKO, K. G.: 'Phase Structure of Generalized Gross-Neveu Models'. *Z. Phys. C* (1988), vol. 37: p. 457 (cit. on pp. 19, 22, 24).

96. ROSENSTEIN, B., B. J. WARR, and S. H. PARK: 'Thermodynamics of (2+1)-dimensional Four Fermi Models'. *Phys. Rev. D* (1989), vol. 39: p. 3088 (cit. on pp. 19, 22, 24).

97. PANNULLO, LAURIN: 'Inhomogeneous condensation in the Gross-Neveu model in noninteger spatial dimensions $1 \leq d < 3$'. *Physical Review D* (2023), vol. 108(3): p. 036022 (cit. on pp. 19, 39, 78).

98. KOENIGSTEIN, ADRIAN and LAURIN PANNULLO. 2023, in preparation (cit. on p. 19).

99. MERMIN, N. D. and H. WAGNER: 'Absence of ferromagnetism or antiferromagnetism in one-dimensional or two-dimensional isotropic Heisenberg models'. *Physical Review Letters* (1966), vol. 17: pp. 1133–1136 (cit. on p. 22).

100. COLEMAN, SIDNEY R.: 'There are no Goldstone bosons in two-dimensions'. *Communications in Mathematical PHysics* (1973), vol. 31: pp. 259–264 (cit. on p. 22).

101. WITTEN, EDWARD: 'Chiral symmetry, the 1/n expansion, and the SU(N) thirring model'. *Nuclear Physics* (1978), vol. B145: pp. 110–118 (cit. on p. 22).

102. ACTOR, ALFRED: 'Zeta function regularization of high-temperature expansions in field theory'. *Nuclear Physics B* (1986), vol. 265(4): pp. 689–719 (cit. on pp. 24, 50).

103. LANDAU, L. D. and E. M. LIFSHITZ: *Statistical Physics, Part 1 & 2*. Vol. 5 & 9. Course of Theoretical Physics. Oxford: Butterworth-Heinemann, 1980 (cit. on p. 25).

104. SCHMIDT, DANIEL: 'Three-Dimensional Four-Fermion Theories with Exact Chiral Symmetry on the Lattice'. PhD thesis. Friedrich-Schiller-Universität Jena (cit. on pp. 27, 55).

105. LI, DAMING: 'The Staggered Fermion for the Gross-Neveu Model at Non-zero Temperature and Density'. (2021), vol. preprint (cit. on p. 27).

106. HANDS, S. J., A. KOCIĆ, and J. B. KOGUT: 'The four-Fermi model in three dimensions at non-zero density and temperature'. *Nuclear Physics B* (1993), vol. 390(2): pp. 355–378 (cit. on p. 27).

107. KOGUT, J. B. and C. G. STROUTHOS: 'Chiral symmetry restoration in the three-dimensional four-fermion model at non-zero temperature and density'. *Physical Review D* (2001), vol. 63(5): p. 054502 (cit. on p. 27).

108. NAMBU, Y. and G. JONA-LASINIO: 'Dynamical Model of Elementary Particles Based on an Analogy with Superconductivity. II'. *Physical Review* (1961), vol. 124(1): pp. 246–254 (cit. on p. 27).

109. NAMBU, Y. and G. JONA-LASINIO: 'Dynamical Model of Elementary Particles Based on an Analogy with Superconductivity. I'. *Physical Review* (1961), vol. 122(1): pp. 345–358 (cit. on p. 27).

110. BASAR, GOKCE, GERALD V. DUNNE, and MICHAEL THIES: 'Inhomogeneous Condensates in the Thermodynamics of the Chiral NJL_2 model'. *Physical Review D* (2009), vol. 79(10): p. 105012 (cit. on pp. 27, 38).

111. LENZ, JULIAN J., MICHAEL MANDL, and ANDREAS WIPF: 'Inhomogeneities in the 2-Flavor Chiral Gross-Neveu Model'. *Physical Review D* (2022), vol. 105(3): p. 034512 (cit. on pp. 27, 52, 55).

112. BRAUN, JENS: 'Fermion Interactions and Universal Behavior in Strongly Interacting Theories'. *Journal of Physics G: Nuclear and Particle Physics* (2012), vol. 39(3): p. 033001 (cit. on p. 27).

113. BRAUN, JENS, MARC LEONHARDT, and MARTIN POSPIECH: 'Fierz-complete NJL model study: fixed points and phase structure at finite temperature and density'. *Physical Review D* (2017), vol. 96(7): p. 076003 (cit. on pp. 27, 36).

114. BRAUN, JENS, MARC LEONHARDT, and MARTIN POSPIECH: 'Fierz-complete NJL model study II: towards the fixed-point and phase structure of hot and dense two-flavor QCD'. *Physical Review D* (2018), vol. 97(7): p. 076010 (cit. on pp. 27, 36).

115. BRAUN, JENS, MARC LEONHARDT, and MARTIN POSPIECH: 'Fierz-complete NJL model study III: Emergence from quark-gluon dynamics'. *Physical Review D* (2020), vol. 101(3): p. 036004 (cit. on pp. 27, 36).

116. Bowler, R. D. and M. C. Birse: 'A nonlocal, covariant generalisation of the NJL model'. *Nuclear Physics A* (1995), vol. 582(3-4): pp. 655–664 (cit. on p. 27).

117. 't Hooft, G.: 'Computation of the quantum effects due to a four-dimensional pseudoparticle'. *Physical Review D* (1976), vol. 14(12): pp. 3432–3450 (cit. on p. 29).

118. Particle Data Group et al.: 'Review of Particle Physics'. *Progress of Theoretical and Experimental Physics* (2022), vol. 2022(8): p. 083C01 (cit. on p. 29).

119. Rapp, R., E. Shuryak, and I. Zahed: 'A chiral crystal in cold QCD matter at intermediate densities?' *Physical Review D* (2001), vol. 63(3): p. 034008 (cit. on p. 33).

120. David Nathan, Walters: 'The 3 1 dimensional lattice NJL model at non-zero baryon density.' 2003 (cit. on pp. 34, 58).

121. Carignano, Stefano, Michael Buballa, and Wael Elkamhawy: 'Consistent parameter fixing in the quark-meson model with vacuum fluctuations'. *Physical Review D* (2016), vol. 94(3): p. 034023 (cit. on p. 35).

122. Fu, Wei-jie: 'QCD at finite temperature and density within the fRG approach: An overview'. *Communications in Theoretical Physics* (2022), vol. 74(9): p. 097304 (cit. on p. 35).

123. Otto, Konstantin, Christopher Busch, and Bernd-Jochen Schaefer: 'Regulator scheme dependence of the chiral phase transition at high densities'. *Physical Review D* (2022), vol. 106(9): p. 094018 (cit. on p. 35).

124. Carignano, Stefano, Dominik Nickel, and Michael Buballa: 'Influence of vector interaction and Polyakov loop dynamics on inhomogeneous chiral symmetry breaking phases'. *Physical Review D* (2010), vol. 82: p. 054009 (cit. on pp. 35, 36, 38, 77).

125. Zhang, Zhao and Teiji Kunihiro: 'Vector interaction, charge neutrality and multiple chiral critical point structures'. *Phys. Rev. D* (2009), vol. 80: p. 014015 (cit. on p. 35).

126. Kitazawa, M., T. Koide, T. Kunihiro, and Y. Nemoto: 'Chiral and Color-superconducting Phase Transitions with Vector Interaction in a Simple Model'. *Progress of Theoretical Physics* (2002), vol. 108(5): pp. 929–951 (cit. on p. 35).

127. Kitazawa, Masakiyo, Tomoi Koide, Teiji Kunihiro, and Yukio Nemoto: 'Chiral and Color-superconducting Phase Transitions with Vector Interaction in a Simple Model (Addenda)'. *Progress of Theoretical Physics* (2002), vol. 108(5): pp. 929–951 (cit. on p. 35).

128. Hong, Seok-In and John B. Kogut: 'Symmetry Nonrestoration in a Gross-Neveu Model with Random Chemical Potential'. *Physical Review D* (2001), vol. 63(8): p. 085014 (cit. on p. 35).

129. Carignano, Stefano and Michael Buballa: 'Inhomogeneous chiral condensates in three-flavor quark matter'. *Physical Review D* (2020), vol. 101(1): p. 014026 (cit. on pp. 37–39).

130. Schnetz, Oliver, Michael Thies, and Konrad Urlichs: 'Full Phase Diagram of the Massive Gross-Neveu Model'. *Annals of Physics* (2006), vol. 321(11): pp. 2604–2637 (cit. on p. 38).

131. Basar, Gokce and Gerald V. Dunne: 'Self-consistent crystalline condensate in chiral Gross-Neveu and Bogoliubov-de Gennes systems'. *Physical Review Letters* (2008), vol. 100: p. 200404 (cit. on p. 38).

132. Nickel, Dominik and Michael Buballa: 'Solitonic ground states in (color-) superconductivity'. *Physical Review D* (2009), vol. 79(5): p. 054009 (cit. on pp. 38, 63).

133. Carignano, Stefano and Michael Buballa: 'Two-dimensional chiral crystals in the NJL model'. *Physical Review D* (2012), vol. 86: p. 074018 (cit. on pp. 38, 67).

134. Abuki, Hiroaki, Daisuke Ishibashi, and Katsuhiko Suzuki: 'Crystalline chiral condensates off the tricritical point in a generalized Ginzburg-Landau approach'. *Physical Review D* (2012), vol. 85(7): p. 074002 (cit. on p. 38).

135. Sasaki, C., B. Friman, and K. Redlich: 'Quark Number Fluctuations in a Chiral Model at Finite Baryon Chemical Potential'. *Physical Review D* (2007), vol. 75(5): p. 054026 (cit. on p. 38).

136. Mori, Yuto, Kouji Kashiwa, and Akira Ohnishi: 'Lefschetz thimbles in fermionic effective models with repulsive vector-field'. *Physics Letters B* (2018), vol. 781: pp. 688–693 (cit. on p. 38).

137. Winstel, Marc, Laurin Pannullo, and Marc Wagner: 'Phase diagram of the 2+1-dimensional Gross-Neveu model with chiral imbalance'. *PoS* (2022), vol. LATTICE2021: p. 381 (cit. on p. 39).

138. Braun, Jens, Stefan Finkbeiner, Felix Karbstein, and Dietrich Roscher: 'On the Search for Inhomogeneous Phases in Fermionic Models'. 2014 (cit. on p. 39).

139. Motta, Theo F., Julian Bernhardt, Michael Buballa, and Christian S. Fischer: 'Towards a Stability Analysis of Inhomogeneous Phases in QCD'. (2023), vol. preprint (cit. on p. 39).

140. Rechenberger, Stefan: *Inhomogeneous phases at high density: In Search for Instabilities*. Talk at the 1st retreat of the CRC-TR 211 presented by D. H. Rischke, March 12-16, ZiF Bielefeld and corresponding private notes. 2018 (cit. on p. 45).

141. Pannullo, Laurin, Marc Wagner, and Marc Winstel. 2023, in preparation (cit. on p. 52).

142. Walters, David N. and Simon Hands: 'The Lattice NJL Model at Non-zero Baryon and Isospin Densities'. *Nuclear Physics B - Proceedings Supplements* (2005), vol. 140: pp. 532–534 (cit. on p. 52).

143. Nielsen, Holger Bech and M. Ninomiya: 'No go theorem for regularizing chiral fermions'. *Physics Letters* (1981), vol. 105B: pp. 219–223 (cit. on p. 54).

144. Drell, Sidney D., Marvin Weinstein, and Shimon Yankielowicz: 'Strong-coupling field theories. II. Fermions and gauge fields on a lattice'. *Physical Review D* (1976), vol. 14(6): pp. 1627–1647 (cit. on pp. 54, 55).

145. Drell, S. D., Marvin Weinstein, and S. Yankielowicz: 'Variational approach to strong coupling field theory. 1. Phi**4 theory'. *Physical Review D* (1976), vol. 14: p. 487 (cit. on pp. 54, 55).

146. Wellegehausen, Björn H., Daniel Schmidt, and Andreas Wipf: 'Critical flavor number of the Thirring model in three dimensions'. *Physical Review D* (2017), vol. 96(9): p. 094504 (cit. on p. 55).

147. Lenz, Julian, Björn Wellegehausen, and Andreas Wipf: 'Absence of chiral symmetry breaking in Thirring models in 1+2 dimensions'. *Physical Review D* (2019), vol. 100(5): p. 054501 (cit. on p. 55).

148. Cohen, Y., S. Elitzur, and E. Rabinovici: 'A Monte Carlo study of the Gross-Neveu model'. *Nuclear Physics* (1983), vol. B220: pp. 102–118 (cit. on pp. 56, 57).

149. Carignano, Stefano and Michael Buballa: 'Inhomogeneous islands and continents in the Nambu–Jona-Lasinio model'. 2012 (cit. on p. 63).

150. Winstel, Marc and Laurin Pannullo: 'Stability of homogeneous chiral phases against inhomogeneous perturbations in 2+1 dimensions'. *PoS* (2023), vol. LATTICE2022: p. 195 (cit. on p. 67).

151. URLICHS, KONRAD: 'Baryons and baryonic matter in four-fermion interaction models'. PhD thesis. Friedrich-Alexander-Universität Erlangen-Nürnberg, 2007 (cit. on pp. 82, 87).

152. INAGAKI, T., D. KIMURA, and A. KVINIKHIDZE: 'π and σ mesons at finite temperature and density in the NJL model with dimensional regularization'. *Physical Review D* (2008), vol. 77(11): p. 116004 (cit. on p. 86).

153. INAGAKI, T., D. KIMURA, H. KOHYAMA, and A. KVINIKHIDZE: 'Phase Diagram of Nambu-Jona-Lasinio Model with Dimensional Regularization'. *Phys. Rev. D* (2012), vol. 86: p. 116013 (cit. on p. 86).

154. ADHIKARI, PRABAL, JENS O. ANDERSEN, and PATRICK KNESCHKE: 'Inhomogeneous chiral condensate in the quark-meson model'. *Physical Review D* (2017), vol. 96(1): p. 016013 (cit. on p. 87).

155. PAIS, ABRAHAM: 'On Spinors in n Dimensions'. *Journal of Mathematical Physics* (2004), vol. 3(6): pp. 1135–1139 (cit. on p. 95).

156. MURAYAMA, HITOSHI: 'Lecture notes on 'Clifford Algebra and Spin(N) representations'' (cit. on p. 95).

157. LENZ, JULIAN J.: 'Spontaneous Symmetry Breaking In Four Fermion Theories'. Master's thesis. Jena: Friedrich-Schiller-Universität Jena, 2018 (cit. on p. 112).

158. GRADSHTEYN, ISRAIL SOLOMONOWITSCH, JOSSIF MOISSEJEWITSCH RYZHIK, and ALAN JEFFREY: *Table of integrals, series, and products*. 7th ed. Amsterdam ; Boston: Academic Press, 2007. 1171 pp. (cit. on p. 112).

List of Figures

Acronyms

CP critical endpoint. 2, 3, 22–25, 34, 36, 40, 65–67, 76, 80, 90, 91, 97

DSE Dyson-Schwinger equation. 2, 40

FF four-fermion. 7–17, 20, 28–30, 36, 39, 40, 52, 58, 70, 83, 91
FRG functional renormalization group. 2, 3, 17, 18, 27, 35, 36, 40, 55

GL Ginzburg-Landau. 39, 40
GN Gross-Neveu. 2–5, 7, 13, 16, 19–23, 25, 27–29, 34–36, 40, 41, 47, 48, 52, 55, 58, 62, 67, 69, 76, 80, 83, 84, 87, 89–93, 95–97, 119, 121
gNJL general Nambu-Jona-Lasinio. 7–10, 19, 28, 92

HBP homogeneously broken phase. 1, 3, 22, 23, 25, 27, 28, 34, 35, 47, 48, 50–52, 65–68, 73–77, 84, 90
HS Hubbard-Stratonovich. 8, 36

IP inhomogeneous phase. 1–5, 22–24, 27, 28, 34–36, 39, 40, 48, 50, 52, 55, 56, 63, 65–67, 69–71, 73–76, 80, 83, 84, 87–93, 95–98
IR infrared. 13, 17, 26, 28

LFT lattice field theory. 15, 39, 40, 56–59, 62, 67, 68, 80, 106, 109, 115, 116
LP Lifshitz point. 3, 22, 34, 36, 40, 52, 66, 67, 76, 80, 90, 97

MFA mean-field approximation. 4, 5, 7, 11–13, 19–21, 32, 35, 36, 39–41, 55, 95, 96, 98

NJL Nambu-Jona-Lasinio. 2, 4, 5, 7, 10, 13, 15–17, 19, 28–31, 34–36, 40, 41, 55, 58, 59, 61–63, 67, 80, 83, 84, 89–92, 95–98
NMR no medium regularization. 17, 18, 72–74, 76, 80, 95, 138

PSFF complete Lorentz-(pseudo)scalar four-fermion model. 35, 36
PV Pauli-Villars. 14–16, 34, 35, 56, 63, 65, 66, 68–77, 80, 81, 91, 95, 97, 105–107, 109–111, 116, 117, 138

QCD Quantum Chromodynamics. 1–4, 7, 11, 12, 16, 19, 28, 30, 35, 40, 90, 96–98
QFT quantum field theory. 13
QM quark-meson. 2, 18, 35, 36, 41, 96

RG renormalization group. 18, 35, 74

SC spatial momentum cutoff. 14–18, 21, 33, 56, 57, 63, 65, 67–69, 71–77, 80, 81, 85, 95, 97, 106–109, 112–114, 116–118, 121, 122, 138
SP symmetric phase. 1, 3, 22, 23, 34, 47, 50–52, 74, 77, 84, 90, 95
STC space-time momentum cutoff. 16, 17, 57

UV ultra-violet. 13, 14, 16, 17, 21, 32–35, 55, 90, 91, 121

Acknowledgments

Foremost, I want to thank Prof. Marc Wagner for his supervision and guidance over the years. He encouraged me to become an independent researcher and gave me the freedom to pursue my own ideas. I could always count on his support. I also want to thank Prof. Christian Fischer for being the second supervisor for my thesis. My thanks also go to Dr. Michael Buballa serving as the second supervisor in my PhD committee and for sharing his vast knowledge about inhomogeneous phases with me in various discussions.

In particular, I want to thank Marc Winstel and Dr. Adrian Koenigstein, with whom I had the absolute pleasure of working over the last couple of years. I am very grateful for the countless discussions and exciting projects that we had the chance to carry out. I also want to thank my other collaborators during the time of my PhD: Julian Lenz, Michael Mandl, Stefan Rechenberger, Martin Steil, Björn Wellegehausen and Andreas Wipf. Furthermore, I want to thank all members of the A03 project of the CRC TR 211 for the many interesting discussions.

Moreover, I want to thank Dr. Alessandro Sciarra for being my mentor and helping me find my own path in physics. I want to thank my office colleague and friend Lasse Müller for the great time we had while sharing an office for the last 5 years.

Last, but certainly not least, I want to thank Laura for keeping me from going mad and supporting me every step of the way.

I acknowledge the support provided by the HGS-HIRe graduate school and the CRC TR 211.